
UNIVERSITAT POLITÈCNICA DE VALÈNCIA

Universitat Politècnica de València

Doctoral Thesis

PhD in Technologies for Health and Well-Being

# Strategies for guidance and electrical and biological stimulation in a neural regeneration device

Fernando Gisbert Roca

September 2022

Supervised by:

Prof. Manuel Monleón Pradas

Dr. Cristina Martínez Ramos

# Acknowledgements

Una vez terminado el trabajo, aprovecho este espacio para recordar y reconocer el apoyo tanto de personas como de instituciones las cuales me han apoyado en esta etapa de formación y han hecho posible la culminación de la presente tesis doctoral. Por ello, a continuación, procedo a expresar en detalle mis agradecimientos a todas ellas.

En primer lugar, agradezco de forma especial a mis directores de tesis el Prof. Manuel Monleón Pradas y la Dr. Cristina Martínez Ramos tanto por aceptarme como doctorando como por todo su apoyo a lo largo de los años de trabajo que han dado lugar a esta tesis doctoral. Al Prof. Manuel Monleón Pradas, por su confianza en mí y por su necesaria guía necesaria tanto para el desarrollo de esta tesis como para mi formación científica, investigadora y docente. A la Dr. Cristina Martínez Ramos por su imprescindible ayuda para el desarrollo de esta tesis, especialmente en el trabajo de laboratorio al que tantísimas horas ha dedicado junto a mí. Gracias Cristina por haber estado siempre dispuesta a prestarme toda la ayuda que he necesitado, tanto a nivel científico como personal. Asimismo, agradezco haber dispuesto siempre de los medios necesarios para poder llevar a cabo las diferentes actividades que he realizado durante el desarrollo de la tesis.

Agradezco también de forma especial al Prof. Lluis Mir y en general al Centro de Aspectos Metabólicos y Sistémicos de la Oncogénesis (METSY) del Instituto Gustave Roussy de la Universidad Paris-Saclay por permitirme realizar una estancia que supuso un gran impulso a mi formación científica. Asimismo, agradezco especialmente al Dr. Franck M. André y a Leslie Vallet por la gran ayuda que me brindaron durante mi estancia, especialmente en el trabajo de laboratorio.

También quiero agradecer al Prof. Enrique Blas Ferrer y al Dr. Eugenio Martínez Paredes por su imprescindible ayuda durante la experimentación *in vivo* presente en esta tesis doctoral. Sin vuestra ayuda no hubiera sido posible.

Quiero recordar y agradecer también a los diferentes profesores que me han tutorizado durante las prácticas docentes de mi fase predoctoral y también me han ayudado durante el trabajo experimental, especialmente a los profesores Jorge Más Estellés, Vicente Compañ Moreno, Abel García Bernabé, José Molina Mateo y Ana Jesús Vidaurre Garayo, entre otros. Asimismo, quiero recordar a mis compañeros del Centro de Biomateriales e Ingeniería Tisular, siempre dispuestos a prestarme su ayuda cuando la he necesitado, en especial a la Dra. Laura Rodríguez Doblado de la que tantas cosas he aprendido.

Por supuesto, quiero agradecer a mi familia todo el apoyo que me ha dado durante mi etapa universitaria y especialmente durante mi etapa predoctoral, siguiendo esta tesis desde casa. Gracias por vuestros ánimos y ayuda y por inculcarme la cultura del esfuerzo, el sacrificio y el trabajo duro que tanto he necesitado durante estos años.

Por último, reconozco la ayuda de los diferentes proyectos del Ministerio de Economía y Competitividad del Gobierno de España que han hecho posible la financiación de esta tesis doctoral: MAT2015-66666-C3-1-R, DPI2015-72863-EXP y AEI RTI2018-095872-B-C21-C22/ERDF. Y, por supuesto, agradezco la ayuda FPU16/01833 del Ministerio de Universidades del Gobierno de España, sin la cual no hubiera podido realizar esta tesis doctoral.

# Resumen

Actualmente las lesiones del sistema nervioso periférico que conllevan una pérdida de continuidad de los haces axonales suelen implicar secuelas de tipo permanente. Es cierto que en el sistema nervioso periférico existe una cierta regeneración natural de los tractos axonales dañados, pero solamente cuando el espacio entre ambos extremos de la lesión es pequeño, como máximo de 5 mm. Si el espacio es mayor que esta distancia la regeneración no sucede de forma natural y se crea un neuroma traumático. Por tanto, estas lesiones largas requieren de una intervención quirúrgica para puentear la lesión, normalmente con un nervio autógrafo del propio paciente o un nervio alógrafo de un cadáver. No obstante, su uso presenta diversos inconvenientes, como la morbilidad del sitio donante donde puede ocurrir un neuroma, la necesidad de realizar una segunda cirugía, la diferencia de tamaño entre nervio receptor y donante o la necesidad de inmunosupresión en el caso de los nervios alógrafos. Por ello, la ingeniería de tejidos trabaja en el desarrollo de los conductos de guiado nervioso que incorporan estrategias para guiar topográficamente la regeneración, así como células y moléculas bioactivas.

La presente tesis doctoral presenta un nuevo conducto de guiado nervioso con una aproximación multimodular para su aplicación en la regeneración de lesiones nerviosas largas (a partir de 15 mm) que hace uso de conductos tubulares huecos modulares de ácido hialurónico (HA) que contienen en su interior una estructura tubular de microfibras de ácido poliláctico (PLA). La estructura fibrilar aporta un guiado topográfico necesario para guiar el crecimiento axonal durante la regeneración a la vez que mantiene unidos los diferentes módulos de HA. Por su parte, los conductos de HA son un hidrogel que evita adherencias con el tejido circundante. A su vez, proporcionan

un soporte sobre el que pueden crecer células presembradas. En concreto se ha optado por presembrar células de Schwann, las cuales son unas células gliales de soporte críticas para la regeneración del sistema nervioso periférico. Se ha observado que dichas células son capaces recubrir por completo las paredes internas de los conductos de HA formando una estructura tipo vaina, así como de recubrir las microfibras de PLA creciendo en dirección longitudinal. Los experimentos *in vivo* en modelo de nervio ciático de conejo han mostrado que la aproximación multimodular mejora significativamente la regeneración nerviosa gracias a proporcionar una mejor neovascularización. A su vez, gracias a las células de Schwann presembradas se ha logrado una mejora adicional de la regeneración nerviosa gracias a su efecto favorecedor del crecimiento axonal.

Además, se han estudiado diferentes mejoras aplicables al conducto de guiado nervioso con el objetivo de mejorar los resultados obtenidos *in vivo*. Gracias a la incorporación de fibroína de seda a los conductos de HA se ha logrado mejorar sus propiedades mecánicas y biológicas. Asimismo, también se ha desarrollado un sustrato electroconductor de microfibras de PLA recubiertas con el polímero electroconductor Polipirrol gracias al cual se ha observado *in vitro* que es capaz de mejorar el crecimiento axonal al aplicar una estimulación eléctrica. Además, mediante un sistema de modificación génica de las células de Schwann por electrotransfección se ha logrado aumentar su secreción del factor neurotrófico derivado del cerebro (BDNF), gracias a lo cual se ha observado que se incrementa la velocidad de crecimiento axonal *in vitro*.

# Resum

Actualment les lesions del sistema nerviós perifèric que comporten una pèrdua de continuïtat dels feixos axonals solen implicar seqüeles de tipus permanent. És cert que al sistema nerviós perifèric hi ha una certa regeneració natural dels tractes axonals danyats, però només quan l'espai entre ambdós extrems de la lesió és petit, com a màxim de 5 mm. Si l'espai és més gran que aquesta distància la regeneració no succeeix de manera natural i es crea un neuroma traumàtic. Per tant, aquestes lesions llargues requereixen una intervenció quirúrgica per pontejar la lesió, normalment amb un nervi autògraf del pacient o un nervi al·lògraf d'un cadàver. No obstant això, el seu ús presenta diversos inconvenients, com la morbilitat del lloc donant on pot ocórrer un neuroma, la necessitat de fer una segona cirurgia, la diferència de mida entre nervi receptor i donant o la necessitat d'immunosupressió en el cas dels nervis al·lògrafs . Per això, l'enginyeria de teixits treballa en el desenvolupament dels conductes de guiatge nerviós que incorporen estratègies per guiar topogràficament la regeneració, així com cèl·lules i molècules bioactives.

Aquesta tesi doctoral presenta un nou conducte de guiatge nerviós amb una aproximació multimodular per a la seva aplicació en la regeneració de lesions nervioses llargues (a partir de 15 mm) que fa ús de conductes tubulars buits modulars d'àcid hialurònic (HA) que contenen al seu interior una estructura tubular de microfibres d'àcid polilàctic (PLA). L'estructura fibril·lar aporta un guiatge topogràfic necessari per guiar el creixement axonal durant la regeneració alhora que manté units els diferents mòduls d'HA. Per part seva, els conductes d'HA són un hidrogel que evita adherències amb el teixit circumdant. Alhora, proporcionen un suport sobre el qual poden créixer cèl·lules presembrades. En concret s'ha optat per presembrar cèl·lules de Schwann, les

quals són unes cèl·lules glials de suport crítiques per a la regeneració del sistema nerviós perifèric. S'ha observat que aquestes cèl·lules són capaces de recobrir completament les parets internes dels conductes d'HA formant una estructura tipus beina, així com de recobrir les microfibres de PLA creixent en direcció longitudinal. Els experiments *in vivo* en model de nervi ciàtic de conill han mostrat que l'aproximació multimodular millora significativament la regeneració nerviosa gràcies a proporcionar una millor neovascularització. Alhora, gràcies a les cèl·lules de Schwann presembrades s'ha aconseguit una millora addicional de la regeneració nerviosa gràcies al seu efecte afavoridor del creixement axonal.

A més, s'han estudiat diferents millores aplicables al conducte de guiatge nerviós per tal de millorar els resultats obtinguts *in vivo*. Gràcies a la incorporació de fibroïna de seda als conductes d'HA s'ha aconseguit millorar les seues propietats mecàniques i biològiques. També s'ha desenvolupat un substrat electroconductor de microfibres de PLA recobertes amb el polímer electroconductor Polipirrol gràcies al qual s'ha observat *in vitro* que és capaç de millorar el creixement axonal quan s'aplica una estimulació elèctrica. A més, mitjançant un sistema de modificació gènica de les cèl·lules de Schwann per electrotransfecció s'ha aconseguit augmentar la secreció del factor neurotròfic derivat del cervell (BDNF), gràcies a la qual cosa s'ha observat que s'incrementa la velocitat de creixement axonal *in vitro*.

# Summary

Currently, lesions of the peripheral nervous system that lead to a loss of continuity of the axonal bundles usually involve permanent sequelae. It is true that in the peripheral nervous system there is some natural regeneration of damaged axonal tracts, but only when the space between the two ends of the lesion is small, at most 5 mm. If the gap is greater than this distance, regeneration does not occur naturally, and a traumatic neuroma is created. Therefore, these long injuries require surgical intervention to bridge the injury, usually with an autograph nerve from the patient or an allograph nerve from a cadaver. However, its use has various drawbacks, such as the morbidity of the donor site where a neuroma can occur, the need to perform a second surgery, the difference in size between the recipient and donor nerves, or the need for immunosuppression in the case of allograft nerves. For this reason, tissue engineering works on the development of nerve guidance conduits that incorporate strategies to topographically guide the regeneration, as well as cells and bioactive molecules.

This doctoral thesis presents a new nerve guidance conduit with a multimodular approach for its application in the regeneration of long nerve lesions (from 15 mm) that makes use of modular hollow tubular conduits of hyaluronic acid (HA) that contain in their inside a tubular structure of microfibers of polylactic acid (PLA). The fibrillar structure provides the necessary topographic guidance to guide axonal growth during regeneration while keeping the different HA modules together. For their part, the HA conduits are a hydrogel that prevents adhesions with the surrounding tissue. In turn, they provide a support on which preseeded cells can grow. Specifically, it has been decided to pre-seed Schwann cells, which are glial support cells that are critical for the regeneration of the peripheral nervous system. It has been observed that these cells are

capable of completely covering the inner walls of the HA conduits, forming a sheath-like structure, as well as covering the PLA microfibers by growing in a longitudinal direction. *In vivo* experiments in a rabbit sciatic nerve model have shown that the multimodular approach significantly improves nerve regeneration by providing better neovascularization. In turn, thanks to the pre-seeded Schwann cells, an additional improvement in nerve regeneration has been achieved thanks to its promoting effect on axonal growth.

In addition, different improvements applicable to the nerve guidance conduit have been studied with the aim of improving the results obtained *in vivo*. Thanks to the incorporation of silk fibroin into HA conduits, their mechanical and biological properties have been improved. Likewise, an electroconductive substrate of PLA microfibers coated with the electroconductive polymer Polypyrrole has also been developed, thanks to which it has been observed *in vitro* that it is capable of improving axonal growth by applying electrical stimulation. In addition, by means of a gene modification system of Schwann cells by electrotransfection, it has been possible to increase their secretion of brain-derived neurotrophic factor (BDNF), thanks to which it has been observed that the speed of axonal growth is increased *in vitro*.

# Abbreviations and acronyms

| | |
|---|---|
| **AC** | Alternating current |
| **ANOVA** | Analysis of variance |
| **ATR** | Attenuated total reflection |
| **BDNF** | Brain-derived neurotrophic factor |
| **BM-MSC** | Bone marrow derived mesenchymal stem cells |
| **BSA** | Bovine Serum Albumin |
| **CD31** | Cluster of differentiation 31 |
| **CMV** | Cytomegalovirus |
| **CNS** | Central nervous system |
| **CNTF** | Ciliary neurotrophic factor |
| **CPLA** | Cast PLA film |
| **CR** | Coating ratio |
| **DAPI** | 4′,6-diamidino-2-phenylindole |
| **DBS** | Dodecylbenzenesulfonate |
| **DC** | Direct current |
| **DCM** | Dichloromethane |
| **DEAE** | Diethylaminoethyl |
| **DMEM** | Dulbecco's modified Eagle's medium |

| | |
|---|---|
| **DMF** | Dimethylformamide |
| **DMFCs** | Direct methanol fuel cells |
| **DNA** | Deoxyribonucleic acid |
| **DPBS** | Dulbecco's phosphate buffered saline |
| **DRG** | Dorsal root ganglion |
| **DVS** | Divinyl sulfone |
| **DXR** | Doxorubicin |
| **EDC** | 1-Ethyl-3-(3-dimethylaminopropyl) carbodiimide |
| **EDTA** | Ethylenediamine tetraacetic acid |
| **EIS** | Electrochemical impedance spectroscopy |
| **ELISA** | Enzyme-Linked ImmunoSorbent Assay |
| **EMA** | European Medicines Agency |
| **EP** | Electrode polarization |
| **EPLA** | Electrospun-PLA membrane |
| **eSCs** | BDNF-SEP transfected SCs |
| **ESC** | Embryonic stem cells |
| **FBS** | Fetal bovine serum |
| **FDA** | Food and drugs administration |
| **FESEM** | Field Emission Scanning Electron Microscopy |

| | |
|---|---|
| **FITC** | Fluorescein IsoTioCyanate |
| **FTIR** | Fourier-transform infrared spectroscopy |
| **GAGs** | Glycosaminoglycans |
| **GDNF** | Glial cell-derived neurotrophic factor |
| **GFP** | Green fluorescent protein |
| **HA** | Hyaluronic acid |
| **HE** | Hematoxylin-Eosin |
| **HEPES** | 4-(2-hydroxyethyl)-1-piperazineethanesulfonic acid |
| **hSC** | Human Schwann cells |
| **HUVEC** | Human Umbilical Vein Endothelial Cells |
| **ICPs** | Intrinsically conductive polymers |
| **IL-6** | Interleukin-6 |
| **iPSC** | Induced pluripotent stem cells |
| **LIF** | Leukemia inhibitory factor |
| **MF** | Microfibre |
| **MMC** | Multimodular conduit |
| **MSC** | Mesenchymal stem cells |
| **N-CAM** | Neural cell adhesion molecule |
| **NF** | Nanofibre |
| **NGC** | Nerve guidance conduit |

| | |
|---|---|
| **NGF** | Nerve growth factor |
| **NS** | Nervous system |
| **NSC** | Neural stem cells |
| **NT-3** | Neurotrophin-3 |
| **PANI** | Polyalanine |
| **PB** | Phosphate buffer |
| **PBS** | Phosphate buffered saline |
| **PC** | Pulsating current |
| **PCL** | Poly-caprolactone |
| **pCMV** | Porcine cytomegalovirus |
| **PEDOT** | Poly(3,4-ethylenedioxythiophene) |
| **PEMFCs** | Polymer electrolyte membrane fuel cells |
| **PFA** | Paraformaldehyde |
| **PGA** | Polyglycolic acid |
| **PLA** | Polylactic acid |
| **PMNs** | Polymorphonuclear leukocytes |
| **PNI** | Peripheral nerve injury |
| **PNS** | Peripheral nervous system |
| **PPy** | Polypyrrole |
| **P/S** | Penicillin/Streptomycin |
| **PSS** | Polystyrene sulfonate |

| | |
|---|---|
| **PTFE** | Polytetrafluoroethylene |
| **pTS** | P-toluenesulfonate |
| **PVA** | Polyvinyl alcohol |
| **Py** | Pyrrole |
| **SCs** | Schwann cells |
| **SCI** | Spinal cord injury |
| **SCM** | Schwann cell culture medium |
| **SD** | Standard deviation |
| **SEM** | Standard error of the mean |
| **SEP** | pH-sensitive fluorophore<br>superecliptic pHluorin |
| **SSA** | Specific surface area |
| **S 100 $\beta$** | S100 calcium-binding protein $\beta$ |
| **TGA** | Thermogravimetric analysis |
| **TNF-$\alpha$** | Tumor necrosis factor-alpha |
| **TUJ-1** | Neuron-specific class III beta-tubulin |
| **UMC** | Unimodular conduit |
| **USA** | United States of America |
| **VEGF** | Vascular endothelial growth factor |

# Index

# 1. General introduction

# 1.1. Previous experience and thesis structure

The previous work carried out by the NeuroCBIT research group in which the present doctoral thesis was developed led, among many other things, to the development of nerve guidance conduits based on hyaluronic acid (HA) [1–3]. The *in vitro* study of these HA conduits made it possible to observe that the Schwann cells (SCs) seeded in their lumen were capable of completely covering their interior, forming an internal sheath of viable cells [2,3]. Likewise, it was also studied the combination of several of these HA conduits, which maintained their structure thanks to a multifilament of polylactic acid (PLA) microfibers that was placed inside them [2]. With this multimodular device of HA channels combined with PLA microfibers, it was observed *in vitro* that the axons of neurons contained in rat dorsal root ganglia seeded at one end of the device were capable of extending along it, where the PLA microfibers served as topographic guidance for axonal extension [2]. Likewise, it was also observed that the SCs seeded inside them favored axonal extension, increasing the distance reached by the axons of the neurons for a given time [2].

Based on these previous results of the research group, the present study addressed the adaptation of the multimodular concept studied *in vitro* for its use *in vivo* in a rabbit sciatic nerve model. In this process, the dimensions of the HA conduits were first scaled, adapting them to the dimensions of the rabbit sciatic nerve, verifying that its porous structure and the inner sheath of pre-seeded SCs could be satisfactorily maintained. Likewise, the use of PLA microfibers was modified, moving from a multifilament to the manufacture of a cylindrical tubular conduit that, while maintaining the structure of the multimodular device, at its ends provided more resistant fixation structures that allowed the suture of the device to the damaged nerve stumps, which led

to a patent of invention [4]. With the subsequent *in vivo* test in a rabbit sciatic nerve model, it was possible to conclude that the multimodular approach of the device was viable, improving the results compared to the use of a long continuous module (Paper 1 of the present doctoral thesis). Likewise, it was observed that the presence of pre-seeded SCs allowed an even greater improvement of nerve regeneration, as was previously observed with *in vitro* studies.

The present study also addresses strategies to improve the performance of the multimodular concept. On the one hand, to improve the mechanical and biological properties of HA conduits, the incorporation of silk fibroin was studied (Paper 2 of the present doctoral thesis), improving the manipulability of the device. On the other hand, to increase the density and speed of nerve fiber growth, electrical and biological stimulation strategies were also studied. First, the coating of PLA fiber substrates with the electroconductive polymer polypyrrole (PPy) was studied to provide electrical conductivity to the fibers used inside the device (Paper 3 of the present doctoral thesis). This allowed us to study different coating protocols, characterizing their physicochemical and electrical properties. Subsequently, *in vitro* biological tests were carried out with PLA fibers coated with PPy studying the SCs behavior and the axonal extension of neurons contained in dorsal root ganglia, comparing the use of nanofibers with the use of microfibers (Paper 4 of the present doctoral thesis). It was possible to conclude, on the one hand, that the PPy coating had beneficial effects on axonal extension and, on the other hand, that the use of microfibers allowed greater axonal growth than the use of nanofibers. Once the best PPy coating method and the best fiber dimension were chosen, a bioreactor was developed for the electrical stimulation of dorsal root ganglia co-cultured with Schwann cells seeded on the electroconductive PLA-PPy microfibers, observing that the electrical stimulation of this substrate had a

favoring effect on axonal growth *in vitro* (Paper 5 of the present doctoral thesis). Also, a method was developed to improve the biological stimulation strategy of the device by using electrotransfected SCs. Modified SCs presented an increased release of brain-derived neurotrophic factor (BDNF) and allowed to increase axonal growth when compared with the use of non-electrotransfected SCs on PLA microfibers coated with PPy (Paper 6 of the present doctoral thesis).

Therefore, in the present doctoral thesis it has been obtained, firstly, a novel multimodular axonal guidance device, which has been patented and tested *in vivo* and, secondly, different upgrades applicable for this device to increase its mechanical and biological properties as well as to include electrical and biological stimulation strategies applicable to the multimodular device in order to improve axonal growth. The future work of this doctoral thesis is the incorporation of the different upgrades to future *in vivo* tests of the device, seeking to improve the results obtained in the first *in vivo* study.

## 1.2. Target population

This project is aimed mainly for the population affected by nerve injuries, both acute and chronic. The work focuses on the treatment of peripheral nerve injuries, although both the device and the techniques that are developed could be applied, with modifications, also for the treatment of central nervous system injuries.

The peripheral nerve injuries (PNI) can disrupt communication signals between the brain and a part of the body and can result in partial or total loss of motor, sensory and autonomic function. PNI are a serious health problem for today's society, with an estimated incidence between 13 and 23 per 100,000 persons per year in the developed countries, what entails that about 20 million people suffer from some type of peripheral neuropathy only in the United States [5,6]. They affect 2.8% of trauma patients, many of

whom become disabled for life. Approximately 360,000 people a year suffer from upper extremity paralytic syndromes due to peripheral nerve injuries in the United States, resulting in more than 8.5 million days with restricted activities and nearly 5 million days in bed or with disability each year [7].

Likewise, worldwide, between 250,000 and 500,000 people suffer a spinal cord injury (SCI) every year [8]. Regarding the global prevalence of SCI, it is between 236 and 1,009 cases per million inhabitants depending on the country studied [9]. To this, it must be added the great economic impact of SCI on health provider systems. In 2013, it was estimated in Canada that the cost associated with a paraplegic patient throughout his life was 1.47 million dollars, while for a tetraplegic patient it was 3.03 million dollars [10].

## 1.3. Nervous system

The nervous system (NS) is divided anatomically into central nervous system (CNS) and peripheral nervous system (PNS). The CNS is made up of the brain and spinal cord, while the PNS is composed of the nerves and the dorsal root ganglia that extend outside the CNS [11]. Among the main functions of the NS we can highlight the coordination of both conscious and reflex movements, the perception of internal and external stimuli and the analysis of sensory information that entails motor responses through muscles or glands [12,13].

The nervous tissue is made up of specialized cells that can be divided into two groups: neurons and glial cells. Neurons are the basic cell unit of the NS and are composed of three differentiated parts: soma or cell body, axons, and dendrites. The axons are responsible for conducting nerve impulses to other neurons or muscle cells, while dendrites are the receptors for these nerve impulses that come from other neurons. Dendrites are usually highly branched, providing many places of communication

between neurons. This is because information flows from the dendrite to the cell body and then to the axon. For this reason, the neuron presents a polarity, so the information flows in a certain direction [11]. The site of nerve impulse transmission between the axon and the dendrite is a specialized area called the synapse. There, chemical substances called neurotransmitters and electrical components are used for the transmission of information [14].

Many axons are surrounded by an insulating substance called myelin, which is made up of glial cells. Myelin acts as an insulator, forming the so-called myelin sheaths. There are gaps in the myelin sheath that are called nodes of Ranvier and play an important role in the way electrical signals travel through the axon [11].

The neuroglia or glial cells are cells whose main function is to support neurons, but they also perform other functions such as defense, myelination, protection or nutrition of neurons [12]. There are six types of glial cells, four belong to the CNS and two to the PNS, as shown in **Table 1**.

| CNS glial cell | PNS glial cells | Basic function |
|---|---|---|
| Astrocytes | Satellite cells | Support |
| Oligodendrocytes | Schwann cells | Isolation, myelination |
| Microglia | | Immune support and phagocytosis |
| Ependymal cells | | Creation of cerebrospinal fluid |

**Table 1.** Glial cell types and their basic function.

The glial cells of the CNS are the astrocytes, the oligodendrocytes, the microglia, and the ependymal cells:

- Astrocytes cover the surface of the blood vessels of the brain and establish contact between the cell bodies of neurons and are responsible for transporting nutrients to neurons. If an injury occurs, astrocytes proliferate to develop scars to repair the nerve tissue. They can intervene in more specific processes such as the passage of chemical substances from the blood to the neurons and also contribute to the blood-brain barrier.
- Oligodendrocytes are the cells that isolate the axons in the CNS. Each of the branches that leave the cell body extends around the axon and isolates it creating a myelin sheath. An oligodendrocyte can provide myelin for various axon segments or for different axons.
- Microglia are the cells whose function is to ingest and digest cellular debris. They act as macrophages in the CNS.
- Ependymal cells are responsible for filtering the blood to produce cerebrospinal fluid that circulates through the CNS. They are similar to epithelial cells because they form a single layer of cells with very tight connections between adjacent cells.

**Figure 1** shows the organization of the cells that constitute the CNS. It can be observed how a single oligodendrocyte can create myelin sheaths for the axons of different neurons.

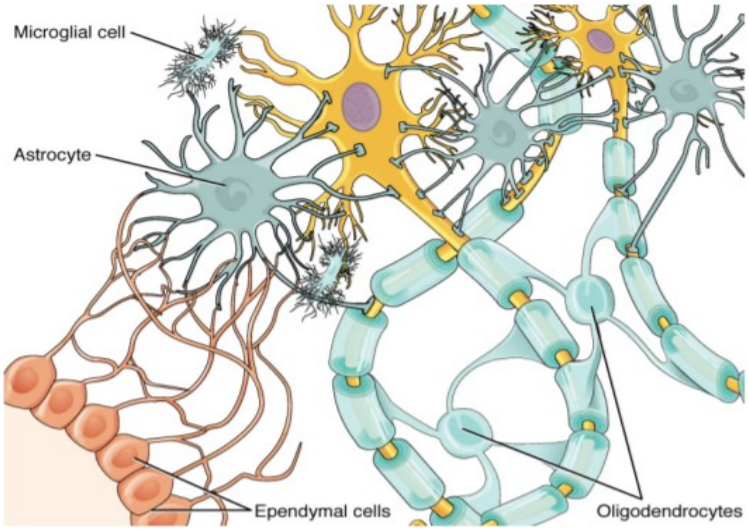


**Figure 1.** Glial cells in the CNS [15].

The glial cells of the PNS are the satellite cells and the Schwann cells:

- Satellite cells are responsible for providing support to the cell bodies of neurons and perform functions similar to those of astrocytes in the CNS.
- Schwann cells are equivalent to oligodendrocytes but in the PNS. They are responsible for isolating axons with myelin, but unlike oligodendrocytes, a Schwann cell envelops a single segment of the axon, so several Schwann cells are required to form the myelin sheath of an axon.

In the same way as for the CNS, the organization of the neuroglia cells in the PNS is shown in **Figure 2**. It can be observed that several Schwann cells are necessary to form the myelin sheath of an axon.

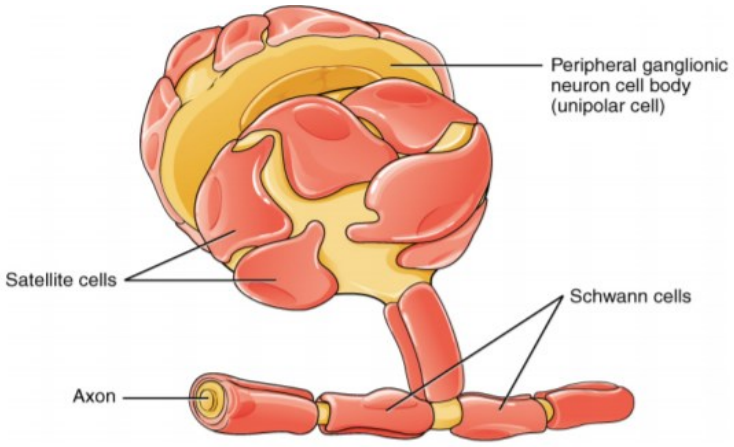


**Figure 2.** Glial cells in the PNS [15].

# 1.4. Nervous system injuries

Given the structural differences between the PNS and the CNS, the mechanisms involved in the regeneration processes after an injury occurs are very different. In addition, the injury can be due to different situations such as traumatic injuries, interruption of the blood supply or neurodegenerative diseases that damage cell bodies, somas or axons [16].

According to the studies that have been carried out over the years, the CNS shows an absence of axonal regeneration capacity after injury compared to the PNS. This is because a hostile environment for axonal growth is created in the CNS after an injury occurs [17]. Neuroinflammation of the injured site occurs in the same way in the PNS and the CNS, but only in the CNS it is accompanied by rapid glial scar formation, while astrocyte-derived extracellular matrix components at the injury site, such as tensin and proteoglycans, inhibit growth [18,19]. In the CNS, the few neurons who survive the injury try to regenerate the tissue, but they find this impenetrable glial scar composed of myelin and cellular debris, as well as astrocytes, oligodendrocytes and microglia that hinder the regeneration process. Fibroblasts, monocytes, and macrophages can also be present in the glial scar. As a result, neurons cannot reach their synaptic target [20]. In

**Figure 3**, the degeneration process produced in the CNS after an injury can be observed.

Therefore, the lack of functional regeneration of axons in the injured CNS is due to an existing imbalance between the mechanisms that promote and those that inhibit axonal growth, as well as the low expression of neurotrophic factors and the presence of powerful molecular barriers that prevent the success of this regeneration. However, various studies have shown that the injured axons of the CNS can show a certain regenerative capacity when the environment is suitable [17]. Furthermore, it has also been shown that CNS neurons had the ability to regenerate in the presence of nerve grafts from the PNS, demonstrating that it is possible to promote axonal growth of damaged CNS neurons when they are in a suitable environment provided by grafts from the PNS [21]. This shows that the type of environment that surrounds the axon is decisive in its regenerative response.

Regarding the PNS, a process called Wallerian degeneration occurs in the first 18-48 hours after the injury, where the distal segment of the axon degenerates and the supporting cells aid neuronal regeneration (**Figure 3**) [16,22]. Schwann cells surrounding the axon undergo various phenotypic changes and begin to remove myelin debris and axonal debris and promote the production of proinflammatory cytokines such as TNF-a to recruit macrophages to the injury site. Then, both phagocytic cells, macrophages and Schwann cells act together to eliminate myelin and axonal debris [20,23]. In addition to cleaning these debris, they produce cytokines such as interleukin-6 and other neurotrophic factors, which stimulate neuronal survival, organize a regeneration pathway to guide axonal growth, and promote axonal growth, creating a favorable environment that promotes the division and proliferation of Schwann in the distal area of the lesion [16,22,24]. Schwann cells secrete growth factors, such as nerve growth factor

(NGF), favoring the survival of neurons, stimulating axonal regeneration and forming the Büngner bands [25]. These bands consist of a cylinder formed by Schwann cells and their basal lamina that helps to guide the axon from the proximal to the distal end. Under optimal conditions, growth can spread at a rate of 1-3 mm/day [26]. This process of Wallerian degeneration and regeneration through the Büngner bands can be seen in **Figure 3**.

It is important to note that regeneration of the PNS is not always achieved naturally, especially for severe PNI, when there is a long gap between the proximal and distal stumps of the injured nerve. When the gap is greater than 5 mm the regeneration cannot be achieved naturally and a traumatic neuroma is created [27]. Therefore, these long lesions require a surgical intervention [27], especially when there is a complete section of the nerve and its supporting structures. Furthermore, when a direct end-to-end connection of the stumps without applying tension is not possible because part of the nerve is lost, an autograph nerve from the patient, a nerve allograph from a cadaver donor or an artificial nerve conduit is required to bridge the gap [28,29].

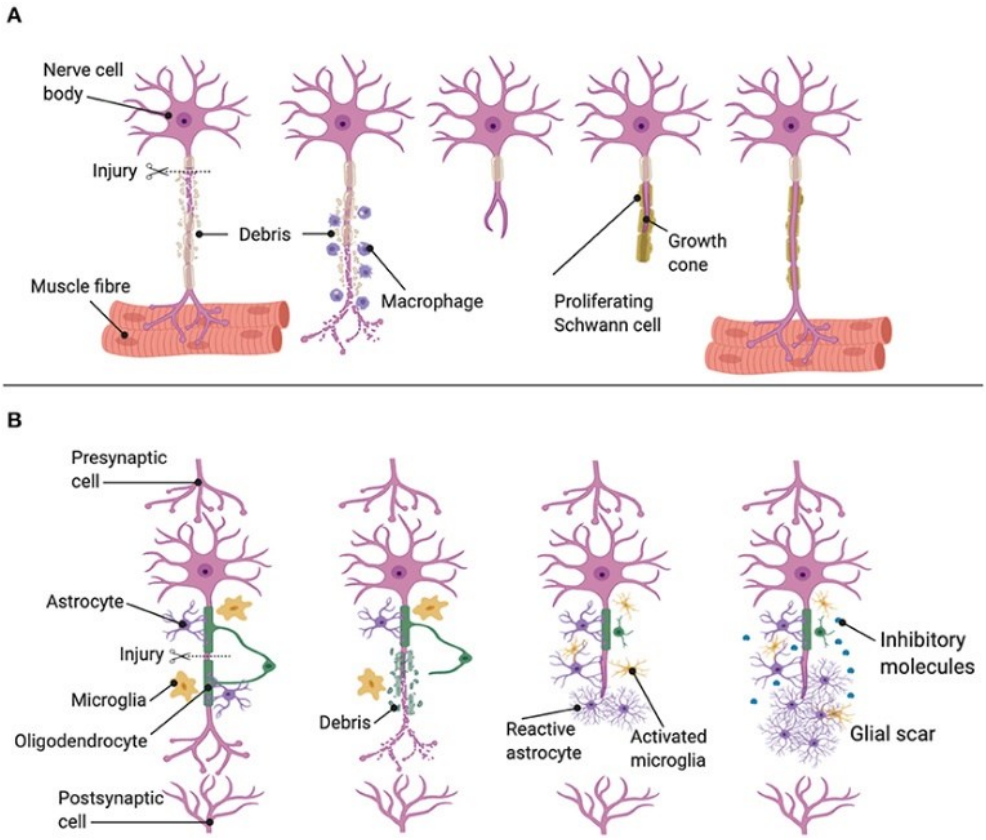


**Figure 3.** A: Regeneration in the PNS. B: Regeneration in the CNS. [16]

On the one hand, the use of autograph nerves presents several disadvantages, such the increase in cost and operative time due to performing a second surgery, and the morbidity of the donor site, where the formation of a neuroma can occur [30–32]. On the other hand, nerve allographs present potential side effects related with host immunosuppression [29,33]. For these reasons, biomaterial engineered constructs called nerve guidance conduits (NGCs) have been developed for the repair of nerve injuries [34–36]. Some of them have been approved by the U.S Food and Drugs Administration (FDA) and the European Medicines Agency (EMA) and are commercially available for the clinical treatment of PNI, such as NeuraGen®, NeuroMatrix™, Neuroflex™, NeuroMend™, and NeuraWrap™ [37,38]. However, they present several disadvantages such as limitations on the gap length and size that can be repaired, poor biocompatibility, and inefficient stimulation of nerve regeneration. For these reasons,

they are only employed in specific clinical cases and more research is needed in the field of NGCs [39–41].

## 1.5. Nervous tissue engineering

Tissue engineering consists in the development of a functional substitute for damaged tissue and has three main components: scaffold for transplantation and cell support, cells to create a functional matrix, and bioactive factors that regulate cell activity (**Figure 4**).

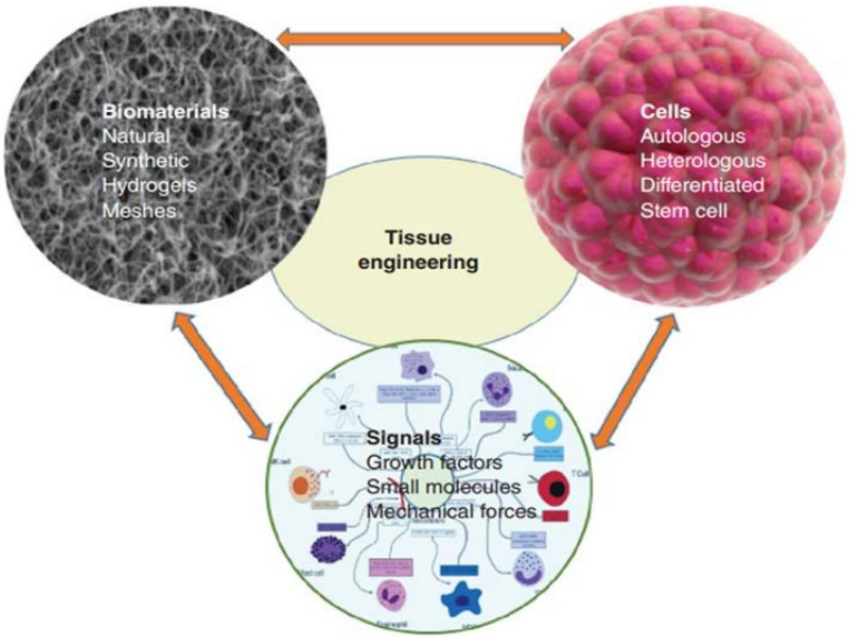


**Figure 4.** Fundamentals of tissue engineering [42].

The main problem of a nerve injury is the alteration of the tissue itself, so the studies have shown that a bridge is necessary to connect both extremes of the injury and to serve as support for regeneration. In addition, this support must imitate the natural nervous structure, achieving certain porosity to allow cell migration and imitating the biological properties of the native environment [43].

Regarding these lesions, autografts, cadaveric donor grafts, or xenografts (animal graft) have been tested [44,45]. However, these types of therapies present

important disadvantages, such as the inefficiency of the donor nerve, incompatibility, or the need for immunosuppression to avoid rejection [44,45]. Therefore, there is a need for the use of tissue engineering to develop scaffolds and biomaterials with the aim of improve the repairing of nerve injuries.

The nervous tissue engineering aims to create a bridge through the length of the lesion that helps to regenerate the damaged tissue while also helps to recover its function. Due to the complex organization of the nervous system, many strategies have been studied over the years to try to achieve these objectives and, therefore, many different scaffolds have been developed.

In the case of NS pathologies, the main objective of the biomaterials is to provide a permissive environment for the regeneration of axons. Thus, the ideal mechanism for regeneration would be to create a suitable artificial substrate for growth that connects the damaged nerve endings [46]. Many devices have been designed to assist regeneration, from natural or synthetic biomaterials to peripheral tissue grafts, acellular muscle tissue, or blood vessels [47–49]. Although they have very different properties, all these approaches have in common the tubular three-dimensional structure, which is intended to mimic the nervous tract.

Tubular supports or nerve canals protect regenerating axons from the external inhibitory environment. These structures, in addition to guiding axonal growth in one direction, are thought to reduce the infiltration of fibrous tissue, provide a conduit for the diffusion of neurotrophic factors, and allow the diffusion of macromolecules between the interior of the device and the surroundings [50,51].

Advances in tissue engineering in recent years have made it possible to combine cells and biomaterials, which provide physical support for cells. For nerve cell adhesion,

migration and subsequent tissue regeneration, scaffolds have been widely applied in tissue engineering.

Some of the most important properties that a NGC must present are summarized in the following points [17,52]:

- Present a tubular structure with the desired dimensions. It must be sterilizable so it can be safely implanted in the body.
- Be biodegradable, but also stable and resistant during regeneration, so that it is replaced by the extracellular matrix of the new cells.
- Be semi-permeable to allow the passage of nutrients, factors, and other components of the extracellular environment into the canal, as well as for cellular debris to escape to the outside and do not create a toxic environment inside the canal. At the same time, the NGC must be impermeable to the passage of cells to allow a better regeneration of the axons by preventing them from being greatly influenced by the external inflammatory and hostile environment.
- It must not provoke a sustained inflammatory or toxic response after implantation in the body.
- It must have an acceptable useful life.
- The degradation time must coincide with the healing or regeneration process.
- It must have appropriate mechanical properties for the indicated application and the variation in mechanical properties with degradation must be compatible with the healing or regeneration process.
- The degradation products must be non-toxic and must be able to be metabolized and eliminated from the body.
- It must have adequate permeability and processability for the intended application.

- Being highly porous and with interconnected pores to allow the seeding of cells in high densities and to facilitate the infiltration and formation of blood vessels.

In conclusion, the ideal structure of a scaffold depends on the tissue to be regenerated. Due to the particularity of nerve regeneration, a NGC can possess other properties that can be beneficial for nervous regeneration (**Figure 5**). Some of these characteristics include aspects such as an aligned structure to guide axonal growth, good electrical conductivity for applying a electrical stimulation that accelerates axonal growth [53], a multichannel or multifilament support or the previous seeding of supportive cells. In addition, the release of bioactive molecules from the material such us growth factors or drugs can be interesting, since its controlled release over time can prolong its effect during the regeneration time.

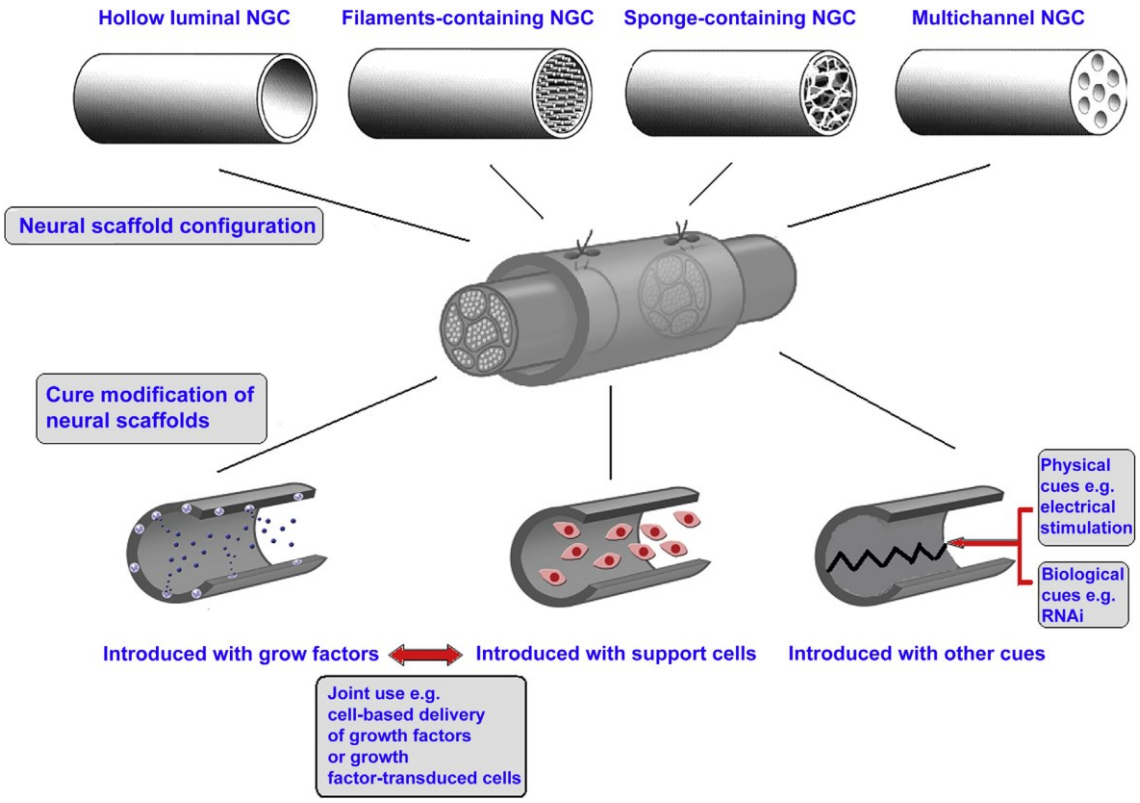


**Figure 5.** Ideal properties of a scaffold for nerve regeneration [54].

Once the two ends of the damaged nerve are sutured to each side of the tube, a regeneration process begins that comprises 5 main phases (**Figure 6**) [55,56]:

- **Fluid phase**: First, the nerve endings exude into the canal a protein-rich fluid that contains growth-promoting substances such as neurotrophic factors and extracellular matrix molecules.
- **Matrix phase:** During the first week a fibrin matrix is formed that provides support for the migration of Schwann cells, fibroblasts, and macrophages.
- **Cell phase**: During the second week the migration of perineural, endothelial and Schwann cells occurs. The cells then line up and proliferate throughout the fibrin matrix. It is important to highlight the importance of the presence of Schwann cells since they can support their own survival thanks to autocrine circuits and block apoptosis, thereby increasing the potential for axonal growth.
- **Axonal phase:** Between the second and fourth week, the axonal phase appears in which the axonal cables lengthen until they connect both ends of the lesion.
- **Myelination phase:** Finally, between weeks 6 to 16, Schwann cells change their proliferative phenotype for a more mature phenotype. These mature Schwann cells envelop the regenerated axons to form the myelin sheath, thus creating mature myelinated axons.

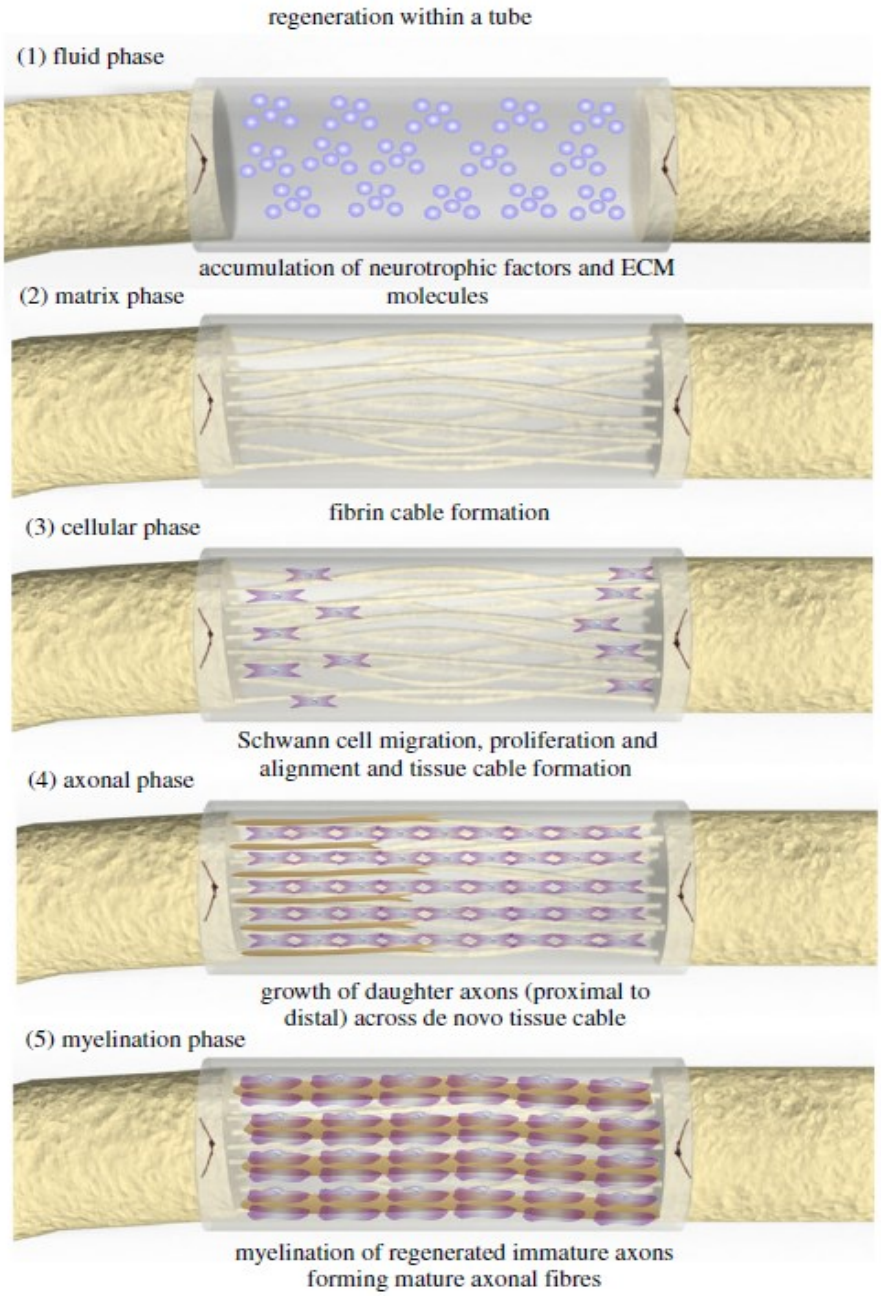


**Figure 6.** Intubation of a damaged nerve and sequence of regenerative events that lead to the growth of a new nerve inside a nerve guidance conduit [55].

# 1.6. Hyaluronic acid

For the fabrication of the NGCs employed in this work, hyaluronic acid (HA) has been chosen, which is one of the most widely used polymers for the assisted regeneration of the nervous system [57,58]. HA is a linear polysaccharide (polymer formed by sugars) that belongs to the glycosaminoglycans (GAGs) since it contains a

type of amino sugar. The monomeric unit of HA is a disaccharide of D-glucuronic acid and D-N-acetylglucosamine linked by β-1,4 and β-1,3 glycosidic bonds, which in the polymer form unbranched chains that can extend up to molecular weights on the scale of the millions of Daltons (**Figure 7**) [59].

HA is found mainly in vertebrates, where it is a component of the extracellular matrix in practically all tissues, mainly skin, joints and bones [60,61]. The highest concentrations of HA in the body appear in connective tissues such as the umbilical cord, synovial fluid, and vitreous humor. In an adult human we can find up to 15 grams of dry HA, 5 of which are renewed every day, being processed continuously through the lymphatic system and the blood [62,63].

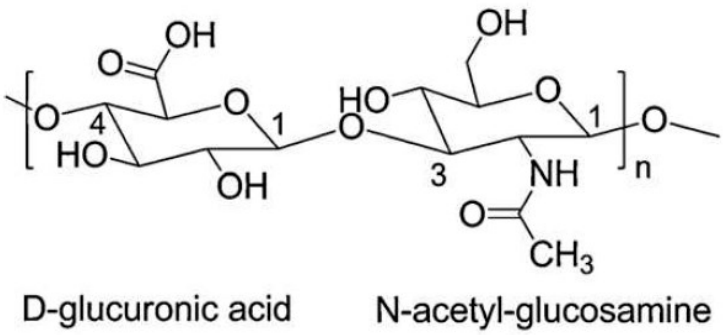


**Figure 7.** Chemical structure of hyaluronic acid. Numbers indicate reactive points [59].

The main properties of HA as a material derive from its structure and folding in aqueous solution. At physiological pH it behaves like a polyanion when the carboxyl group of glucuronic acid ionizes, acquiring a high capacity to attract and bind water molecules [64]. HA has unique physicochemical and biological properties, some of the most outstanding are its hygroscopic nature, which allows it to have functions of filling spaces and absorption of proteins, and its viscoelastic properties, which allow it to adapt and modify according to the cellular and extracellular environment [62]. It is also highly biocompatible, completely biodegradable, and non-immunogenic [62,65].

However, its properties as a biomaterial-vehicle for the transplantation of cells in therapeutic formulations are normally insufficient, being limited to injections containing cells in suspension since it is a viscous fluid and not a solid. Even so, these applications require the use of chemical crosslinking reactions for *in situ* crosslinking, creating relatively stable hydrogels capable of retaining cells [66,67].

There are different types of chemical modifications of HA, most of them focused on the formation of hydrogels to improve its properties in terms of manageability and functionality as a biomaterial. Another reason for cross-linking HA is its relatively short residence time in tissues. There are several molecules and chemical reactions with the ability to crosslink HA chains [68]. Most of them make use of the carboxyl group of its D-glucuronic sugar due to its reactivity and accessibility to create esters. Another possibility is to make use of hydroxyl groups to create ethers. Other strategies include the use of chemical derivatives of HA, which contain thiol groups or are functionalized with other groups [69,70]. The most widely used crosslinkers to obtain hydrogels from HA are glutaraldehyde, 1-ethyl-3-(3-dimethylaminopropyl) carbodiimide (EDC), diepoxy polyethylene glycol and divinylsulfone (DVS). In this work, we will focus on the second type of crosslinking, where under alkaline conditions (pH>12) and at room temperature, the crosslinking agent (DVS) reacts with HA, generating a bis-ethylsulfone crosslink between the hydroxyl groups of the HA chains. In this way, covalent bonds are formed between several different chains of HA in a few minutes. Although the crosslinkers like DVS can be cytotoxic (especially due to their reactivity), this problem disappears once they react with HA and the reaction residues are removed.

The type of molecule used for cross-linking is normally not as important in the final product as any effect caused on the HA molecule during the reaction. What is most decisive for the final properties of the hydrogel is the crosslinking density, whose

maximum value will be in 1:1 proportion of crosslinker with respect to the disaccharide unit of HA, assuming 100% effectiveness of the reaction [71]. This crosslinking will affect the swelling capacity, mechanical properties, and degradability of the hydrogels, which will condition the factors release, the integrity after implantation, and the migration capacity of the cells through the material [67,70,72,73]. The crosslinking of HA not only allows to obtain stable hydrogels, also opens the possibility of creating three-dimensional structures or scaffolds. These structures could be created prior to seeding with cells, facilitating the design of implants applicable to different therapies.

Regarding the biological properties of HA, if its molecular weight is high (>100 kDa), it inhibits cell proliferation, and has anti-inflammatory, antiangiogenic and immunosuppressive properties [65]. However, if its molecular weight is low (<100 kDa), HA has opposite effects since it promotes cell migration and proliferation in addition to having a pro-inflammatory and immunostimulatory function and favoring the formation of blood vessels [59]. This characteristic makes HA a very suitable material for regeneration since, initially, the polymer will have a high molecular weight in the form of a scaffold and will produce an anti-inflammatory and immunosuppressive effect in the environment that will be favorable for the good adaptation of the porous structure into the environment. As it is a biodegradable biopolymer, as time goes by, small chains of HA will be released, decreasing their molecular weight, generating a favorable effect for cell proliferation and angiogenesis.

For these reasons, HA is gaining relevance in the field of tissue engineering since it manages to mimic the extracellular matrix, offering a multitude of advantages. In addition, recent studies have proved the usefulness of HA scaffolds and hydrogels for nervous tissue regeneration, as it reduces the glial scar formation [57,58].

The use of HA is approved by the FDA (Food and Drug Administration) in multiple applications and clinical therapies. It is commonly used as a biomaterial in ophthalmology, otology, aesthetic medicine, and rheumatology, among other fields. It is also employed to lubricate and protect soft tissues during surgeries, as a separator to prevent adhesions between organs and tissues, and as a coating on skin wounds and ulcers to prevent desiccation, protect against damaging agents, and promote healing [74]. Other more advanced uses include its use as a hydrogel (after chemical crosslinking) for drug delivery, alone or loaded with drug-bearing microparticles [75]. Cross-linked HA microspheres have also been used to transport and release DNA plasmids and antibodies [76]. There are multiple patents about the use of hyaluronic acid in new products and clinical applications, with several products currently available in the market [77–79].

# 1.7. Silk fibroin

Silk is a natural protein that can be obtained from the cocoons of various types of caterpillars or silkworms. Silk obtained from the cocoons of the captive-bred Chinese silk moth *Bombyx mori* was used in this work. The silk emitted by the silkworm is made up of two main proteins, fibroin and sericin. Fibroin forms the structural core of silk, while sericin is a sticky material that surrounds the fibroin, as shown in **Figure 8** [80]. The total mass of silk is composed of 20 to 30% sericin and 70 to 80% silk fibroin (SF). SF is the protein responsible for biocompatibility and bioactivity, while sericin has been shown to cause undesirable inflammatory and immune responses. For this reason, the silk undergoes a degumming process that consists of boiling the silk cocoons in an alkaline solution in order to obtain pure silk fibroin (without traces of sericin) that can be used as a biomaterial [81–83]. Several tests with degummed SF (without sericin) have revealed that only very mild inflammatory responses occur *in vivo* with this material,

and these responses are much lower than those observed with other commonly used biomaterials such as collagen or polylactic acid [84]. Therefore, SF has proven to be a biomaterial with high biocompatibility in both *in vitro* and *in vivo* studies, avoiding unwanted immune responses caused by sericin [82].

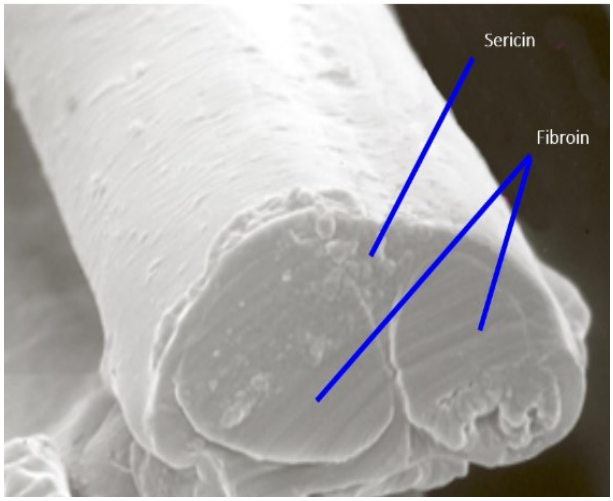


**Figure 8.** Scanning electron microscope (SEM) image showing the two components of silk: fibroin forming the center and sericin around it [80].

Regarding its chemical composition, the SF of *Bombyx mori* is mostly composed of the repetitive structure shown in **Figure 9**, formed by the amino acids glycine (Gly), alanine (Ala) and serine (Ser) in an approximate molar ratio of 3:2:1, respectively [80]. Regarding its amino acid composition, the SF of *Bombyx mori* contains a higher proportion of the three amino acids that form its repeating structure (**Figure 9**), with 45% glycine, 29% alanine and 12% serine. The remaining 13% is made up of tyrosine, valine, aspartic acid, arginine, glutamic acid, isoleucine, leucine, phenylalanine and threonine [80].

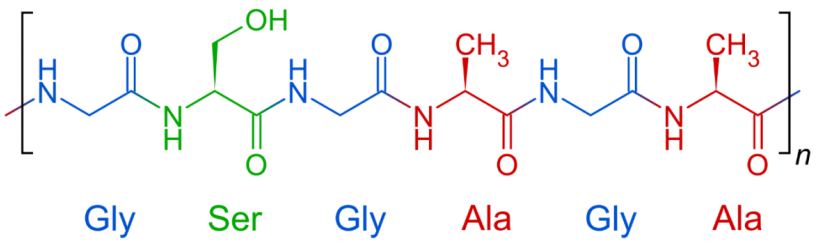


**Figure 9.** Primary structure of the SF of *Bombyx mori* [80].

The high proportion of glycine, which is the smallest amino acid, is what allows the tight packing of SF, obtaining strong fibers resistant to breakage. The high tensile strength of SF comes from the large number of hydrogen bonds it presents, which are not easily broken since the force is distributed among all of them [80].

*Bombyx mori* SF fibers have been employed as suture materials for centuries [82]. SF has mechanical, chemical and biological properties superior to those of most natural or synthetic polymers, presenting a unique combination of excellent mechanical properties, biocompatibility, and biodegradability in a physiological environment, as well as easy handling, sterilization and functionalization of its surface [81,85]. This has led to its wide use in biomedical applications, especially for wound healing and engineering of bone tissue, cartilage, tendons, and ligaments [81,82,85]. For example, in applications related to wound healing, SF-based materials have been shown to improve the adhesion of keratinocytes and fibroblasts *in vitro*, while inducing less inflammation compared to other commercially used products [86].

SF has been proposed for various tissue engineering applications in a wide variety of forms, including membranes, sponges, hydrogels, and three-dimensional scaffolds [84,86]. More recently, the application of SF as a biomaterial for peripheral nerve regeneration has grown to become a new field of research. SF has been shown to be biocompatible with dorsal root ganglia and Schwann cells without showing significant cytotoxic effects under *in vitro* conditions. In addition, NGCs based on SF have been implanted in rat sciatic nerve lesions with a gap of 1 cm in length with a positive nerve regeneration [81]. In addition to its application in the PNS, the application of SF in CNS regeneration has also been investigated. It has been concluded that SF has good biocompatibility with hippocampal neurons, supporting their survival and growth without showing any significant cytotoxic effect on their phenotype or cellular

functions. This supports the possible potential use of SF in the manufacture of NGCs to treat CNS injuries or diseases [81].

# 1.8. Polylactic acid

Several natural polymers such as collagen, gelatin or hyaluronic acid have been applied in the regeneration of the NS, having great potential since they favor and promote cell adhesion and growth in addition to being able to be manufactured in multitudes. However, their mechanical properties are quite poor and in many cases the degradation is much greater than the rate of regeneration of the host tissue, so they may not provide adequate support for regeneration [16,43]. For this reason, synthetic materials like polyglycolic acid (PGA), polylactic acid (PLA) or poly-caprolactone (PCL) are the best option for some applications, since they can compensate the deficiencies of natural biomaterials such as control over biodegradability to ensure better support in regeneration [87].

In this work we will focus on the use of PLA (**Figure 10**). It is a polymer synthesized from lactic acid, which is biocompatible, biodegradable and bioabsorbable in a medium such as the human body. It is widely used in tissue engineering as it safely degrades along the same metabolic pathway as lactic acid [88]. Its degradation range may depend on the degree of crystallization of the material itself or on whether it is conjugated with another material. PLA can be combined with other materials to improve its mechanical properties, resistance, or electrical conductivity, among many others [89–91].

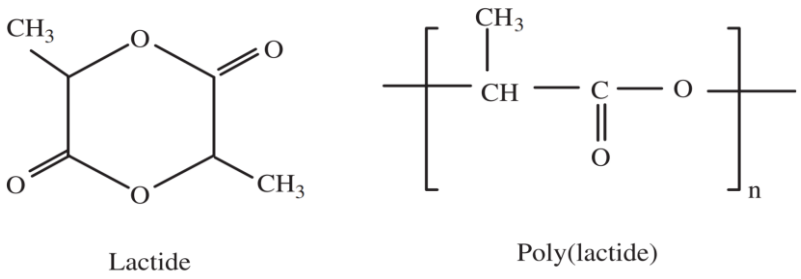


**Figure 10.** Chemical structure of the monomer (left) used to synthesize polylactic acid (right) [52].

PLA allows to form very resistant fibers and has been approved by the FDA since 1971 for the development of improved sutures. Due to the great resistance of PLA fibers, it has been investigated as a scaffold for the replacement of ligaments or non-degradable fibers [92]. Devices based on PLA fibers that act as long-term blood vessels are under investigation [93] and the FDA has also approved an injectable form of PLA to restore or correct facial fat loss or lipoatrophy in people with human immunodeficiency virus [52].

It has been confirmed that PLA is a great biomaterial for the regeneration of the nervous system, especially in the form of a fibrous scaffold since it improves the function of damaged tissue by favoring cell union or drug administration, being tested in rat sciatic nerve regeneration with good results [16,94,95]. These studies confirm that PLA conduits are fully viable scaffolds for long-term replacement of nerve injury.

It also has been studied the efficacy of scaffolds composed of aligned PLA fibers and their application in neural tissue engineering, compared to PLA fiber membranes with a random distribution. The substrates made of PLA aligned fibers highly support neural stem cell culture and improve neurite growth, guiding axonal growth in an aligned direction [96]. Due to these properties of PLA and the positively developed

studies in the field of nerve regeneration, this material has been used in the present work for the regeneration of neural tissue.

# 1.9. Cell therapy in the nervous system

Cell therapy has been widely used in recent years to treat nerve injuries and numerous types of cells have been evaluated to promote axonal growth and achieve regeneration and functional recovery, providing adequate support where axons can regenerate, synthesize growth factors and replace dead cells after an injury [97].

Some cell transplants have been carried out with embryonic stem cells (ESC) that promoted nerve repair in mice, as well as generated precursors similar to SCs, demonstrating that they express myelin protein in the regeneration of peripheral nerves *in vitro*. Studies with ESC for the repair of spinal cord injuries have shown the ability of these cells to differentiate into motor neurons and other cell types such as glial cells or mesenchymal cells that have shown to favor axonal growth [98]. In addition, neural stem cells (NSC) have shown similar results to autografts when seeded on nerve guides, and this type of cells can be modified to overexpress growth factors and improve the regenerative potential [22,97,99].

The regenerative capacity of other cell types has also been studied, such as induced pluripotent stem cells (iPSC) or adult mesenchymal stem cells (MSC), specifically those derived from bone marrow (BM-MSC). They have shown molecular and functional characteristics similar to the SCs of the tissue, so they are a promising source of cells for nerve repair [22,97].

Regarding cell therapies that do not include stem cells, the most promising of all is therapy with SCs. These cells support the axons within the peripheral nervous system and generate the myelin sheath, which isolates the axon segment and thus increases the conduction speed, which is particularly important for those axons with lengths of up to

one meter [25,100,101]. They can be easily isolated from peripheral nerve fibers and expanded for therapeutic use [101].

SCs transplants have been tested for the regeneration of peripheral nerves, since they are capable of synthesizing and secreting neurotrophic factors and adhesion molecules to promote and guide axonal growth and remyelination (**Figure 11**) [97,102]. In addition, SCs secrete signaling molecules that attract macrophages, thus supporting neuronal survival and promoting axonal growth (**Figure 11**) [103]. It has also been observed that exogenous SCs can remyelinate demyelinated axons of the CNS, improving their conduction [17,104].

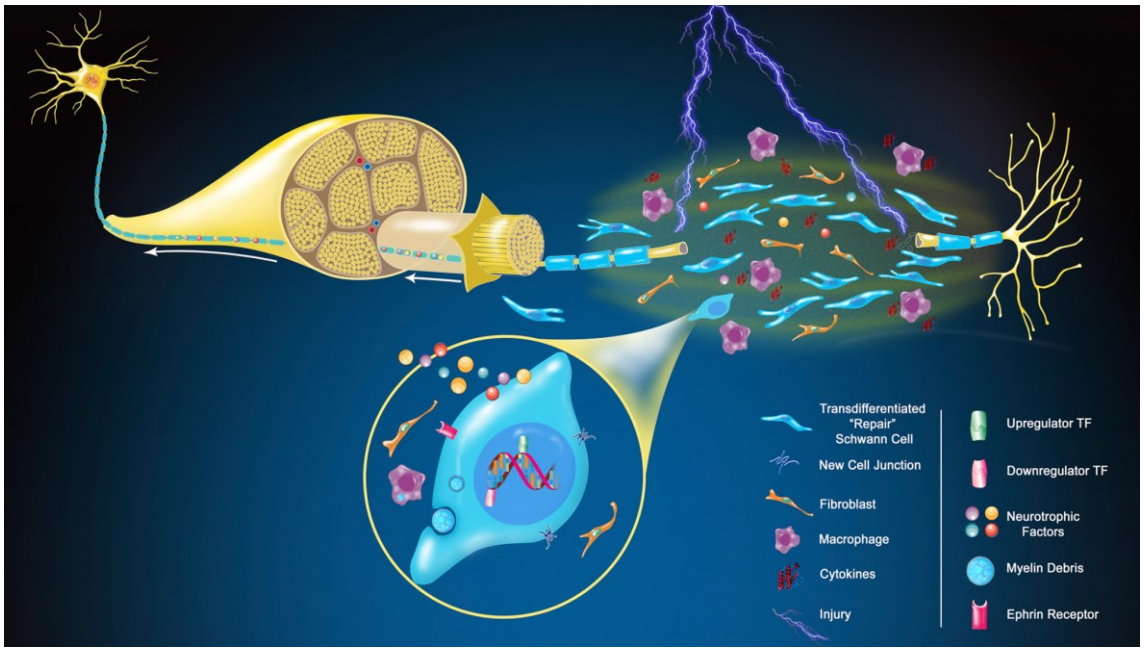


**Figure 11.** SCs repair phenotype in response to a nerve injury [104].

SCs progressively secrete different neurotrophic factors such as nerve growth factor (NGF), glial cell-derived neurotrophic factor (GDNF), brain-derived neurotrophic factor (BDNF), neurotrophin-3 (NT-3), and ciliary neurotrophic factor (CNTF), which promote neuronal regeneration, axonal remodeling and remyelination [104]. Following injury, SCs also secrete extracellular components, adhesion molecules and cytokines to

recruit macrophages and neutrophils [105]. For example, the leukemia inhibitory factor (LIF) and the interleukin-6 (IL-6) act directly on neurons to promote their survival [106]. Subsequently, the recruited macrophages act by maintaining the source of cytokines, since local macrophages are polarized by SCs towards the M2 phenotype, which promotes axonal growth through the release of essential anti-inflammatory mediators [104].

SCs also release the vascular endothelial growth factor (VEGF) and other factors to promote vascularization [107] and together with macrophages, SCs remove myelin that inhibits the regeneration of new axons. Furthermore, SCs improve recovery after injury as they produce cell adhesion molecules (N-CAM, N-cadherin, and integrins) and extracellular matrix proteins (collagens and laminin).

However, the nervous system is a set of organs with a very complex structural organization and despite the numerous studies that have been carried out, cells implanted in the places of injury or degeneration have not been able to establish synaptic connections such as to recover the necessary functionality in the tissue [98]. This is the reason why when dealing with a large lesion it is not enough the exclusive use of cell therapy to regenerate the injury in a satisfactory way. The most promising studies nowadays are those that combine the use of biomaterials as a guide for nerve regeneration with cell therapy [22,102]. Thus, the application of cellular and molecular therapies combined with scaffolds has increased the regenerative capacity in the nervous system [102].

# 1.10. Electrical stimulation in the nervous system

As previously commented, the regeneration of the nervous system is a great challenge due to its scarce intrinsic repair, which is why electrical stimulation plays a very important role in promoting said regeneration. **Figure 12** shows the cellular

processes that are affected by applying electrical stimulation, such as promoting the alignment, migration, proliferation and differentiation of stimulated cells, as well as improving adhesion and the interaction between cells and the biomaterial on which they have been seeded [108].

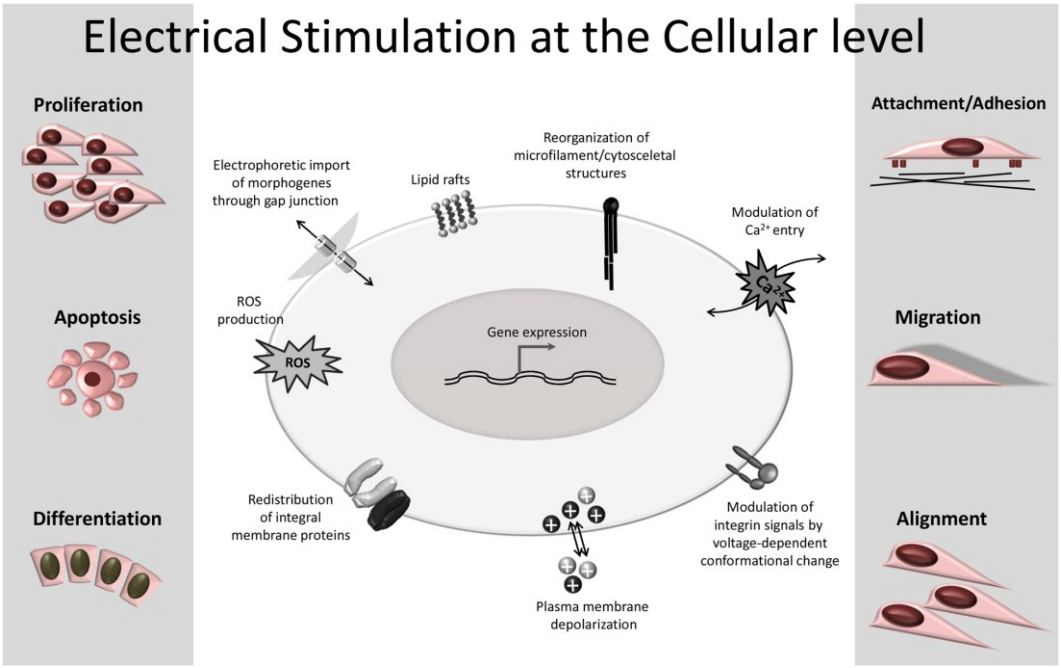


**Figure 12.** Cell mechanisms and functions activated by electrical stimulation [108].

The benefits of electrical stimulation are related to the instantaneous application and the control of the direction, being able to regulate the frequency and the applied voltage. Generally, the electrical stimulation is generated from an external energy source and the currents are classified as direct, alternating and pulsating. Direct current (DC) refers to a current whose magnitude and direction do not change over time, while alternating current (AC) refers to a current whose magnitude and direction change periodically. Pulsating current (PC) is a unidirectional or bidirectional current flow with a short time duration [109].

Exogenous electrical stimulation consists of artificially generating action potentials by inducing electrical charges in the cell. It is a physical method that can be

used both *in vivo* and *in vitro*. Electrical stimulation has been shown to increase the proliferation and the differentiation of neural stem cells into neurons [110] and to guide cell migration [111]. This occurs due to the biophysical changes that are triggered on the cell surface by altering the distribution of charges, which affects the functions of membrane proteins, such as enzymatic activity, complex membrane receptors and ionic transport channels [112]. Given the intrinsic electrical characteristics of neurons, electroactive biomaterials are useful for electrical stimulation.

Commonly, the method used for *in vitro* electrical stimulation consists of applying electrical currents to biological cells or tissues through electrodes. That is, an electric field is established from an electrolytic cell. However, there are other ways to induce a current, such as passing it through a conductive surface, thereby stimulating nerve cells. This type of stimulation is localized, and therefore it is possible to shape the substrate and control it to guide axonal growth. It has been observed that the electrical stimulation of SCs deposited on a conductive support can increase their proliferation and specifically promote their secretion of nerve growth factors. Also functions such as cell adhesion, cell migration, protein secretion and DNA replication are regulated by modifying voltage and current density [113]. This supports the hypothesis that the involvement of SCs at the injury site is a rate limiting factor in PNS repair. *In vivo*, both neurons and supporting cells are exposed to a natural endogenous current created by the epithelium during development and after injury. Hence the importance of not only stimulating neuronal cells but also supporting cells since they support the growth of axons.

**Figure 13** shows the effect of electrical stimulation on SCs when they are on a biocompatible electroconductive material. The alignment with the electric field is explained because as the cell membrane is polarized, the membrane proteins, including

adhesion receptors, are redistributed and move towards the cathode. This occurs because as these membranes are conductive, the electric field impacts negatively charged chemical groups on the cell membrane that are key components of pumps, transport proteins, and proteins that regulate cellular activities. These signals are also transmitted to the integrins of the focal adhesions, regulating cell alignment [114].

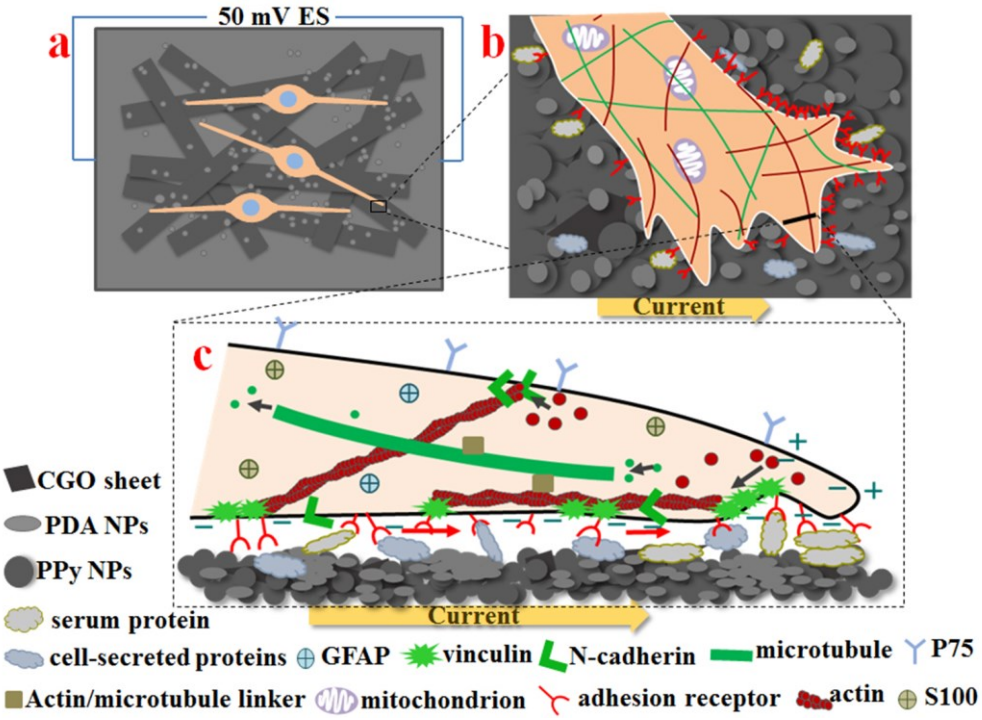


**Figure 13.** Schematic illustration of the alignment of SCs grown in electroconductive materials and subjected to an electric current: (a) alignment of SCs, (b) redistribution of cell membrane receptors, and (c) sectional view of filopodia (red arrows show the direction of movement of adhesion receptors) [114].

Likewise, the mechanism by which an increased neurite extension is achieved under electrical stimulation is related to membrane depolarization, leading to an action potential. The applied electric field results in the enrichment of electric charges on top of the conductive substrate surface, enhancing the extension of filopodia actin in the peripheral domain of the neural growth cone (**Figure 14**). In addition, electrical charges would enrich at the top of the conductive substrate, improving the aggregation of

adhesion receptors and the interaction of adhesion receptors at the leading edge with adhesion molecules on the substrate [115].

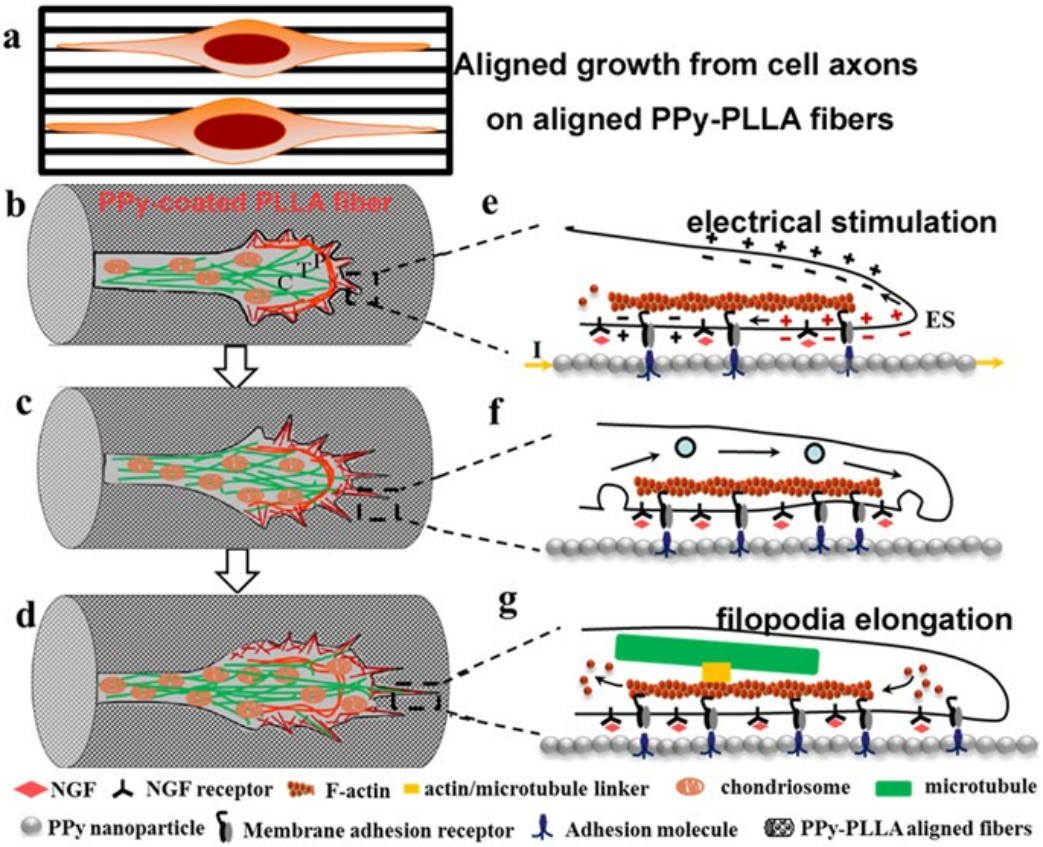


**Figure 14.** Schematic of neurite elongation on aligned electrically conductive PLLA fibers coated with PPy, showing the change of growth cone and the inner change of filopodia during elongation [115].

Thus, one of the important properties that a material applied to tissue engineering must have in the case of regeneration of nervous tissue is the electrical conductivity, since the electrical stimulation of an electroconductive substrate has shown to be beneficial for axonal growth and elongation [16,114–120]. For this reason, it is important to use some electroconductive material that, combined with PLA that is an insulating polymer, is capable to provide electrical conductivity to the substrates. This is the case of conductive polymers, which are materials that combine the properties of metals and conventional polymers. They have great electrical and optical properties

combined with flexibility in processing and ease of synthesis [121]. However, it must be considered that conductive polymers, for the most part, are not biodegradable [121].

Among the conductive polymers that have been applied in tissue engineering, one of them is poly(3,4-ethylenedioxythiophene) (PEDOT), a biomaterial with great electrical and chemical stability that is currently used in biosensors and bioengineering such as neural electrodes [121,122]. Another conductive polymer widely investigated is polyalanine (PANI), a polymer with great ease of synthesis, low cost, and good electrical conductivity. However, it has low flexibility and processability which, combined with its non-biodegradability, has been shown to cause chronic inflammation if implanted. For this reason, PANI is used mainly for biosensors, neuronal probes or for controlled drug administration [121].

One of the emerging electrically conductive materials in nerve regeneration is graphene, which is capable of being chemically modified to control its electrical activity and favor the regeneration of nervous tissue. However, it must be treated to increase cell adhesion and 3D scaffolds can present a small neuroinflammation, although it has not yet been evaluated in enough *in vivo* tests [123]. Another carbon-based materials are carbon nanotubes (CNT), which present excellent electroconductive properties. Despite this, many studies have tried to improve their biocompatibility since they exhibit major safety problems, leading to inflammation and DNA damage. Due to this, CNTs are normally used as additives in biomaterials to improve their conductive properties [123,124]. These coatings have been shown to favor neurite extension and cell migration along nanofibers [122].

# 1.11. Polypyrrole

In this work we have focused on the use of polypyrrole (PPy), the most studied conductive polymer with applications in tissue engineering. It is a material with very good biocompatibility both *in vitro* and *in vivo*, good chemical stability, long-term ambient stability, and high electrical conductivity under physiological conditions [121]. In addition, it can be easily synthesized by chemical or electrochemical polymerization with a low cost [125–128]. **Figure 15** shows the chemical structure of polypyrrole.

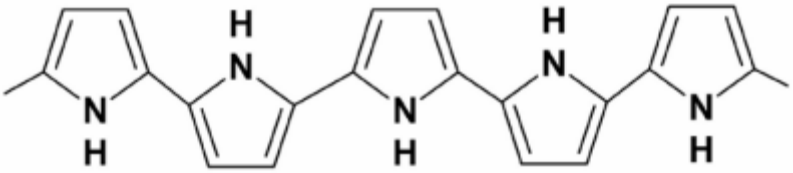

**Figure 15.** Chemical structure of polypyrrole [129].

PPy can be synthesized with different porosities and surfaces, which makes it an ideal material for biomedical applications [121,130]. However, it is not biodegradable and once synthesized it is difficult to process due to its highly cross-linked structures, which limits its direct application in order to produce scaffolds with a specific topography [16,130]. For this reason, PPy is usually employed as a coating for another insulating host polymer with greater mechanical processability, since once polymerized the PPy becomes an intractable and brittle solid [128]. This strategy allows exploiting both the mechanical properties of the insulating host polymer and the electroconductive properties of PPy [128,131,132]. In addition, despite PPy is not biodegradable, if the PPy content of the coating is low it has been observed that it does not prevent the biodegradation of the host polymer and it only could retard it slightly [133–135].

It should be noted that the intrinsically conductive polymers (ICPs) like PPy, PEDOT or PANI are electrical insulators in native state and the electrical conductivity

is achieved by the incorporation of a dopant (an anionic compound) into the polymer matrix. In this process an electron is removed from the valence band or added to the conduction band, generating charge carriers in the form of polarons, bipolarons or solitons that move when subjected to an exogenous electric field [125]. In the case of PPy, several anionic dopants have been studied, such as $Cl^-$, $SO_4^{2-}$, $BF_4^-$, $ClO_4^-$, dodecylbenzenesulfonate (DBS), polystyrene sulfonate (PSS) and p-toluenesulfonate (pTS) [136–141].

PPy has been widely used in biomedical applications, particularly in nerve tissue engineering, exploiting its good biocompatibility and high electrical conductivity [125,128,132,142–145]. PPy has shown in different studies to improve the axonal extension of neurons, favor cell adhesion and induce a greater secretion of growth factors by glial cells when used as a scaffold in conjunction with other materials such as PLA and subjected to an exogenous electric field [114–117].

Apart from biomedical applications, PPy has been applied in many commercial applications such as biosensors, antistatic coatings, solid electrolytic capacitors, polymeric batteries or wearable electronics, among others [131,146–152]. In addition, membranes based on PPy can also be applied in fuel cells as catalyst supports for direct methanol fuel cells (DMFCs) and proton-exchange polymer electrolyte membrane fuel cells (PEMFCs), which extends the range of application of the developed membranes to other fields apart from tissue engineering [153–155].

## 1.12. Gold

Another electrically conductive material that is employed in this work is gold. It is considered chemically inert, and its surfaces show low chemisorption capacity. This causes gold to exhibit low chemical reactivity and little catalytic activity. It was used in

dentistry in the past for its chemical properties such as resistance to acid attacks, stability against corrosion and oxidation and its inert mineral condition. Therefore, clinically, gold presents biocompatibility when in contact with body fluids and tissues, adequate characteristics to avoid immunogenic reactions [156,157].

Furthermore, as it is a metal, it has excellent conductivity and has been used in electrodes and substrates for the electrical stimulation of cells. The use of gold as a material in nerve regeneration has increased in recent years and it can be easily conjugated with other materials and favor a certain cellular orientation [158,159]. In the field of stimulation and modulation of neural activity, due to its excellent conductivity, gold has been used for different applications such as improving cell growth in a satisfactory way [158].

Gold has been commonly used in the form of nanoparticles for its application in biomedicine, due to its properties for the controlled administration of drugs, its excellent biocompatibility, and its low toxicity [160,161]. These nanoparticles are very versatile since they can be conjugated with other materials or molecules. For example, they are being widely studied for diagnosis and therapy in cancer, since their accumulation as a contrast in the tumor site allows their detection, and their conjugation with drugs allows a controlled release of these substances [157]. Also the benefit of gold nanoparticles in the regeneration of the PNS has been proven, observing a growth of neurites 24 hours after applying the treatment [158], and it has also been used as a coating of the surface of a tubular scaffold favoring guidance of axonal growth [116]. In another study, frog sciatic nerves were placed in a matrix composed of flat gold microelectrodes. These were electrically stimulated in order to study the modulation of $Ca^{2+}$ ion concentrations dependent on the electrical current in the muscle [162].

# 1.13. Gene delivery methods. Gene transfer by electroporation.

In recent decades, the development of recombinant DNA technology has occurred, which makes gene transfer possible. The development of these procedures is necessary for the introduction of molecules inside the cells to study the effect that said molecule produces on the cell or to synthesize another molecule. In the second case, the cell is used as a factory for the synthesis of molecules, which has required the optimization of transfer methods to be able to apply them with high efficiency and safety, as well as with the minimal invasiveness [163–165].

The possibility of transferring genetic material into cells has allowed to increase the knowledge about gene regulation and about the function of proteins in eukaryotic cells, tissues, and organisms [163,166]. Living cells present a barrier to the free diffusion of molecules, the plasma membrane, which prevents the loss of fundamental components and prevents the entry of external molecules, thus allowing the existence of product concentration gradients across the membrane [163,166]. To overcome this barrier, many experimental strategies have been designed, some based on the formation of pores, and others based on the transport of molecules through endocytosis, which is the natural macromolecule entry mechanism [163–166].

To introduce molecules into the interior of the cell overcoming its natural barrier, different techniques have been developed that are highly useful in molecular and cellular biology studies, standing out the transduction (viral methods) and transfection (non-viral methods) techniques [163,166,167]. The choice of one of these methods largely depends on the final objective of the experiment and on the availability of suitable equipment [163–165].

Regarding transduction techniques, they consist of processes by which the target cells are infected with a virus that carries the sequence of interest in its genome [163,166,168]. The introduction of DNA into cells by infection is a more complex process than transfection, requiring a greater number of steps, and requiring a longer time. The biological safety problem that the manipulation of certain viruses implies must be considered also. Furthermore, the efficiency of infection can be highly variable, extreme in permissive cells or very low in resistant cells [163,166,168]. The advantage of using viral vectors resides in their innate ability to transfer genetic information into the target cell with high specificity and efficiency [163,166,168]. In addition, it easily achieves a stable transfection, integrating the foreign DNA into the genome of the cell, replicating it as the host genome does, which allows a sustainable transgene expression [163,166,168]. However, viral vectors integrate into the host genome randomly, so tumor suppressor genes can be disrupted, oncogenes can be activated, or essential genes can be interrupted, leading to malignant transformation [166]. Insertional mutagenesis or excessive immune response of the host may make this an unsafe method [166,167]. Therefore, developing alternative non-viral methods for gene delivery is key for medical care.

Regarding cell transfection techniques, these are based on the insertion of exogenous material into the genome without the use of viruses [163,166]. These techniques have been developed specifically for the introduction of nucleic acids into cells and have made it possible to expand the knowledge about replication, gene regulation and the functioning of cells at the molecular level. Cell transfection is currently applied in the field of genetics to produce transgenic plants and animals [169], modified cell lines [170], and the construction of recombinant DNA [171]. In this way, the introduction of a plasmid with a coding and regulatory sequence that allows the production of a desired

protein by the cell is achieved, so the host cell is used as a "factory" for this product [163,166]. There are various methods for introducing and expressing genes into cells. Some are used for the transient or temporary expression of genes, making it possible to obtain the transcription or replication of transfected genes several days after the introduction of DNA [163,166]. Other methods allow stable or permanent expression, at least for an extended period, which is useful in experiments where the formation of cell lines containing genes that are integrated into chromosomal DNA is required [163,166].

In general, transfection techniques can be divided into two groups: chemical methods and physical methods. Chemical methods of cell transfection are those in which complexes are formed so that cells can accept or incorporate a certain molecule into their cytoplasm, through the normal endocytosis mechanism [163,166]. Over the years, various transfection reagents have been developed for this purpose, all with their own characteristics. Among them we can mention calcium phosphate, diethylaminoethyl (DEAE) dextran and lipofection. The first two bind to DNA, forming complexes that can be assimilated by the cell, while lipofection is based on the coating of the DNA molecule in a complex of lipids capable of crossing the membrane [163,166]. Regarding physical methods, they are those in which a mechanical introduction of DNA takes place, such as microinjection, electroporation, protoplast fusion and bombardment of DNA-coated microprojectiles [163–166].

In this work we are going to focus on the method of electroporation, which is a technique to introduce DNA into cells in culture that is carried out by applying electrical pulses to the cells. It causes the opening of pores in the membrane of these cells with the consequent penetration of the DNA present in the electroporation medium (**Figure 16**) [163,166,167,172]. It is based on the application of a high voltage to the cells for a very short period of time to achieve the permeabilization of the membrane. Thus, cells

depolarize their membranes and small holes are formed through which the surrounding molecules penetrate. The electrical impulses used transiently modify the properties of the cell membrane, resulting in reversible permeabilization of the cell [163,166,167,172].

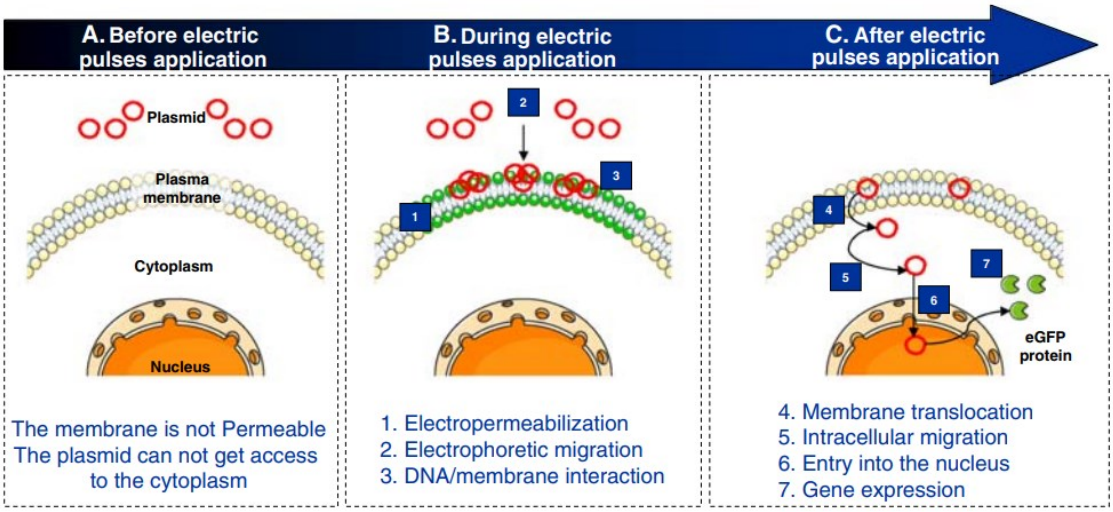


**Figure 16.** DNA electrotransfection [172].

The efficiency of transfection by electroporation is influenced by a series of factors, which need to be optimized to achieve the desired results, among these are: the magnitude of the applied electric field; the duration of the electrical pulse; temperature; concentration, purity, and type of DNA; and ionic composition of the medium [163,166,167,172].

The main advantages of electroporation are that it allows the transfection of refractory cell lines to other methods (its optimization is required for each cell type), it is applied to millions of cells at the same time and the cell transfection efficiency is usually near to 100% for cells that survive the electrical pulse [163,166,167,172]. The biggest disadvantage of electroporation is its cost, since most of the commercially available equipment is expensive, including accessories such as cuvettes and adapters [163,166].

Among gene-based vaccines, 43% of the clinical trials employ naked/plasmid DNA, showing the potential that nonviral methods of gene delivery have in clinical

medicine [173]. Thanks to its safety, efficacy, flexibility and ease of application, electroporation is a promising substitute to virus-mediated gene delivery methods [166,167].

# 1.14. References


1. C. Martínez-Ramos *et al.*, *J. Tissue Eng. Regen. Med.* **2019**, *13*, 509.
2. L. R. Doblado, C. Martínez-Ramos, J. M. García-Verdugo, V. Moreno-Manzano, M. M. Pradas, *J. Neural Eng.* **2021**, *18*, 0460c5.
3. G. Vilariño-Feltrer *et al.*, *Acta Biomater.* **2016**, *30*, 199.
4. M. Monleón Pradas, C. Martínez Ramos, L. Rodríguez Doblado, F. Gisbert Roca, **2021**, ES20210030065 20210127.
5. NIH National Institute of Neurological Disorders and Stroke, **2018**, at <https://www.ninds.nih.gov/Disorders/Patient-Caregiver-Education/Fact-Sheets/Peripheral-Neuropathy-Fact-Sheet>.
6. R. Li *et al.*, *Cell Biochem. Biophys.* **2014**, *68*, 449.
7. J. S. Belkas, M. S. Shoichet, R. Midha, *Neurol. Res.* **2004**, *26*, 151.
8. World Health Organization, **2013**, at <https://www.who.int/news-room/fact-sheets/detail/spinal-cord-injury>.
9. A. Singh, L. Tetreault, S. Kalsi-Ryan, A. Nouri, M. G. Fehlings, *Clin. Epidemiol.* **2014**, *6*, 309.
10. H. Krueger, V. K. Noonan, ; L M Trenaman, ; P Joshi, C. S. Rivers, *Chronic Dis. Inj. Can.* **2013**, *33*.
11. J. A. Betts, J. G., Desaix, P., Johnson, E., Johnson, J. E., Korol, O., Kruse, De., Poe, B., Wise, K. A. Womble, M., & Young, *Acta Otolaryngol.* **1934**, *19*, 6.
12. T. Fortoul, **2013**.

13. J. P. J. Pinel, *Biopsicología* **2006**.

14. P. Brodal, **2010**, at <https://psycnet.apa.org/record/2010-05606-000>.

15. M. A. Clark, M. Douglas, Jung Choi, **2018**, at <https://openstax.org/books/biology-2e/pages/35-1-neurons-and-glial-cells>.

16. L. R. Doblado, C. Martínez-Ramos, M. M. Pradas, *Front. Nanotechnol.* **2021**, *0*, 21.

17. C. E. Schmidt, J. B. Leach, *Annu. Rev. Biomed. Eng.* **2003**, *5*, 293.

18. R. J. McKeon, R. C. Schreiber, J. S. Rudge, J. Silver, *J. Neurosci.* **1991**, *11*, 3398.

19. D. R. Canning, A. Höke, C. J. Malemud, J. Silver, *Int. J. Dev. Neurosci.* **1996**, *14*, 153.

20. K. S. Houschyar *et al.*, *Plast. Surg. Int.* **2016**, *2016*, 1.

21. S. David, A. J. Aguayo, *Science (80-. ).* **1981**, *214*, 931.

22. A. Faroni, S. A. Mobasseri, P. J. Kingham, A. J. Reid, *Adv. Drug Deliv. Rev.* **2015**, *82–83*, 160.

23. D. Purves *et al.*, **2004**, at <https://www.ncbi.nlm.nih.gov/books/NBK10799/>.

24. P. Dubový, I. Klusáková, I. H. Svíženská, *Biomed Res. Int.* **2014**, *691041*.

25. K. R. Jessen, R. Mirsky, *J. Physiol.* **2016**, *594*, 3521.

26. J. W. Griffin, M. C. V. Hogan, A. B. Chhabra, D. N. Deal, *J. Bone Joint Surg. Am.* **2013**, *95*, 2144.

27. X. Jiang, S. H. Lim, H. Q. M. Hai-Quan, S. Y. Chew, *Exp. Neurol.* **2010**, *223*.

28. M. Siemionow, G. Brzezicki, *Int. Rev. Neurobiol.* **2009**, *87*, 141.

29. W. Z. Ray, S. E. Mackinnon, *Exp. Neurol.* **2010**, *223*, 77.

30. J. S. Belkas, M. S. Shoichet, R. Midha, *Neurol. Res.* **2004**, *26*, 151.

31. B. Battiston, S. Geuna, M. Ferrero, P. Tos, *Microsurgery* **2005**, *25*.

32. F. F. A. Ijpma, J. P. A. Nicolai, M. F. Meek, *Ann. Plast. Surg.* **2006**, *57*.
33. A. M. Moore *et al.*, *Muscle and Nerve* **2011**, *44*.
34. J. Moskow *et al.*, *Bioact. Mater.* **2019**, *4*.
35. B. Ferrigno *et al.*, *Bioact. Mater.* **2020**, *5*.
36. M. Zheng *et al.*, *Bioact. Mater.* **2021**, *6*.
37. S. Kehoe, X. F. Zhang, D. Boyd, *Injury* **2012**, *43*, 553.
38. B. J. Parker, D. I. Rhodes, C. M. O'Brien, A. E. Rodda, N. R. Cameron, *Acta Biomater.* **2021**, *135*, 64.
39. P. Chrząszcz *et al.*, *Neurol. Neurochir. Pol.* **2018**, *52*.
40. P. A. Wieringa, A. R. G. de Pinho, S. Micera, R. J. A. van Wezel, L. Moroni, *Adv. Healthc. Mater.* **2018**, *7*.
41. E. O. Johnson, P. N. Soucacos, *Injury* **2008**, *39*.
42. N. Almouemen, H. M. Kelly, C. O'Leary, *Comput. Struct. Biotechnol. J.* **2019**, *17*, 591.
43. L. Tian, M. P. Prabhakaran, S. Ramakrishna, *Regen. Biomater.* **2015**, *2*, 31.
44. W. A. Lackington, A. J. Ryan, F. J. O'Brien, *ACS Biomater. Sci. Eng.* **2017**, *3*, 1221.
45. W. Z. Ray, S. E. Mackinnon, *Exp. Neurol.* **2010**, *223*, 77.
46. N. Zhang, H. Yan, X. Wen, *Brain Res. Rev.* **2005**, *49*, 48.
47. S. M. Hall, K. Enver, *J. Hand Surg. Br.* **1994**, *19*, 444.
48. B. Strauch *et al.*, *J. Reconstr. Microsurg.* **1996**, *12*, 521.
49. C. H. Chau *et al.*, *FASEB J.* **2004**, *18*, 194.
50. J. Lu, P. Waite, *Spine (Phila. Pa. 1976).* **1999**, *24*, 926.
51. E. C. Tsai, P. D. Dalton, M. S. Shoichet, C. H. Tator, *J. Neurotrauma* **2004**, *21*, 789.

52. L. S. Nair, C. T. Laurencin, *Prog. Polym. Sci.* **2007**, *32*, 762.

53. Q. Z. Yu, S. L. Xu, K. H. Zhang, Y. M. Shan, *Neural Regen. Res.* **2013**, *8*, 31.

54. X. Gu, F. Ding, D. F. Williams, *Biomaterials* **2014**, *35*, 6143.

55. W. Daly, L. Yao, D. Zeugolis, A. Windebank, A. Pandit, *J. R. Soc. Interface* **2012**, *9*, 202.

56. S. Kehoe, X. F. Zhang, D. Boyd, *Injury* **2012**, *43*, 553.

57. T. W. Wang, M. Spector, *Acta Biomater.* **2009**, *5*, 2371.

58. X. Wang, J. He, Y. Wang, F. Z. Cui, *Interface Focus* **2012**, *2*, 278.

59. C. E. Schanté, G. Zuber, C. Herlin, T. F. Vandamme, *Carbohydr. Polym.* **2011**, *85*, 469.

60. T. C. Laurent, U. B. G. Laurent, J. R. Fraser, *Ann. Rheum. Dis.* **1995**, *54*, 429.

61. J. R. E. Fraser, T. C. Laurent, U. B. G. Laurent, *J. Intern. Med.* **1997**, *242*, 27.

62. Y. Lei, S. Gojgini, J. Lam, T. Segura, *Biomaterials* **2011**, *32*, 39.

63. J. Lam, N. F. Truong, T. Segura, *Acta Biomater.* **2014**, *10*, 1571.

64. T. Fujii, Y. L. Sun, K. N. An, Z. P. Luo, *J. Biomech.* **2002**, *35*, 527.

65. A. J. Day, C. A. De La Motte, *Trends Immunol.* **2005**, *26*, 637.

66. T. Segura *et al.*, *Biomaterials* **2005**, *26*, 359.

67. M. N. Collins, C. Birkinshaw, *J. Mater. Sci. Mater. Med.* **2008**, *19*, 3335.

68. M. N. Collins, C. Birkinshaw, *J. Appl. Polym. Sci.* **2007**, *104*, 3183.

69. J. B. Leach, C. E. Schmidt, *Biomaterials* **2005**, *26*, 125.

70. S. A. Bencherif *et al.*, *Biomaterials* **2008**, *29*, 1739.

71. A. A. M. Shimojo, A. M. B. Pires, R. Lichy, M. H. A. Santana, *undefined* **2015**, *26*, 506.

72. O. Jeon *et al.*, *Carbohydr. Polym.* **2007**, *3*, 251.

73. D. Eng, M. Caplan, M. Preul, A. Panitch, *Acta Biomater.* **2010**, *6*, 2407.

74. M. Morra, *Biomacromolecules* **2005**, *6*, 1205.

75. A. Vashist, A. Vashist, Y. K. Gupta, S. Ahmad, *J. Mater. Chem. B* **2013**, *2*, 147.

76. G. Kogan, L. Šoltés, R. Stern, P. Gemeiner, *Biotechnol. Lett.* **2007**, *29*, 17.

77. L. Huang, **2014**, US8790683B2.

78. J. Johann, **2013**, EP0413016B1.

79. E. H. Hermida Ochoa, **2004**, US6906044B2.

80. R. J. Lancashire, *Dep. Chem. Univ. West Indies* **2011**, at <http://wwwchem.uwimona.edu.jm/courses/CHEM2402/Textiles/Animal_Fibres.html>.

81. X. Tang *et al.*, *J. Biomed. Mater. Res. - Part A* **2009**, *91*, 166.

82. C. Vepari, D. L. Kaplan, *Prog. Polym. Sci.* **2007**, *32*, 991.

83. L. S. Wray *et al.*, *J. Biomed. Mater. Res. - Part B Appl. Biomater.* **2011**, *99 B*, 89.

84. A. R. Murphy, D. L. Kaplan, *J. Mater. Chem.* **2009**, *19*, 6443.

85. Y. Cheng *et al.*, *J. R. Soc. Interface* **2014**, *11*, 20140305.

86. Z. Karahaliloglu, B. Ercan, E. B. Denkbas, T. J. Webster, *J. Biomed. Mater. Res. - Part A* **2015**, *103*, 135.

87. L. Lu *et al.*, *Biomaterials* **2000**, *21*, 1837.

88. R. Fitzgerald, L. M. Bass, D. J. Goldberg, M. H. Graivier, Z. P. Lorenc, *Aesthetic Surg. J.* **2018**, *38*, S13.

89. C. Liliana Serna, S. Aída Rodríguez de, A. Fred Albán, *Ing. Y Compet.* **2003**, *5*, 16.

90. T. Sudwilai *et al.*, *J Biomater Sci Polym Ed.* **2014**, *25*, 1240.

91. J. F. Zhou *et al.*, *Neural Regen. Res.* **2016**, *11*, 1644.

92. H. H. Lu *et al.*, *Biomaterials* **2005**, *26*, 4805.

93. M. Zilberman, K. D. Nelson, R. C. Eberhart, *J. Biomed. Mater. Res. Part B Appl.*

*Biomater.* **2005**, *74B*, 792.

94. G. R. D. Evans *et al.*, *J Biomater Sci Polym Ed.* **2012**, *11*, 869.
95. Y. Xu, Z. Huang, X. Pu, G. Yin, J. Zhang, *Cell Prolif.* **2019**, *52*.
96. F. Yang, R. Murugan, S. Wang, S. Ramakrishna, *Biomaterials* **2005**, *26*, 2603.
97. X. Navarro, J. Hernández, *Rev. Sobre Ruedas* **2010**, *75*, 16.
98. F. Prósper *et al.*, *An. Sist. Sanit. Navar.* **2006**, *29*, 219.
99. J. M. Moraleda *et al.*, *Artículo revisión Rev Hematol Mex* **2011**, *12*, 144.
100. K. R. Jessen, R. Mirsky, A. C. Lloyd, *Cold Spring Harb. Perspect. Biol.* **2015**, *7*, a020487.
101. K. R. Jessen, P. Arthur-Farraj, *Glia* **2019**, *67*, 421.
102. V. Guardo-Gómez *et al.*, *Rev. Chil. Neuropsiquiatr.* **2020**, *58*, 50.
103. Q. Min, D. B. Parkinson, X. P. Dun, *Glia* **2021**, *69*, 235.
104. N. El Seblani, A. S. Welleford, J. E. Quintero, C. G. van Horne, G. A. Gerhardt, *J. Neurosci. Methods* **2020**, *335*, 108623.
105. A. Badner, A. M. Siddiqui, M. G. Fehlings, *Expert Opin. Biol. Ther.* **2017**, *17*, 529.
106. J. A. Lindborg, M. Mack, R. E. Zigmond, *J. Neurosci.* **2017**, *37*, 10258.
107. B. Barrette *et al.*, *J. Neurosci.* **2008**, *28*, 9363.
108. L. Leppik *et al.*, *Eur. J. Trauma Emerg. Surg.* **2020**, *46*, 231.
109. R. Zhu *et al.*, *Exp. Neurol.* **2019**, *319*, 112963.
110. M. Yamada *et al.*, *Stem Cells* **2007**, *25*, 562.
111. S. Y. Park *et al.*, *Adv. Mater.* **2011**, *23*, H263.
112. Y. Xu, Z. Huang, X. Pu, G. Yin, J. Zhang, *Cell Prolif.* **2019**, *52*, e12588.
113. H. T. Nguyen *et al.*, *J. Neural Eng.* **2013**, *10*, 046011.
114. Y. Li *et al.*, *Colloids Surfaces B Biointerfaces* **2020**, *191*, 1.

115. Y. Zou *et al.*, *ACS Appl. Mater. Interfaces* **2016**, *8*, 12576.

116. A. F. Quigley *et al.*, *Adv. Mater.* **2009**, *21*, 4393.

117. Y. Zhao *et al.*, *Biomaterials* **2020**, *255*, 120164.

118. Z. Zhou *et al.*, *Biomater. Sci.* **2018**, *6*, 2375.

119. S. Aznar-Cervantes *et al.*, *Mater. Sci. Eng. C* **2017**, *79*, 315.

120. M. Imaninezhad *et al.*, *J. Neural Eng.* **2018**, *15*.

121. R. Balint, N. J. Cassidy, S. H. Cartmell, *Acta Biomater.* **2014**, *10*, 2341.

122. T. Blachowicz, A. Ehrmann, *Mater. 2020, Vol. 13, Page 152* **2019**, *13*, 152.

123. M. Bordoni *et al.*, *Int. J. Mol. Sci.* **2020**, *21*.

124. C. Xiang, Y. Zhang, W. Guo, X. J. Liang, *Acta Pharm. Sin. B* **2020**, *10*, 239.

125. T. H. Le, Y. Kim, H. Yoon, *Polymers (Basel).* **2017**, *9*.

126. C. Li, H. Bai, G. Shi, *Chem. Soc. Rev.* **2009**, *38*, 2397.

127. G. Sabouraud, S. Sadki, N. Brodie, *Chem. Soc. Rev.* **2000**, *29*, 283.

128. L. X. Wang, X. G. Li, Y. L. Yang, *React. Funct. Polym.* **2001**, *47*, 125.

129. V. Rao, P. Praveen, D. Latha, *J. Polym. Res.* **2016**, *23*, 1.

130. J. Mao, Z. Zhang, *Adv. Exp. Med. Biol.* **2018**, *1078*, 347.

131. D. Hao, B. Xu, Z. Cai, *J. Mater. Sci. Mater. Electron.* **2018**, *29*, 9218.

132. J. Y. Lee, C. A. Bashur, A. S. Goldstein, C. E. Schmidt, *Biomaterials* **2009**, *30*, 4325.

133. Y. Wan, D. Wen, *J. Memb. Sci.* **2005**, *246*, 193.

134. G. Shi, M. Rouabhia, Z. Wang, L. H. Dao, Z. Zhang, *Biomaterials* **2004**, *25*, 2477.

135. Z. Wang *et al.*, *J. Biomed. Mater. Res. - Part A* **2004**, *70*, 28.

136. J. Wang *et al.*, *Phys. Chem. Chem. Phys.* **2017**, *19*, 21165.

137. T. Uyar, L. Toppare, J. Hacaloglu, *J. Macromol. Sci. - Pure Appl. Chem.* **2001**,

*38 A*, 1141.

138. B. Zinger, P. Shaier, A. Zemel, *Synth. Met.* **1991**, *40*, 283.

139. R. C. D. Peres, V. F. Juliano, M. A. De Paoli, S. Panero, B. Scrosati, *Electrochim. Acta* **1993**, *38*, 869.

140. C. Arribas, D. Rueda, *Synth. Met.* **1996**, *79*, 23.

141. C. Jin, F. Yang, W. Yang, *J. Appl. Polym. Sci.* **2006**, *101*, 2518.

142. M. Mattioli-Belmonte *et al.*, *Mater. Sci. Eng. C* **2005**, *25*, 43.

143. S. Aznar-Cervantes *et al.*, *Bioelectrochemistry* **2012**, *85*, 36.

144. J. F. Zhou *et al.*, *Neural Regen. Res.* **2016**, *11*, 1644.

145. P. M. George *et al.*, *Biomaterials* **2005**, *26*, 3511.

146. J. Rubio Retama, E. López Cabarcos, D. Mecerreyes, B. López-Ruiz, *Biosens. Bioelectron.* **2004**, *20*, 1111.

147. S. I. Brahim, D. Maharajh, D. Narinesingh, A. Guiseppi-Elie, *Anal. Lett.* **2002**, *35*, 797.

148. S. M. M. Morsi, M. E. A. El-Aziz, R. M. M. Morsi, A. I. Hussain, *J. Coatings Technol. Res.* **2019**, *16*, 745.

149. H. Yamamoto, M. Fukuda, I. Isa, K. Yoshino, *Electron. Commun. Japan (Part II Electron.* **1993**, *76*, 88.

150. H. Yamamoto, M. Oshima, M. Fukuda, I. Isa, K. Yoshino, *J. Power Sources* **1996**, *60*, 173.

151. I. Sultana *et al.*, *Electrochim. Acta* **2012**, *83*, 209.

152. R. M. A. P. Lima, J. J. Alcaraz-Espinoza, F. A. G. Da Silva, H. P. De Oliveira, *ACS Appl. Mater. Interfaces* **2018**, *10*, 13783.

153. H. Zhao, L. Li, J. Yang, Y. Zhang, *J. Power Sources* **2008**, *184*, 375.

154. S. Y. Huang, P. Ganesan, B. N. Popov, *Appl. Catal. B Environ.* **2009**, *93*, 75.

155. H. S. Park, Y. J. Kim, Y. S. Choi, W. H. Hong, D. Jung, *J. Power Sources* **2008**, *178*, 610.

156. M. Das, K. H. Shim, S. S. A. An, D. K. Yi, *Toxicol. Environ. Health Sci.* **2011**, *3*, 193.

157. S. Alex, A. Tiwari, *J. Nanosci. Nanotechnol.* **2015**, *15*, 1869.

158. C. Paviolo, P. R. Stoddart, *Nanomater. 2017, Vol. 7, Page 92* **2017**, *7*, 92.

159. Z.-R. Lu, S. Sakuma, **2016**, at <http://link.springer.com/10.1007/978-1-4939-3121-7>.

160. D. F. Báez, E. Gallardo-Toledo, M. P. Oyarzún, E. Araya, M. J. Kogan, *Int. J. Nanomedicine* **2021**, *16*, 2187.

161. D. Cabuzu, A. Cirja, R. Puiu, A. Grumezescu, *Curr. Top. Med. Chem.* **2015**, *15*, 1605.

162. A. M. S. Ibrahim *et al.*, *Plast. Reconstr. Surg.* **2012**, *130*, 879.

163. M. González, A. Vega, *Rev. Salud Anim.* **2007**, *29*, 8.

164. S. Mehier-Humbert, R. H. Guy, *Adv. Drug Deliv. Rev.* **2005**, *57*, 733.

165. X. Du *et al.*, *Drug Deliv.* **2018**, *25*, 1516.

166. T. K. Kim, J. H. Eberwine, *Anal. Bioanal. Chem.* **2010**, *397*, 3173.

167. C. Rosazza, S. H. Meglic, A. Zumbusch, M.-P. Rols, D. Miklavcic, *Curr. Gene Ther.* **2016**, *16*, 98.

168. W. Walther, U. Stein, *Drugs* **2000**, *60*, 249.

169. K. Chang *et al.*, *BMC Biotechnol.* **2002**, *2*, 1.

170. A. Faussner, A. Bauer, I. Kalatskaya, M. Jochum, H. Fritz, *Am. J. Physiol. - Hear. Circ. Physiol.* **2003**, *284*.

171. D. Vázquez-Blomquist, S. González, C. A. Duarte, *Biotechnol. Appl. Biochem.* **2002**, *36*, 171.

172. J. M. Escoffre *et al.*, *Mol. Biotechnol.* **2009**, *41*, 286.

173. Y. Nakayama, A. Aruga, *Vaccines* **2015**, *3*, 186.

# 2. Objectives

The peripheral nervous system regeneration can be achieved naturally only when the injury implies a short distance (<5 mm). However, in many cases the lesions are longer, and a nerve guidance conduit is needed to bridge the gap and achieve a functional regeneration. In addition, regeneration distances longer than 15 mm are still a challenge for researchers and new approaches are needed to provide a long structure that axonal bundles can use to grow in an aligned and unidirectional way with enough supply of oxygen and nutrients.

The present doctoral thesis hypothesizes that a multimodular approach of single-channel hyaluronic acid (HA) tubular conduits with an inner microfibrillar tubular structure made of polylactic acid (PLA) can be a new approach for long nerve gaps regeneration. On the one hand, the multimodular approach with several HA conduits one after the other can provide a high adaptability to the structure, preventing its breakage, while the micrometrical gaps between modules can give space for a better vascularization of the central part of the device. On the other hand, PLA microfibers can guide the axonal growth, leading the axons in an aligned and unidirectional way, helping them to reach the distal stump of the nerve as fast as possible. In addition, the different modules can be previously functionalized with pre-cultured glial cells such as Schwann cells (SCs), that have a beneficial effect on axonal growth. Moreover, different upgrades can be applied to the multimodular system, like the incorporation of proteins to the HA tubular modules to improve their mechanical and biological properties. Likewise, other upgrades that can have a beneficial effect on axonal growth such as the incorporation of SCs with an increased release of growth factors and the incorporation of electrically conductive microfibers that allow the electrical stimulation of the system can be introduced into the system.

To prove the hypothesis, the following objectives have been addressed in this Doctoral Thesis:

1. Adaptation to the *in vivo* model of the multimodular device previously studied *in vitro* by the research group.

2. Study of the *in vivo* behavior of the adapted multimodular device.

3. Study of the combination of HA with silk fibroin to obtain modular conduits with improved mechanical and biological properties.

4. Development and characterization of fibrillar, highly aligned, biocompatible and electroconductive substrates.

5. Study of the effect of electrical stimulation on axonal growth employing the developed electroconductive substrates.

6. Obtention of transfected glial cells that act as pumps of neurotrophic factors and application to the device, studying the effect on axonal growth.

# 3. Paper 1: Novel tissue-engineered multimodular hyaluronic acid-polylactic acid conduits for the regeneration of sciatic nerve defect

# Novel tissue-engineered multimodular hyaluronic acid–polylactic acid conduits for the regeneration of sciatic nerve defect

Fernando Gisbert Roca[a], Luis Gil Santos[a], Manuel Mata Roig[b], Lara Milian Medina[b], Cristina Martínez-Ramos[a], [c] and Manuel Monleón Pradas[a], [d], *

[a] Center for Biomaterials and Tissue Engineering, Universitat Politècnica de València, Cno. de Vera s/n, 46022, Valencia, Spain

[b] Department of Pathology. Faculty of Medicine and Dentistry. Universitat de València. Valencia, Spain.

[c] Universitat Jaume I, Unitat predepartamental de Medicina, Avda/Sos Baynat, s/n, 12071 Castellón de la Plana, Spain

[d] CIBER-BBN, Biomedical Research Networking Center in Bioengineering Biomaterials and Nanomedicine, Spain

*Corresponding author: Manuel Monleón Pradas. Center for Biomaterials and Tissue Engineering, Universitat Politècnica de València, Camino de Vera s/n E-46022 Valencia, España. Tel.: +34963877000. E-mail: mmonleon@ter.upv.es

**Keywords:** nerve guidance conduit, hyaluronic acid, polylactic acid, aligned substrates, Schwann cells, nerve regeneration

Published online: 21 April 2022

# 3.1. Abstract

The gold standard for the treatment of peripheral nerve injuries, the autograft, presents several drawbacks, and engineered constructs are currently suitable only for short gaps or small diameter nerves. Here, we study a novel tissue-engineered multimodular nerve guidance conduit for the treatment of large nerve damages based in a polylactic acid (PLA) microfibrillar structure inserted inside several co-linear hyaluronic acid (HA) conduits. The highly aligned PLA microfibers provide a topographical cue that guides axonal growth, and the HA conduits play the role of an epineurium and retain the pre-seeded auxiliary cells. The multimodular design increases the flexibility of the device. Its performance for the regeneration of a critical-size (15 mm) rabbit sciatic nerve defect was studied and, after six months, very good nerve regeneration was observed. The multimodular approach contributed to a better vascularization through the micrometrical gaps between HA conduits, and the pre-seeded Schwann cells increased axonal growth. Six months after surgery, a cross-sectional available area occupied by myelinated nerve fibers above 65% at the central and distal portions was obtained when the multimodular device with pre-seeded Schwann cells was employed. The results validate the multi-module approach for the regeneration of large nerve defects and open new possibilities for surgical solutions in this field.

# 3.2. Introduction

Peripheral nerve injury (PNI) is a common condition that results from trauma, laceration, stretching and/or compression of peripheral nerves. It can result in a wide range of symptoms, including severe sensor and motor deficits [1,2]. After the nerve injury occurs, the endogenous repair and regeneration process is initially characterized

by a Wallerian degeneration, which involves both morphological and biochemical changes to support the new growth. The nerve regeneration begins at the proximal stump within the first 48 h, as the growing axons attempt to bridge the lesion gap and reinnervate the distal target organ [3]. However, this endogenous repair process is extremely slow, with an average rate of axonal growth of around 1 mm/day, which also cannot sustain itself for more than 12 months [4–6].

Treatments that provide complete functional recovery are lacking for severe PNI where the gap between the proximal and distal stumps of the injured nerve is long. If this gap is longer than 5 mm, regeneration cannot be achieved naturally [7]. Therefore, these long lesions are not capable of regenerating by themselves and require a surgical intervention [7]. Furthermore, when the injury cannot be repaired through a direct end-to-end connection without applying tension, it is necessary to use an autograft nerve from the patient himself (current standard action), a nerve allograft from a cadaver donor, or an artificial nerve conduit to bridge the gap [8,9].

The use of autograft nerves produces a morbidity of the donor site, where the formation of a neuroma can occur, in addition to the increase in cost and operative time due to having to perform a second surgery [10–12], and nerve allografts present potential side effects of host immunosuppression [1,9]. For these reasons, biomaterial engineered constructs, called nerve guidance conduits (NGC), are very interesting for the repair of nerve injuries [13–15]. Several NGC have been approved by the US Food and Drug Administration (FDA) and the European Medicines Agency (EMA) for the treatment of PNI [16,17]. However, they present several disadvantages, such as limits on the size of the nerve gap that can be repaired, poor biocompatibility and inefficient regeneration mainly due to poor revascularization of the nerve tissue. Thus, more research is needed in this field [18–20].

Structural cues on macro- and microscopic levels are being used to improve clinical results of NGC during the last years [21]. NGC have achieved an improvement of the guidance of regeneration, but currently only satisfactorily for short defects (gap < 15 mm) [22–25]. Conduits with multiple channels that increase the surface area of growth, the incorporation of extracellular matrix molecules and the use of supportive cells and growth factors have been shown to be more efficient compared to the use of hollow NGC [13,26,27]. However, they have not yet been able to match the regenerative capacity that is provided by autologous nerves [28].

Another factor to consider is the maximum length that can be repaired. It is still a challenge to achieve the repair of nerve injuries greater than 4 cm in length, which have limited expectations of functional recovery even with use of nerve autografts [29,30]. This can be explained by a multitude of factors, such as the limited regenerative capacity of neurons, the creation of a substrate that prevents axonal growth, the lack of trophic support, errors in axonal guidance or the reinnervation of dysfunctional targets [31,32]. Most of the repair alternatives that attempt to address some of these factors have only resulted in a modest improvement [33].

In the device that is here presented we employ two different types of biomaterials: cylinders (modules) made from hyaluronic acid (HA) and a polylactic acid (PLA) microfiber tubular bundle located in the common lumen of the co-aligned module assembly. On the one hand, HA is one of the main components of the extracellular matrix and can be crosslinked to form three-dimensional networks (hydrogels) [34–36]. HA presents low immunogenicity, high biocompatibility and a good biodegradability, as well as mechanical properties similar to soft nervous tissues [37,38]. Furthermore, HA hydrogels have an anti-inflammatory and inhibitory effect on astrocyte activation, thus reducing glial scar formation [39]. On the other hand, PLA is a synthetic polyester with

good mechanical properties, biocompatibility and biodegradability [40,41]. PLA has a good performance for the regeneration of the nervous system, especially in the form of a fibrous scaffold [42–44]. The PLA microfibers located inside our HA conduits provide support for cell adhesion and migration as well as for the guidance of axonal growth [45,46]. To select the diameter of the PLA fibers, we relied on our previous experience showing that PLA microfibers with a diameter of 10 µm presented better guided axonal growth [45].

It is important to highlight that our device is not made up of a single long HA conduit, but from several short HA modules. They are kept together colinearly by the (common) internal PLA microfiber bundle and by external fixing structures at the ends of the device [47]. This multimodular approach presents several prospective advantages. It can afford longer lengths than usual unimodular concepts, providing a greater flexibility and adaptability of the device in long lesions to avoid flexural breakage. In the case of cell transplantation, this is accompanied by a better survival of the transplanted cells within the conduits, due to better fluid transport. For this very same reason, when placed *in vivo*, a better vascularization of the newly formed tissue inside the device is expected, thanks to the interstitial micrometrical spaces between the modules, which allow for the exchange of cells and fluids with the close neighborhood and thus the vascularization of locations far from the ends of the device. Blood vessels play a very important role in regenerating nerves to provide blood supply and nutrients, serving as pathways over which Schwann cells (SCs) can migrate to form bands of Büngner that promote axonal regeneration [24,48–51]. In addition, the multi-module concept opens the possibility of differential functionalization, with different kinds of cells or bioactive molecules of each module, thus enabling a gradient of stimuli. Among all these bioactive cues, supportive cells are frequently incorporated into the lumen of

NGC [23,25,52,53]. In this study. the modules have been biofunctionalized with pre-seeded human Schwann cells (hSC).

It was previously observed that SCs seeded inside HA tubular conduits with a suitable inner diameter and filled with PLA microfibers were capable of proliferating and self-organizing, forming a cell sheath that covers the inside of the conduit while also covering the surface of the microfibers [54–57]. In this way, it is possible to exploit these SCs structures as support for axonal growth. In addition, we have previously observed that HA conduits filled with PLA microfibers were capable of inducing preferential neuronal differentiation of progenitor cells *in vitro*, and presented good biocompatibility and beneficial effects in a spinal cord injury in an *in vivo* model [56,57].

SCs are responsible for axon myelination and play a key role in regeneration and protection in the peripheral nervous system (PNS) [58,59]. Following a nerve injury in the PNS, SCs contribute to nerve repair by activating, de-differentiating, dividing and proliferating distally [60]. SCs act as a source of neurotrophic and angiogenic factors as well as surface proteins involved in the maintenance of normal PNS function and in the activation of immune response after an injury occurs [61]. Therefore, SCs have been proposed for regenerative purposes both in the peripheral and central nervous system [62–65].

In this study, we combined SCs and biomaterials to build a NGC that tries to imitate the supportive action of these cells in the natural process of regeneration. We reasoned that the presence of pre-seeded SCs offered a favorable environment that could stimulate the proliferation, migration and regeneration of both neuronal and non-neuronal cell populations at the injury site, offering a more robust and efficient method for repairing critical gap nerve injuries. In addition, the highly aligned PLA microfibers

would favor the guidance of cell migration and axonal growth, and the multimodular approach would entail a better vascularization of the regenerated tissue.

Here, we present a study of the performance of the multi-module implant in a rabbit sciatic nerve defect model. We initially characterized our bioengineered constructs *in vitro* to ensure they had the necessary properties for *in vivo* implantation. The animal model consisted of a critical-size (15 mm) sciatic nerve defect in the rabbit, which is an animal model that is more translational for nerve regeneration research than a rat model, and allows for testing larger NGC [66]. The effects of repair and regeneration were evaluated over a period of 6 months using several histology techniques. The primary focus of our *in vivo* study was to establish the benefits of both the pre-seeded SCs and the multimodular conduit approach for nerve regeneration, comparing the results obtained against those for implants of one module and of a non-pre-seeded multimodular conduit.

# 3.3. Experimental section

## Preparation of HA-PLA conduits

Conduits of crosslinked HA from Streptococcus equi (1.5–1.8 MDa, Sigma-Aldrich, Spain) were synthesized, as previously described [54,55,57] in a PTFE mould designed to obtain the desired dimensions. The conduits were hydrated in distilled water and cut to 7.5 or 15 mm length. The 7.5 mm length crosslinked hollow cylinder constitutes the unit module. Implants with one (15 mm-long) module and two (7.5 mm-long) modules were prepared for this study. A bundle of polylactic acid (PLA) microfibers was placed in the lumen of the single- or bi-module HA conduits. It was manufactured with 3600 parallel PLA microfibers with a diameter of 10 μm each (AITEX Textile Research Institute, Alicante, Spain) that were joined at their ends with

an adhesive material based on cellulose. First, the microfibers were arranged parallel in various planes, and then they were held in that position by the cellulose-based adhesive. Subsequently, the flexibility of the adhesive allowed it to be rolled into a conduit, the curvature of which was maintained by adding more adhesive, forming a ring that allowed its suture to the nerve stump. Once the microfiber bundle was inserted inside of one HA module or two HA modules, the total length of the device was 20 mm, because the suture rings extended 2.5 mm at each side to introduce the nerve stumps. The final conduits were first sanitized for 2 h with 70% ethanol (Scharlab, Spain), and then they were immersed in 50%, 30% ethanol and ultrapure water (Mili-Q®) for 10 min. The preconditioning of the conduits was carried out by immersion in Dulbecco's Modified Eagle Medium with a high glucose level (4.5 g/L) (DMEM, 21331020, Life Technologies, Spain), supplemented with 10% Fetal Bovine Serum (FBS, 10270-106/A3381E, Life Technologies, Spain) and 1% Penicillin/Streptomycin (P/S, 15140122, Life Technologies, Spain), and incubation took place at 37 °C for 24 h in a humidified atmosphere containing 5% $CO_2$. Three groups of HA-PLA conduits were studied: a unimodular conduit (UMC) with a 15 mm-long HA conduit, a multimodular conduit (MMC) formed by two contiguous HA conduits with a length of 7.5 mm each and a multimodular conduit with human Schwann cells (hSC) pre-seeded inside the HA conduits (MMS + hSC).

## Dimensions of HA tubular scaffolds and inflation test

Longitudinal and cross-sectional images of the HA conduits were taken with a magnifying glass (Leica, Mz Apo, Germany) to measure their dimensions. The images were then processed with ImageJ software to obtain the measurements. Lengths were obtained from the images of the longitudinally arranged tubes, and the measurements of

the external and internal diameters were acquired from the images of the cross sections. In total, four measurements were made for each of the parameters.

To assess the water absorption capacity of HA conduits, a swelling test was carried out, studying the differences in size between the dry and swollen conduits. For this, cross sections of approximately 1 mm in length were made of the conduits, and they were introduced for 2 h in distilled water. After this time, images were taken in the magnifying glass and, with the ImageJ software, the dimensions of the external and internal diameters were measured. The swelling ratio was calculated following **Equation (1)**, where D refers to the diameter, external (ext) or internal (int) of the conduits, which were measured in dry (d) and swollen (h) states.

$$Swelling\ ratio = \left(D_{ext,s} - D_{int,s}\right)/\left(D_{ext,d} - D_{int,d}\right) \quad (1)$$

## Human Schwann cells culture

Human Schwann cells (hSC, P10351, Innoprot, Spain) at the third cell pass were employed for cell cultures in the conduits to study cell adhesion and proliferation. After the expansion of hSC in a cell culture flask, they were washed with PBS, and a Trypsin/EDTA solution (T/E; 25200-072, Life Technologies, Spain) was added to break the cell–matrix and cell–cell interactions to remove the cells from the bottom of the culture flask. Cells were centrifugated at 1080 rpm for 5 min, and the pellet was resuspended in the Schwann cell culture medium (SCM, P60123, Innoprot, Spain). The seeding with hSC was carried out for the MMC+hSC group, with a seeding density of 625,000 cells per module (the total number of cells was $1.25 \times 10^6$). Then, the conduits were introduced in an incubator at 37 °C with a humid atmosphere containing 5% $CO_2$ for 5 and 10 days, renewing the Schwann cell culture medium every 48 h.

## Morphological characterization by field emission scanning electron microscopy

The morphology of the HA-PLA conduits was observed by means of field emission scanning electron microscopy (FESEM). Samples were cut longitudinally to obtain a complete view of the lumina of the conduit, mounted over aluminum tape and sputtered with platinum before the FESEM analysis (ULTRA 55, ZEISS, Oxford Instruments, Germany), using a voltage of 2 kV.

To study the inside of the cellular conduits (MMC + hSC) after 10 days of cell culture, the conduits were fixed in a 3.5% glutaraldehyde (GA; Electron Microscopy Sciences, Spain) solution for 1h at 37 °C, post-fixed with 1% $OsO_4$ (Electron Microscopy Sciences, Spain) for 2h at room temperature and dehydrated in a series of increasingly concentrated ethanol. Then, the conduits were processed in a critical point dryer (critical point values: 328 °C, 1100 psi). The conduits were cut longitudinally to expose their internal lumina and were mounted over aluminum tape and sputtered with platinum before analysis. Samples were finally observed in a Hitachi S4800 electron microscope using a voltage of 10 kV.

## Morphology and attachment of human Schwann cells

After 5 and 10 days of hSC culture, samples were rinsed twice in PB 0.1M and fixed in 4% paraformaldehyde (PFA; 47608, Sigma-Aldrich, Spain) for 20 min at room temperature. After cell fixation, PFA residues were removed with 3 washes of 10 min with DPBS. Then, cells were permeabilized and blocked in DPBS with 3% bovine serum albumin (BSA; A7906, Sigma-Aldrich, Spain) and 0.1% Tween20 (P1379, Sigma-Aldrich, Spain) for 1 h at room temperature.

To observe the cytoskeleton of the cells, samples were incubated with Alexa Fluor™ 555 Phalloidin (A34055, ThermoFisher Scientific, Spain) and diluted 1:200 at room temperature for 1 h. Cell nuclei were stained with DAPI (1/1000, D9542, Sigma-Aldrich, Spain) for 10 min. Finally, the conduits were cut longitudinally to obtain a complete view of the lumina, and a confocal microscope (LEICA TCS SP5, Leica microsystems, Spain) was used to obtain the images.

## Implantation of nerve conduits in rabbit sciatic nerve

The study was conducted according to the guidelines established by the European Communities Council Directive (210/63/EU) and the Spanish regulation 1201/2005. All experimental procedures were approved by the Animal Care and Use Committee of the Polytechnic University of Valencia (2019/VSC/PEA/0142). The minimal number of animals was considered for each group due to ethical concerns (n = 4).

Twelve male white rabbits (Oryctolagus cuniculus, three-way crossing of lines of the Polytechnic University of Valencia) aged 12 weeks and weighing 3.0–3.5 kg were randomly divided into three groups, as follows: unimodular conduit (UMC), multimodular conduit (MMC) and multimodular conduit with pre-seeded human Schwann cells (MMC + hSC) groups. The rabbits were pre-anesthetized via intramuscular injection of ketamine–xylazine (ketamine 15 mg/kg and xylazine 3 mg/kg) into the back of the neck, and then the rabbits were anesthetized via intravenous injection of Propofol (3 mg/kg for induction and 20 mg/kg/h for maintenance). The corneas of the rabbits were lubricated with a 0.2% carbomer ophthalmic gel (artificial tear) to prevent them from drying out and to prevent the appearance of corneal ulcers.

After shaving and disinfecting the area with chlorhexidine, an incision was made in the skin, taking as reference the greater trochanter of the femur and the region near the lateral condyles of the femur. A dissection was performed between the gluteus maximus

and the biceps femoris that revealed the sciatic nerve. After releasing the nerve from the underlying tissue, it was irreversibly transected. A 15 mm-long segment of sciatic nerve was resected 0.5 cm proximal to the bifurcation of the nerve into the tibial and peroneal nerve branches. Then, the nerve gap (15 mm) was bridged by the unimodular or multimodular conduits with 8/0 Prolene sutures, and the wound was closed in layers using a 4/0 resorbable suture.

At the end of the surgery, immediate postoperative analgesia was administered (Butorphanol, intravenously, 0.2 mg/kg), as well as delayed postoperative analgesia 48 h after surgery (Butorphanol, intramuscularly, 0.4 mg/kg). All the animals were housed in specific pathogen-free conditions for 6 months. They moved freely and had free access to water and food. To prevent and control self-mutilation of the operated limb and the appearance of pressure ulcers during the postoperative period, rabbits wore Elizabethan collars for 1 week after surgery, the operated foot was bandaged with tape stirrups, and a softer ground was placed in the cages. The collar and the bandage were removed if there were no signs of self-mutilation, but they were applied again if signs of self-trauma were observed. The bandage was also applied again if signs of pressure ulcers were observed, after healing the affected area.

## Histological and morphometric analysis

Histological evaluation of the defected nerves was performed 6 months after surgery. Our investigation did not evaluate different time points of the regenerative process; only the final time point after 6 months was evaluated. However, we thought that this was enough time to obtain a significant axonal regeneration based on previous similar studies in rabbits that demonstrate a good sciatic nerve regeneration of smaller gaps after 3 months [67,68].

Prior to the sacrifice of the animals, it was observed that the operated leg responded to the stimulus by exerting manual pressure, exerting some resistance. After anesthetizing the rabbits, the sciatic nerve containing the guidance conduit was removed from the animals, fixed in 4% PFA for 24 h and cut into three portions: proximal (approx. 3.5 mm from the proximal end of the HA conduit), central (approx. 7.5 mm from the proximal end of the HA conduit) and distal (approx. 3.5 mm from the distal end of the HA conduit). The portions were embedded in paraffin and cut transversely (5 μm thickness). Slices were stained for Hematoxylin-Eosin (HE) according to standard procedures. The analysis of the distribution and content of myelinated nerve fibers was performed using the modified Luxol fast blue method described by Sajadi et al. [69]. The cross sections of all specimens were examined by light microscope (Leica DMD 108 microscope, Leica, Spain).

Neovascularization was determined by immunohistochemistry using a specific mouse monoclonal CD31 anti-human antibody predicted for a rabbit antibody (ab212712; Abcam; Cambridge, United Kingdom), as previously reported [70]. The sections were deparaffinized and rehydrated using a series of graded ethanol, rinsed in distilled waters and treated with 0.3% $H_2O_2$ to block endogenous peroxidase. Then, nonspecific binding was blocked by washing with a Tween 20 buffer (Fischer Scientific; Madrid, Spain). Antigens were retrieved by boiling in a pressure cooker for 3 min in a high-pH Envision FLEX Target Retrieval Solution (Dako; Barcelona, Spain). Samples were incubated overnight with the primary antibody at 4 °C using 1:250 dilution in Envision FLEX antibody diluent. After washing with PBS, the secondary antibody (goat anti-mouse IgG-HRP, 1:200 dilution) was incubated at RT for 2 h, and then developed using the 3,3′-diaminobenzidine chromogen (Dako; Barcelona, Spain) according to the manufacturer's instructions, which resulted in brown staining in the

immunoreactive structures. Finally, the sections were counterstained with Mayer's hematoxylin (Merk; Kenilworth, NJ, USA).

Morphometric analysis was carried out in the central and distal sections of each of the animals included using the Image Pro Plus 7.0 software (Media Cybernetics, Rockville, MD, USA). Collagen and myelinated nerve fibers were measured in five different fields of each of the Luxol fast blue-stained sections (**Figure 1**). The areas of the nerve fibers and collagen were normalized to the available area once the area of the PLA microfibers, vessels and cavities was subtracted, in order to compare samples with different available areas. The central and distal sections of each of the animals included were considered. CD31+ vessel density was measured by counting the number of immunostained vessels in five different fields.

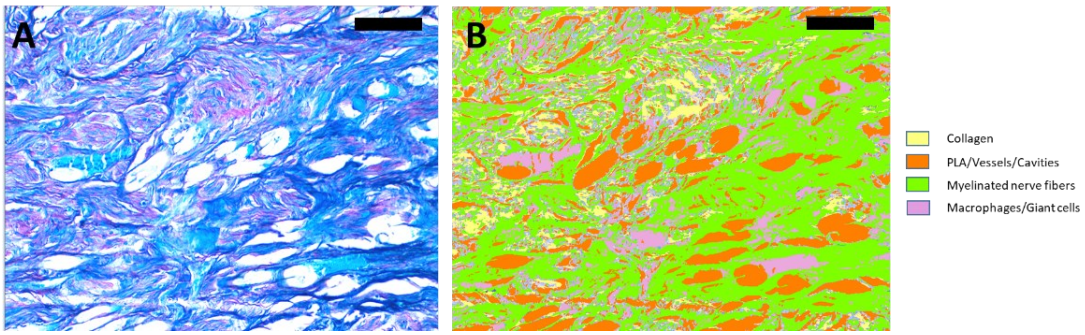


**Figure 1.** Example of a Luxol fast blue image and its segmentation. (**A**) Luxol fast blue image. (**B**) Segmentation of image (**A**). As can be observed with this example, Luxol fast blue images were segmented to quantify the area of collagen, PLA/vessels/cavities, myelinated nerve fibers and macrophages/giant cells. Collagen (red) is segmented in yellow, PLA/vessels/cavities (white) are segmented in orange, myelinated nerve fibers (dark blue) are segmented in green, and macrophages/giant cells (light blue) are segmented in purple. Scale bar = 100 µm.

## Statistical Analysis

The data are expressed as the mean ± SEM, and GraphPad Prism® software was employed for the statistical analysis. The two-way ANOVA test, together with a

multiple sample mean comparison (Tuckey's multiple comparisons test with a significance degree of 95%), was used to reveal significant differences between conditions. Statistically significant differences are indicated by *, **, *** or ****, indicating a p-value below 0.05, 0.01, 0.001 or 0.0001, respectively.

# 3.4. Results and discussion

## Fabrication and characterization of HA-PLA conduits

Three different types of nerve guidance conduits were studied, consisting of a 3600 PLA microfiber bundle with a cylindrical arrangement within one long or two short HA conduits (**Figure 2**). In the UMC (unimodular conduit) group, the microfiber bundle was inserted into a single HA conduit with a length of 15 mm. In the MMC (multimodular conduit) group, the microfiber bundle was inserted into two consecutive HA conduits with a length of 7.5 mm each, reaching a total length of 15 mm. Finally, in the group MMC + hSC (multimodular conduit + human Schwann cells), the MMC was pre-seeded with $1.25x10^6$ hSC that were cultured during 10 days prior to the intervention to obtain a continuous coverage of the PLA microfibers and the lumen of HA conduits. At both extremes of the PLA microfiber bundle, a 2.5 mm-long fastener ring maintains the structure of the microfibers and allows the suture to the nerve stump that is inserted into it. The three types of implants were employed to bridge a 15 mm-long defect in a rabbit sciatic nerve model. These experimental groups allow for observing the effect of the unimodular approach versus the multimodular approach (UMC vs MMC groups) and the effect of pre-seeded Schwann cells (MMC vs MMC + hSC groups). The inclusion of the UMC + hSC group would have provided little additional information and was not included in the study, following the reduction principle in animal experimentation.

For the morphological characterization of the HA-PLA implants, FESEM images of the HA conduits and the PLA microfiber bundle were obtained (**Figure 3**). As can be observed in **Figure 3C**, the HA conduit walls present a porous microscopic structure that allows for the diffusion of water and small molecules. The lumen's inner surface of the conduits has a much smaller porosity (**Figure 3D**) that impedes cell migration and helps keep the seeded cells inside the conduit. The dimensions of the dry HA conduits were 3.0 ± 0.1 mm in internal diameter and 6.0 ± 0.2 mm in external diameter. The HA conduits had a great capacity to absorb water, and the dimensions of the swollen HA conduits were 5.9 ± 0.1 mm in internal diameter and 10.1 ± 0.6 mm in external diameter, with a swelling ratio of 1.4 ± 0.3. The diameter of the rabbit sciatic nerve is comprised between 2 and 4 mm [66,71]. Thus, the internal diameter of HA conduits in the swollen state is big enough to avoid a possible compression of the nerve. In addition, some space is necessary for the PLA microfiber bundle that is placed inside the HA conduits, whose ends are the ones that adapt and are sutured to the nerve stumps.

HA presents groups capable of forming hydrogen bonds with water, such as -OH and -$NH_2$, thanks to which the HA can absorb large amounts of water. The amount of water absorbed can be diminished with the crosslinking degree [72] and, in this way, the dimensional change due to swelling can be adjusted to the size of the injured nerves. The high water content of HA in its swollen state is critical for the non-adherent properties of the HA conduit, which prevents undesired adherences to the surrounding tissues [73]. Many pharmaceutical agents such as Doxorubicin have been tried to prevent nerve scarring and adhesion in different experimental studies, but results have been poor. Therefore, the antiadherent action of HA cannot be replaced by drugs at the moment [73]. In addition, other beneficial effects of HA associated with nerve

regeneration (number of axons, nerve fiber diameter and myelin thickness) have also been reported [73].

In **Figure 3E**, the end of the PLA microfiber bundle can be observed, with the flat ring used to keep the cylindrical arrangement of PLA microfibers marked with asterisks. At the same time, this ring represents a convenient surface for the suture of the nerve stumps to the microfiber bundle. As can be observed in **Figure 3F**, the PLA microfibers present a highly aligned distribution, which is necessary to obtain a high directionality of the axons, as has been observed in previous studies [45,46].

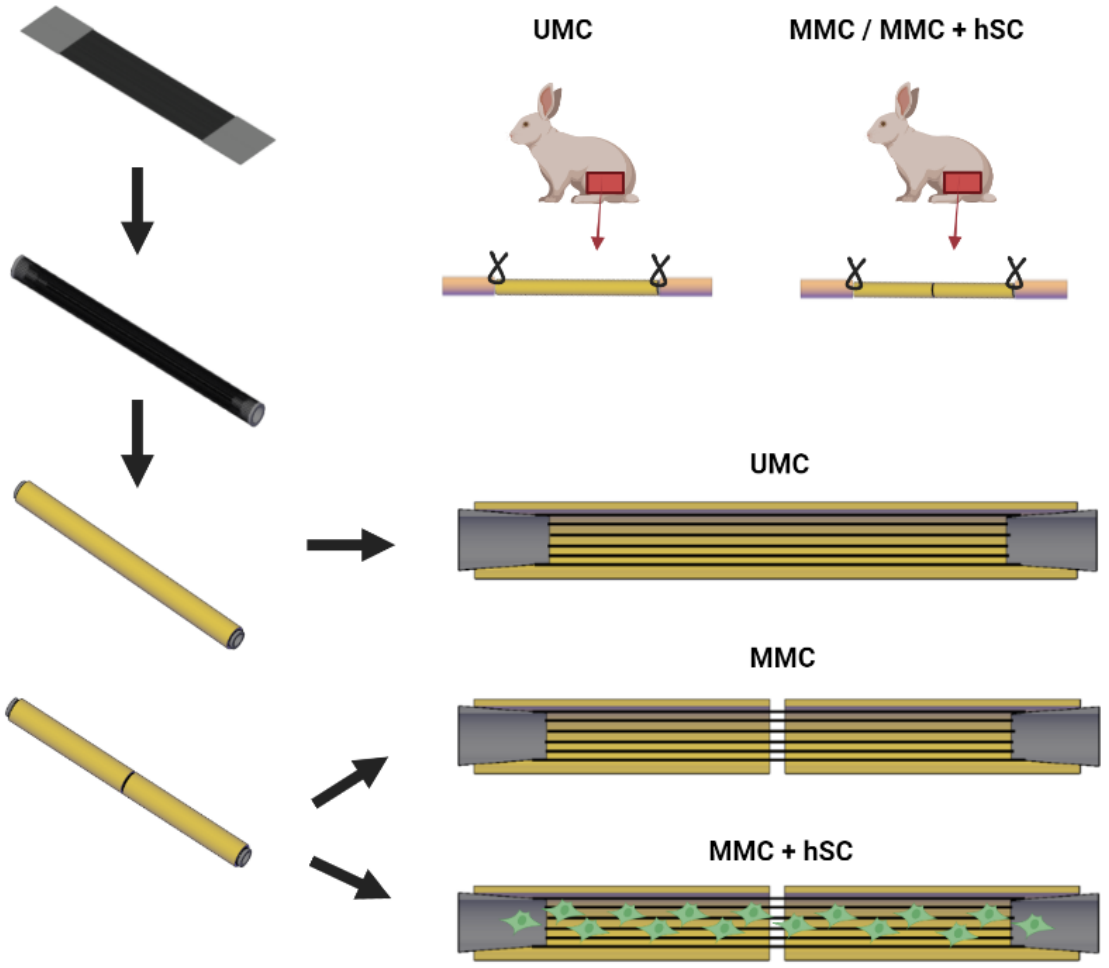


**Figure 2.** Scheme representing the differences among the three different guidance conduits that are studied. For all groups, the starting point is a PLA planar microfiber bundle formed by 3600 parallel PLA microfibers with a diameter of 10 microns each. The bundle is rolled up to obtain a cylindrical bundle. For the unimodular conduit

(UMC) group, the PLA microfiber bundle is inserted into a 15 mm-long HA conduit. For the multimodular conduit (MMC), the PLA microfiber bundle is inserted into two consecutive HA conduits with a length of 7.5 mm each. The multimodular conduit plus human Schwann cells (MMC + hSC) is obtained in the same way as the MMC, but it was pre-seeded with $1.25x10^6$ human Schwann cells (hSC) 10 days before the implantation. At both extremes of the conduits, a 2.5 mm-long ring maintains the structure of PLA microfibers and allows the suture to the nerve stump that is inserted into it. The total length of the implant is of 20 mm. All three types of implants are used to bridge a 15 mm-long sciatic nerve defect in rabbits. Picture created with BioRender.com.

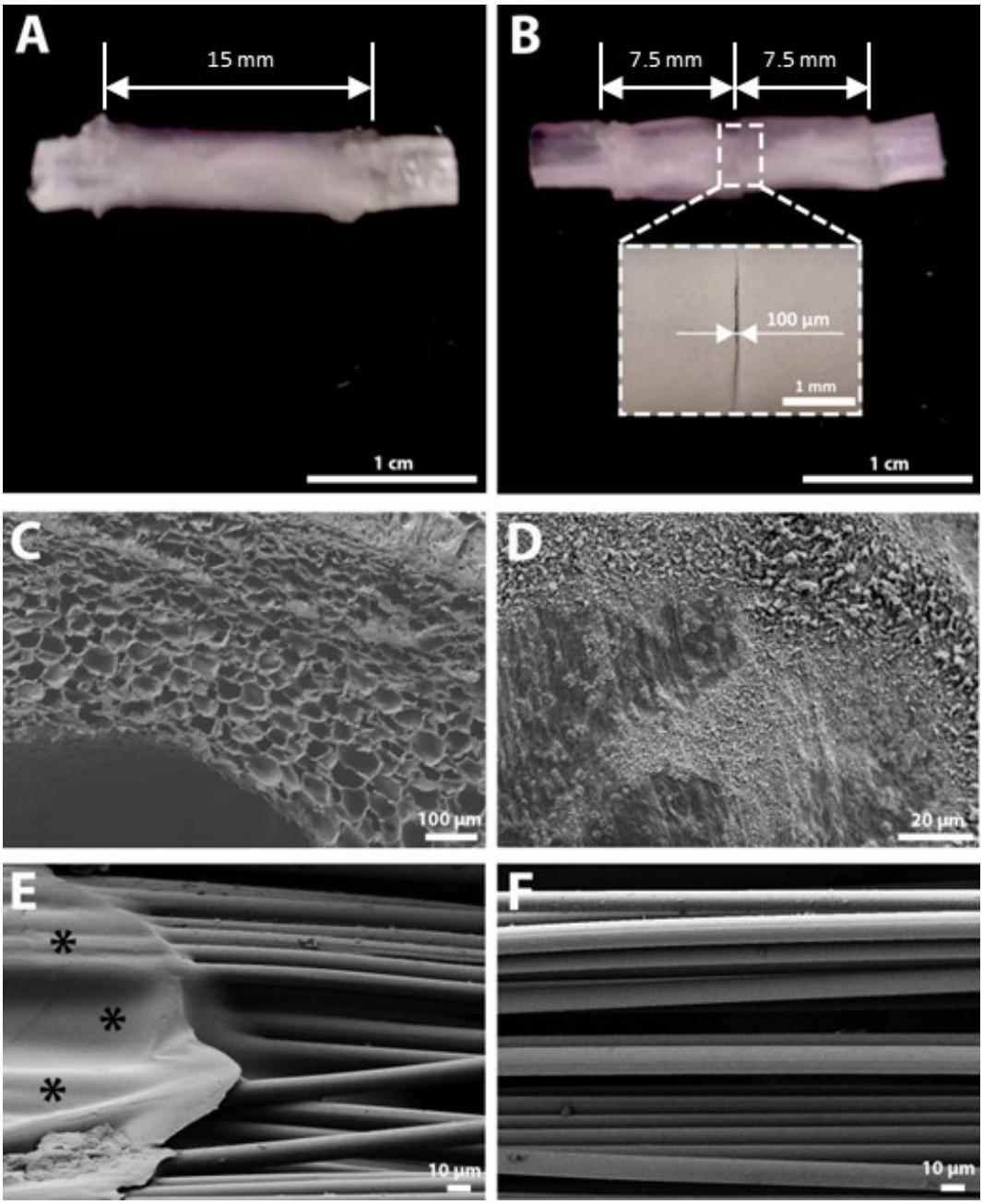


**Figure 3.** Macroscopic and field emission scanning electron microscope (FESEM) images of the acellular conduits. (**A**) Macroscopic image of the unimodular conduit (UMC). (**B**) Macroscopic image of the multimodular conduit (MMC) incorporating a detail of the central zone of the conduit to appreciate the gap between both HA modules. An arrow indicates the inter-module separation. (**C**) FESEM image of a cross section of the hyaluronic acid (HA) conduit showing the porous structure. (**D**) FESEM image of the HA conduit inner surface. (**E**) FESEM image of an end of the polylactic acid (PLA) microfiber bundle showing the flat ring (marked with *) that holds microfibers in

position and allows the suture of the conduit to the nerve stump. (**F**) FESEM image of the PLA microfiber bundle showing the high alignment of PLA microfibers.

## Growth and distribution of human Schwann cells in HA-PLA conduits

Schwann cells are one of the main cells of the peripheral nervous system, and if they are pre-seeded into a nerve guidance conduit, they can promote the growth of neurites by the secretion of neurotrophic and angiogenic factors [58–61]. To assess the behavior of hSC seeded on top of the PLA microfiber bundle, confocal and FESEM images of the cells were taken after the stablished culture time ($1.25x10^6$ hSC cultured for 10 days). As can be observed in **Figure 4A**, hSC form a continuous multilayer of cells that cover all the PLA microfibers, even bridging the spaces between microfibers. **Figure 4B,C** show FESEM images of the hSC attached and growing on top of PLA microfibers, wrapping them. In **Figure 4C**, it can be clearly appreciated how the cytoskeleton of hSC is elongated in the direction of the PLA microfibers, leading to an alignment of the cells. This topographical guidance of PLA microfibers will also guide the growth of axons in the direction of the microfibers, as previously observed [45,46]. Therefore, the well-distributed hSC on the whole PLA microfiber bundle provide a convenient microenvironment for the subsequent axonal extension during the *in vivo* nerve regeneration process.

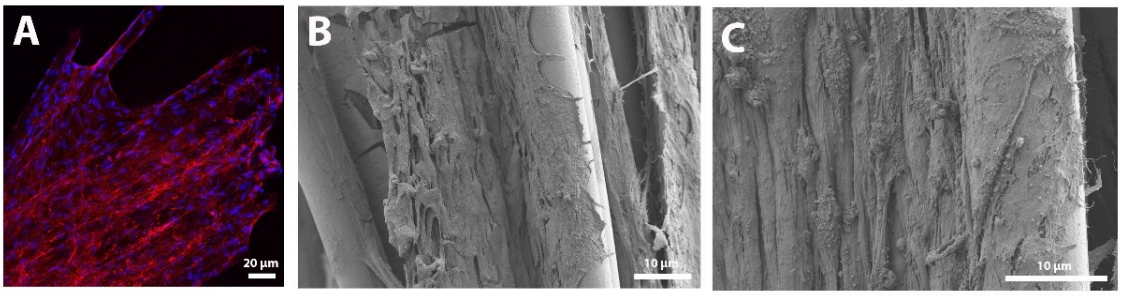


**Figure 4.** Confocal and field emission scanning electron microscope (FESEM) images of the cellular conduits. (**A**) Confocal image of human Schwann cells (hSC) seeded on the polylactic acid (PLA) microfiber bundle. The cytoskeleton of hSC is observed in red (phalloidin) and the nuclei of cells is observed in blue (DAPI). (**B**, **C**) FESEM images of hSC seeded on the PLA microfiber bundle. It can be observed how hSC can attach and grow on PLA microfibers, wrapping them (**B**). Further, an alignment of hSC cytoskeleton is observed, thanks to the topographical guidance of PLA microfibers (**C**).

Besides embracing the PLA microfibers, the pre-seeded SCs form a continuous planar cell sheath of a few cells' thickness that coats the inner surface of the lumina of the HA conduits, as can be observed in **Figure S1** and **Figure 5**. To compare differential SCs coverage when using a UMC or a MMC, $2.5x10^6$ and $1.25x10^6$ cells were seeded on both conduits and cultured for 5 and 10 days, respectively. As can be observed in **Figure S1**, when a UMC was employed, an incipient SCs sheath was visible when $2.5x10^6$ cells were cultured for 5 days (**Figure S1A–C**). When $1.25x10^6$ cells were cultured for 10 days, (**Figure S1D–F**) a more developed SCs sheath was observed, but it was not enough to cover all the lumen of the HA conduit. In the case of the MMC (**Figure 5**), when $2.5x10^6$ cells were cultured for 5 days (**Figure 5A–C**) a clearly thicker and larger SCs sheath was obtained, but some bald spots could still be observed. However, when $1.25x10^6$ cells were cultured for 10 days (**Figure 5D–F**), a thick and continuous SCs sheath was clearly observed. These results proved that it was better to culture $1.25x10^6$ cells for 10 days than to culture $2.5x10^6$ cells for 5 days in

both cases. In addition, a thicker and more continuous SCs sheath was obtained when using a MMC than a UMC, probably a consequence of a better distribution of the seeded cells in the case of the shorter modules of the MMC sample than in the longer UMC module. The multimodular design entails a more uniform distribution of the pre-seeded Schwann cells because it facilitates the seeding process: the cells are seeded at both ends of each module, so a shorter module reduces the distance between the seeding zones. For this reason, a better coverage of the lumen of the conduit is achieved. In addition, the use of shorter modules allows a better exchange of nutrients than the use of a longer module, whose center has fewer nutrients available [52,74,75]. This can also affect the cell distribution in the central part of the lumen of the conduit.

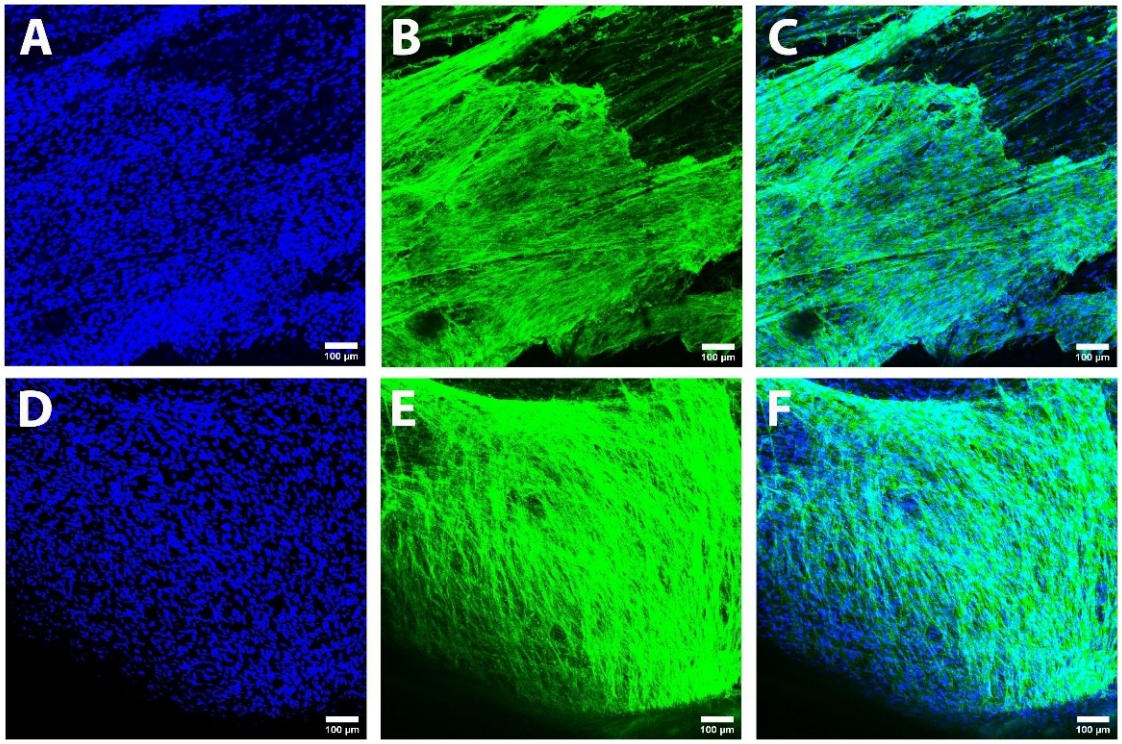


**Figure 5.** Confocal images of human Schwann cells (hSC) seeded on a multimodular conduit (MMC). (**A**–**C**) Images after the culture of $2.5x10^6$ hSC for 5 days. (**D**–**F**) Images after the culture of $1.25x10^6$ hSC for 10 days. The cytoskeleton of hSC is observed in green color (Phalloidin) and the nuclei of hSC is observed in blue color (DAPI). As can be seen, the cells have formed a sheath that fills the lumen of the HA conduit and that also covers the surface of PLA microfibers. A more continuous and

thicker cell sheath is observed when $1.25x10^6$ hSC are cultured for 10 days (**D-F**). Further, the higher degree of coating by hSC can be appreciated when using MMC instead of UMC (Figure S1).

## *In vivo* sciatic nerve regeneration

Unimodular and multimodular versions of our construct were implanted into a 15 mm-long rabbit sciatic nerve defect for 6 months. Three different groups were studied (**Figure 2**): a unimodular conduit (UMC) with a single 15-mm long HA module, a multimodular conduit (MMC) with two 7.5-mm long HA modules and a multimodular conduit with pre-seeded hSC (MMC + hSC). The total length of the conduits was 20 mm, including the 2.5 mm-long end bands used to keep the microfibril bundle in place and to suture the constructs to the nerve stumps (**Figure 6**).

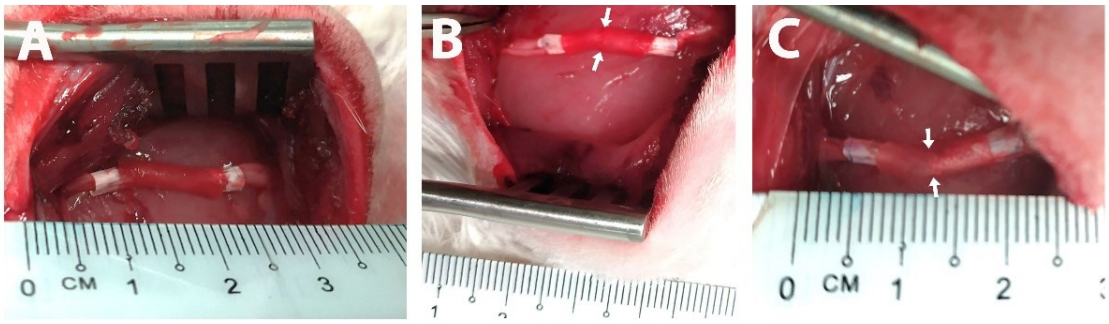


**Figure 6.** Photographs of the surgery after the insertion of the implants. (**A**) Unimodular conduit (UMC). (**B**) Multimodular conduit (MMC). (**C**) Multimodular conduit with pre-seeded human Schwann cells (MMC + hSC). In white are the end bands employed for the insertion and suture of the distal and proximal nerve stumps. The total length of the implants (one conduit for the UMC group and two conduits for the MMC and MMC + hSC groups) was 20 mm, including the 2.5 mm-long end bands. The length of the nerve gap was 15 mm. The arrows in B and C indicate the separation between both HA modules.

Hematoxylin-eosin staining (**Figure 7**) shows the HA conduit (marked with *) enclosing the PLA microfibers (marked with arrows), which are found inside the lumen of the HA conduit. The PLA microfibers are homogeneously distributed, covering a

large cross-sectional area of the lumen. The HA conduit presents quite a preserved structure, with only an incipient degradation 6 months after its implantation (**Figure 7A–C,G–I**), so it will retain its structure long enough for nerve regeneration to complete before being replaced by new tissue. The incipient degradation of the HA conduit is based on the detailed visualization of the histological images, where the HA porous structure presents voids and breaks in continuity for all the experimental groups (marked with circles in **Figure 7** and **Figure 8**). The same is presumed to happen to the PLA microfibers, but in longer term this is due to their slower degradation rate (median half-life around 30 weeks) [76]. Until its complete degradation, the HA conduit has protected the PLA microfibers inside from possible adhesions with the surrounding tissue, maintaining the disposition of the PLA microfibers. In addition, the HA conduit has served to maintain the structure of the hSC sheath previously cultivated inside its lumen for the MMC + hSC group.

Commonly used NGC for the regeneration of the peripheral nervous system made of type I collagen, polyglycolic acid or porcine small intestinal submucosa degrade after 3 to 4 months [16]. By contrast, the HA conduit in our experiments lasted for 6 months with quite a preserved structure. This may represent an advantage, so that the HA conduit can fulfill its function during the entire time that the nerve regenerates, which takes several months. Since it will, nonetheless, eventually be resorbed, the HA hydrogel conduit is preferable to non-biodegradable NGC employed in the clinic made of materials like polyvinyl alcohol or silicon, whose destiny is to remain undegraded forever, usually encapsulated [16].

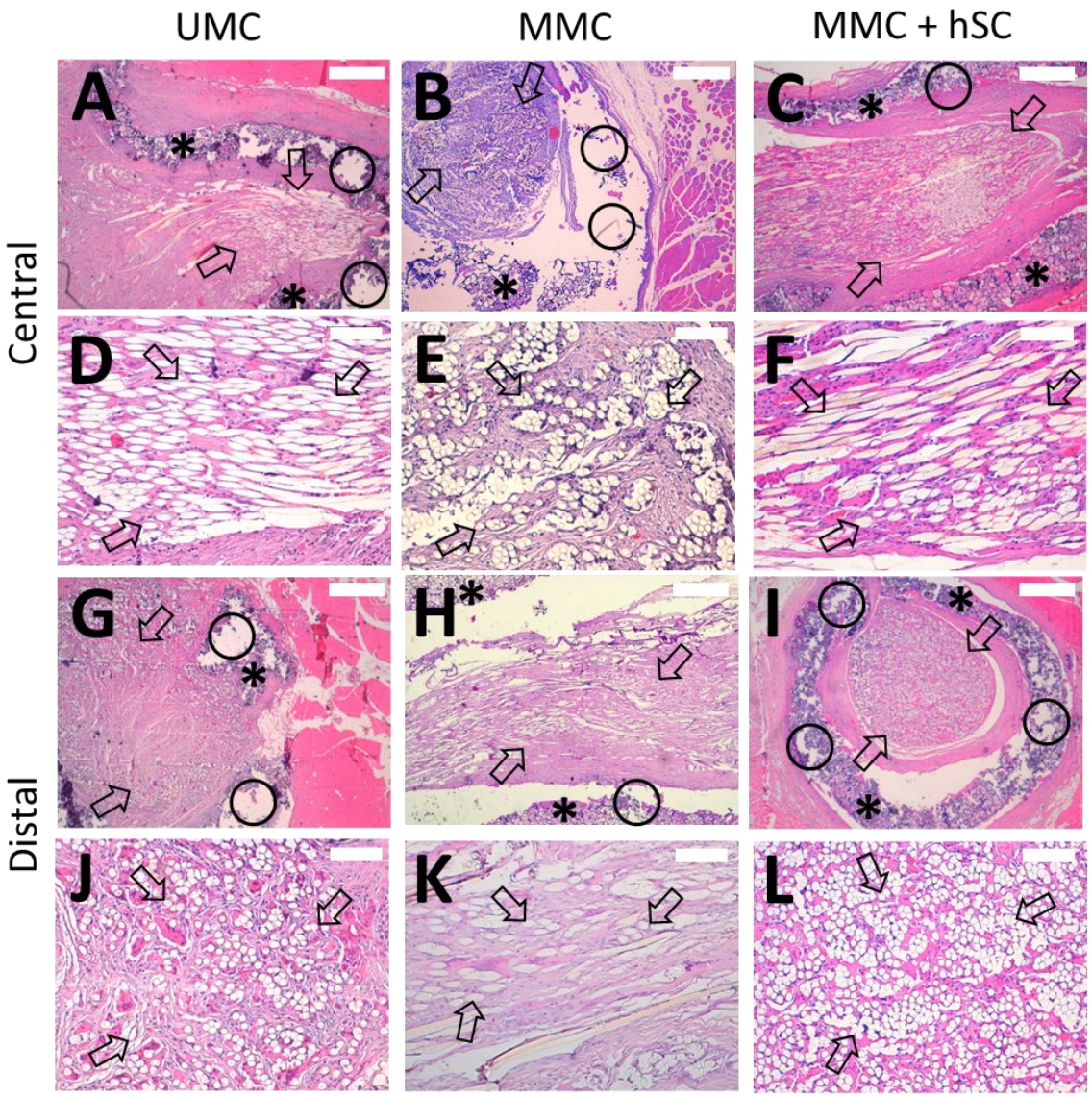


**Figure 7.** Hematoxylin and eosin staining of tissue samples from the three experimental groups 6 months after surgery. Representative images of central portions of UMC (**A, D**), MMC (**B, E**) and MMC + hSC (**C, F**) groups as well as distal portions of UMC (**G, J**), MMC (**H, K**) and MMC + hSC (**I, L**) groups are shown, with magnifications of 4× (A, B, C, G, H, I) and 20× (D, E, F, J, K, L). Cross sections of the HA conduit (marked with *) can be observed enclosing the PLA microfiber bundle (marked with arrows), which is placed inside the lumen of the HA conduit. The HA conduit walls present signs of incipient degradation in all experimental groups, since their porous structure presents voids and breaks in continuity (marked with circles). The PLA microfibers appear quite separated, occupying much of the lumen of the HA conduit to support and guide axonal growth. A well-organized connective tissue can be observed, with the presence of collagen and nerve fibers. The presence of an inflammatory response was not detected. Scale bar = 500 µm for 4× images, 100 µm for 20× images.

In all the studied specimens, the presence of a newly formed connective tissue was observed, which was well-organized, with collagen fibers (mainly type I collagen) and fibroblasts, along with a variable number of nerve fibers (**Figure 7**). The presence of an inflammatory response was not detected at 6 months. No aggregates of lymphocytes or PMNs were observed in any of the samples studied. In the same way, no adipose infiltrate was observed. Other normal cell types of the conjunctiva, mainly fibroblasts, were also observed. Inflammatory infiltrates of lymphocytes, neutrophils, eosinophils, or plasma cells were not observed. This is indicative of the absence of inflammation.

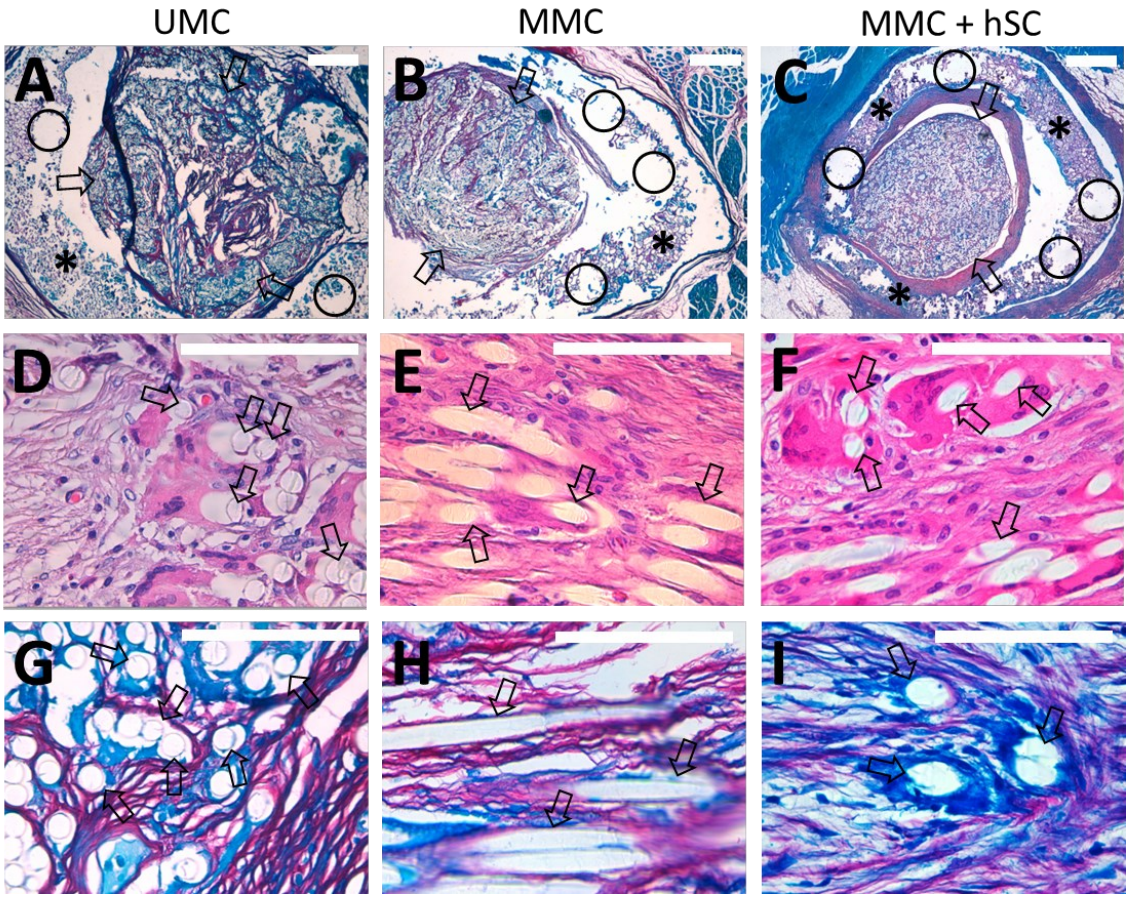


**Figure 8.** Luxol fast blue staining of tissue samples from the three experimental groups 6 months after surgery at the distal portion (**A**–**C**) and details of hematoxylin and eosin staining (**D**–**F**), as well as Luxol fast blue (**G**–**I**), with the aim of studying the interaction of PLA microfibers with the surrounding tissue. (**A**–**C**) Luxol fast blue stains (4×) of cross sections showing the distribution of PLA microfibers (marked with

arrows) within the HA conduit (marked with *). The HA conduit walls present signs of incipient degradation in all experimental groups, since their porous structure presents voids and breaks in continuity (marked with circles). (**D**–**F**) Hematoxylin-eosin staining (63×) showing the distribution of the tissue and the PLA microfibers for the UMC, MMC and MMC + hSC groups, respectively. Some voids are observed between the tissue and the PLA microfibers for the UMC (**D**) and MMC (**E**) groups, whereas closer contact between the tissue and PLA microfibers is observed for the MMC + hSC group (**F**). (**G**–**I**) Luxol fast blue stains (63×) showing the interaction between PLA microfibers and myelinated nerve fibers (in dark blue), macrophages (in light blue) and collagen (in red) for the UMC, MMC and MMC + hSC groups, respectively. For the UMC (**G**) and MMC (**H**) groups, some voids are observed between myelinated nerve fibers and PLA microfibers, whereas a much closer distribution of myelinated nerve fibers and PLA microfibers without voids is appreciated for the MMC + hSC group (**I**). Scale bar = 500 μm for 4× images, 100 μm for 63× images.

The PLA microfibers appeared quite separated, occupying much of the lumen of the HA conduit. The presence of PLA microfibers coincided with the presence of a neo-formed well-configured and balanced connective tissue where the presence of nerve fibers was appreciated (**Figure 7D–F, J–L**). Macrophages and giant cells were observed associated with PLA microfibers, embracing them where they appear as giant foreign body cells (**Figure 8D–F**). Macrophages are related to the resorption of the material and the regeneration of connective tissue, given their ability to eliminate detritus of the lesion and to control the functioning of fibroblasts. For the UMC and MMC groups (**Figure 8G, H**), some void spaces were observed between the PLA microfibers and myelinated nerve fibers. However, for the MMC + hSC group (**Figure 8I**), the myelinated nerve fibers were much closer to the PLA microfibers, embracing them completely. We think that this is due to the presence of pre-seeded Schwann cells on the surface of the PLA microfibers, which associate with the nerve fibers, causing the nerve fibers to remain much closer to the PLA microfibers.

Modified Luxol fast blue method was employed to characterize the presence and distribution of myelinated nerve fibers [69], and morphometric studies were carried out. Since we assume a good regeneration in the proximal portion with respect to the lesion, we focused on the analysis of the central and distal groups. In general, we were able to detect the presence of a high amount of myelinated nerve fibers in all the experimental groups, with a similar content of myelinated nerve fibers at the central and distal portions.

In the central portion, the area occupied by myelinated nerve fibers from the total available area was higher in the MMC group than in the UMC group (**Figure 9**). For the UMC group, a content in myelinated nerve fibers of 28 ± 7% was measured, whereas for the MMC group, it increased to 47 ± 14% (**Figure 9D**). Regarding the animals with two modules and pre-seeded hSC (MMC + hSC group), an additional increase in the area occupied by myelinated nerve fibers was observed, arriving at 69 ± 9%, confirming the beneficial effect of pre-seeded hSC. This trend was maintained in the distal portions of the scaffolds studied, with 27 ± 9%, 45 ± 14%, and 65 ± 5% of the area occupied by myelinated nerve fibers for the UMC, MMC and MMC + hSC groups, respectively. The amount of collagen presented an opposite trend, where groups with a higher amount of myelinated nerve fibers presented a lower amount of collagen, and vice versa (**Figure 9E**).

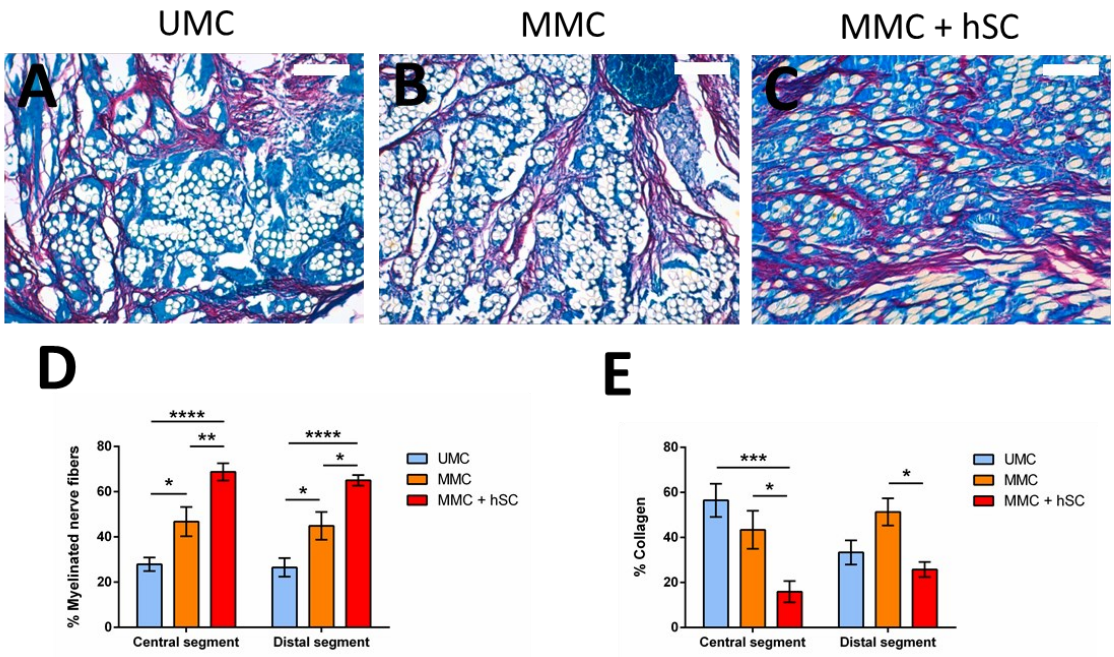


**Figure 9.** Luxol fast blue staining of tissue samples from the three experimental groups 6 months after surgery at the distal portion and quantification of the area of myelinated nerve fibers and collagen. (**A**–**C**) Luxol fast blue images of UMC, MMC and MMC + hSC, respectively, showing the collagen in red, the myelinated nerve fibers in dark blue, the macrophages/giant cells in light blue and the PLA/vessels/cavities in white. Magnification of 20×. Scale bar = 100 µm. (**D**, **E**) Quantification of the area occupied by myelinated nerve fibers and collagen, respectively, after excluding the area occupied by PLA microfibers, vessels and cavities. Statistically significant differences are indicated by *, **, *** or ****, indicating a p-value below 0.05, 0.01, 0.001 or 0.0001, respectively.

Several studies have evaluated the *in vivo* regeneration of the sciatic nerve after a crush injury, correlating the histological findings with the functional and electrophysiological recovery [77,78]. It was observed that 2 weeks after injury, almost all axons presented a Wallerian degeneration, a decomposition of the myelinated structure. This implied that, after 2 weeks, the number of axons and the area of myelinated axons significantly decreased compared with week 0, without an observable motor function recovery. The regenerating nerve fibers appeared histologically 4 weeks post-injury, but

the motor function recovery remained missing. At 6 weeks after injury, the area of myelinated axons increased significantly to 30%, correlating to an increased motor function recovery. At 8 weeks after injury, the area of myelinated axons had an additional increased 50%, correlating to a good motor function recovery, scoring 4/4 in the toe-spreading index (TSI) for behavioral analyses. In our case, at 6 months after injury, the area of myelinated nerve fibers was above 60% in both the central and distal segments, which is a value correlated to a total motor function recovery [77,78].

Different studies have also evaluated the correlation between the histological and electrophysiological outcomes after the full section of the sciatic nerve, bridging the gap with a NGC [25,67]. An equivalent performance of both techniques was observed, and when the histological images showed regenerated nerve fibers in the distal stump, the electrophysiological analysis showed the functional reinnervation of downstream muscles, with a direct correlation between the number of regenerated nerve fibers and the compound muscle action potential (CAMP) amplitude of the gastrocnemius muscle [25].

One of the greatest challenges in the implantation of long NGC in the peripheral nervous system is a lack of oxygen and nutrient diffusion, specially at the central zone of the graft, which prevents the migration of SCs and axons. After the guidance conduit is implanted, the growth of capillaries in the central part of the lumen may be too slow to provide adequate nutrients to the cells, inhibiting tissue formation in the scaffold core. This is due to the slow neovascularization process of the regenerated nerve, which starts from both ends of the implant. Therefore, achieving a successful vascularization is one of the main objectives in nervous tissue engineering. The multimodular design of our NGC was presumed to favor the vascularization of the neo-formed tissue, since the

inter-module gap represents a way for cell migration at the midpoint of the implant's length.

To study this process, immunohistochemistry for CD31 was used. To avoid artifacts derived from the immunohistochemical technique, all the studied sections were stained at the same time. As shown in **Figure 10**, the number of CD31 positive vessels was higher in the central and distal portions of the MMC (**Figure 10C, D**) and MMC + hSC groups (**Figure 10E, F**) when compared to the UMC group (**Figure 10A, B**). For the central portion, 12 ± 2 vessels/mm$^2$ were counted for the UMC group, and 39 ± 3 vessels/mm$^2$ and 34 ± 3 vessels/mm$^2$ were counted for the MMC and MMC + hSC, respectively (**Figure 10G**). The same trend was observed for the distal portions, with 20 ± 1 vessels/mm$^2$ for the UMC group, 47 ± 5 vessels/mm$^2$ for the MMC group and 47 ± 11 vessels/mm$^2$ for the MMC + hSC group (**Figure 10G**). Therefore, the MMC groups presented more microvessels, which correlates with an increased expression of angiogenic markers, as reported previously [79].

The higher vascularization of the MMC and MMC + hSC groups when compared with the UMC group may be traced to the gap (around 100 μm) between the two HA modules of the implant. This inter-module gap improves the oxygen and nutrients exchange of the central portion of the guidance conduit, leading to an improved vascularization of this zone and, therefore, to a more efficient nerve regeneration.

An upgrade that could be incorporated into the concept of our implant is a prior seeding of the modules with HUVEC, which can give rise to a pre-vascularization inside the conduit [80]. This pre-vascularization of scaffolds can improve the construct maturity and the blood perfusion after its implantation *in vivo* [81,82]. Long NGC require an adequate blood supply throughout their entire length, and the central zone usually lacks it. An early vascularization of the whole length of the guidance conduit could

improve nutrient availability for Schwann cells and contribute to the growth of new axons.

Several limitations of this study should be considered. Firstly, the study would have benefited from the inclusion of more rabbits in each surgical group, but it must be considered that it is a pilot trial to assess which of the three studied groups achieved a better nerve regeneration, and the number of animals had to be small. Future studies will increase the number of animals employing the MMC + hSC group, which was the better one. Secondly, it should be noted that the demonstration of axonal regeneration through the injured nerve does not necessarily translate to the recovery of the function. The path of the axon until its arrival to the final organ is one of the most interesting phases of the regeneration process, but its arrival alone does not guarantee the return of useful function [83]. Therefore, new electrodiagnostic studies are required to reveal conduction through our NGC.

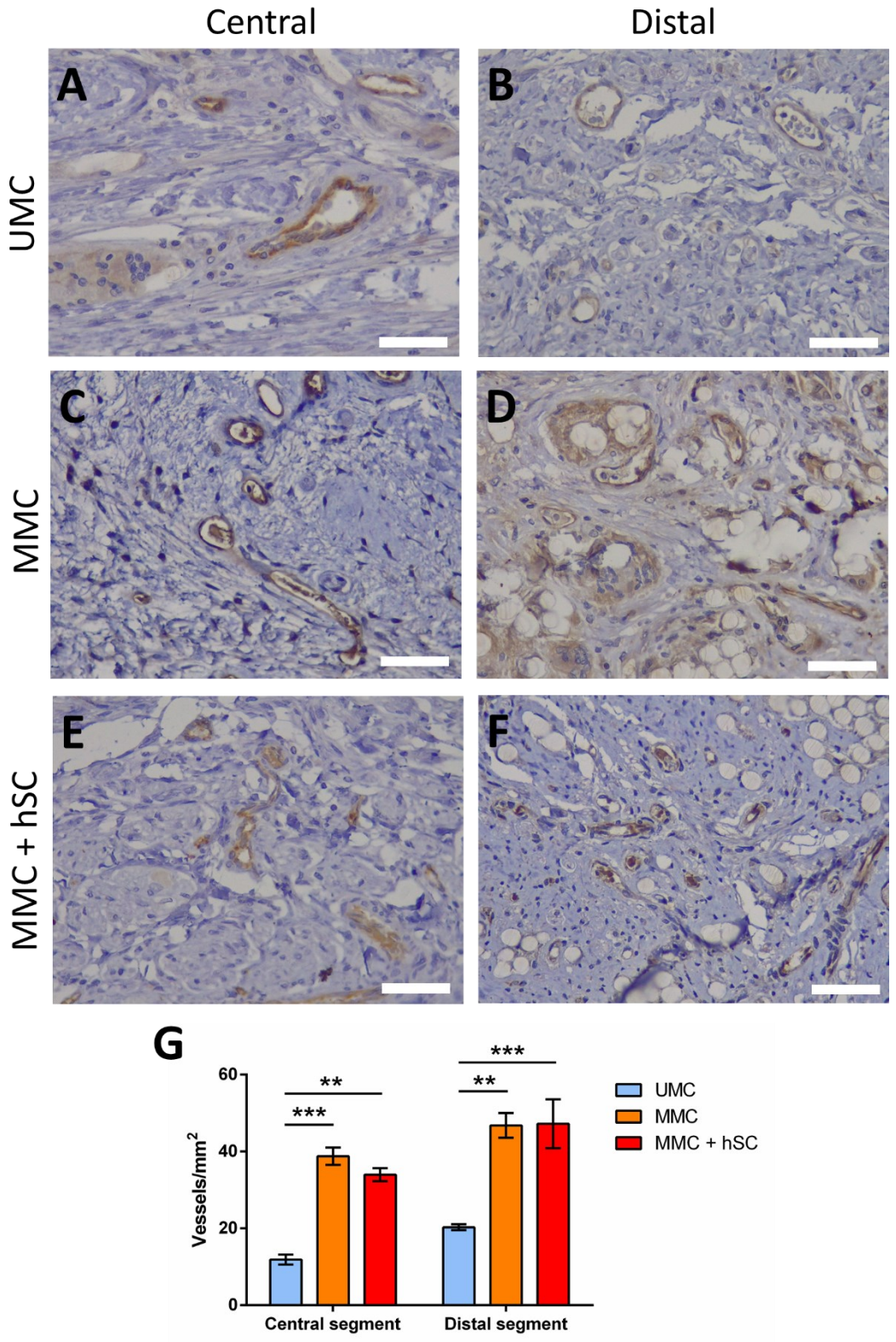


**Figure 10.** CD31 immunostaining images at central and distal portions and quantification of the number of vessels. (**A**,**B**) CD31 immunostaining of the UMC group at the central and distal portion, respectively. (**C**,**D**) CD31 immunostaining of the MMC group at the central and distal portion, respectively. (**E**,**F**) CD31 immunostaining

of the MMC + hSC group at the central and distal portion, respectively. Blood vessels are marked with brown color. Scale bar = 50 μm. (**G**) Quantification of the number of vessels/mm$^2$ for the three groups at the central and distal portions. Statistically significant differences are indicated by ** or ***, indicating a p-value below 0.01 or 0.001, respectively.

# 3.5. Conclusions

A multimodular concept for a nerve guidance conduit based on a PLA microfiber bundle inside HA conduits has been manufactured and studied *in vivo* in a long-defect lesion model. The inner diameter and length of the elements were adapted to meet the size requirements of a long-gap (15 mm) rabbit sciatic nerve defect. Schwann cells supporting axonal growth were seeded into the implant and cultured prior to surgery. The device provides a highly flexible structure with an aligned microfibrillar core inside hollow hydrogel modules that serves as a substrate for cell colonization, thus supporting axonal growth in a directional manner. The HA cylinders prevent adherences to the surrounding tissues, retain the pre-seeded auxiliary Schwann cells in place and protect the regeneration process from outer inflammatory cells. The multimodular design facilitates a more uniform distribution of pre-seeded cells in the conduit than in the case of a single, equal-length module. The multimodularity of the concept allows for achieving greater total lengths by placing different numbers of modules consecutively. Implanted for 6 months in a sciatic nerve defect model in rabbits, the device enabled the regeneration of the nerve, with a high percentage of myelinated fibers reaching the central and distal portions of the length. The multimodular design achieved a better neovascularization than the unimodular design and led to a better regeneration. The pre-seeded Schwann proved to be beneficial for the regeneration process since an additional increment of the quantity of myelinated nerve fibers was observed. Thus, the group that combined the multimodular design with the pre-seeded Schwann cells had the highest

nerve regeneration, accompanied by a higher vascularization. These results validate the combination of multimodularity and cell supply as a means to increase the efficiency of nerve regeneration.

## 3.6. Authorship contribution statement

F.G.R.: Methodology, Validation, Formal analysis, Investigation, Writing—Original Draft, Visualization. L.G.S.: Investigation, Writing—Review and Editing, Supervision. M.M.R.: Formal analysis, Writing—Review and Editing. L.M.M.: Formal analysis, Writing—Review and Editing. C.M.-R.: Conceptualization, Methodology, Validation, Writing—Review and Editing, Supervision, Funding acquisition. M.M.P.: Conceptualization, Methodology, Validation, Writing—Review and Editing, Supervision, Project administration, Funding acquisition. All authors have read and agreed to the published version of the manuscript.

## 3.7. Conflicts of interest

There are no conflicts to declare.

## 3.8. Acknowledgements

F.G.R. acknowledges the scholarship FPU16/01833 from the Spanish Ministry of Universities. The authors thank the technical support of Enrique Blas Ferrer (University Institute of Animal Science and Technology, Universitat Politècnica de València) and the Electron Microscopy Service of the Universitat Politècnica de València, where the FESEM images were obtained.

## 3.9. References

1. R. M. G. Menorca, T. S. Fussell, J. C. Elfar, *Hand Clin.* **2013**, *29*.

2. A. M. Moore *et al.*, *Muscle and Nerve* **2011**, *44*.

3. P. Chen, X. Piao, P. Bonaldo, *Acta Neuropathol.* **2015**, *130*.

4. O. A. R. Sulaiman, T. Gordon, *Glia* **2000**, *32*.

5. B. J. Pfister *et al.*, *Crit. Rev. Biomed. Eng.* **2011**, *39*.

6. K. S. Katiyar *et al.*, *Front. Bioeng. Biotechnol.* **2020**, *8*, 1.

7. X. Jiang, S. H. Lim, H. Q. M. Hai-Quan, S. Y. Chew, *Exp. Neurol.* **2010**, *223*.

8. M. Siemionow, G. Brzezicki, *Int. Rev. Neurobiol.* **2009**, *87*, 141.

9. W. Z. Ray, S. E. Mackinnon, *Exp. Neurol.* **2010**, *223*, 77.

10. J. S. Belkas, M. S. Shoichet, R. Midha, *Neurol. Res.* **2004**, *26*, 151.

11. B. Battiston, S. Geuna, M. Ferrero, P. Tos, *Microsurgery* **2005**, *25*.

12. F. F. A. Ijpma, J. P. A. Nicolai, M. F. Meek, *Ann. Plast. Surg.* **2006**, *57*.

13. J. Moskow *et al.*, *Bioact. Mater.* **2019**, *4*.

14. B. Ferrigno *et al.*, *Bioact. Mater.* **2020**, *5*.

15. M. Zheng *et al.*, *Bioact. Mater.* **2021**, *6*.

16. S. Kehoe, X. F. Zhang, D. Boyd, *Injury* **2012**, *43*, 553.

17. B. J. Parker, D. I. Rhodes, C. M. O'Brien, A. E. Rodda, N. R. Cameron, *Acta Biomater.* **2021**, *135*, 64.

18. P. Chrząszcz *et al.*, *Neurol. Neurochir. Pol.* **2018**, *52*.

19. P. A. Wieringa, A. R. G. de Pinho, S. Micera, R. J. A. van Wezel, L. Moroni, *Adv. Healthc. Mater.* **2018**, *7*.

20. E. O. Johnson, P. N. Soucacos, *Injury* **2008**, *39*.

21. S. Houshyar, A. Bhattacharyya, R. Shanks, *ACS Chem. Neurosci.* **2019**, *10*.

22. V. Chiono, C. Tonda-Turo, *Prog. Neurobiol.* **2015**, *131*.

23. M. Yu *et al.*, *Acta Biomater.* **2021**, *134*, 190.

24. P. Muangsanit, V. Roberton, E. Costa, J. B. Phillips, *Acta Biomater.* **2021**, *126*,

224.

25. M. L. D. Rayner, A. G. E. Day, K. S. Bhangra, J. Sinden, J. B. Phillips, *Acta Biomater.* **2021**, *135*, 203.

26. C. R. Carvalho, J. M. Oliveira, R. L. Reis, *Front. Bioeng. Biotechnol.* **2019**, *7*.

27. L. Yao *et al.*, *Biomaterials* **2010**, *31*.

28. A. Pabari, H. Lloyd-Hughes, A. M. Seifalian, A. Mosahebi, *Plast. Reconstr. Surg.* **2014**, *133*.

29. A. Höke, T. Brushart, *Exp. Neurol.* **2010**, *223*.

30. D. Grinsell, C. P. Keating, *Biomed Res. Int.* **2014**, *2014*.

31. S. Y. Fu, T. Gordon, *J. Neurosci.* **1995**, *15*.

32. C. Krarup, S. J. Archibald, R. D. Madison, *Ann. Neurol.* **2002**, *51*.

33. A. M. Moore *et al.*, *Hand* **2009**, *4*.

34. D. D. Allison, K. J. Grande-Allen, *https://home.liebertpub.com/ten* **2006**, *12*, 2131.

35. M. N. Collins, C. Birkinshaw, *Carbohydr. Polym.* **2013**, *92*, 1262.

36. Z. Zhang, O. Ortiz, R. Goyal, J. Kohn, *Princ. Tissue Eng. Fourth Ed.* **2013**, 441, doi:10.1016/B978-0-12-398358-9.00023-9.

37. Y. Liang, P. Walczak, J. W. M. Bulte, *Biomaterials* **2013**, *34*, 5521.

38. S. K. Seidlits *et al.*, *Biomaterials* **2010**, *31*, 3930.

39. X. Wang, J. He, Y. Wang, F.-Z. Cui, *Interface Focus* **2012**, *2*, 278.

40. M. Salehi *et al.*, *J. Biomed. Mater. Res. Part B Appl. Biomater.* **2018**, *106*, 1463.

41. M. C. Araque-Monrós *et al.*, *Polym. Degrad. Stab.* **2013**, *98*, 1563.

42. M. Santoro, S. R. Shah, J. L. Walker, A. G. Mikos, *Adv. Drug Deliv. Rev.* **2016**, *107*, 206.

43. S. hui Hsu, S. H. Chan, C. M. Chiang, C. Chi-Chang Chen, C. F. Jiang,

*Biomaterials* **2011**, *32*, 3764.

44. J.-J. Liu, C.-Y. Wang, J.-G. Wang, H.-J. Ruan, C.-Y. Fan, *J. Biomed. Mater. Res. Part A* **2011**, *96A*, 13.
45. F. Gisbert Roca, J. Más Estellés, M. Monleón Pradas, C. Martínez-Ramos, *Int. J. Biol. Macromol.* **2020**, *163*, 1959.
46. F. Gisbert Roca *et al.*, *Macromol. Biosci.* **2021**, *21*, 2000391.
47. M. Monleón Pradas, C. Martínez Ramos, L. Rodríguez Doblado, F. Gisbert Roca, **2021**, ES20210030065 20210127.
48. P. Carmeliet, M. Tessier-Lavigne, *Nature* **2005**, *436*, 193.
49. J. M. Grasman, D. L. Kaplan, *Sci. Rep.* **2017**, *7*, 1.
50. C. Leventhal, S. Rafii, D. Rafii, A. Shahar, S. A. Goldman, *Mol. Cell. Neurosci.* **1999**, *13*, 450.
51. A. L. Cattin *et al.*, *Cell* **2015**, *162*, 1127.
52. M. D. Sarker, S. Naghieh, A. D. McInnes, D. J. Schreyer, X. Chen, *Prog. Neurobiol.* **2018**, *171*, 125.
53. X. Zhao *et al.*, *ACS Nano* **2020**, *14*, 12579.
54. G. Vilariño-Feltrer *et al.*, *Acta Biomater.* **2016**, *30*, 199.
55. F. Gisbert Roca *et al.*, *Int. J. Biol. Macromol.* **2020**, *148*, 378.
56. C. Martínez-Ramos *et al.*, *J. Tissue Eng. Regen. Med.* **2019**, *13*, 509.
57. L. R. Doblado, C. Martínez-Ramos, J. M. García-Verdugo, V. Moreno-Manzano, M. M. Pradas, *J. Neural Eng.* **2021**, *18*, 0460c5.
58. P. Armati, E. Mathey, *J. Neurol. Sci.* **2013**, *333*, 68.
59. K. R. Jessen, *Int. J. Biochem. Cell Biol.* **2004**, *36*, 1861.
60. G. Nocera, C. Jacob, *Cell. Mol. Life Sci.* **2020**, *77*, 3977.
61. K. R. Jessen, R. Mirsky, *J. Physiol.* **2016**, *594*, 3521.

62. M. Georgiou *et al.*, *Biomaterials* **2013**, *34*, 7335.

63. L. Ning *et al.*, *Biofabrication* **2018**, *10*, 035014.

64. Y.-S. Lee, S. Wu, T. L. Arinzeh, M. B. Bunge, *J. Vis. Exp.* **2017**, *2017*, 56077.

65. J. Bastidas *et al.*, *Glia* **2017**, *65*, 1278.

66. A. Merolli, M. Li, G. Voronin, L. Bright, *J. Mater. Sci. Mater. Med.* **2022**, *33*.

67. T. Jeon *et al.*, *Eur. Radiol. Exp.* **2018**, *2*, 1.

68. A. Barmpitsioti *et al.*, *Microsurgery* **2011**, *31*, 545.

69. E. Sajadi, A. Raoofi, S. Abdi, H. Azimi, M. A. Abdollahifar, *Int. J. Morphol.* **2020**, *38*, 1197.

70. N. J. Martínez-Hernández *et al.*, *Artif. Organs* **2021**, *45*, 1491.

71. J. Shen, H. Q. Wang, C. P. Zhou, B. L. Liang, *Microsurgery* **2008**, *28*, 32.

72. S. Ibrahim, Q. K. Kang, A. Ramamurthi, *J. Biomed. Mater. Res. Part A* **2010**, *94A*, 355.

73. R. Li *et al.*, *Mol. Med. Rep.* **2018**, *17*, 4360.

74. A. R. Nectow, K. G. Marra, D. L. Kaplan, *Tissue Eng. - Part B Rev.* **2012**, *18*, 40.

75. M. Sarker, S. Naghieh, A. D. McInnes, D. J. Schreyer, X. Chen, *Biotechnol. J.* **2018**, *13*.

76. D. da Silva *et al.*, *Chem. Eng. J.* **2018**, *340*, 9.

77. T. Yamasaki *et al.*, *Magn. Reson. Imaging* **2015**, *33*, 95.

78. M. Bendszus, C. Wessig, L. Solymosi, K. Reiners, M. Koltzenburg, *Exp. Neurol.* **2004**, *188*, 171.

79. A. Ruiz-Saurí *et al.*, *Pathol. Oncol. Res.* **2016**, *22*, 807.

80. J. Shen *et al.*, *Cite This ACS Appl. Mater. Interfaces* **2021**, *13*, 50801.

81. A. Newman Frisch, L. Debbi, M. Shuhmaher, S. Guo, S. Levenberg, *Curr. Opin. Biotechnol.* **2022**, *73*, 188.

82. S. Ben-Shaul, S. Landau, U. Merdler, S. Levenberg, *Proc. Natl. Acad. Sci. U. S. A.* **2019**, *116*, 2955.

83. J. Z. Young, *Physiol. Rev.* **1942**, *22*, 318.

## 3.10. Supporting information

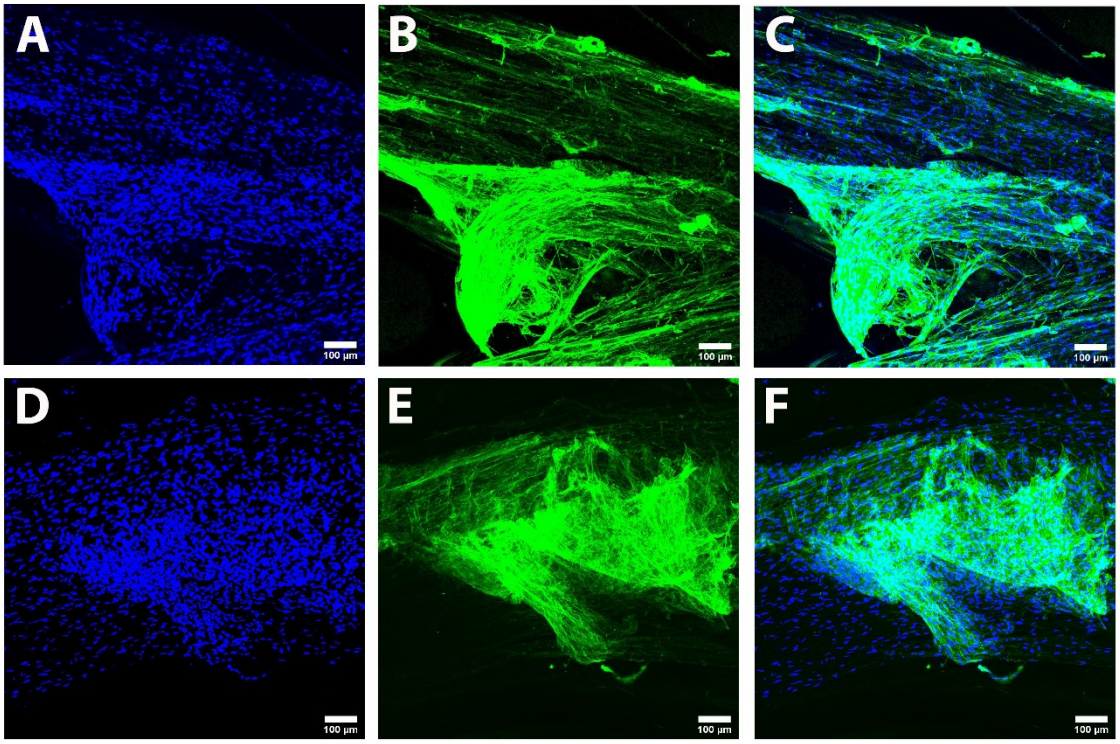


**Figure S1.** Confocal images of human Schwann cells (hSC) seeded on a unimodular conduit (UMC). A-C: Images after the culture of $2.5 \cdot 10^6$ hSC for 5 days. D-F: Images after the culture of $1.25 \cdot 10^6$ hSC for 10 days. The cytoskeleton of hSC is observed in green color (Phalloidin) and the nuclei of hSC is observed in blue color (DAPI). As can be seen, the cells have formed a sheath that fills the lumen of the conduit and that also covers the surface of PLA microfibers. However, the cell sheath is not continuous, and some bald spots are observed. These discontinuities are more pronounced when $2.5 \cdot 10^6$ hSC are cultured for 5 days.

# 4. Paper 2: Conduits based on the combination of hyaluronic acid and silk fibroin: characterization, *in vitro* studies and *in vivo* biocompatibility

# Conduits based on the combination of hyaluronic acid and silk fibroin: characterization, *in vitro* studies and *in vivo* biocompatibility

Fernando Gisbert Roca [a], Paloma Lozano Picazo [c], [d], José Pérez-Rigueiro [b], [c], [d], Gustavo Víctor Guinea Tortuero [b], [c], [d], Manuel Monleón Pradas [a], [b] and Cristina Martínez-Ramos [a], *

[a] Center for Biomaterials and Tissue Engineering. Universitat Politècnica de València. Camino de Vera s/n, 46022, Valencia, Spain.

[b] CIBER-BBN, Biomedical Research Networking Center in Bioengineering Biomaterials and Nanomedicine, Spain.

[c] Centro de Tecnología Biomédica. Universidad Politécnica de Madrid. 28223 Pozuelo de Alarcón (Madrid), Spain.

[d] Departamento de Ciencia de Materiales. ETSI Caminos, Canales y Puertos., Universidad Politécnica de Madrid, 28040, Madrid.

*Corresponding author: Cristina Martínez Ramos. Centro de Biomateriales e Ingeniería Tisular, C.P.I. Edificio 8E, Acceso F, Nivel 1, Universidad Politécnica de Valencia, Camino de Vera s/n E-46022 Valencia, España. Tel.: +34963877000. E-mail: cris_mr_1980@hotmail.com.

**Keywords:** biomaterials, hyaluronic acid, silk fibroin, tissue engineering, nerve guidance conduits.

Published online: 16 January 2020

Reprinted with permission from Macromolecular Materials and. Engineering 2021, 306, 2000584 

# 4.1. Abstract

We address the production of structures intended as conduits made from natural biopolymers, capable of promoting the regeneration of axonal tracts. We combine hyaluronic acid (HA) and silk fibroin (SF) with the aim of improving mechanical and biological properties of HA. The results show that SF can be efficiently incorporated into the production process, obtaining conduits with tubular structure with a matrix of HA-SF blend. HA-SF has better mechanical properties than sole HA, which is a very soft hydrogel, facilitating manipulation. Culture of rat Schwann cells shows that cell adhesion and proliferation are higher than in pure HA, maybe due to the binding motifs contributed by the SF protein. This increased proliferation accelerates the formation of a tight cell layer, which covers the inner channel surface of the HA-SF tubes. Biocompatibility of the scaffolds was studied in immunocompetent mice. Both HA and HA-SF scaffolds were accepted by the host with no residual immune response at 8 weeks. New collagen extracellular matrix and new blood vessels were visible and they were present earlier when SF was present. The results show that incorporation of SF enhances the mechanical properties of the materials and results in promising biocompatible conduits for tubulization strategies.

# 4.2. Introduction

Injuries and diseases affecting the nervous system have very high incidence and prevalence, affecting millions of people around the world. New concepts and solutions are in demand for both the central nervous system (CNS) and the peripheral nervous system (PNS). In the human CNS axons do not regenerate spontaneously after damage or degeneration, causing life-long functional deficit as in the case of spinal cord injury, traumatic brain damage or cerebral infarction [1]. Failure of axonal regeneration is

probably due, among other factors, to the formation of an impenetrable glial scar, composed mainly of astrocytes, that inhibits axonal growth and myelination [2]. This causes regenerative neurons to be blocked and unable to reach their synaptic target. In the PNS there is successful endogenous axon regeneration in adult humans for distances of few centimetres [1]. Here damage is followed by a degeneration of the distal segment of the nerve, known as Wallerian degeneration, while the proximal segment of the nerve suffers only minimal damage [3,4]. After the distal segment degeneration, Schwann cells and phagocytic cells such as macrophages remove myelin and axonal debris while producing cytokines that improve the axonal growth, creating a growth cone able to direct axon regrowth until reconnection with the distal target. Finally, Schwann cells myelinate the re-growing axon forming new myelin sheaths [4,5]. Nonetheless, in cases of larger damages the process of regeneration is not successful.

In order to improve over the limitations of current therapies tissue engineering approaches invoke the combination of cell supply, bioactive molecules and scaffolds based on biomaterials [6,7]. conduits typically consist in hollow tubes used to connect the two ends of a damaged nerve, guiding the axonal regeneration between both sides of the injury [8]. Their main goal is to protect the spontaneous regeneration process. Conduits must guide tissue regeneration from one end to the other of the lesion, avoiding the growth of fibrous tissue and retaining the neurotrophic factors secreted by the damaged nerve remnants [9]. Tubular scaffolds should have a porosity large enough to allow the exchange of oxygen and nutrients, and small enough to prevent the infiltration of inflammatory cells into the conduit and to minimize the outflow of cells and growth factors out of the structure; furthermore, they should possess adequate mechanical properties to allow its manipulation during surgery and be flexible and soft enough not to compress the regenerated axons [6,9].

Here we present conduits made from hyaluronic acid (HA), a natural biomaterial that is widely present in the extracellular matrix of most tissues [10]. HA is a non-branched glycosaminoglycan formed by repetitions of D-glucuronic acid and D-N-acetylglucosamine [10]. HA has an excellent biocompatibility and unique biological properties, as it regulates the immune and inflammatory response, the cell differentiation, the vascularization, the scar tissue formation and the cell adhesion to extracellular matrix (ECM) proteins [10,11]. In addition, HA modulates the behaviour of glial and immune cells [10]. A very important characteristic of HA is its high hydrophilicity, due to hydrogen bonding interactions between its chains and water [12,13]. Scaffolds made out of HA have been studied for the regeneration of the CNS, showing their biocompatibility and ability to induce neural regeneration [14–18].

Tubular scaffolds made out of HA are able to induce seeded Schwann cells to form highly organized structures *in vitro* [19,20]. The HA tubes acted as a template in organizing the growth of the Schwann cells into cylindrical cell sheets. To improve the properties of such biohybrids (structures composed by NGCs with cells) and their biological response here we incorporate *Bombyx mori* silk fibroin (SF) in the production process of the scaffolds. SF is the term conventionally used for referring to the heavy chain protein which is the main constituent of the silk fibers of the cocoons [21] . SF is a protein with a molecular weight in excess of 300 kDa [22] that presents the specific motif of sequence –GAGAGS–. Due to its biological function, SF has robust mechanical properties and, in addition, a notable biocompatibility [23] and remarkable cell adhesion. This latter property might be favoured by the presence of arginine residues in the sequence of SF. The arginine residues might be recognized by cell membrane adhesion proteins such as integrins and would contribute to the good biological response to the material [22–25]. Besides its excellent *in vitro* and *in vivo* biocompatibility SF also shows

a slow proteolytic biodegradation [23,26–28]. Combinations of HA and SF have been previously studied as patches for cardiac reparation [29–31], films for growth factor release [32] and dermal tissue regeneration [33], 3D matrices for cartilage tissue engineering [34], and scaffolds for osteoarthritis surgery [35], tissue engineering [36–39] and dermal tissue reconstruction [40]. The presence of SF enhances the mechanical properties of the structures and increases the resistance to degradation when compared to those based only on HA [39,41,42], while the presence of HA increases the water retention and the cell growth when compared to scaffolds made only of SF [38,39,41–43]. Regarding the methods of combination of HA and SF previously studied, these are based on the physical [42], covalent [44] or enzymatic [39] cross-linking of both materials, being the SF the majority component.

The present work aimed at combining SF and HA in a way such that the cell-templating ability of the HA tubes was preserved, while their mechanical properties and biological response were improved. Our interest thus was in combining both materials but with a majority fraction of HA. It may be noted that both HA and SF are materials currently approved by the United States Food and Drug Administration (FDA) for different uses in biomedical applications in humans, particularly in guidance of peripheral nerve regeneration. [45–48].

# 4.3. Experimental section

## SF preparation

Fibroin was extracted from Bombyx mori cocoons. Initially, the cocoons were degummed in an aqueous $Na_2CO_3$ solution (0.2 w/v) and heated to 121 °C in an autoclave (Sturdy SA-252F) for 50 minutes. The degumming process solubilizes the sericin coating that covers the fibroin fibers, so that it can be removed. Fibroin was

washed with distilled water for 20 minutes and the washing step was repeated three times. The fibers were allowed to dry overnight and then immersed in a 9.3 M LiBr solution and introduced in a furnace at 60 °C for 4 hours, so that a fibroin solution was obtained. After being dissolved, the silk solution was dialyzed against deionized water to remove the LiBr salt. Dialysis membranes (BioDesign Dialysis Tubing) with a MWCO of 3500 Da were used. Water was changed every 8 hours and the whole process proceeded for 48 hours. After dialysis the fibroin solution was centrifuged at 5000 rpm for 20 minutes at 21 °C to remove any debris. Finally, the fibroin was lyophilized and stored in a freezer at -20 °C.

## HA and HA-SF films preparation

A 5 % w/w solution of HA derived from *Streptococcus equi* (1.5-1.8 MDa, 53747, Sigma-Aldrich) in NaOH 0.2 M was elaborated by gently stirring for 24 hours under normal conditions of temperature and pressure (NCTP, 25 °C, 100 kPa). The solution was then homogenized by agitation at NCTP for 20 minutes and mixed with the divinyl sulfone cross-linker (DVS; V3700, Sigma-Aldrich) in a 9:10 DVS:HA monomeric units molar ratio. This mixture (hereinafter referred to as HA) was kept under stirring for 10 seconds to achieve the correct mixing and to begin the crosslinking process.

The elaboration of biomaterials based on the combination of HA and SF is analogous to that of HA, with the exception that, after the elaboration of the HA solution, it was mixed with SF in a concentration of 3 % w/v (hereinafter referred to as HA-SF). The process was then continued by homogenization of the solution by stirring for 20 minutes and cross-linking with DVS, as it was done for HA.

Then, the material was injected by pipetting into a polytetrafluoroethylene (PTFE) mold formed by two flat faces on both sides of a U-shaped intermediate plate. After the injection of the material into the mold, it was left for 1 hour in NCTP to achieve the

complete crosslinking of the material. Afterwards, it was frozen for 4 hours at -20 °C and then for 24 hours at -80 °C. Once frozen, the material was lyophilized (LyoQuest-85, Telstar Life Science) for 24 hours at 20 Pa and -80 °C. Finally, the different parts of the mold were separated to proceed to the extraction of the film.

## HA and HA-SF conduits preparation

To obtain the conduits, the biomaterials were injected by pipetting into a PTFE mold formed by elongated channels with a square profile of 2 mm per side. A polycaprolactone fiber (PCL; Polysciences) with a diameter between 950 and 1050 μm was introduced into the center of each channel to form the lumen of the conduit. At both ends of the PCL fiber, a PTFE sheath was inserted with a thickness slightly greater than 2 mm. By pressing the ends of the fiber it was fixed in the center of the channel at the same approximate distance from all the walls. After the injection of the material into the mold, it was left for 10 minutes in NCTP to achieve the complete crosslinking of the material. Subsequently, it was subjected to freezing and lyophilization with the same parameters used for films. Finally, the PCL fibers were removed from the inside, forming the lumen of the conduit.

To study the effect of the dissolution of SF in a basic medium, unprocessed SF (hereinafter referred to as untreated SF) was compared with a 3 % w/v SF solution in deionized water (hereinafter referred to as water-treated SF) and with a 3 % w/v SF solution in NaOH 0.2 M (hereinafter referred to as NaOH-treated SF). The solutions were homogenized by stirring in NCTP for 20 minutes and then they were spilled into a PTFE plate to give them a film shape. They were then frozen and lyophilized with the same parameters as the other films.

## Morphology characterization

For the characterization of the surface morphology and of the geometry of axial and cross-sectional cuts of conduits, a field emission scanning electron microscope (FESEM; ULTRA 55, ZEISS Oxford Instruments) was used. The preparation of the samples consisted primarily in a desiccation under vacuum conditions during the 24 hours prior to the test to avoid interferences due to evaporated water. Subsequently samples were placed on a carbon tape and a carbon bridge was created between the sample and the carbon tape. Finally, samples were coated with a thin layer of platinum. Conduits were cut longitudinally and transversally to observe the interior of the lumen and the morphology of the porosity of the walls. The voltage used was 2 kV. The study was performed with three different samples (n = 3) made of HA and HA-SF.

## Elemental analysis

The FESEM was also used to carry out an elemental analysis through an energy dispersive X-ray spectroscopy (EDS) to verify the presence of SF, by studying the nitrogen (N) content. Samples were prepared as above. The elemental analysis provided the mass fraction (ω) of N, oxygen (O) and sulfur (S) in each selected area of the material. The voltage used was 2 kV. The study was performed with three different samples (n = 3) of films made of HA and HA-SF.

## Stability against swelling and drying cycles

This study was carried out to evaluate the possible loss of material in cycles of swelling and drying. For this purpose, both the amount of non-crosslinked mass and the water uptake were studied. Disc-shaped films of 8 mm dry diameter ($D_0$) of HA and HA-SF were used. Samples were first vacuum desiccated for 6 hours at 50 °C. They were then weighed ($m_0$) using a balance (AX205, Mettler-Toledo Inc., sensitivity of

0.01 mg). After that, discs were swollen in deionized water for 24 hours to attain the maximum degree of swelling and the diameter was measured ($D_1$). The process was then carried out a second time: samples were first air-dried for 6 hours and then dried in a desiccator for 6 hours with continuous vacuum and a temperature of 50 °C; they were then weighed (m). Finally, discs were swollen in deionized water for 24 hours and the diameter was measured ($D_2$). To study the loss of mass, the parameter $m/m_0$ was calculated, while the water uptake was characterized through the parameter $D_i/D_0$ for the first (i=1) and the second (i=2) swelling. The swelling ratio (Q) was also calculated as $(D_i/D_0)^3$ for the first (i=1) and the second (i=2) swelling. The procedure was repeated for 4 different discs (n = 4) of each material.

## Dimensional change in swelling

To study the swelling characteristics, conduits dimensions were measured before and after the absorption of water. For this purpose, conduits made of HA and HA-SF were prepared with two different lengths: samples of approximately 4 mm in length to study the change in length and samples of approximately 1 mm in length to study changes in the lumen diameter. Samples were examined and photographed using a binocular magnifying glass (MZ APO, Leica Microsystems). Once images of dry samples were acquired, they were swollen in deionized water for 24 hours and images in swelling state were acquired. The measurement of the dimensions was performed using the ImageJ/FIJI image processing software [49]. The dimensions (length, lumen diameter) in dry and swollen conditions were calculated for 4 different samples (n=4). The variation of the dimensions of the conduits was calculated by the ratios L/L0 (length in swelling state (L) divided by length in dry state (L0)) and D/D0 (lumen diameter in swelling state (D) divided by lumen diameter in dry state (D0)).

## Density and porosity

Density and porosity of samples were determined gravimetrically, using a balance (AX205, Mettler-Toledo Inc., sensitivity of 0.01 mg) equipped with a density measurement kit. First, the weight of the NGC in air ($W_a$) was measured. Subsequently, the sample was immersed in n-octane (n-octane: 412236, Sigma-Aldrich) and placed under vacuum for 30 minutes to replace the air inside the pores by n-octane. After removing the n-octane from the lumen of the conduit with an absorbent paper, the weight of the conduits was measured with n-octane in the pores ($W_p$). Finally, the NGC with n-octane in the pores was completely submerged in n-octane and the apparent weight of the conduits immersed in n-octane ($W_i$) was measured. Following Archimedes, the density of the sample without considering the air inside the pores was obtained applying **Equation (1)**, were $\rho_o$ is the density of n-octane. The porosity was then calculated applying **Equation (2)**. This procedure was performed for 3 samples (n = 3) of HA and HA-SF.

$$Density = \frac{W_a}{W_a - W_i} \cdot \rho_o \quad (1)$$

$$Porosity = \frac{V_{pores}}{V_{total}} = \frac{W_p - W_a}{W_p - W_i} \quad (2)$$

## Thermogravimetric analysis (TGA)

A thermogravimetric analyzer (TGA/SDTA 851 Mettler-Toledo operated using the STARexx software) was used to study the thermal degradation and composition of the materials. To study the effect of the basic manufacture conditions on SF, untreated, water-treated and NaOH-treated samples of SF were measured. Samples were first

maintained at a temperature of 30 °C for 2 minutes. Then a heating ramp was applied from 30 °C to 120 °C with a heating rate of 10 °C/min. After that, a preheating stage consisting of maintaining a temperature of 120 °C for 30 minutes was applied to eliminate all the water content of the sample. Finally, a heating ramp was applied from 120 °C to 720 °C with a heating rate of 10 °C/min. The procedure was performed under a positive nitrogen flow ($N_2$) of 20 ml/min and was repeated for three different samples (n=3) of each of the materials mentioned above. As a result, thermograms in which the mass loss of the sample is represented as a function of temperature were obtained. These curves were normalized dividing through the weight existing at the end point of the preheating plateau.

Assuming that thermal degradation proceeds in composite HA-SF samples as it would for both pure separate components, an estimate of mass loss in composites is given by **Equation (3)**, were $\Delta m_{HA}$ and $\Delta m_{SF}$ are the experimental curves of pure HA and SF, respectively, and $\omega_{SF}$ is the mass fraction of SF.

$$\Delta m_{comp}=\omega_{SF}\cdot\Delta m_{SF}+(1-\omega_{SF})\cdot\Delta m_{HA} \quad (3)$$

This equation was employed to deduce a value of $\omega_{SF}$ from the measured curves of $\Delta m_{HA}$, $\Delta m_{SF}$, $\Delta m_{exp}$. For this purpose, $\Delta m_{comp}$ given by **Equation (3)** was least-squares fitted to $\Delta m_{exp}$ taking $\omega_{SF}$ as fitting parameter.

## Characterization of mechanical properties

The mechanical characterization of the materials was performed by rotational rheometry (Discovery Hybrid Rheometer DHR, TA Instruments) in order to study the effect of incorporating SF on the shear modulus (G) of the material. The samples

(circular films 20 mm in diameter) were studied in a state of swelling in deionized water for 24 hours.

An oscillation test was performed with a frequency of 1 Hz and torque amplitudes ranging from 10 to 100 μN· m with a logarithmic sweep. Since the samples' diameter, 20 mm, didn't coincide with the diameter of the rheometer plates, 25 mm, the modulus values calculated by the equipment's software were corrected to take this mismatch into account, by multiplying the software's data with the ratio of both areas.

## Schwann cell culture

Culture of rat Schwann cells (rSCs; P10301, Innoprot) was performed on 8 mm diameter films and on NGCs made of HA and HA-SF to study the cell adhesion and proliferation.

A sanitization of the materials (films and conduits) was first carried out by immersion in 70 % ethanol (ET00021000, Scharlab) for 2 hours, in 50 % ethanol for 10 minutes and in 30 % ethanol for another 10 minutes. Thereafter the ethanol residues were removed by performing 3 washes of 10 minutes with ultrapure water (Mili-Q®). The preconditioning of the materials was done by immersion in culture medium (Dulbecco's modified Eagle medium with a high glucose level (4.5 g/L) (DMEM; 21331020, Life Technologies) supplemented with 10 % of fetal bovine serum (FBS; 10270-106/A3381E, Life Technologies) and 1 % penicillin/streptomycin (P/S; 15140122, Life Technologies)) and incubation at 37 °C for 24 hours in a humidified atmosphere containing 5 % $CO_2$.

After the expansion of the rSCs in a cell culture flask, they were washed with PBS and a trypsin/EDTA solution (T/E; 25200-072, Life Technologies) was then added to break the cell-matrix and cell-cell interactions in order to remove the cells from the bottom of the culture bottle. After centrifugation at 1080 rpm for 5 minutes, the pellet

was resuspended in Schwann cell culture medium (P60123, Innoprot). At this moment, the seeding with rSCs in passage 5 was performed with a seeding density of 10.000 cells per film and 250.000 cells per NGC. Finally, the culture was introduced in an incubator at 37 °C with a humid atmosphere containing 5 % $CO_2$ for 1 and 5 days in the case of films and for 1, 5 and 10 days in the case of NGCs, renewing the Schwann cell culture medium every 48 hours.

## Fluorescent staining of the cytoskeleton

The morphologies of the cells were examined by fluorescently staining their F-actin cytoskeletons. Stains were performed on the cultured rSCs to carry out the labelling of specific proteins and observe the cellular arrangement. The following procedure was repeated after 1 and 5 days of culture in the case of films and after 1, 5 and 10 days in the case of conduits.

First, the Schwann cell medium was removed and the materials (films and conduits) were washed with PBS. Thereafter, cells were fixed with 4 % paraformaldehyde (PFA; 47608, Sigma-Aldrich) for 20 minutes at room temperature. After cell fixation, 3 washes of 10 minutes with DPBS were performed to remove PFA residues. At this point, the non-specific bindings were blocked and the cell membrane was permeabilized by the use of a blocking buffer composed of DPBS with 3 % bovine serum albumin (BSA; A7906, Sigma-Aldrich) and 0.1 % Tween20 (P1379, Sigma-Aldrich) for 45 minutes at room temperature. Cells were finally stained with FITC-phalloidin (B607, Life Technologies) to mark the cytoskeleton actin filaments (green colour) and with DAPI (D9564, Sigma-Aldrich) at a 1/5000 dilution for 10 minutes to mark the cells nuclei (blue colour). The imaging was performed using a confocal microscope (LEICA TCS SP5, Leica microsystems).

From the images obtained by confocal microscopy, and thanks to staining with FITC-phalloidin, the total area occupied by the cells cytoskeleton was calculated. ImageJ/FIJI image processing software was used for this purpose [49]. Four different samples (n = 4) of HA and HA-SF films and conduits were studied.

## MTS cell proliferation assay

To evaluate the cell proliferation inside the conduits, MTS assays (CellTiter 96 Aqueous One Solution Cell Proliferation Assay, Promega) were carried out on HA and HA-SF conduits (n = 3 each). When incorporated to the cells, the MTS was bioreduced by metabolically active cells at different times of cell culture (1, 5 and 10 days) in a rate proportional to the number of live cells. After 3 hours of incubation with the reagent, the medium was removed and its absorbance was measured with a Victor Multilabel Counter 1420 spectrophotometer (Perkin-Elmer) at 490 nm.

## Biocompatibility of subcutaneously implanted scaffolds

All procedures were performed under the Spanish Regulations for animal experimentation (Laws 53/2013, 178/2004) with the approval of Animal Care Committee of the Polytechnic University of Madrid (Madrid, Spain) and according to the ARRIVE (Animal Research: Reporting *In Vivo* Experiments) guidelines. *In vivo* studies were conducted in adult male CD-1 mice (35-40 g body weight; 12-15 weeks old; n=5 mice for each group). All mice were bred and housed in the animal facility of the Centre for Biomedical Technology. All animals were kept at constant temperature (±22°C) and humidity (~52 %) with free access to food and water in 12 hours light/dark cycle.

HA and HA-SF scaffolds (1.5 x 6 mm) were subcutaneously implanted at different locations in each mouse to compare the bioresponse of both scaffolds in the same

animal and reduce data dispersion due to inter-animal variability. A sanitization of the materials was previously carried out by immersion in 70 % ethanol for 2 hours, in 50 % ethanol for 10 minutes and in 30 % ethanol for another 10 minutes. Afterwards the ethanol residues were removed by performing 4 washes of 10 minutes with ultrapure water. The preconditioning of the materials was done by immersion in PBS for 24 hours.

Surgeries were performed under anaesthesia with 2% Isoflurane in air. The back of each mouse was shaved, and the skin was disinfected with povidone-iodine. All surgeries were made under aseptic conditions and Vaseline was administrated to protect the eyes from dehydration. To implant the scaffolds, an incision of approximately 1 cm was made on the dorsal part of each mouse and the subcutaneous space was separated with scissors. The incisions were then sutured with 3-0 surgical Nylon. Buprenorphine (0.05-0.1 mg/kg) was administered as a pain reliever for 48 hours post-surgery and, if signs of pain were seen, Ibuprofen (30 mg/kg) was dispensed via oral in drinking water for 1 week. All animals were then carefully monitored for the following 3 days by animal care services. Sham-operated animals as negative controls were subjected to identical procedures, but no scaffolds were implanted in this case.

At different time points after scaffolds implantation (1, 4 and 8 weeks), the mice were euthanized in 100 % $CO_2$ atmosphere (5-10 min) followed by cervical dislocation. The dorsal skin was carefully resected and immediately immersed in PBS solution. The skin sections containing the scaffolds together with the surrounding tissues were excised and fixed in 4% paraformaldehyde for 7 days. Before cutting, skin sections were cryoprotected in 30% sucrose. Samples were embedded in optimal cutting temperature compound and serial 10 µm thick sections were cut with a Microm HM550 cryostat (Thermo Scientific, Kalamazoo, USA). Cryostat sections were stained with

hematoxylin-eosin (H&E) and Masson's trichrome. To examine cell infiltration, extracellular matrix deposition and neovascularisation, micrographs were captured through an Olympus BX51 microscope (Olympus DP70, Olympus America Inc. Center Valley, PA, EEUU).

## Statistical analysis

Results were expressed as mean ± standard deviation (SD). The statistical analysis of the results was performed with the software GraphPad Prism 6 using the non-parametric Mann-Whitney test based on rank comparison. Statistically significant differences are indicated by an asterisk (*), indicating a p-value below 0.05. Four asterisks (****) indicate a p-value below 0.0001.

# 4.4. Results and discussion

## Effect of preparation procedures on material composition

The crosslinking reaction of HA with DVS takes place in basic pH [10]. Since an aqueous solution of SF was mixed with the basic HA-DVS solution during the material preparation process, it was necessary to assess the effect of exposure of SF to the basic solution. A thermogravimetric analysis (TGA) of untreated SF, water-treated SF and NaOH-treated SF (**Figure 1A**) shows slight modifications of the temperature-dependent mass loss. Prolonged exposure of SF to a basic medium causes hydrolysis of peptide bonds [50]. Therefore, when SF is added to the solution of 5 % HA in 0.2 M NaOH, it is subjected to a basic medium throughout the process and it suffers the hydrolysis of a number of peptide bonds. Chemical alteration of silk by immersion in a NaOH solution accumulates to the reduction in the molecular weight induced by the degumming process. It was found that this reduction is larger when $Na_2CO_3$ is added to the

degumming medium due to the resulting pH of the solution [51]. TGA data reflects an alteration as a difference in both curves in the range between 500 °C and 700 °C. **Figure 1B** shows the thermograms of untreated HA, NaOH-treated SF and of HA-SF films. The composite HA-SF materials have degradation patterns somehow intermediate, as expected. With these data, an estimate of the SF mass fraction in the composite sample can be obtained by least-square fitting the parameter in **Equation (3)**, as explained above. This gives a figure of $\omega_{SF,exp}$= 37±5, close enough to the theoretical $\omega_{SF,th}$ = 37.50±0.01, confirming efficient incorporation of SF to the HA matrix during the manufacturing process.

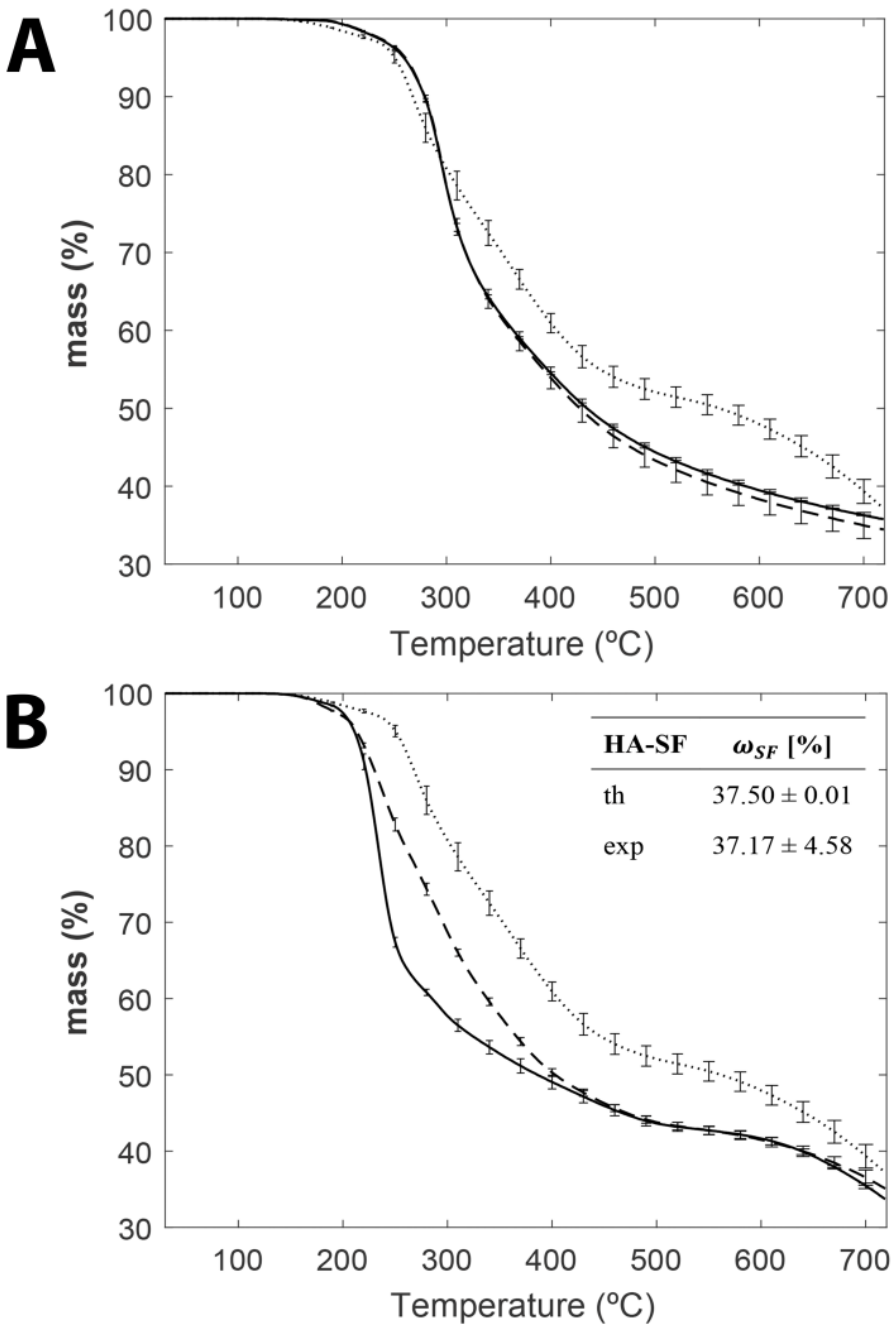


**Figure 1. A**: Experimental thermograms of NaOH-treated SF (dotted line), water-treated (solid line) and untreated SF (dashed line). Values are expressed as mean ± SD. The thermograms show that SF exposed to a basic medium suffers a chemical alteration. **B**: Experimental thermograms of HA (solid line), HA-SF (dashed line) and NaOH-treated SF (dotted line). Values are expressed as mean ± SD. In the temperature range between 220 °C and 370 °C there is an intermediate behavior of the HA-SF thermogram, indicating the presence of SF. The theoretical and the experimental mass fraction of SF in the HA-SF material is also indicated.

The different N content of SF and HA is reflected in the EDS data in **Table 1**. Theoretically, the mass fractions of N ($\omega_N$) in HA and in HA-SF samples are 2.60 % and 6.75 %, respectively. As shown in **Table 1**, the experimental mass fractions of N were lower than the theoretical ones. It should be noted that the elemental analysis is performed on very small areas of material, so a non-homogeneous distribution of SF could produce this difference. In addition, elemental analysis by EDS is sensitive solely to surface composition. **Table 1** shows also the ratios between $\omega_N$ and the mass fractions of O and S. All these parameters were substantially higher in the HA-SF samples than in the HA samples, proving the presence of SF in the matrices.

## Stability against swelling and drying cycles

The loss of mass of HA and HA-SF films after prolonged immersion in water was analysed to determine the stability against solution of the SF incorporated to the HA matrix, and whether the presence of SF could alter the sol fraction of HA in the crosslinked gel. As seen on **Table 1**, there were no significant differences in the mass loss between HA and HA-SF films after being swollen in water. A similar sol fraction (around 30 %) obtained in both systems.

Dimensional change upon swelling was expressed by computing the ratio of measured diameters of discs after swelling (D) and dry ($D_0$). Though small, the effect of SF is to constrain swelling and dimensional change, as expected (**Table 1**).

| | HA | HA-SF |
|---|---|---|
| $\omega_{N_{exp}}$ [%] | 1.0 ± 0.1 | 3.8 ± 0.9 |
| $\omega_N/\omega_O$ | 0.04 ± 0.01 | 0.20 ± 0.01 |
| $\omega_N/\omega_S$ | 0.18 ± 0.03 | 1.2 ± 0.2 |
| $m/m_0$ | 0.72 ± 0.01 | 0.70 ± 0.01 |
| $D/D_0$ (1st swelling) | 2.0 ± 0.1 | 1.78 ± 0.06 |
| $D/D_0$ (2nd swelling) | 2.1 ± 0.1 | 1.92 ± 0.09 |
| Q (1st swelling) | 8 ± 1 | 5.7 ± 0.6 |
| Q (2nd swelling) | 9 ± 2 | 7± 1 |

**Table 1**. Physicochemical properties of HA and HA-SF films. The quantities are defined in the text. Mass fraction from elemental analysis (ω); swelling parameters: mass ($m/m_0$), diameter ($D/D_0$) and swelling (Q) ratios. Values are expressed as mean ± SD.

## Mechanical properties of HA-SF

The mechanical behaviour of HA and HA-SF discs was assessed in shear experiments, in a rotational rheometer. **Figure 2A** shows the storage modulus (G', the real part of the complex shear modulus) obtained as a function of the oscillatory torque. G' quantifies the recoverable energy in a cycle, and thus measures the elasticity of the material. There is a clear increase of G' in samples containing SF, practically doubling the G' value for all the oscillation torques. This implies that the addition of SF allows the material to store more energy without suffering permanent deformation, indicating that interactions between SF and HA molecules make the HA chains less pliable to deformation, resulting in a greater stiffness of the material. There is a slight decrease in G' when the magnitude of the applied torque increases. This non-linear behaviour of the

material is indicative of strain-softening, and may be due to the rupture of SF···HA and HA···HA intermolecular interactions with larger values of torque. The loss modulus (G", the imaginary part of the complex shear modulus) is shown on **Figure 2B**. G" is a measure of the non-recoverable energy in a cycle due to different dissipative processes, and characterizes the viscous component of the material's response. Large values of G" are typical of soft hydrogels, and originate in internal friction due to water diffusion and chain slippage during deformation. Presence of SF in the material results in an increase of G", especially for low torque amplitudes, where the increase is almost double. This is indicative of the occurrence of new, additional frictional processes in the medium, arising from the SF···HA interactions as relative slippage and as formation and diffusion of defects. When the oscillation torque exceeds 40 μN · m, the difference decreases considerably. The fact that this difference is sensibly higher at lower deformations may suggest that it be related to the diffusion of water molecules in both gels, which is altered in the presence of the protein molecules. As already commented, the stiffness of the HA-SF material, as characterized by G', is greater than that of HA; however, its viscoelasticity, as characterized by the ratio G'/G", doesn't change very much (see **Table 2**).

| | **HA** | | **HA-SF** | |
|---|---|---|---|---|
| | $\mathbf{10\ \mu N \cdot m}$ | $\mathbf{100\ \mu N \cdot m}$ | $\mathbf{10\ \mu N \cdot m}$ | $\mathbf{100\ \mu N \cdot m}$ |
| G'/G" | 6.8± 0.7 | 6± 1 | 7± 2 | 7± 2 |

**Table 2**. G'/G" ratios for HA and HA-SF at two different torque values, 10 μN · m and 100 μN · m. Values are expressed as mean ± SD.

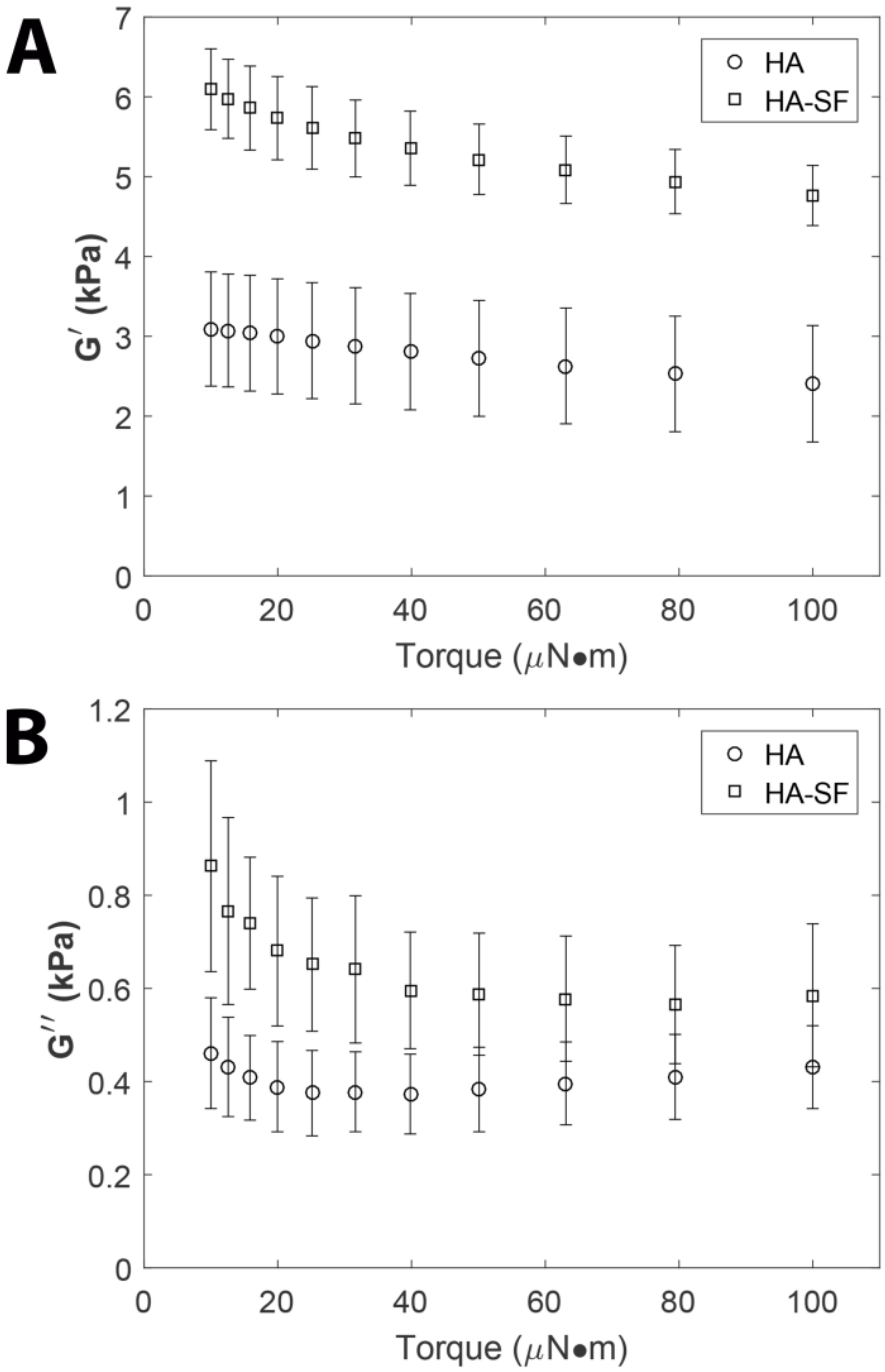


**Figure 2.** Storage modulus (**A**) and loss modulus (**B**) as a function of the oscillation torque for HA (circles) and HA-SF (squares). Values are expressed as mean ± SD. Presence of SF increases both the storage and the loss moduli.

## Adhesion and proliferation of Schwann cells on HA-SF films

Rat Schwann cells (rSCs) were seeded and cultured for 1 and 5 days on HA and HA-SF films in order to assess differences in adherence and proliferation. For the

visualization of the cells by confocal microscopy, a staining process was performed with FITC-phalloidin 488 to visualize their cytoskeletal actin fibers (green color) and with DAPI to visualize the cell nucleus (blue color). For the day 1, **Figure 3A** and **3C** show representative images of both studied cases in order to appreciate the differences in the total extent of the cytoskeleton, which is indicative of the cell adhesion characteristics on the material. On HA substrates (**Figure 3A**) early cell adhesion was scarce, and the cells had a marked globular morphology, in conformity with known facts [52]. This is a consequence of the highly hydrophilic nature of HA: the enormous amounts of water molecules which surround the HA chains hinder ECM protein deposition on its surface and thus difficult cell adhesion. This means that cell adhesion on the surface of HA materials must rely primarily on physical phenomena such as the surface roughness, where differential accumulation of HA molecules offers more stable anchoring sites to ECM proteins. With the material containing SF (**Figure 3C**) early cell adhesion was clearly greater, with the cells exhibiting a much more developed cytoskeleton. Several studies have shown that SF has good cell adhesion properties [25,53]. Although the RGD (Arg-Gly-Asp) cell binding motif as such is not present in the aminoacid sequence of *Bombyx mori* SF, an amino acid sequence has been observed in a non-repetitive C-terminal region with a large number of basic amino acids, especially arginine, which play a key role in the cell adhesion properties of SF [25]. Arginine residues can be recognized by transmembrane cell adhesion proteins such as integrins, which mediate in the interaction between cell and substrate [54,55].

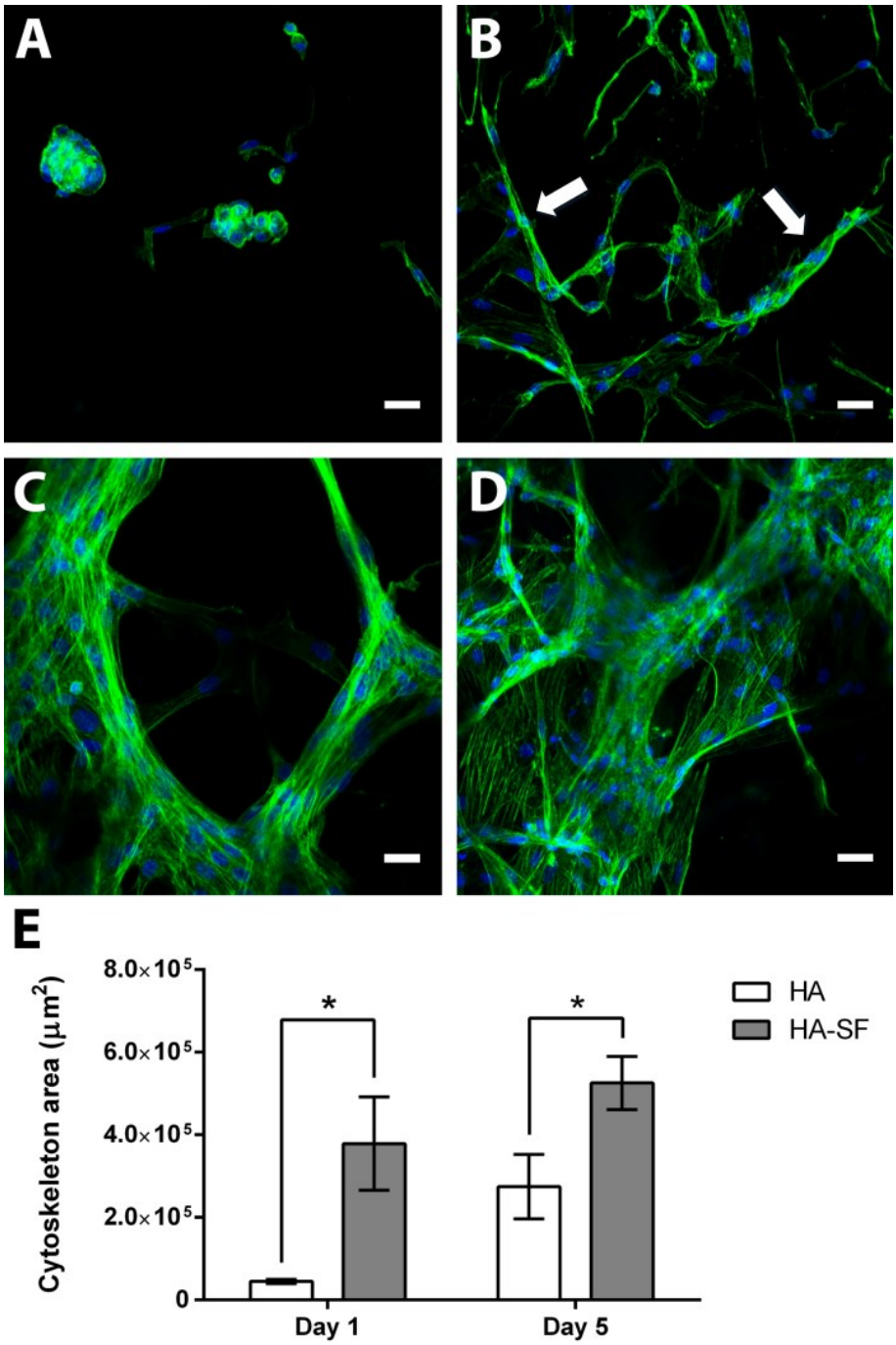


**Figure 3. A-D**: Confocal microscopy images corresponding to rSCs cultured on HA for 1 (A) and 5 days (B) and on HA-SF for 1 (C) and 5 days (D). The cytoskeleton is shown in green and the nuclei are shown in blue. Scale bar = 30 µm. **E**: Total area of rSCs cytoskeleta after 1 and 5 days of culture on HA and HA-SF. Cells cultured on HA-SF films presented a larger cytoskeleton area when compared to HA films, indicating a greater cell adhesion thanks to the presence of SF.

In order to quantify somehow the extent of cell adhesion, the total area occupied by the cytoskeleton of the cells was measured (**Figure 3E**), confirming the conclusions

obtained in a qualitative way. It can be seen that early cell adhesion in HA films is very low, while addition of SF clearly enhances early cell adhesion.

The same features were analysed after 5 days of cell culture (**Figure 3B** and **3D**) in order to compare early with late cell adhesion characteristics. On HA films cells now exhibited an elongated shape (arrows in **Figure 3B**). Some cells have been able to attach to specific sites on the material surface due to mediated cell···HA interactions, but preferentially the cells entertain cell···cell bonds forming filamentary structures with the shape of a necklace. In contrast, cells cultured on films with SF (**Figure 3D**) show larger fibrillary cytoskeleta spread on the material, indicative of a greater cell···surface interaction. When quantified (**Figure 3E**), this conclusion is further reinforced.

## Morphology and physicochemical properties of conduits

Longitudinal (axial) and transverse cuts of conduits show the lumina of the conduits and the porous walls, **Figure 4**. Both in HA and HA-SF conduits the lumen surface is always tighter and less porous than the walls, which is important to ensure that the cells seeded within the lumen are retained inside the conduit and cannot protrude across its walls. This is due to the fact that the surface of the PCL fiber used as a template of the lumen is hydrophobic; thus, in its vicinity non-swollen HA chains are predominant [19,20]. Water crystallization and subsequent lyophilization then produce a thin layer of denser HA close to the lumen. The pores observed in the conduit's wall matrix are produced by the phase-separation of water during the crystallization process. This structure ensures good diffusion of molecules across the conduit (water, oxygen, nutrients, factors), while efficiently retains the cells seeded inside the tube. The addition of SF to the HA matrix of the conduits thus didn't modify the main features of the original HA conduits. **Figure 4D'** shows a detail of the internal surface of the HA-SF

conduit, where elongated structures arranged on the surface (indicated with arrows) could correspond to SF fibers.

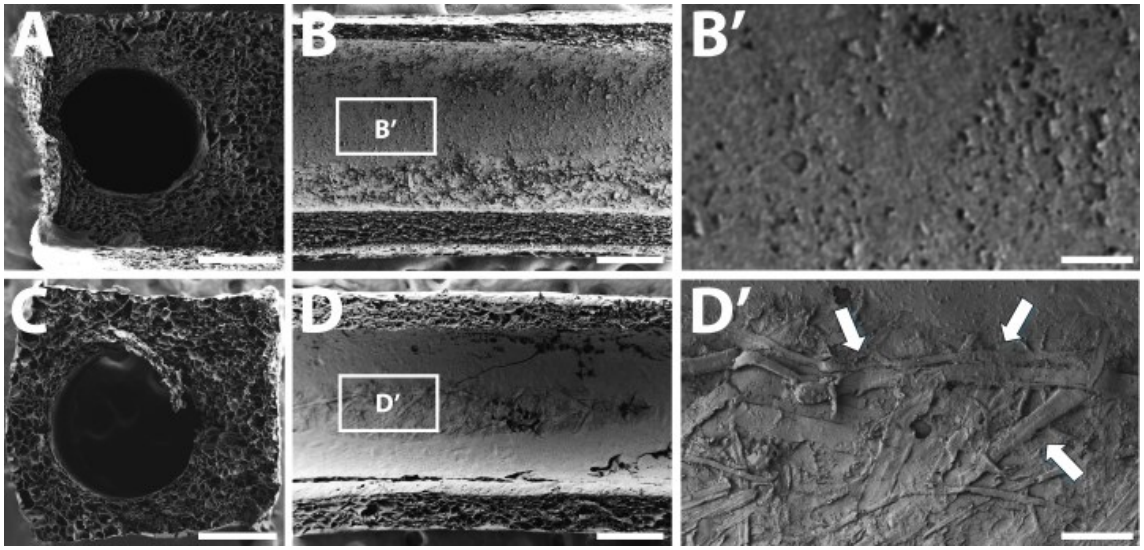


**Figure 4.** FESEM images of axial cuts and cross sections of HA (**A**, **B** and **B'**) and HA-SF (**C**, **D** and **D'**) NGCs. B' and D' show a detail of the internal surface of the conduit. Scale bar = 500 μm (A, B, C and D) and 100 μm (B' and D'). Matrix porosity is produced by the lyophilization process. The inner channel surface is less porous, due to the hydrophobic nature of the channel template. Arrows in D' indicate the presence of elongated structures on the surface of HA-SF NGCs that may correspond to SF fibers.

The swelling behaviour of HA and HA-SF conduits was characterized by the change in dimensions of conduit length and lumen diameter, **Table 3**. There is no significant difference in dimensional change between HA and HA-SF samples. Though very small, the effect of SF seems to be to introduce some anisotropy in the conduit's swelling as compared with the HA tubes: the HA-SF tubes swell somewhat less than the HA tubes transversally to their axis, while they swell somewhat more axially. This may have to do with anisotropies of the SF fibril distribution induced during the phase separation of crystallized water, a process which is determined by the geometry of the heat transfer between gel and mold during cooling.

**Table 3** shows the density and porosity of conduits made of HA and HA-SF. Regarding the density values, there's a slight decrease for HA-SF conduits, but it is not enough to show a statistical difference. This slight decrease may be due to the incorporation of SF, since SF has a lower density than HA [56,57]. Regarding the porosity values, the slight differences are not significant. This could be expected, since the pores are produced by the crystallization of the large amounts of water present in the samples, which are insignificantly influenced by the presence of the SF molecules.

| | **HA** | **HA-SF** |
|---|---|---|
| $L/L_0$ | 1.41 ± 0.06 | 1.6 ± 0.2 |
| $D_{lumen}/D_{lumen_0}$ | 1.21 ± 0.06 | 1.11 ± 0.05 |
| Density [g $cm^{-3}$] | 1.22 ± 0.08 | 1.1 ± 0.1 |
| Porosity [%] | 79 ± 1 | 78 ± 5 |

**Table 3**. Physicochemical properties of HA and HA-SF conduits. Density was calculated by Equation (1) and porosity by Equation (2). Swelling ratios L/L0 (length) and D/D0 (diameter) are explained in the text. Values are expressed as mean ± SD.

## HA-SF-Schwann cells biohybrids

Schwann cells seeded within the lumen of HA tubular scaffolds create a continuous cylinder which adapts to the inner channel surface, which acts as a template for the formation of such a cell sheath [19,20]. In HA tubes this process needs 9 days, and it is the result of the interplay of cell proliferation and cell···cell contacts being preferred over cell···material contacts, due to the highly hydrophilic nature of the HA matrix. To study this process in HA-SF tubes rSCs were seeded and cultured for 1, 5 and 10 days. Staining with FITC-phalloidin and DAPI permit to visualize the cell cytoskeleton (green in **Figure 5**) and nuclei (blue), respectively. A comparison of

**Figure 5A** and **5D** shows that at day 1 there are already differences between both materials, cell density and spread being higher in the HA-SF tubes. At day 5 (**Figure 5B** and **5E**) considerable proliferation of SCs has occurred in both cases. However, while the number of cells inside the HA conduit is still not enough to form the rSCs sheath, in the case of the HA-SF conduit the cell population is already organized as a cell cylinder (arrows in **Figure 5E** indicate how this sheath folds). This indicates that the higher cell adhesion and proliferation obtained by the incorporation of SF to the conduits allows us to obtain the rSCs sheath earlier when compared with NGCs based solely on HA. After 10 days culture the cell sheath is fully developed in both scaffolds, **Figure 5C** and **5F**. Previous studies showed that this kind of cell structure took 9 days to develop in HA tubular scaffolds [19,20]. We now see that the presence of SF protein in the HA matrix preserves the templating ability of the scaffold channel to induce the formation of the cell cylinder and accelerates it. Thus, while SF significantly increases cell adhesion on the channel surface due to the supply by SF of additional binding motifs, still cell···cell binding is preferred over cell···surface binding, as revealed by the easiness with which the cell cylinder gets unstuck from the scaffold (**Figure 5E** and **5F**).

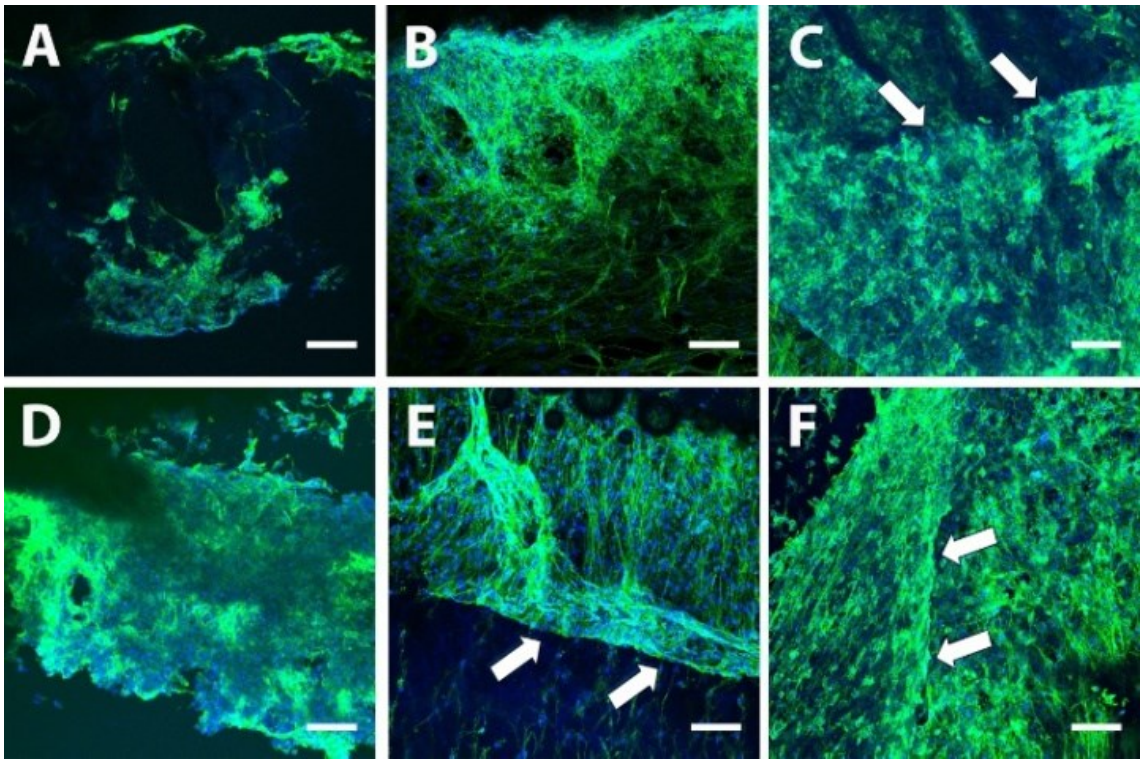


**Figure 5.** Confocal microscopy images corresponding to rSCs cultured inside HA tubes for 1 (**A**), 5 (**B**) and 10 days (**C**), and inside HA-SF tubes for 1 (**D**), 5 (**E**) and 10 days (**F**). The cytoskeleton is shown in green and the nuclei are shown in blue. Scale bars = 100 μm. The presence of SF seems to accelerate the formation of the cell sheath, which is completely developed in the HA-SF conduits at day 5 (arrows in E showing a fold of this structure), while it took 10 days to fully develop in HA tubes (arrows in C).

An MTS assay performed after 1, 5 and 10 days of cell culture (**Figure 6**) shows that the presence of SF significantly translates into higher cell proliferation inside the conduits, explaining the earlier formation of the cell sheath in the HA-SF conduits.

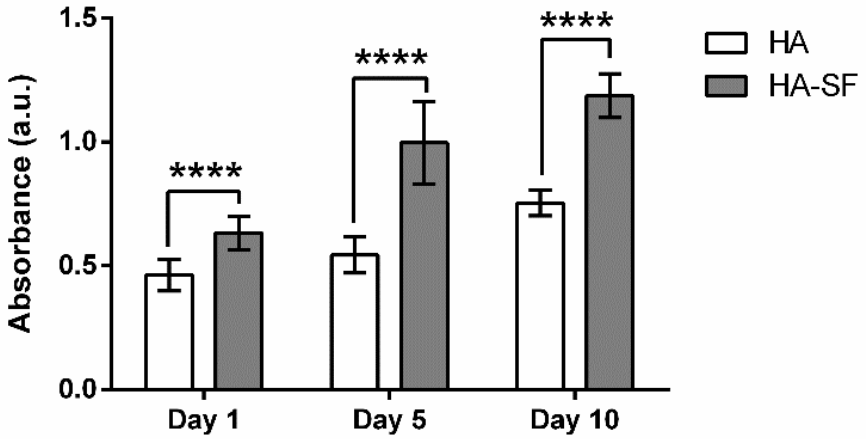


**Figure 6.** MTS proliferation assays on rSCs cultures inside HA and HA-SF NGCs at different culture times (1, 5 and 10 days). The presence of SF increases cell proliferation, explaining the earlier formation of the cell sheath in the HA-SF conduits.

## Biocompatibility of subcutaneously implanted biomaterials

During the study there were no cases of pain, inflammation or infection caused by the implantation of scaffolds. The skin sections containing the scaffolds were photographed at 1, 4 and 8 weeks after their implantation (**Figure 7**). As can be seen in **Figure 7**, the scaffolds are surrounded by healthy tissue since the first week. The presence of blood vessels near to or in direct contact with the scaffolds is also always visible (white arrows in **Figure 7**).

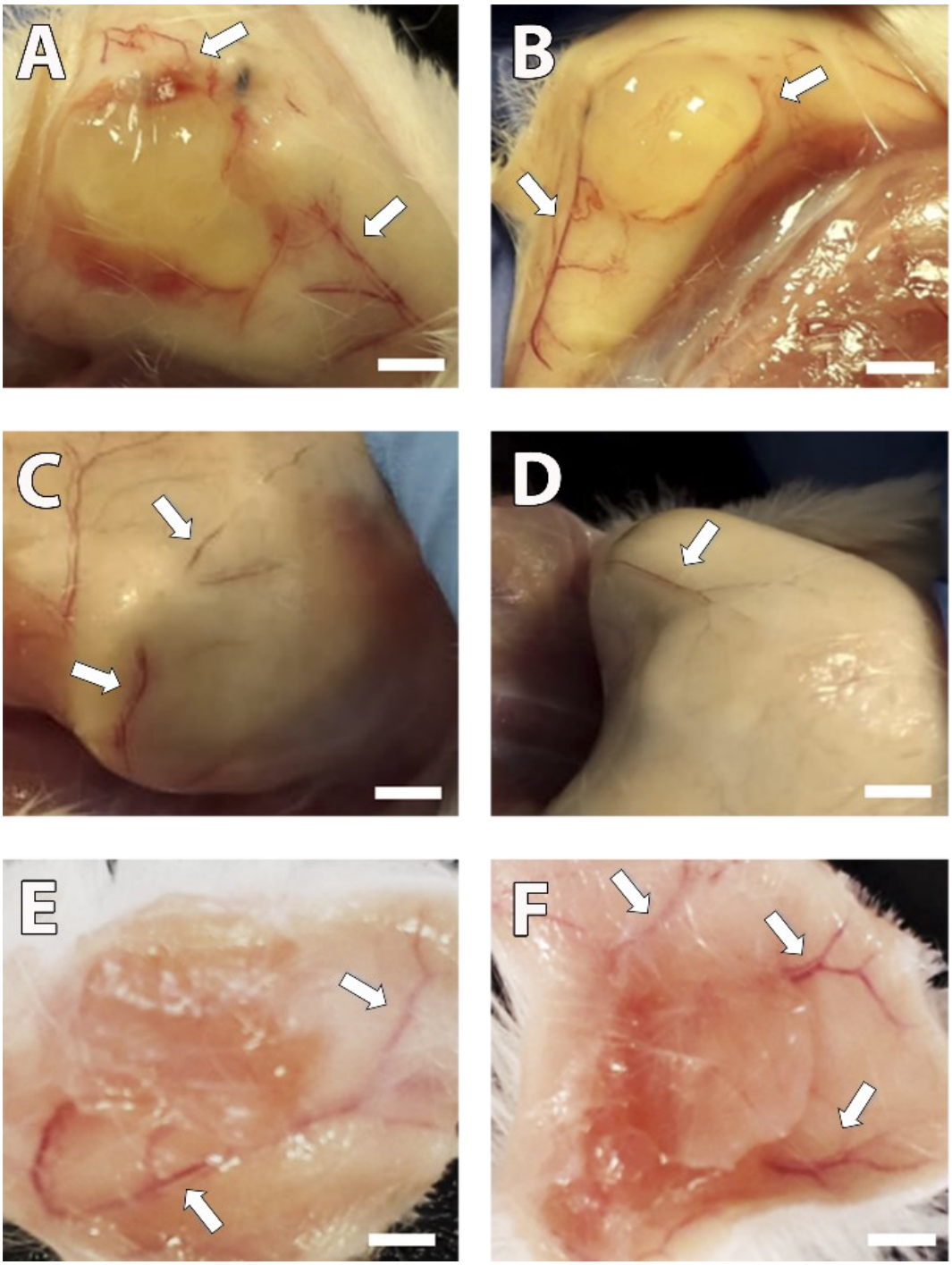


**Figure 7.** HA and HA-SF scaffolds were implanted subcutaneously by means of two independent skin incision of approximately 1 cm on the back of each mouse. The skin sections containing the scaffolds were photographed at 1 (A and B for HA and HA-SF scaffolds, respectively), 4 (C and D for HA and HA-SF scaffolds, respectively) and 8 (E and F for HA and HA-SF scaffolds, respectively) weeks after their implantation. Healthy tissue can be observed surrounding the scaffolds since week 1. A high

capillarity (white arrows) that is near to or in direct contact with the scaffolds is also visible since the first week. Scale bars = 2 mm.

Biocompatibility of subcutaneously implanted biomaterials was assessed by H&E and Masson's trichrome staining of fixed scaffolds after its implantation for 1, 4 and 8 weeks (**Figure 8** for HA scaffolds and **Figure 9** for HA-SF scaffolds). An overall view of a representative longitudinal section of each scaffold is shown in first place (A, E and I for H&E staining; C, G and K for Masson's trichrome staining), and a magnified view of the perimeter of each biomaterial is shown in second place (B, F and J for H&E staining; D, H and L for Masson's trichrome staining), at each post-implantation time point.

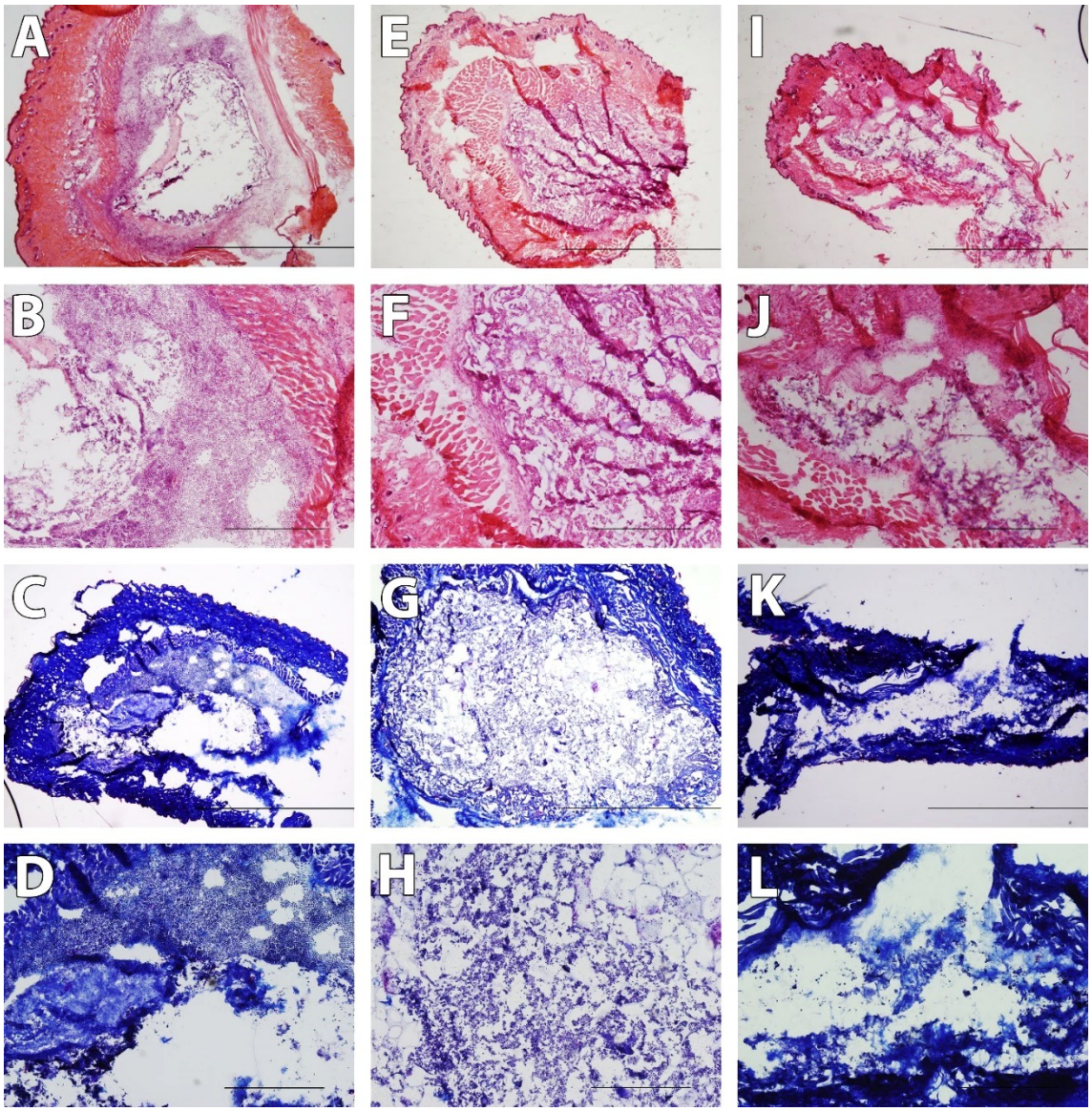


**Figure 8.** Cross sections of representative HA scaffolds stained with H&E and Masson's trichrome. One week after the implantation of the scaffold, an acute moderate foreign body reaction can be observed, with a large infiltration of granulocyte populations (A and B for H&E staining, C and D for Masson's trichrome staining). A fibrous capsule surrounding the scaffold is clearly visible which is a typical reaction after the implantation of a biomaterial. After 4 weeks, a reduction of the immune response can be observed, corresponding to a mild foreign body reaction (E and F for H&E staining, G and H for Masson's trichrome staining). The population of granulocytes has been reduced and there is a greater presence of macrophages. After 8 weeks, the scaffold has been completely resorbed and assimilated into the native tissue (I and J for H&E staining, K and L for Masson's trichrome staining). The fibrous capsule has disappeared and there are no granulocytes present. Now the cells present are

mainly macrophages and active fibroblasts. Also, an increase of collagen structures inside the scaffold can be observed thanks to the fact that active fibroblasts have managed to invade the biomaterial. Many cross-sections of blood vessels are also visible after 8 weeks. Scale bar = 2 mm (A, C, E, G, I and K) and 500 μm (B, D, F, H, J and L).

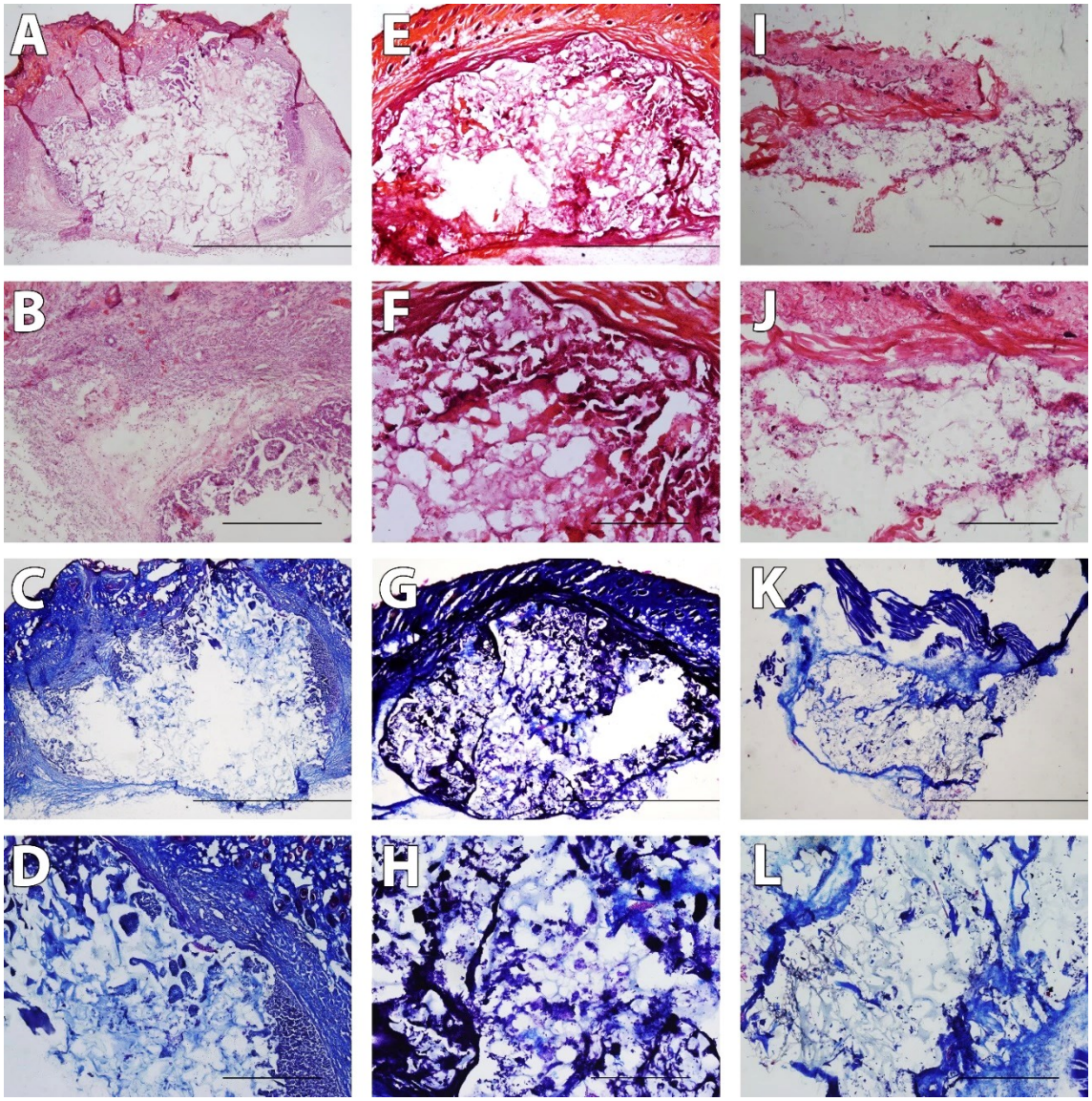


**Figure 9.** Cross sections of representative HA-SF scaffolds stained with H&E and Masson's trichrome. One week after the implantation of the scaffold a fibrous capsule surrounding the scaffold is clearly visible, corresponding to an acute moderate foreign body reaction (A and B for H&E staining, C and D for Masson's trichrome staining). An infiltration of granulocyte populations is also observed. After 4 weeks, a clear reduction of the immune response can be observed, since there is a clear presence of blood vessels and collagen networks inside the scaffold and the population of

granulocytes has been reduced (E and F for H&E staining, G and H for Masson's trichrome staining). After 8 weeks, the fibrous capsule has disappeared and there are no granulocytes present, so the scaffold has been completely resorbed and assimilated into the native tissue (I and J for H&E staining, K and L for Masson's trichrome staining). Now the cells present are mainly macrophages and active fibroblasts. Many collagen structures and cross-sections of blood vessels can be observed. Scale bar = 2 mm (A, C, E, G, I and K) and 500 μm (B, D, F, H, J and L).

One week after the scaffold implantation, a moderate immune response can be observed for both HA (**Figure 8 A-D**) and HA-SF (**Figure 9 A-D**) scaffolds. In both cases a fibrous capsule surrounding the scaffold is clearly visible, which is a typical reaction after the implantation of a biomaterial. There is also a dense population of granulocytes surrounding the scaffolds. Notably, some collagen structures and some cross sections of blood vessels and capillaries are present, although small and isolated.

After 4 weeks, a reduction of the immune response can be observed, corresponding to a mild foreign body reaction for both HA (**Figure 8 E-H**) and HA-SF (**Figure 9 E-H**) scaffolds. The population of granulocytes has been reduced and it has infiltrated inside the scaffold. Now, a greater presence of macrophages is observable, which indicates that the bioresorption process of the scaffold has begun. Remarkably, there is an increase of the number and extension of collagen structures, indicating that new extracellular matrix is being deposited. In addition, more cross sections of blood vessels and capillaries and more red blood cells are observable around and inside the scaffold. It seems that this process of collagen deposition and vascularization inside the scaffold is accelerated when SF is present, since more collagen structures and more blood vessels can be observed inside the scaffold.

Finally, after 8 weeks, the immune response has been drastically reduced, so both HA (**Figure 8 I-L**) and HA-SF (**Figure 9 I-L**) scaffolds have been completely resorbed. The fibrous capsule has disappeared and the population of granulocytes and

macrophages at the scaffold site has almost disappeared, with the epidermis tissue surrounding the scaffold appearing normal. There is a clear increase of the deposition of collagen structures around and inside the cavities of the scaffolds, compared with week 4, and individual collagen fibres are clearly visible within the collagen matrix (**Figure 10**). This increased presence of collagen structures is associated to the presence of active fibroblasts (spindle shaped cells in **Figure 10 B** and **Figure 10 D** for HA and HA-SF scaffolds, respectively), that can be observed infiltrating into the scaffold from the surrounding epidermis. Regarding the vascularization process, it is quite similar to the one observed after 4 weeks. Multiple cross sections of blood vessels and capillaries are observed around and inside the scaffold, as well as populations of isolated blood cells (**Figure 10**). At this time there is not a notably difference between HA and HA-SF scaffolds regarding the collagen deposition and the vascularization.

These results suggest that both HA and HA-SF scaffolds are biointegrated by the host after 8 weeks of implantation and that, furthermore, the processes of extracellular matrix deposition and angiogenesis are accelerated when SF is present.

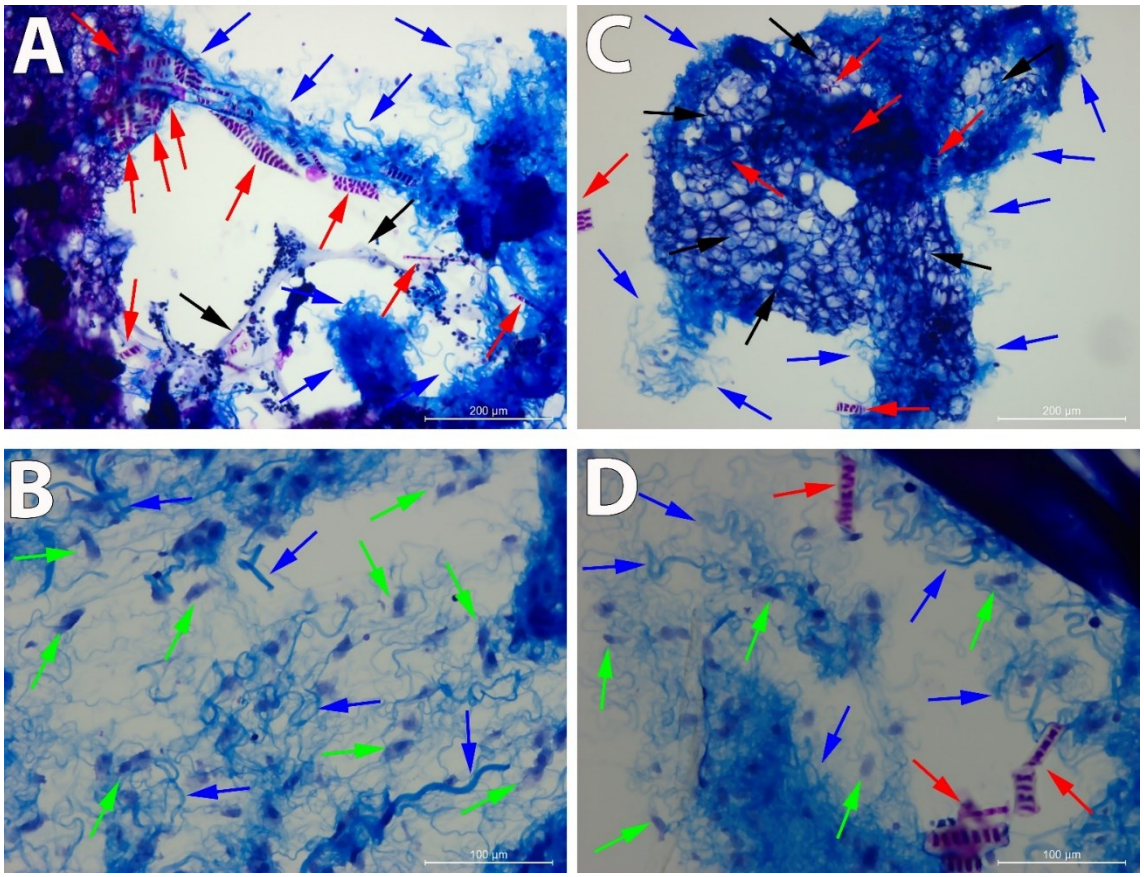


**Figure 10.** Details of cross sections of representative HA and HA-SF scaffolds after 8 weeks of implantation. A and B: HA scaffold stained with Masson's trichrome. C and D: HA-SF scaffold stained with Masson's trichrome. In these images both the collagen deposition and the vascularization of HA and HA-SF scaffolds after 8 weeks of implantation are observable. Multiple collagen fibres (blue arrows) surrounded by active fibroblasts (green arrows) and cross-sections of blood vessels (red arrows) within the scaffold confirm the deposition of new extracellular matrix and the process of angiogenesis, respectively. The scaffold walls are indicated by black arrows. Scale bar = 200 µm (A, C) and 100 µm (B, D).

## 4.5. Conclusions

Silk fibroin protein can be efficiently incorporated into the manufacturing process of HA-based tubular scaffolds intended as nerve conduits. The developed materials are stable over time after swelling and drying cycles. SF supplies cell-binding sequences which lead to higher Schwann cell adhesion and proliferation in the HA-SF

materials when compared with the HA ones. While most physicochemical properties (density, porosity and swelling degree) of both materials are indistinguishable, manipulability and mechanical shear modulus are improved by the presence of SF. The HA-SF tubular scaffolds can act as templates of Schwann-cell macrocylinders, as had the HA scaffolds, but the process is significantly accelerated in HA-SF scaffolds. The biocompatibility of both HA and HA-SF scaffolds has been proven, and both biomaterials were accepted by the host after 8 weeks of implantation. This finding is of importance when thinking of the HA-SF-Schwann cells constructs as transplantable biohybrids, since it considerably shortens the *in vitro* and *in vivo* strategies, where tubulisation techniques are required for regeneration.

## 4.6. Authorship contribution statement

F.G.R.: Investigation, Methodology, Formal analysis, Writing - original draft. P.L.P.: Resources. J.P.-R.: Resources. G.G.T.: Resources. M.M.P.: Conceptualization, Writing – review & editing, Supervision, Funding acquisition. C.M-R.: Conceptualization, Methodology, Writing - review & editing, Supervision, Funding acquisition.

## 4.7. Conflicts of interest

There are no conflicts to declare.

## 4.8. Acknowledgements

The authors acknowledge financing from the Spanish Ministry of Economy and Competitiveness through grants RTI2018-095872-B-C22/ERDF, DPI2015-72863-EXP, MAT2016-79832-R, MAT2016-76847-R and, and community of Madrid through grant Neurocentro-B2017/BMD-3760. FGR acknowledges scholarship FPU16/01833 of the

Spanish Ministry of Education, Culture and Sports. We thank the Electron Microscopy Service at the UPV, where the FESEM images were obtained.

# 4.9. References

1. E. a Huebner, S. M. Strittmatter, *Results Probl. Cell Differ. Author Manuscr.* **2009**, *48*, 339.
2. J. W. Fawcett, R. A. Asher, *Brain Res. Bull.* **1999**, *49*, 377.
3. A. H. Koeppen, *J. Neurol. Sci.* **2004**, *220*, 115.
4. S. Hall, *J. bone Jt. Surg.* **2005**, *87*, 1309.
5. P. Dubový, I. Klusáková, I. Hradilová Svíženská, *Biomed Res. Int.* **2014**, *2014*.
6. K. S. Houschyar *et al.*, *Plast. Surg. Int.* **2016**, *2016*, 1.
7. L. Tian, M. P. Prabhakaran, S. Ramakrishna, *Regen. Biomater.* **2015**, *2*, 31.
8. A. Muheremu, Q. Ao, **2015**, *2015*.
9. S. Kehoe, X. F. Zhang, D. Boyd, *Injury* **2012**, *43*, 553.
10. H. G. Garg, C. A. Hales, **2004**.
11. M. N. Collins, C. Birkinshaw, *Carbohydr. Polym.* **2013**, *92*, 1262.
12. J. E. Scott, *Ciba Found. Symp.* **1989**, *143*, 6.
13. M. K. Cowman, S. Matsuoka, *Carbohydr. Res.* **2005**, *340*, 791.
14. Y. Liang, P. Walczak, J. W. M. Bulte, *Biomaterials* **2013**, *34*, 5521.
15. T.-W. Wang, M. Spector, *Acta Biomater.* **2009**, *5*, 2371.
16. J. Ma *et al.*, *Biomed. Mater.* **2007**, *2*, 233.
17. W. M. Tian *et al.*, *Tissue Eng.* **2005**, *11*, 513.
18. M. Pérez-Garnes, J. A. Barcia, U. Gómez-Pinedo, M. Monleón Pradas, A. Vallés-Lluch, *Cells Biomater. Regen. Med.* **2014**, doi:10.5772/59339.
19. G. Vilariño-Feltrer *et al.*, *Acta Biomater.* **2016**, *30*, 199.

20. I. Ortuno-Lizarán, G. Vilarino-Feltrer, C. Martinez-Ramos, M. M. Pradas, A. Vallés-Lluch, *Biofabrication* **2016**, *8*.

21. R. J. Lancashire, *Dep. Chem. Univ. West Indies* **2011**, at <http://wwwchem.uwimona.edu.jm/courses/CHEM2402/Textiles/Animal_Fibres.html>.

22. Q. Xia *et al.*, *Science (80-. ).* **2004**, *306*, 1937.

23. C. Vepari, D. L. Kaplan, *Prog. Polym. Sci.* **2007**, *32*, 991.

24. A. R. Murphy, D. L. Kaplan, *J. Mater. Chem.* **2009**, *19*, 6443.

25. N. Minoura *et al.*, **1995**, *208*, 511.

26. S. Sofia, M. B. McCarthy, G. Gronowicz, D. L. Kaplan, *J. Biomed. Mater. Res.* **2001**, *54*, 139.

27. G. H. Altman *et al.*, *Biomaterials* **2003**, *24*, 401.

28. R. L. Horan *et al.*, *Biomaterials* **2005**, *26*, 3385.

29. N. H. Chi, M. C. Yang, T. W. Chung, N. K. Chou, S. S. Wang, *Carbohydr Polym* **2013**, *92*, 591.

30. N. H. Chi *et al.*, *Biomaterials* **2012**, *33*, 5541.

31. M. C. Yang *et al.*, *Biomaterials* **2010**, *31*, 854.

32. J. Zhou *et al.*, *Carbohydr Polym* **2016**, *143*, 301.

33. S. Yan, M. Li, Q. Zhang, J. Wang, *Fibers Polym.* **2013**, *14*, 188.

34. C. Foss, E. Merzari, C. Migliaresi, A. Motta, *Biomacromolecules* **2013**, *14*, 38.

35. J. Jaipaew, P. Wangkulangkul, J. Meesane, P. Raungrut, P. Puttawibul, *Mater Sci Eng C Mater Biol Appl* **2016**, *64*, 173.

36. Z. Fan, F. Zhang, T. Liu, B. Q. Zuo, *Int J Biol Macromol* **2014**, *65*, 516.

37. T. W. Chung, Y. L. Chang, *J Mater Sci Mater Med* **2010**, *21*, 1343.

38. M. Garcia-Fuentes, A. J. Meinel, M. Hilbe, L. Meinel, H. P. Merkle,

*Biomaterials* **2009**, *30*, 5068.

39. N. R. Raia *et al.*, *Biomaterials* **2017**, *131*, 58.
40. S. Yan *et al.*, *Acta Biomater* **2013**, *9*, 6771.
41. M. Garcia-Fuentes, E. Giger, L. Meinel, H. P. Merkle, *Biomaterials* **2008**, *29*, 633.
42. X. Hu *et al.*, *Biomacromolecules* **2010**, *11*, 3178.
43. Y. J. Ren, Z. Y. Zhou, B. F. Liu, Q. Y. Xu, F. Z. Cui, *Int J Biol Macromol* **2009**, *44*, 372.
44. E. Pavlovic, M. A. Serban, X. Yu, N. J. Manesis, **2014**, 16.
45. F. S. Brandt, A. Cazzaniga, *Clin. Interv. Aging* **2008**, *3*, 153.
46. S.-F. Sun, Y.-J. Chou, C.-W. Hsu, W.-L. Chen, *Curr. Rev. Musculoskelet. Med.* **2009**, *2*, 78.
47. T. Yucel, M. L. Lovett, D. L. Kaplan, *J. Control. Release* **2014**, *190*, 381.
48. C. J. Bettinger *et al.*, *Adv. Mater. Mater.* **2007**, *19*, 2847.
49. J. Schindelin *et al.*, *Nat. Methods* **2012**, *9*, 676.
50. P. Taddei, E. Pavoni, M. Tsukada, *J. Raman Spectrosc.* **2016**, *47*, 731.
51. G. B. Perea *et al.*, *Eur. Polym. J.* **2016**, *78*, 129.
52. M. Hu, E. E. Sabelman, C. Tsai, J. Tan, V. R. Hentz, *Tissue Eng.* **2000**, *6*, 585.
53. Y. Jo *et al.*, **2011**, *54*, 166.
54. G. A. Monteiro, A. V Fernandes, H. G. Sundararaghavan, D. I. Shreiber, *Tissue Eng. Part A* **2011**, *17*, 1663.
55. C. Calcagno, M. E. Lobatto, P. M. Robson, A. Millon, *Hum Mutat.* **2016**, *28*, 1304.
56. A. U. Ude *et al.*, *Mater. Des.* **2014**, *57*, 298.
57. E. D. T. Atkins, C. F. Phelps, J. K. Sheehan, *Biochem. J.* **1972**, *128*, 1255.

# 5. Paper 3: Solid polymer electrolytes based on polylactic acid nanofiber mats coated with polypyrrole

# Solid polymer electrolytes based on polylactic acid nanofiber mats coated with polypyrrole

Fernando Gisbert Roca [a], Abel García-Bernabé [b], Vicente Compañ Moreno [b], Cristina Martínez-Ramos [a] and Manuel Monleón Pradas [a], [c], *

[a] Center for Biomaterials and Tissue Engineering. Universitat Politècnica de València. Camino de Vera s/n, 46022, Valencia, Spain.

[b] Departamento de Termodinámica Aplicada. Universitat Politècnica de València. Camino de Vera s/n, 46022, Valencia, Spain

[c] CIBER-BBN, Biomedical Research Networking Center in Bioengineering Biomaterials and Nanomedicine, Spain

*Corresponding author: Manuel Monleón Pradas. Center for Biomaterials and Tissue Engineering, Universitat Politècnica de València, Camino de Vera s/n E-46022 Valencia, España. Tel.: +34963877000. E-mail: mmonleon@ter.upv.es

**Keywords:** dielectric properties, ion exchangers, membranes, polyelectrolytes, polypyrroles

Published online: 15 February 2021

Reprinted with permission from Macromolecular Materials and. Engineering 2021, 306, 2000584 

# 5.1. Abstract

The production of electroconductive nanofiber membranes made from polylactic acid (PLA) coated with polypyrrole (PPy) is investigated, performing a scanning of different reaction parameters and studying their physicochemical and dielectric properties. Depending on PPy content a transition between conduction mechanisms is observed, with a temperature-dependent relaxation process for samples without PPy, a temperature-independent conduction process for samples with high contents of PPy and a combination of both processes for samples with low contents of PPy. A homogeneous and continuous coating is achieved from 23 wt% PPy, observing a percolation effect around 27 wt% PPy. Higher wt% PPy allow us to obtain higher conductivities, but PPy aggregates appear from 34% wt% PPy. The high conductivity values obtained for electrospun membranes both through-plane and in-plane (above 0.05 S/cm and 0.20 S/cm, respectively, at room temperature) for the highest wt% of PPy, their porous structure with high specific surface area and their thermal stability below 140°C make them candidates for many potential applications as solid polymer electrolytes in, for example, batteries, supercapacitors, sensors, photosensors or polymer electrolyte membrane fuel cells (PEMFCs). In addition, the biocompatibility of PLA-PPy membranes expand their potential applications also in the field of tissue engineering and implantable devices.

# 5.2. Introduction

Intrinsically conductive polymers (ICPs) were discovered by B. Bolto and D. Weiss[1–5] and popularized by Alan J. Heeger, Alan G. MacDiarmid and Hideki Shirakawa[6,7]. They have been widely studied during the last decades due to their characteristic physicochemical properties. Within this type of materials, polypyrrole

(PPy) has been one of the most studied conductive polymers due to its high electrical conductivity, long-term ambient stability, good biocompatibility, low cost and facile synthesis by chemical or electrochemical polymerization.[8–17] PPy has been used for many commercial applications such as biosensors[13,18], gas sensors[19,20], microactuators[21], transducers[22], antistatic coatings[23], solid electrolytic capacitors[24,25], polymeric batteries[26], solar cells[27,28], wearable electronics[29,30], electromagnetic interference shielding[31–33], corrosion protection[8,34,35], etc. In addition, PPy has also been applied in fuel cells as catalyst supports for direct methanol fuel cells (DMFCs)[36] and proton-exchange polymer electrolyte membrane fuel cells (PEMFCs)[37], as membranes for DMFCs[38] and as anodes for microbial fuel cells[39]. Furthermore, PPy has become a widely used material in biomedical applications, especially in nerve tissue engineering scaffolds, due to its good biocompatibility and high electrical conductivity[40–43].

As a common characteristic of ICPs, they are semiconductors with wide bandgaps (electrical insulators) in native state and the electrical conductivity is achieved by the incorporation of an anionic compound (dopant) into the polymer matrix. In the doping process an electron is removed from the valence band (p-doping) or added to the conduction band (n-doping) via oxidation/reduction interaction between the conducting polymer and the dopant, generating charge carriers in the form of polarons, bipolarons or solitons that move when subjected to an electric field.[17] Different anionic dopants have been studied to improve the electrical conductivity of PPy, such as $Cl^-$ [44], $SO_4^{2-}$ [44], $BF_4^-$ [45],$ClO_4^-$ [46,47], dodecylbenzenesulfonate (DBS) [48–51], polystyrene sulfonate (PSS) [52,53] and p-toluenesulfonate (pTS) [54–58]. Among all the conducting polymers based on PPy, PPy films doped with pTS (PPy/pTS) have been tested as valid for practical applications due to their good physicochemical properties and long-term stable

redox cycling.[59–63] In addition, PPy/pTS films have shown a good ion exchange behavior, presenting both cation and anion transporting properties.[54,64–67] This ion exchange ability is crucial for many practical applications were PPy/pTS films are used as solid polymer electrolytes.

However, the ion diffusion process in the PPy matrix can be blocked when the PPy films present a flat surface with a very compact structure and/or a large thickness, decreasing its electrochemical performance.[44,54] Therefore, with the aim of improving the ion exchange rate of PPy/pTS composites, the thickness of the material must be reduced, and the specific surface area must be increased in order to improve the kinetics of ion exchange. For that reason, in recent years the surface of fibers (both natural and synthetic), fabrics or particles has been coated with conductive PPy, obtaining new composite materials with a high specific surface area that provides a larger interface in sensing, enhances the ionic transportation in electrodes and promotes the cell growth in scaffolds.[29,40,75–77,42,68–74] In addition, it must be considered that PPy is an intractable and brittle solid with poor mechanical processability, which limits its direct application.[14] For that reason, the strategy of coating the surface of other insulating polymers with PPy is interesting in order to exploit both the intrinsic electrical conductivity of PPy and the better mechanical properties of the insulating host polymer.[14,29,40,42,73,74,78]

In this study we chose the polylactic acid (PLA) as host polymer of the membranes because it is a low cost, renewable, environmentally friendly and biodegradable substrate.[79,80] According to previous studies, the melting peak temperature of PLA is located at around 150-160°C, starting to melt for temperatures above 140°C [81,82]. This thermal stability of PLA for temperatures below 140°C allows us to use it in almost all the commercial applications[79], while its biocompatibility

makes it possible to use the membranes in tissue engineering applications.[83,84] In order to achieve a high specific surface area of the material, PLA was electrospun to obtain nanofiber membranes that present porous structure with small pore size and high pore volume fraction. Then, the electrospun-PLA membrane was coated by in situ chemical polymerization of pyrrole using ferric chloride ($FeCl_3$) as oxidant and pTS as dopant.

By performing a scan of the reaction parameters of the PPy coating process we obtained membranes with different dielectric properties. A physicochemical and dielectric characterization of these PLA-PPy nanofiber membranes allowed us to study the different electrical behavior of them as the wt% PPy varies, establishing the range of wt% PPy were the coating is homogeneous and continuous and the electrical conductivity that is achieved both through-plane and in-plane. This characterization of the membranes will help to choose the appropriate reaction parameters for the desired application, as the electrical conductivity can be adjusted by varying the reaction parameters. These high conductive membranes may have interesting applications in devices where the electrodes are placed both perpendicular to the membrane (through-plane) and in the plane of the membrane (in-plane). For the through-plane disposition, the membranes can be used as solid, low cost, durable and tunable polymer electrolytes for batteries, supercapacitors and fuel cell applications. In addition, the high surface conductivity of the membranes for the in-plane disposition, together with the biocompatibility of both PLA and PPy, also makes them have potential applications in the field of tissue engineering and biomedical implantable devices.

# 5.3. Experimental section

## Preparation of PLA nanofiber membranes

Random and aligned PLA nanofiber membranes were obtained by the electrospinning technique. First, PLA (INGEO 40420 RESINEX) (10% wt%) was dissolved in dichloromethane (DCM) / dimethylformamide (DMF) (70/30 v/v) and stirred for 12 hours at room temperature. Then, the solution was introduced into a 12 ml syringe with an internal diameter of 15.77 mm attached to a precision stainless steel needle with 0.15 mm of internal diameter (30G). On the one hand, randomly oriented nanofibers were obtained by applying a voltage of 20 kV between the needle tip and the collector, maintaining the flow rate at 4 ml/h and collecting the nanofibers during 1 hour on a flat plate wrapped with an aluminium foil located 20 cm from the needle tip. On the other hand, aligned nanofibers were obtained by applying a voltage of 20 kV between the needle tip and the collector, maintaining the flow rate at 3 ml/h and collecting the nanofibers during 1.5 hours on a round plate wrapped with an aluminium foil with a diameter of 15.5 cm which centre was located 20 cm from the needle tip and that was rotating at 32 rps. These parameters were chosen from preliminary experiments carried out to establish the optimal conditions (homogeneous fibers, absence of precipitates, etc).

After electrospinning, PLA membranes were air dried for 2 days and introduced in a desiccator with fixed vacuum at room temperature for another 2 days. Finally, PLA membranes were introduced between two glass plates subjected to compression and they underwent a tempering process consisting of stove heating at 90°C with 100% of ventilation for 15 min and subsequent cooling at -20°C for 2 hours. With this tempering

process, a stiffening of the PLA membranes was achieved, which prevented them from wrinkling when they were introduced into water.

## Preparation of PLA cast membranes

Non-porous PLA membranes were obtained by the casting technique. First, PLA (2% wt%) was dissolved in chloroform and stirred for 2 hours at room temperature. Then, the solution was casted into a glass petri dish with ratio between the mass of solution that was casted and the diameter of the petri dish of 1.5 g/cm. After the casting process, the solution was air dried for 2 days in order to allow the evaporation of chloroform. Finally, the PLA membrane was dried in a desiccator with fixed vacuum at 40°C for 2 days.

## PPy coating

Electrospun and cast PLA membranes were coated with the conductive polymer PPy via *in situ* polymerization. As a previous step, electrospun membranes were immersed in deionized water under compression and a fixed vacuum was applied until they stopped floating and, therefore, the introduction of water inside the spaces between nanofibers was achieved, in order to obtain a homogeneous coating of all nanofibers, not only the most superficial ones. Next, each PLA membrane was put into a polypropylene tube with an aqueous solution of pyrrole monomer (Py, Sigma-Aldrich 131709) and sodium para-toluene sulfonate (pTS, Sigma-Aldrich, 152536), followed by ultrasonication for 1 min in order to allow the membrane to be saturated with Py solution. The membrane was incubated with shaking at 4°C for 1 h. The ratio between the membrane area and the final volume of the Py/pTS aqueous solution was 0.6 $cm^2$/ml and the different concentrations of Py and pTS that were used are described in **Table 1**. Then, an aqueous solution of ferric chloride ($FeCl_3$, Sigma-Aldrich 157740) was added

and incubated with shaking at 4°C for 48 h for the polymerization and deposition of polypyrrole (PPy) on the PLA membrane. The ratio between the membrane area and the final volume of the $FeCl_3$ aqueous solution was 0.6 $cm^2$/ml and the different concentrations of $FeCl_3$ that were used are described in **Table 1**. PPy-coated membranes were washed with deionized water with agitation during 10 min for three times, ultrasonicated for 30 min in deionized water for three times and washed with pure ethanol during 5 min for two times. Finally, the membranes were dried in a desiccator with fixed vacuum at 40°C for 2 days.

| Sample | Coating ratio | [Py] (mM) | [pTS] (mM) | [$FeCl_3$] (mM) | Reaction time (h) | PPy mass fraction (%) |
|---|---|---|---|---|---|---|
| C1 | CR1 | 7.0 | 7.0 | 19.0 | 48.0 | 0.6 ± 0.1 |
| C2 | CR2 | 14.0 | 14.0 | 38.0 | 48.0 | 2.0 ± 0.1 |
| E4 | CR1 | 7.0 | 7.0 | 19.0 | 48.0 | 4.0 ± 2.0 |
| E13 | CR1.5 | 10.5 | 10.5 | 28.5 | 48.0 | 13.0 ± 3.0 |
| E18 | CR2 | 14.0 | 14.0 | 38.0 | 48.0 | 18.2 ± 0.7 |
| E23 | CR2.5 | 17.5 | 17.5 | 47.5 | 48.0 | 23.0 ± 5.0 |
| E27 | CR3 | 21.0 | 21.0 | 57.0 | 48.0 | 27.0 ± 2.0 |
| E34 | CR4 | 28.0 | 28.0 | 76.0 | 48.0 | 34.0 ± 4.0 |

**Table 1.** Reaction parameters used for the PPy coating and mass fraction of PPy for the different PLA cast (C) and electrospun (E) membranes.

# Characterization of PLA-PPy composites

## Porosity and specific surface area of electrospun membranes

The porosity ($\pi$) of electrospun membranes was calculated using **Equation (1)**, where $\varphi_{PLA}$ is the density of PLA as a non-porous film and $\varphi_{EM}$ is the density of the electrospun membranes (n=5).

$$\pi = \frac{\varphi_{PLA} - \varphi_{EM}}{\varphi_{PLA}} \cdot 100 \quad (1)$$

To obtain $\varphi_{EM}$, **Equation (2)** was applied, where $m$, $V$, $e$ and $A$ are, respectively, the mass, the volume, the thickness and the area of electrospun membranes.

$$\varphi_{EM} = \frac{m}{V} = \frac{m}{e \cdot A} \quad (2)$$

The specific surface area (SSA) of electrospun membranes was calculated following **Equation (3)**, where r is the average radius of the nanofibers, $n_{NF}$ is the number of nanofibers, $V_{1\,NF}$ is the volume of one nanofiber, $\varphi_{PLA}$ is the density of PLA as a non-porous film and $L$, $m$ and $V$ are, respectively, the length, the mass and the volume of electrospun membranes.

$$SSA = \frac{2 \cdot \pi \cdot r \cdot L \cdot n_{NF}}{m} = \frac{2 \cdot \pi \cdot r \cdot L \cdot \frac{V}{V_{1\,NF}}}{m} = \frac{2 \cdot \pi \cdot r \cdot L \cdot \frac{\frac{m}{\varphi_{PLA}}}{\pi \cdot r^2 \cdot L}}{m} = \frac{2}{\varphi_{PLA} \cdot r} \quad (3)$$

The average radius of nanofibers (r) was considered as 381 ± 80 nm (obtained from FESEM images using the ImageJ/FIJI image processing software[85]) and the density of PLA ($\varphi_{PLA}$) was considered as 1.25 g/cm$^3$[86].

## Mass fraction of PPy

The mass fraction of PPy deposited on PLA electrospun membranes was measured by weighing the PLA membranes before and after covering them with PPy using a precision balance (AX205, Mettler-Toledo Inc., sensibility of 0,01 mg) and applying **Equation (4)**.

$$\omega_{PPy} = \frac{m_{PPy}}{m} = \frac{m_f - m_0}{m_f} \quad (4)$$

## Morphological characterization by field emission scanning electron microscopy (FESEM)

For the characterization of the surface morphology of membranes, a field emission scanning electron microscope (FESEM; ULTRA 55, ZEISS Oxford Instruments) was used. The preparation of the samples consisted primarily in a desiccation under vacuum conditions during the 24 hours prior to the test to avoid interferences due to evaporated water. Subsequently samples were placed on a carbon tape and a carbon bridge was created between the sample and the carbon tape. Finally, samples were coated with a thin layer of platinum. The voltage used was 2 kV.

## Fourier transform infrared spectroscopy (FTIR) analysis

FTIR spectra of membranes were obtained using a Cary 630 FTIR (Agilent Technologies) in the attenuated total reflection mode (ATR). The spectra resulted from averages of 24 scans at 4 $cm^{-1}$ resolution, between 400 and 4000 $cm^{-1}$. Three different samples of each material were studied, plotting the most representative curve for each one.

## Thermogravimetric analysis (TGA)

A thermogravimetric analyzer (TGA/SDTA 851 Mettler-Toledo operated using the STARexx software) was used to study the thermal degradation and composition of the materials. Samples with a mass of approximately 2 mg were processed, monitoring the mass loss while heating up to 800°C at a rate of 10°C/min under a positive nitrogen ($N_2$) flow of 20 ml/min. As a result, thermograms in which the mass loss of the sample is represented as a function of temperature were obtained. Three different samples of each material were studied, plotting the most representative curve for each one. The

mass fraction of PPy of the different PLA-PPy samples was calculated from TGA residues by applying **Equation (5)**.

$$m_{sample} = m_{PLA} \cdot (1 - \omega_{PPy}) + m_{PPy} \cdot \omega_{PPy} \quad (5)$$

### Electrochemical impedance spectroscopy (EIS)

The complex conductivity and permittivity of the compounds was measured by impedance spectroscopy at several temperatures within the 273K (0°C)–333K (60°C) range and frequency window $10^{-1} < f < 10^{7}$ Hz using a Novocontrol Broadband Dielectric Spectrometer (Hundsangen, Germany) integrated with an SR 830 lock-in amplifier with an Alpha dielectric interface. The experiments were performed with 100 mV amplitude. The samples were placed between two gold electrodes. During the conductivity measurements, temperature was kept isothermally or changed stepwise within the entire temperature range controlled by a nitrogen jet (QUATRO from Novocontrol) with a temperature error of 0.1K during every single scan in frequency.

## 5.4. Results and discussion

## PPy coating characterization and morphological properties

First, we proceeded to cover with PPy non-porous films of PLA created by casting following 2 different Coating Ratios (CR1 and CR2), as an idealized control without air. Since the amount of PPy deposited was very small, the mass fraction of PPy was obtained from the TGA residues (**Figure S5**). As can be seen in **Table 1** and **Figure S1**, using non-porous PLA films entails that the mass fraction of PPy deposited on the membranes is very small: 1% for samples coated using CR1, hereinafter named as C1 (Casting 1 wt% PPy), and 2% for samples coated using CR2, hereinafter named as C2 (Casting 2 wt% PPy). This occurs because the films do not present any porosity

and, therefore, the PPy is not able to penetrate inside the film and only remains on its surface. As can be observed in **Figure S1**, there is a linear relationship between the mass fraction of PPy and the concentration of Py used for the coating.

From the FESEM images (**Figure S2**) it can be observed that the Cast PLA film (CPLA) is non-porous, with a flat and smooth surface without porosity. However, when the film has 1 wt% PPy (C1), a rougher surface is observed due to the presence of PPy. This roughness increases when the mass fraction of PPy rises to 2 wt% (C2), forming PPy aggregates.

Next, we proceeded to cover with PPy the electrospun membranes of PLA following 6 different coating ratios (CR1, CR1.5, CR2, CR2.5, CR3 and CR4). Since the amount of PPy deposited was sufficiently large, the mass fraction of PPy was obtained by weighing the membranes before and after their coating with PPy. As can be seen in **Table 1** and **Figure 1**, using electrospun membranes instead of non-porous films entails that the amount of PPy deposited is much higher, becoming 4 times higher for CR1 and 9 times higher for CR2, thanks to the greater specific surface area and porosity of electrospun membranes (specific surface area of $4.2 \pm 0.9$ $m^2/g$ and porosity of $67 \pm 3\%$). Electrospun membranes with both random and aligned orientation of the nanofibers were coated with PPy, without observing significant differences in the amount of PPy deposited. As can be observed in **Figure 1**, there is a linear relationship between the mass fraction of PPy and the concentration of Py used for the coating.

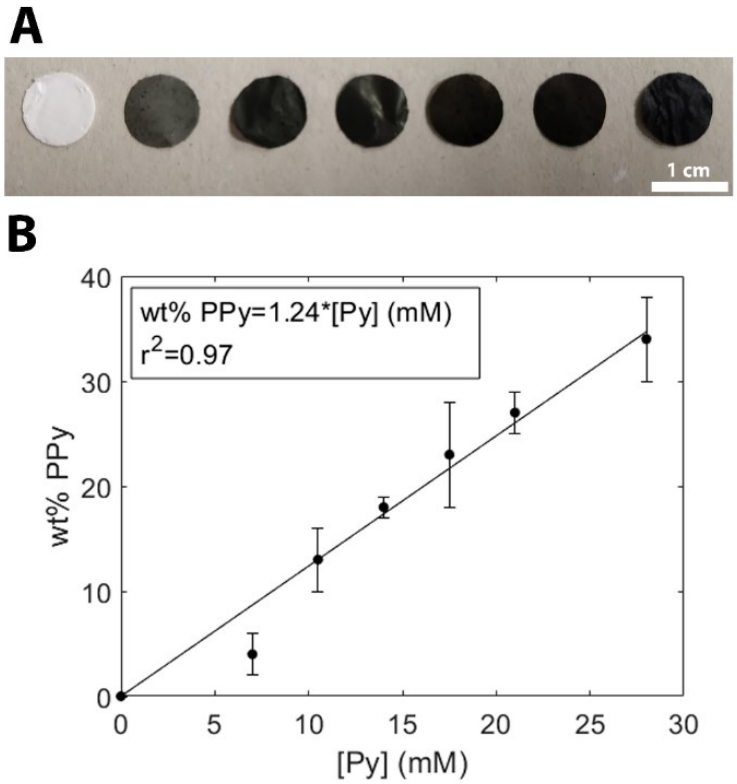


**Figure 1. A**: From left to right, macroscopic images of PLA (EPLA) and PLA-PPy (E4, E13, E18, E23, E27 and E34) electrospun membranes. **B**: PPy mass fraction of electrospun membranes for the different Py concentrations used in the coating process. A linear relationship between both parameters can be observed.

From the FESEM images of electrospun membranes with random orientation of the nanofibers (**Figure 2**) it can be observed that the Electrospun-PLA membrane (EPLA) presents nanofibers with a flat and smooth surface. However, when the PLA nanofibers are coated with different amounts of PPy, changes appear in their surface morphology. When the mass fraction of PPy is low (Electrospun membranes with 4 wt% PPy (E4), 13 wt% PPy (E13) and 18 wt% PPy (E18), coated using CR1, CR1.5 and CR2, respectively), the layer of PPy deposited on the nanofibers of PLA is not homogeneous and presents discontinuities, so that there are accumulations of PPy isolated from each other. These discontinuities in the PPy coating are more significant for the samples with the least amount of PPy (E4), causing the deposited PPy mass fraction to move significantly away from the linear trend followed by the other samples

as the Py concentration increases (**Figure 1B**). For an intermediate mass fraction of PPy (Electrospun membranes with 23 wt% PPy (E23) and 27 wt% PPy (E27), coated using CR2.5 and CR3, respectively), the layer of PPy deposited on the nanofibers of PLA is continuous and homogeneous, without aggregates of consideration. Here all the PPy is in contact with each other, without forming isolated accumulations. Finally, when the mass fraction of PPy is high (Electrospun membranes with 34 wt% PPy (E34), coated using CR4), the continuous and homogeneous coating is maintained but aggregates of PPy are formed.

The detail of a cross-section of the PPy coating is indicated by an arrow in **Figure S3** for E23, where the coating is continuous and homogeneous without forming PPy aggregates. An analysis of the image allows to know the thickness of the PPy coating, which is around 100 nm.

The same effect of PPy coating seen before for electrospun membranes with a random orientation of the nanofibers can be observed for electrospun membranes with an aligned orientation of the nanofibers (**Figure 3**). Low mass fractions of PPy entail an inhomogeneous coating of the nanofibers (E4 and E18), with chipping and with areas not covered with PPy. However, higher concentrations (E27 and E34) achieve a homogenous and continuous coating of the nanofibers. The highest concentration (E34) also presents PPy aggregates.

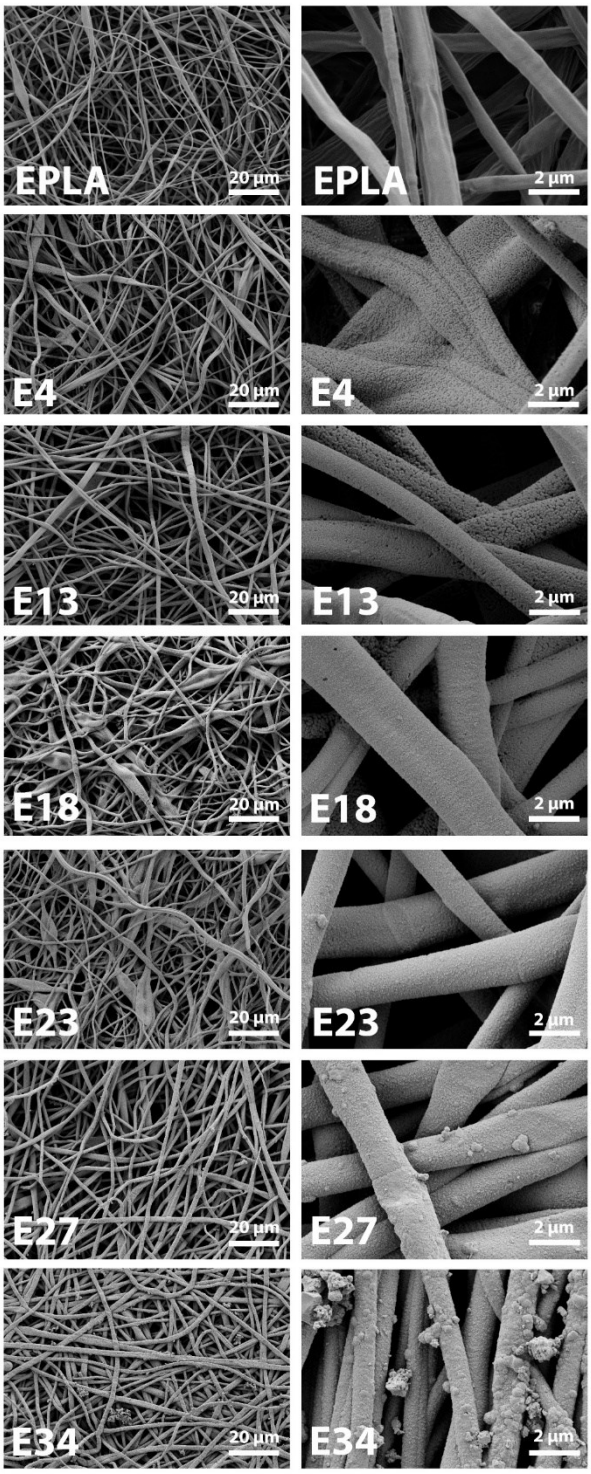


**Figure 2.** FESEM images of PLA (EPLA) and PLA-PPy (E4, E13, E18, E23, E27 and E34) electrospun membranes with a random orientation of the nanofibers. EPLA: Smooth surface. E4 and E13: Inhomogeneous coating with discontinuities. E18: More homogeneous coating, but still with some discontinuities. E23 and E27: Homogeneous coating without aggregates. E34: Homogeneous coating, but with PPy aggregates.

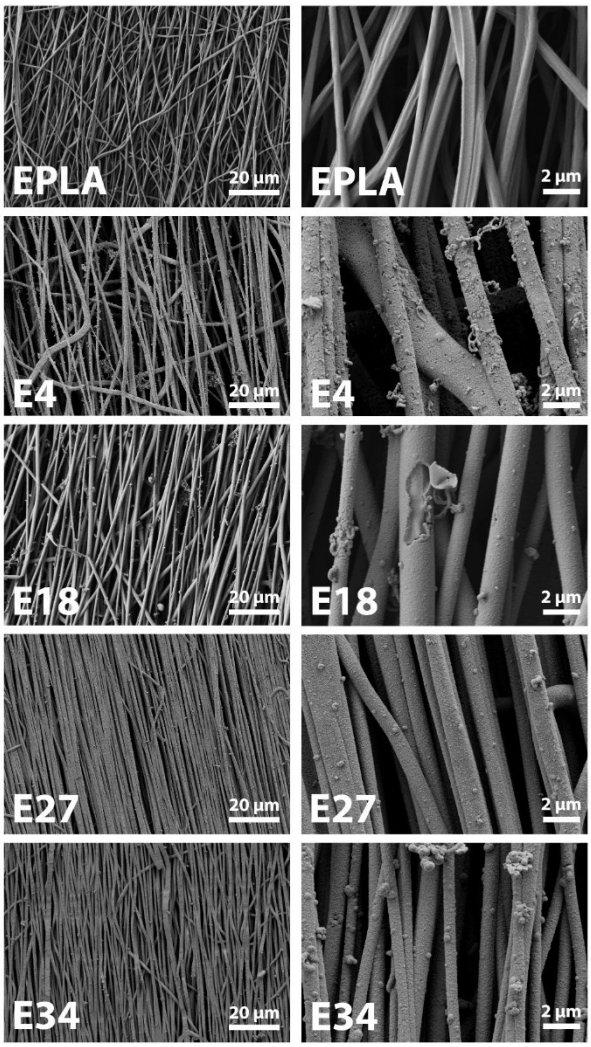


**Figure 3.** FESEM images of PLA (EPLA) and PLA-PPy (E4, E18, E27 and E34) electrospun membranes with an aligned orientation of the nanofibers. EPLA: Smooth surface. E4: Inhomogeneous coating with discontinuities. E18: More homogeneous coating, but still with some discontinuities. E27: Homogeneous coating. E34: Homogeneous coating, but with PPy aggregates.

## Fourier transform infrared spectra (FTIR)

First, cast-PLA films (CPLA) and electrospun-PLA membranes (EPLA) were analyzed and characteristic peaks corresponding to PLA were observed: 2995 $cm^{-1}$ (-$CH_3$ asymmetric stretching), 2944 $cm^{-1}$ (-$CH_3$ symmetric stretching), 1752 $cm^{-1}$ (C=O stretching), 1181 $cm^{-1}$ (C-O-C stretching) and 1084 $cm^{-1}$ (C-O stretching). [87,88] These characteristic peaks of PLA are indicated in **Figure 4A** for EPLA. Powder of pure PPy

doped with pTS (PPy) was also analysed and peaks corresponding both to PPy and pTS appeared (**Figure 4B**). PPy characteristic peaks where found at 3375 $cm^{-1}$ (N-H bond), 1643 $cm^{-1}$ (C=C bond), 1532 $cm^{-1}$ and 1451 $cm^{-1}$ (fundamental vibrations of PPy ring), 1291 $cm^{-1}$ (C-H deformation) and 773 $cm^{-1}$ (C-N bond) [89], while pTS characteristic peaks where found at 1150 $cm^{-1}$ (C-H in-plane bending vibration), 1126 $cm^{-1}$ (stretching vibration of $-SO_3^-$ groups), 1010 $cm^{-1}$ (S=O stretching vibration of $-SO_3^-$ groups), 812 $cm^{-1}$ (C-H stretch of the para-positioned $-CH_3$ group), 676 $cm^{-1}$ (C-H out-of-plane bending vibration) and 563 $cm^{-1}$ (benzene ring C-C vibrations)[66].

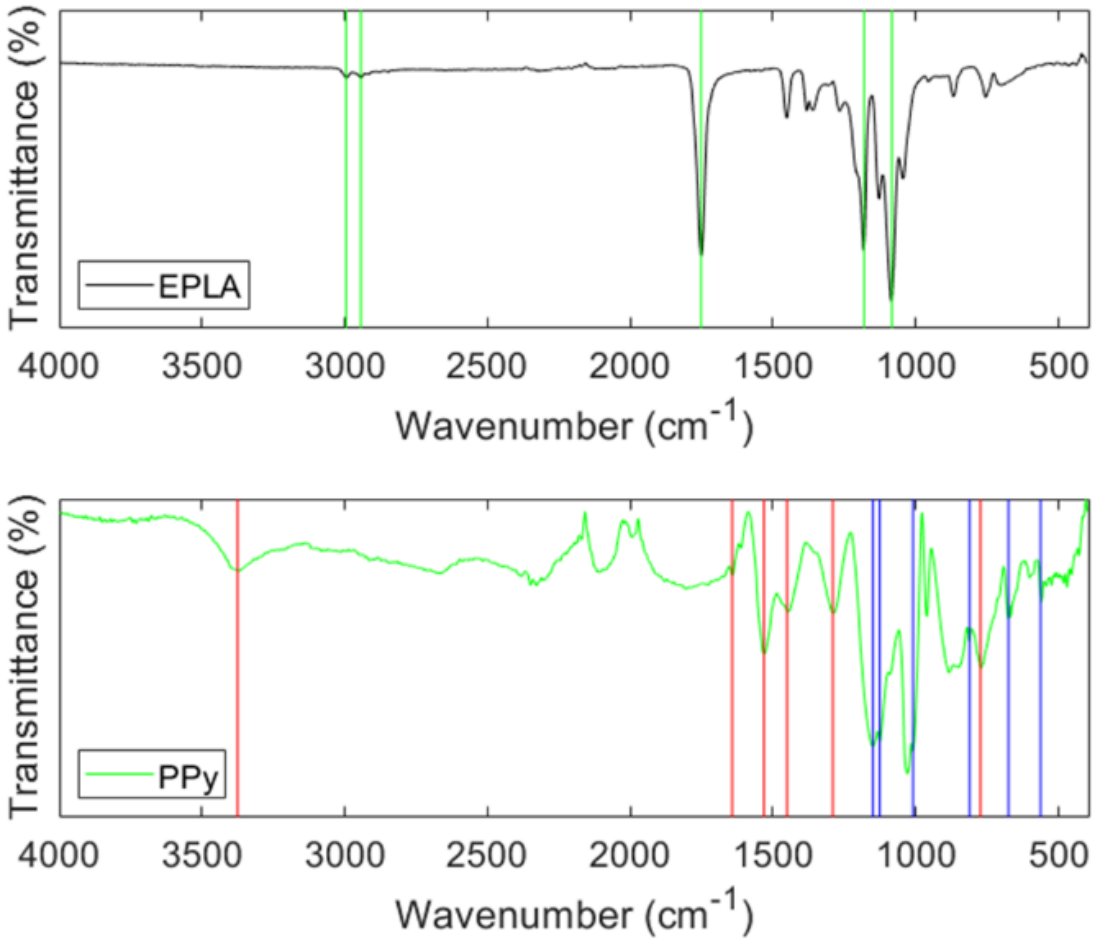


**Figure 4.** FTIR spectra of electrospun-PLA membrane (EPLA), as well as pure PPy doped with pTS (PPy). Green, red and blue vertical lines indicate the characteristic peaks of PLA, PPy and pTS, respectively.

Then, the presence of the PPy coating on PLA-PPy composites was corroborated by FTIR (**Figure S4** for cast films and **Figure 5** for electrospun membranes). As can be observed, both cast PLA-PPy films and PLA-PPy electrospun membranes maintain the characteristic peaks of PLA (2995 $cm^{-1}$, 2944 $cm^{-1}$, 1752 $cm^{-1}$, 1181 $cm^{-1}$ and 1084 $cm^{-1}$, marked with green vertical lines), even though their intensity decreases as the amount of PPy increases. Regarding the PPy and pTS characteristic peaks, some of them are hidden by PLA peaks, but others are clearly visible (marked with red and blue vertical lines for PPy and pTS, respectively). For both cast and electrospun PLA-PPy composites, the peak corresponding to the fundamental vibration of the PPy ring at 1532 $cm^{-1}$ is clearly visible, but slightly shifted towards higher wavelengths as the amount of PPy decreases. For PLA-PPy electrospun membranes with a higher content of PPy (above 23 wt%), the PPy characteristic peaks at 1291 $cm^{-1}$ and 773 $cm^{-1}$ are also visible. Regarding the pTS characteristic peaks, those located at 676 $cm^{-1}$ and 563 $cm^{-1}$ are clearly visible both for cast and electrospun PLA-PPy samples, while the peak located at 1010 $cm^{-1}$ is visible for PLA-PPy electrospun membranes with a higher amount of PPy. As the mass fraction of PPy increases in the samples, the intensity of the peaks corresponding to the PLA decreases, while the intensity of the peaks corresponding to the PPy and pTS increases, indicating the greater presence of PPy and pTS on the surface of PLA nanofibers.

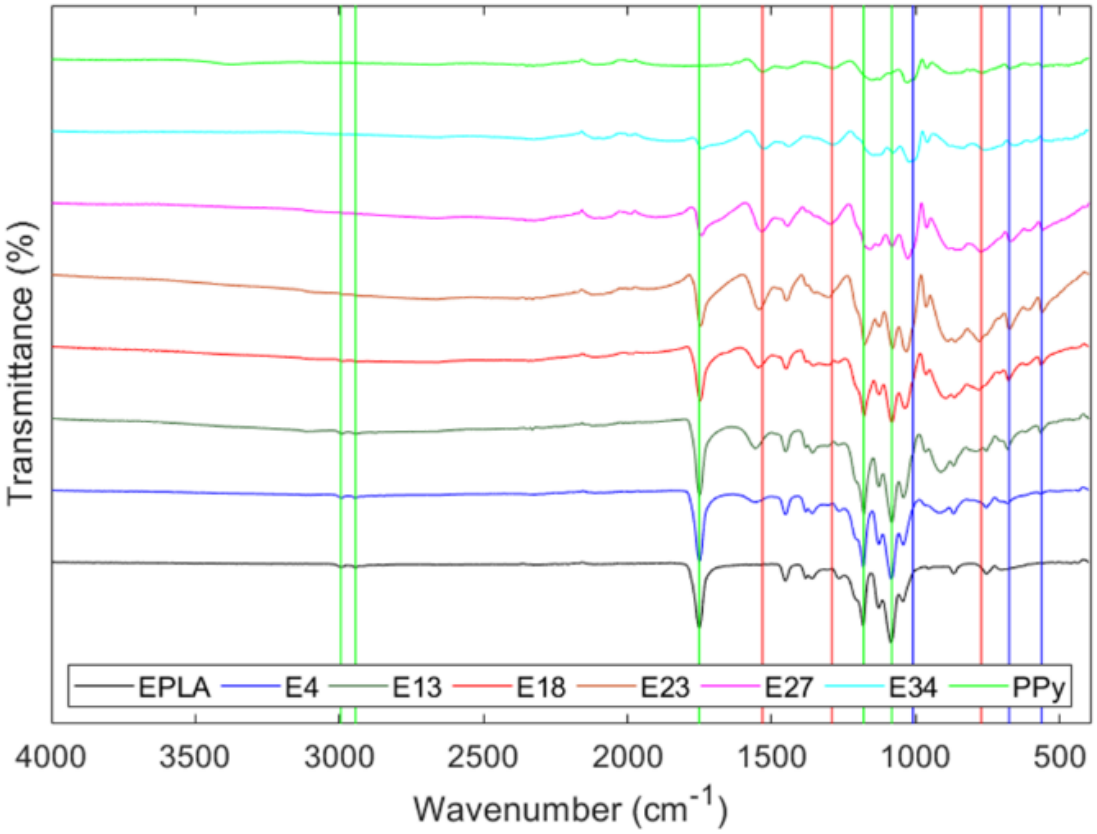


**Figure 5.** FTIR spectra of PLA (EPLA) and PLA-PPy (E4, E13, E18, E23, E27 and E34) electrospun membranes, as well as pure PPy. Green, red and blue vertical lines indicate the characteristic peaks of PLA, PPy and pTS, respectively.

## Thermogravimetric analysis (TGA)

The degradation temperature and thermal stability of PLA, PLA-PPy and PPy samples, as well as the presence of the PPy coating on PLA-PPy materials was studied by a thermogravimetric analysis (TGA). Regarding the cast films (**Figure S5**), a first mass loss between 100°C and 170°C can be observed for C2 that does not occur for either CPLA or for C1, indicative of the higher presence of PPy. The study of the TGA residues shows that, although the amount of PPy deposited on the PLA film is small, it is enough to observe a greater residue as the amount of PPy increases. These residues were used to obtain the mass fraction of PPy present on PLA-PPy cast films applying **Equation (5)**.

Regarding the electrospun membranes (**Figure 6**), a first mass loss between 50°C and 100°C is observed for PLA-PPy composites that increases as more PPy contains the sample. As previously observed for pTS doped PPy, this is mainly due to evolution of adsorbed pTS and $H_20$.[90] It has also been observed that the thermal decomposition of pTS doped PPy starts above 180°C[90], leading to the increased mass loss that can be observed for the PPy curve above this temperature. This leads to the mass loss observed for the PLA-PPy composites above this temperature, which increases proportionally to the amount of PPy present in the samples. A delay in thermal degradation can also be observed as more PPy contains the sample. For example, EPLA and E4 suffer the loss of 30% of their mass at 350°C, while E34 suffers it at 360°C. This indicates that the PPy coating of PLA nanofibers is continuous and homogeneous, being thicker as the mass fraction of PPy increases.

The study of TGA residues of PLA-PPy electrospun membranes clearly indicates the presence of the PPy coating, since the residues increase as more PPy contains the sample. These residues were used to obtain the samples composition by applying **Equation (5)**. When we compared the mass fraction of PPy obtained by TGA residues with the one obtained by weighing the samples before and after covering them with PPy (**Figure S6**), an oversizing of 50% of the mass fraction of PPy when using TGA residues. It could be produced by a greater retention of PLA volatiles by the PPy coating, so the extra residue is formed by both PLA and PPy and not only by PPy.

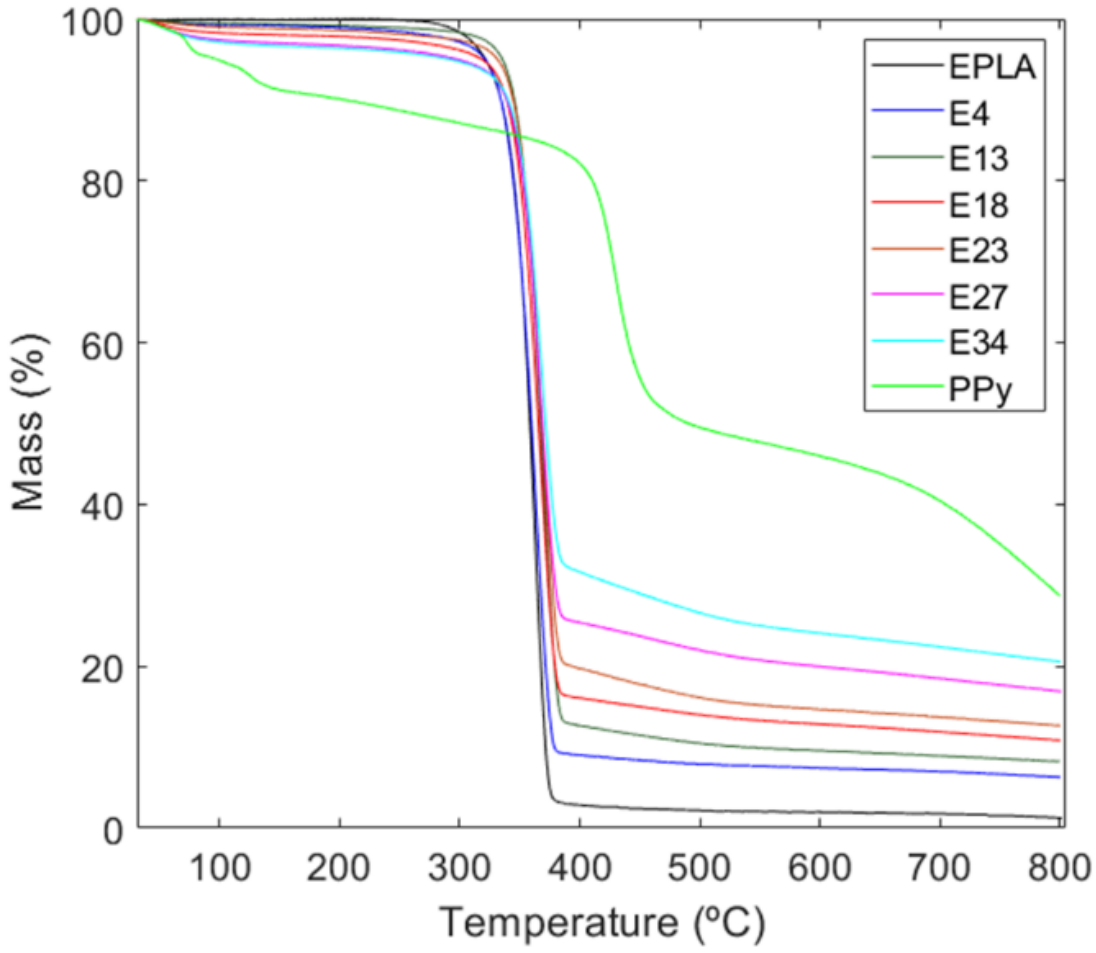


**Figure 6.** TGA of PLA (EPLA) and PLA-PPy (E4, E13, E18, E23, E27 and E34) electrospun membranes, as well as pure PPy.

## Electrical characterization

The electrical behavior of PLA-PPy materials was studied for both through-plane and in-plane applications.

### Through-plane electrical measurements

Electrospun membranes with a random orientation of the nanofibers (E4, E13, E18, E23, E27 and E34) were studied for through-plane applications. Cast films (C1 and C2) through-plane electrical behavior was also studied as a control without air. Through-plane electrical behavior was studied by electrochemical impedance spectroscopy (EIS).

**PLA-PPy cast films**

EIS measurements were carried out on PLA (CPLA) and PLA-PPy (C1 and C2) cast films in dry conditions at several temperatures to obtain the conductivity of the samples. The experimental data were analyzed in terms of the complex dielectric permittivity function, $\varepsilon^*(\omega,T)$, and the complex conductivity $\sigma^*(\omega,T) = j \cdot \omega \cdot \varepsilon_0 \cdot \varepsilon^*(\omega,T)$ where $j$ is the imaginary unity, $\varepsilon_0$ is the vacuum permittivity and $\omega$ the angular frequency of the applied electric field ($\omega = 2 \cdot \pi \cdot f$).

**Figure 7** presents the spectra of the real and imaginary part of the complex permittivity, Ɛ' and Ɛ", respectively, for each one of the samples at different temperatures in the interval from 0°C to 60°C. Different behavior is observed when we compare the PLA sample with the PLA-PPy samples with different mass fractions of PPy (1% and 2%). We can observe a decreasing of effective permittivity as frequency increases. This is because at low frequencies the dipoles that are formed and the charges in the polymer chains can follow the electric field below the electrode polarization (EP) effect, but when the frequency increases both dipoles and polymer chains have more difficult to follow the electric field and then the effective permittivity decreases. For example, for $f = 10^7 Hz$, while the real part of the permittivity for PLA membranes varies with temperature between 6.5 at 0°C to 7.2 at 60°C, for the PLA-PPy membranes it is practically independent of temperature, being around 3.7 and 6.4 for C1 and C2, respectively.

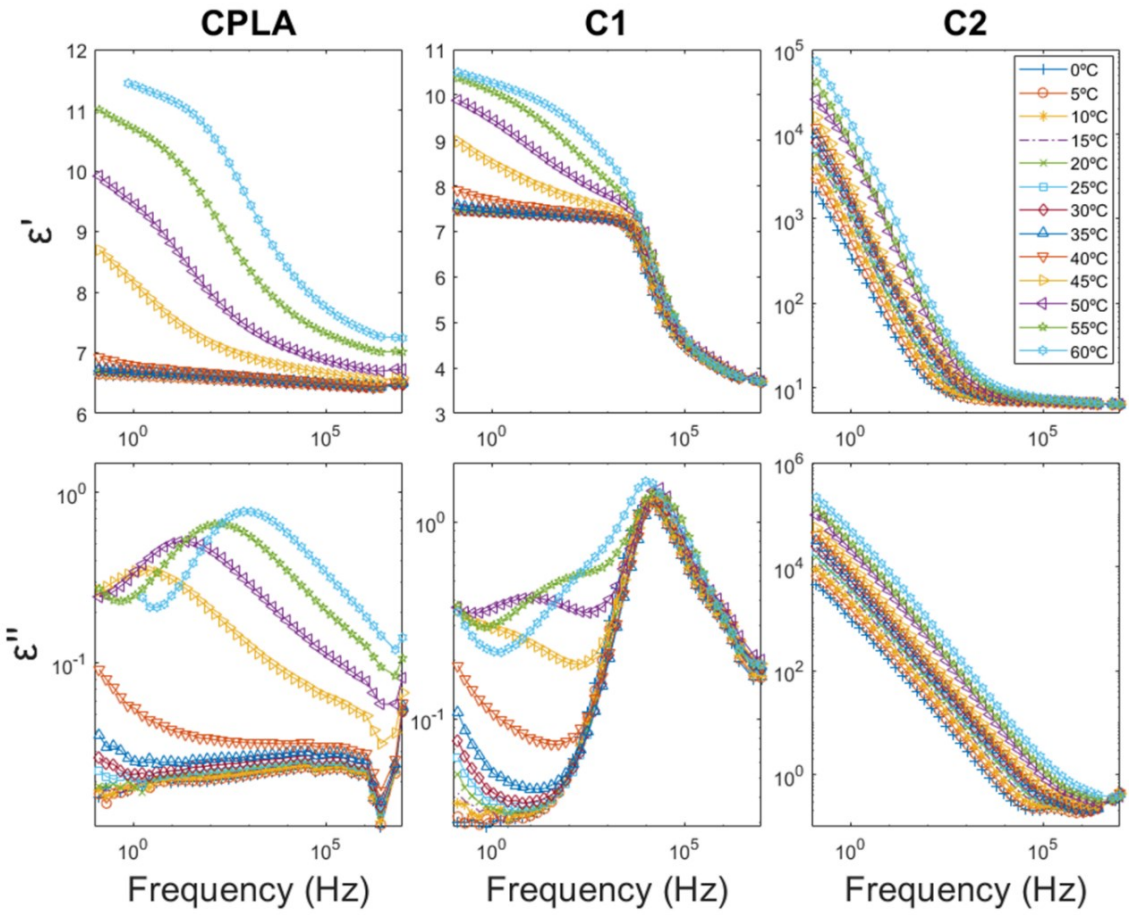


**Figure 7.** Real and imaginary part of the complex permittivity, Ɛ' and Ɛ'', respectively, for PLA (CPLA) and PLA-PPy (C1 and C2) cast films at different temperatures in the interval from 0°C to 60°C.

Regarding the loss permittivity, Ɛ", it presents a relaxation process for CPLA and C1 films when the temperature approaches to the glass transition temperature ($T_g$) of PLA. However, when the amount of PPy increases in the matrix of PLA (C2), the relaxation disappears because the conduction process generated inside the membrane is dominant in comparison with the polymer relaxation. The analysis of this relaxation process allows us to observe that it starts at 45°C, so the relaxation is not noticeable below this temperature, at least in the range of frequencies studied.

The dielectric spectra were fitted using a Havriliak-Negami function given by **Equation (6)**.

$$\varepsilon^* = \varepsilon_\infty + \frac{\Delta\varepsilon}{[1+(j\omega\tau)^\alpha]^\beta} \quad (6)$$

In **Figure 8** we can see an example of the fitting. The values of the parameters for the temperatures where the relaxation is present are plotted in **Figure 9A**. From this plot we can see for CPLA that $\varepsilon_\infty$, α and β are constants, while Δε increases slightly with temperature. Moreover, the relaxation peaks shift with the increase in temperature towards higher frequencies. There is a characteristic frequency for each temperature for CPLA, showing that the relaxation time decreases as temperature increases (**Figure 9B**).

**Figure 9A** also shows the variation of the fitting parameters with temperature for the sample C1. In our sample we have obtained that $\varepsilon_\infty$, α and β are constants being the values of $\varepsilon_\infty$ and α smaller than the CPLA ones. From **Figure 9B**, we observe for C1 that the incorporation of PPy produces an additional relaxation process with a relaxation time that is practically independent of temperature, indicative of its predominantly conductive nature, preserving the temperature-dependent relaxation processes previously observed for CPLA. Such relaxations observed in CPLA and C1 films at sub-$T_g$ temperatures usually originate from molecular motions that are restricted to the scale of few bond lengths.

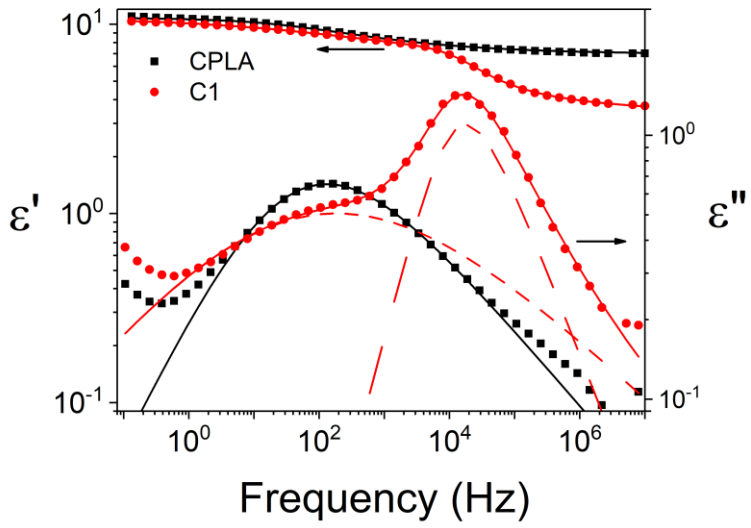


**Figure 8.** Deconvolutions of the real and imaginary part of the complex permittivity at 55°C for PLA (CPLA) and PLA-PPy (C1) cast films, respectively.

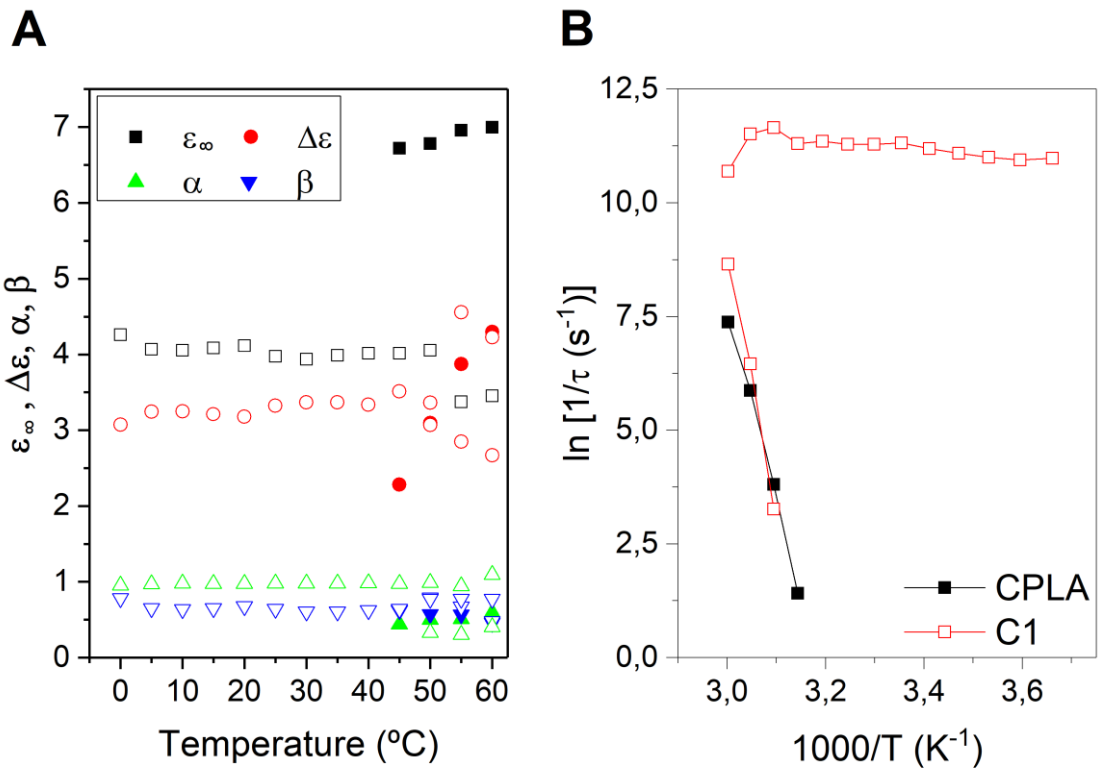


**Figure 9. A**: Values of the parameters $\Delta\varepsilon$, $\varepsilon_\infty$, $\alpha$ and $\beta$ for the temperatures where the relaxation is present for the PLA (CPLA) (solid) and PLA-PPy (C1) (open) cast films. **B**: Variation of the relaxation time with temperature for the PLA (CPLA) and PLA-PPy (C1) cast films.

The bulk conductivity was obtained from the Bode diagrams in the interval of temperatures from 0°C to 60°C. **Figure 10** shows the Bode diagrams of the CPLA, C1 and C2 samples. For CPLA we observe the behavior of a pure capacitor, as the conductivity increases linearly with the frequency with a slope practically equal the unit, and the phase angle is between -85° and -90°. A similar behavior is observed for C1.

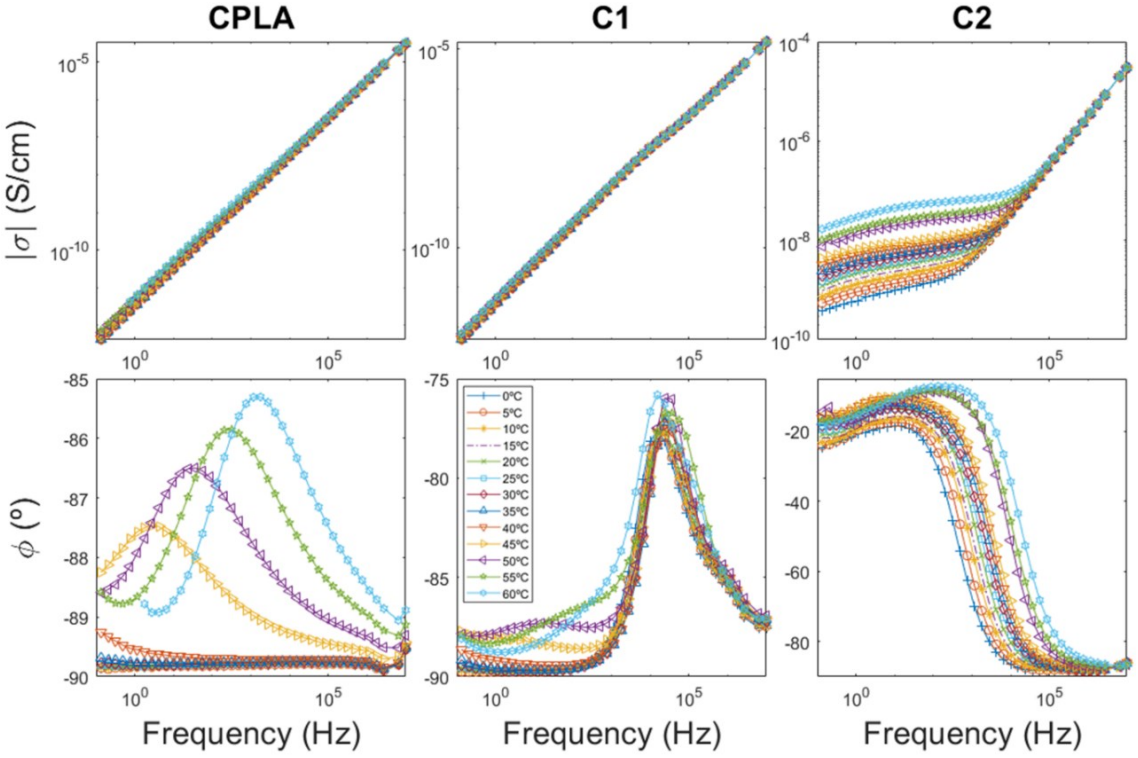


**Figure 10.** Bode diagram for the PLA (CPLA) and PLA-PPy (C1 and C2) cast films.

For the other samples (CPLA and C1) the behavior is, in agreement with our results, completely capacitive. Moreover, the capacity of the samples is dependent of the temperature. For example, for CPLA the capacity increases from 30pF at 0°C to 55pF at 60°C, however at 40°C we can observe a behavior at low temperatures where the capacity is practically constant, and an abrupt change of slope at 40°C increasing the capacity from 31pF to 55pF. For the sample C1 we can observe an increasing from 34pF at 0°C until 38pF at 40°C, to then decrease until 29pF at 60°C. Finally, for the

sample C2 the capacity increase with temperature from 40pF at 0°C until 51pF at 60°C. For such sample we also observe a similar increasing around 35°C.

However, when the mass fraction of PPy increases, such is the case of the sample C2, the spectra reveals that the real part of the conductivity increases with the frequency and tends to a constant value when the phase angle, $\varphi$, reaches a maximum, for each temperature. We also can observe that in the range of high frequencies the conductivity varies linearly (slope ~ 1) with the frequency, following a capacitive behavior. The length of the plateau in the Bode diagram of C2 increases as temperature increases until a critical frequency fc dependent on temperature is reached, at which log $|\sigma|$ collapses along a straight line with a slope equal to 1. This is a typical behavior of a parallel $R_0C$ circuit, where at high frequencies the modulus of the impedance can be expressed as **Equation (7)**.

$$\lim_{\omega\to\infty} log|Z^*(\omega)| = \lim_{\omega\to\infty} log\left|\frac{R_0}{1+j\omega R_0 C}\right| \cong log\left(\frac{1}{C\omega}\right) \quad (7)$$

From the straight line of the plot of log |Z| vs. log $\omega$, we can obtain from the intercept the capacity of the sample. On the other hand, at low frequencies where $\omega C$<<1, the limit of **Equation (7)** is the bulk resistance ($R_0$). This resistance is related with the DC-conductivity through $\sigma = L/(R_0 A)$, being L and A the sample thickness and surface area sandwiched between the two electrodes, respectively. At the same time the phase angle increases from -90° to -5°. However, above the critical frequency, $f_c = \omega_c/2\pi$, being $\omega_c \geq 1/(R_0 C)$, the impedance is completely capacitive and $|Z^*(\omega)| \propto \omega^{-1}$, in agreement with the results shown for C2.

The DC-conductivity of the sample C2, $\sigma_{DC}$, can be extracted from the plateau in the moderate frequency range (**Figure S7**), reaching a conductivity value of $4.6\cdot10^{-9}$ S/cm when setting the frequency at 15.4 Hz and the temperature at 30ºC. Furthermore,

the frequency value where the plateau is reached is shifted to higher frequencies by increasing the temperature, as consequence of the thermally activated nature of the charge transport. However, at moderate and low frequencies the conductivity decreases from $\sigma_{DC}$. The deviation from the plateau is attributed to the electrode polarization resistance, which results from the blocking of charge carriers at the electrodes.[91–96]

**PLA-PPy electrospun membranes**

In this case the EIS measurements were carried out on PLA (EPLA) and PLA-PPy (E4, E13, E18, E23, E27 and E34) electrospun membranes with a random orientation of the nanofibers in dry conditions at different temperatures (0°C to 60°C) in order to obtain information about the conductivity of the samples. Data for the real part of the conductivity was analyzed in terms of the corresponding Bode diagrams, where variations of the conductivity with the frequency for all the PLA and PLA-PPy electrospun membranes are shown in **Figure 11** (EPLA, E4, E13 and E18) and **Figure S8** (E23, E27 and E34). A close inspection of these figures shows that, in the case of EPLA, a plateau of the real part of the conductivity is not observed, presumably, because it is at very low frequencies, outside the range of measurement of our experiments, showing a dielectric behavior of PLA membranes. For such PLA membranes, our results show straight lines with slope ca. 1, indicating that the material is purely capacitor, where the values of the geometrical capacitance (C) are around 40pF. For PLA-PPy membranes with a content in PPy equal to 4%wt (E4), we observe that the conductivity is practically constant in the range of frequencies between 0.1 Hz and $10^3$ Hz, depending of temperature, showing a cut-off frequency where it starts increasing linearly with the frequency, as if the sample was a capacitor. However, when the mass fraction of PPy is greater or equal to 13%wt (E13, E18, E23, E27 and E34), the real part of the conductivity is constant for all range of frequencies (0.1 Hz to $10^6$

Hz), meaning that the impedance has only a resistive contribution and its value represents the electrical conductivity of the nanocomposite. This behavior is the typical demeanor of a conductive material.

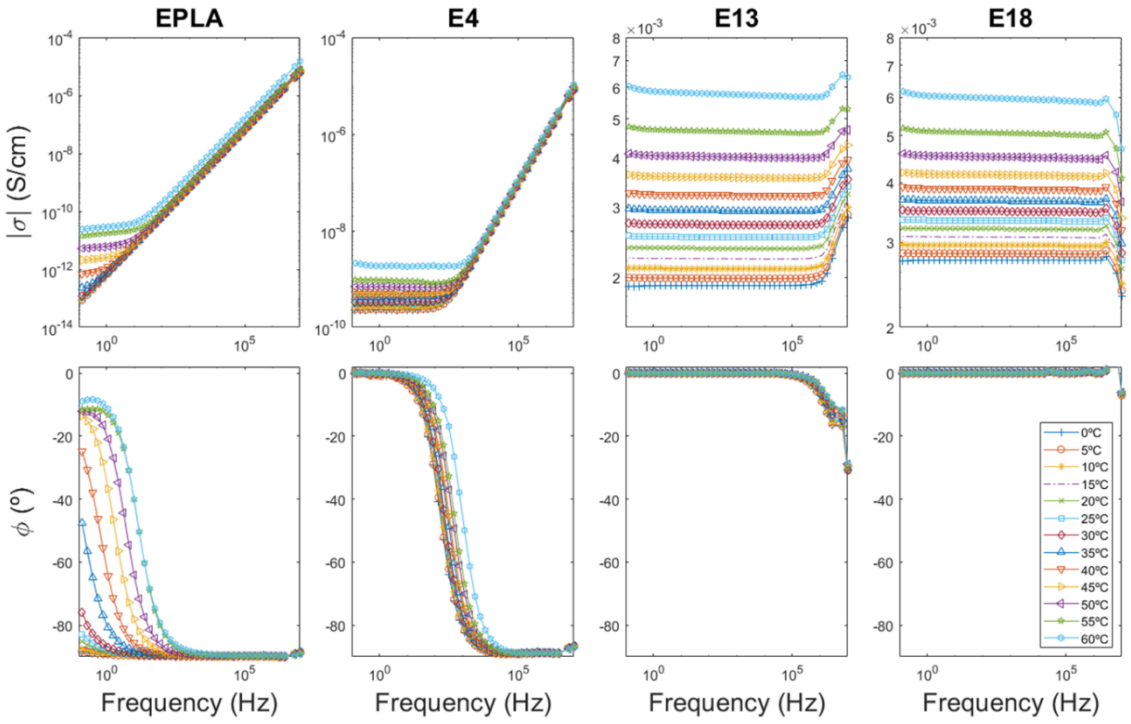


**Figure 11.** Bode diagram for PLA (EPLA) and PLA-PPy (E4, E13 and E18) electrospun membranes.

A quantitative analysis of the conductivity with temperature for the PLA-PPy nanocomposites can be observed in **Figure 12**. A comparison between the different nanocomposites shows that the conductivity ($\sigma_{DC}$) is a function of the amount of PPy that we have incorporated on the surface of the nanofibers of PLA, so the conductivities increase when the amount of PPy increases (**Figure 12A** and **12C**), observing an Arrhenius behavior for all the nanocomposites (**Figure 12A**). For example, the conductivities obtained from the Bode diagrams at 30°C with a fixed frequency of 15.4 Hz were $1 \cdot 10^{-11}$ S/cm, $6.3 \cdot 10^{-9}$ S/cm, $2.7 \cdot 10^{-3}$ S/cm, $3.5 \cdot 10^{-3}$ S/cm, $9.6 \cdot 10^{-3}$ S/cm, $3.9 \cdot 10^{-2}$ S/cm and $5.2 \cdot 10^{-2}$ S/cm for EPLA, E4, E13, E18, E23, E27 and E34,

respectively. This is in accordance with the conductivities obtained in other studies where a combination of an insulting polymer and PPy is employed in order to obtain electrically conductive electrospun membranes, where similar conductivities are obtained.[41,97,98] A similar trend is observed for all the range of temperatures, but with an increase in conductivity (**Figure 12C**). This suggests that the interaction between the ions and the nanofiber polymer matrix may play an important role in determining the relationship between the ionic transport and the structural relaxation in terms of the temperature and PPy incorporated to the composite.

If we compare these conductivity values with those obtained for cast membranes (C1 and C2) we observe that, for a coating ratio of 1 (CR1), a conductivity value of $5.46 \cdot 10^{-11}$ S/cm is achieved for cast films, while a conductivity value of $6.3 \cdot 10^{-9}$ S/cm is achieved with electrospun membranes (115 times higher). The same trend is observed with the coating ratio 2 (CR2), since $4.6 \cdot 10^{-9}$ S/cm are achieved with non-porous films and $3.5 \cdot 10^{-3}$ S/cm are achieved with electrospun membranes (more than $7.6 \cdot 10^{5}$ times higher).

Therefore, a greater conductivity is achieved when using electrospun membranes instead of non-porous films for the same coating parameters thanks to the greater specific surface area and greater porosity of electrospun membranes. They allow a greater PPy deposition as well as a simpler entry of PPy to the core of the material, connecting the two external surfaces of the membrane with PPy. The improved electrical behavior of electrospun membranes is also observed for the activation energy (**Figure 12B**), which is almost 6 times higher for C2 than for E18 (cast and electrospun samples coated with CR2). A lower activation energy is indicative of a greater ease of transport of electric charges.

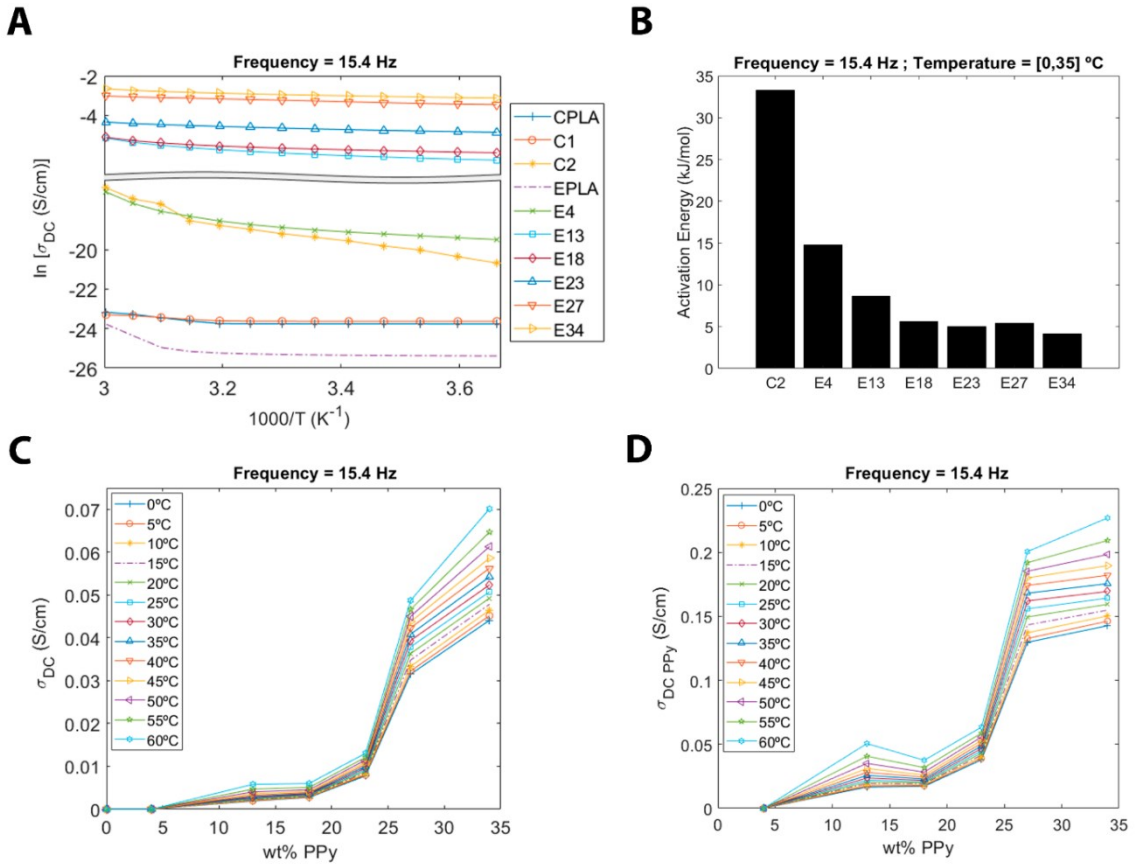


**Figure 12.** Through-plane electrical characterization of PLA-PPy composites. **A**: Arrhenius plot for the DC conductivity obtained from the Bode diagrams for CPLA, C1, C2, EPLA, E4, E13, E18, E23, E27 and E34 (frequency = 15.4 Hz). **B**: Activation energy for C2, E4, E13, E18, E23, E27 and E34 (frequency = 15.4 Hz, temperature = [0, 35] °C). **C**: Electrical conductivity vs. mass fraction of PPy for PLA-PPy electrospun membranes. **D**: PPy electrical conductivity vs. mass fraction of PPy for electrospun membranes.

In order to calculate the intrinsic conductivity of PPy, we proceeded to divide the apparent conductivity values between the volumetric fraction of PPy (**Figure 12D**), which was obtained by applying **Equation (8)**.

$$\emptyset_{PPy} = \frac{V_{PPy}}{V_{PPy}+V_{PLA}} = \frac{\frac{m\cdot\omega_{PPy}}{\varphi_{PPy}}}{\frac{m\cdot\omega_{PPy}}{\varphi_{PPy}}+\frac{m\cdot\omega_{PLA}}{\varphi_{PLA}}} = \frac{\frac{\omega_{PPy}}{\varphi_{PPy}}}{\frac{\omega_{PPy}}{\varphi_{PPy}}+\frac{1-\omega_{PPy}}{\varphi_{PLA}}} \quad (8)$$

This allows us to observe a percolation effect from E27, so the conductivity for E34 does not increase, as it does with the values of apparent conductivity, and remains constant with an approximate value of 0.17 S/cm for a frequency of 15.4 Hz and a temperature of 30°C, which is consistent when compared with the DC conductivity obtained for pure PPy in other studies.[99,100] This is indicative that from 27 wt% PPy there is a perfect continuity between the PPy grains. The homogeneity and continuity of the PPy coating can also be observed with the activation energy (**Figure 12B**), since it decreases as the mass fraction of PPy increases, until it stabilizes for the higher contents of PPy.

## In-plane electrical measurements

Electrospun membranes with an aligned orientation of the nanofibers (E4, E18, E27 and E34) were studied for in-plane applications. In-plane electrical behavior was studied by measuring superficially the circulating electric current (DC) when applying a known voltage. This allowed us to calculate the apparent surface electrical resistance of the materials (R) by Ohm's law, normalizing by the distance between contacts (l), at room temperature (**Figure 13A**). As can be observed, the effect of the amount of PPy deposited on the surface of the PLA membrane is very remarkable, so the surface electrical resistance of the materials decreases following a potential function when the wt% PPy increases.

In addition, after measuring the cross section of the membranes (S), the in-plane apparent DC-conductivity ($\sigma_{DC,IP}$) of the materials could be obtained by **Equation (9)**.

$$\sigma_{DC,IP} = \frac{l}{R \cdot S} \quad (9)$$

As can be observed in **Figure 13B**, there is a relationship between the electrical conductivity and the mass fraction of PPy very similar to that obtained for through-plane measurements (**Figure 12C**). The conductivity increases rapidly and practically linearly from 20 wt% of PPy, having very small conductivities for PPy mass fractions below this value. The in-plane conductivity values are approximately 4 times higher than those measured through-plane. This means that the charge carriers find less resistance when traveling superficially than when travelling across the material. In addition, the aligned disposition of the nanofibers aims to improve the conductivity for in-plane applications.

Finally, the intrinsic conductivity of PPy was calculated by applying **Equation (10)**.

$$\sigma_{PPy} = \frac{1}{\frac{R}{l} \cdot A_{PPy}} = \frac{1}{\frac{R}{l} \cdot \frac{V_{PPy}}{l}} = \frac{l^2}{R \cdot V_{PPy}} = \frac{l^2}{R \cdot \frac{m_{PPy}}{\varphi_{PPy}}} == \frac{l^2}{R \cdot \frac{m \cdot \omega_{PPy}}{\varphi_{PPy}}} = \frac{l^2 \cdot \varphi_{PPy}}{R \cdot m \cdot \omega_{PPy}} \quad (10)$$

As can be observed in **Figure 13C**, a behavior like that previously observed for the through-plane measurements (**Figure 12D**) was obtained. There is a percolation phenomenon from 27 wt% PPy, indicating a perfect continuity between PPy grains from this mass fraction value of PPy. The PPy conductivities obtained in-plane are approximately 6 times higher than those obtained through-plane, following the trend observed with the apparent conductivities.

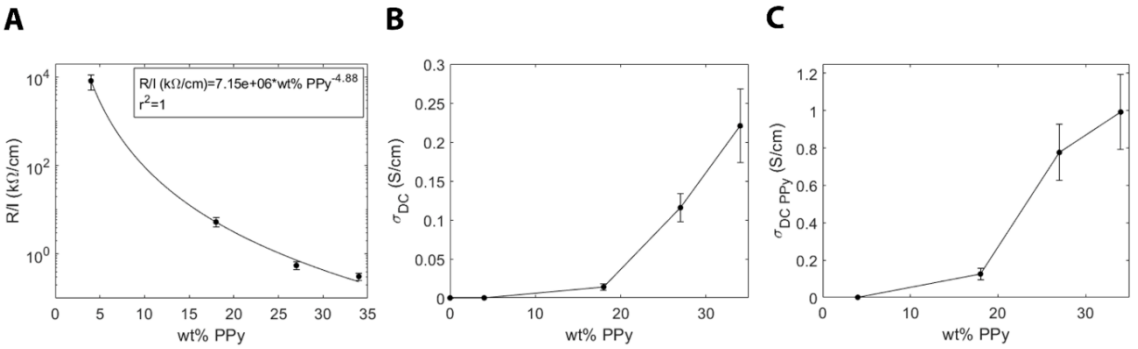


**Figure 13.** In-plane electrical characterization of PLA-PPy electrospun membranes (E4, E18, E27 and E34) at room temperature. **A**: Surface resistance normalized by the distance between contacts. **B**: Electrical conductivity vs. mass fraction of PPy. **C**: PPy conductivity vs. mass fraction of PPy.

# 5.5. Conclusions

In this work, both non-porous films and electrospun membranes made of PLA were coated with different mass fractions of PPy. Its physicochemical and dielectric characterization allowed us to conclude that the use of nanofiber membranes entails a greater PPy deposition due to their greater specific surface area and porosity, leading to higher conductivity values. The dielectric measurements for both cast films and electrospinning membranes showed a transition between conduction mechanisms depending on PPy content. While for samples without PPy a temperature-dependent relaxation process appeared as the temperature approached to the glass transition temperature of PLA, for samples with a high content of PPy a temperature-independent conduction process was present, hiding the polymer relaxation. For samples with a low content of PPy, an intermediate behavior was observed, with a combination of both processes. Both FESEM and EIS analysis allowed us to conclude that a continuous and homogeneous coating of PLA nanofibers with PPy is achieved from 23wt% PPy. We can also conclude that the electrical conductivity of PLA-PPy electrospun membranes depends directly on the amount of PPy deposited on the PLA nanofibers. Therefore,

greater conductivities are achieved as wt% PPy increases where a percolation effect was observed around 27 wt% PPy for E27 membranes, reaching conductivity values above 0.05 S/cm for through-plane applications and above 0.20 S/cm for in-plane applications for the highest wt% PPy. This indicates that from threshold percolation there is a perfect continuity between the PPy grains. The high conductivity values obtained both through-plane and in-plane for PLA-PPy electrospun membranes confirm its possible application both in systems where the electrodes are located perpendicular to the membrane and in applications where the electrodes are in the plane of the membrane. This, in combination with its high specific surface area, high porosity and thermal stability for temperatures below 140°C allows its application with the through-plane disposition as solid, low cost, durable and tunable polymer electrolytes in applications such as PEMFCs, batteries, supercapacitors, sensors and photosensors. Likewise, the high surface conductivity of the membranes for the in-plane disposition, together with the biocompatibility of both PLA and PPy, extend the applications of these electrically conductive membranes to other fields such as tissue engineering and biomedical implantable devices.

## 5.6. Authorship contribution statement

F.G.R.: Methodology, Formal analysis, Investigation, Writing – original draft, Visualization. A.G.B.: Investigation, Writing – Review & Editing, Visualization. V.C.M.: Methodology, Writing – Review & Editing, Funding acquisition. C.M.-R.: Conceptualization, Methodology, Writing – Review & Editing, Supervision, Funding acquisition. M.M.P.: Conceptualization, Methodology, Writing – Review & Editing, Supervision, Funding acquisition.

## 5.7. Conflicts of interest

There are no conflicts to declare.

## 5.8. Acknowledgements

The authors acknowledge financing from the Spanish Government's State Research Agency (AEI) through projects DPI2015-72863-EXP and RTI2018-095872-B-C22/ERDF. FGR acknowledges the scholarship FPU16/01833 of the Spanish Ministry of Universities. We thank the Electron Microscopy Service at the UPV, where the FESEM images were obtained.

## 5.9. References

1. R. McNeill, R. Siudak, J. H. Wardlaw, D. E. Weiss, *Aust. J. Chem.* **1963**, *16*, 1056.
2. B. A. Bolto, D. E. Weiss, *Aust. J. Chem.* **1963**, *16*, 1076.
3. B. A. Bolto, R. McNeill, D. E. Weiss, *Aust. J. Chem.* **1963**, *16*, 1090.
4. R. McNeill, D. E. Weiss, D. Willis, *Aust. J. Chem.* **1965**, *18*, 477.
5. B. A. Bolto, D. E. Weiss, D. Willis, *Aust. J. Chem.* **1965**, *18*, 487.
6. H. Shirakawa, E. J. Louis, A. G. MacDiarmid, C. K. Chiang, A. J. Heeger, *J. Chem. Soc. Chem. Commun.* **1977**, 578, doi:10.1039/C39770000578.
7. N. Hall, *Chem. Commun.* **2003**, 1, doi:10.1039/b210718j.
8. H. Hammache, L. Makhloufi, B. Saidani, *Corros. Sci.* **2003**, *45*, 2031.
9. M. Mattioli-Belmonte *et al.*, *Mater. Sci. Eng. C* **2005**, *25*, 43.
10. M. A. Careem, K. P. Vidanapathirana, S. Skaarup, K. West, *Solid State Ionics* **2004**, *175*, 725.
11. D. Ge *et al.*, *Electrochim. Acta* **2009**, *55*, 271.

12. R. K. Sharma, A. C. Rastogi, S. B. Desu, *Electrochem. commun.* **2008**, *10*, 268.

13. J. Rubio Retama, E. López Cabarcos, D. Mecerreyes, B. López-Ruiz, *Biosens. Bioelectron.* **2004**, *20*, 1111.

14. L. X. Wang, X. G. Li, Y. L. Yang, *React. Funct. Polym.* **2001**, *47*, 125.

15. G. Sabouraud, S. Sadki, N. Brodie, *Chem. Soc. Rev.* **2000**, *29*, 283.

16. C. Li, H. Bai, G. Shi, *Chem. Soc. Rev.* **2009**, *38*, 2397.

17. T. H. Le, Y. Kim, H. Yoon, *Polymers (Basel).* **2017**, *9*.

18. S. I. Brahim, D. Maharajh, D. Narinesingh, A. Guiseppi-Elie, *Anal. Lett.* **2002**, *35*, 797.

19. K. J. Dunst, K. Cysewska, P. Kalinowski, P. Jasiński, *IOP Conf. Ser. Mater. Sci. Eng.* **2016**, *104*.

20. H. K. Jun *et al.*, *Sensors Actuators, B Chem.* **2003**, *96*, 576.

21. Y. Zhong, S. Lundemo, E. W. H. Jager, *Smart Mater. Struct.* **2018**, *27*.

22. A. Kisiel *et al.*, *Electrochem. commun.* **2010**, *12*, 1568.

23. S. M. M. Morsi, M. E. A. El-Aziz, R. M. M. Morsi, A. I. Hussain, *J. Coatings Technol. Res.* **2018**, doi:10.1007/s11998-018-00152-8.

24. H. Yamamoto, M. Fukuda, I. Isa, K. Yoshino, *Electron. Commun. Japan (Part II Electron.* **1993**, *76*, 88.

25. H. Yamamoto, M. Oshima, M. Fukuda, I. Isa, K. Yoshino, *J. Power Sources* **1996**, *60*, 173.

26. I. Sultana *et al.*, *Electrochim. Acta* **2012**, *83*, 209.

27. J. Xia, L. Chen, S. Yanagida, *J. Mater. Chem.* **2011**, *21*, 4644.

28. F. M. A. Almuntaser, S. Majumder, P. K. Baviskar, J. V. Sali, B. R. Sankapal, *Appl. Phys. A Mater. Sci. Process.* **2017**, *123*, 1.

29. D. Hao, B. Xu, Z. Cai, *J. Mater. Sci. Mater. Electron.* **2018**, *29*, 9218.

30. R. M. A. P. Lima, J. J. Alcaraz-Espinoza, F. A. G. Da Silva, H. P. De Oliveira, *ACS Appl. Mater. Interfaces* **2018**, *10*, 13783.

31. J. Avloni *et al.*, *Screening* **2006**, 6, doi:10.1177/0892705707076718.

32. C. Y. Lee *et al.*, *Polym. Adv. Technol.* **2002**, *13*, 577.

33. E. Håkansson, A. Amiet, S. Nahavandi, A. Kaynak, *Eur. Polym. J.* **2007**, *43*, 205.

34. A. H. El-Shazly, A. A. Wazzan, *Int. J. Electrochem. Sci.* **2012**, *7*, 1946.

35. T. G. DRAGICA CHAMOVSKA, ALEKSANDRA PORJAZOSKA KUJUNDZISKI, *Zaštita Mater.* **2013**, *54*, 229.

36. H. Zhao, L. Li, J. Yang, Y. Zhang, *J. Power Sources* **2008**, *184*, 375.

37. S. Y. Huang, P. Ganesan, B. N. Popov, *Appl. Catal. B Environ.* **2009**, *93*, 75.

38. H. S. Park, Y. J. Kim, Y. S. Choi, W. H. Hong, D. Jung, *J. Power Sources* **2008**, *178*, 610.

39. C. Feng *et al.*, *Biosens. Bioelectron.* **2010**, *25*, 1516.

40. J. Y. Lee, C. A. Bashur, A. S. Goldstein, C. E. Schmidt, *Biomaterials* **2009**, *30*, 4325.

41. J. F. Zhou *et al.*, *Neural Regen. Res.* **2016**, *11*, 1644.

42. S. Aznar-Cervantes *et al.*, *Bioelectrochemistry* **2012**, *85*, 36.

43. P. M. George *et al.*, *Biomaterials* **2005**, *26*, 3511.

44. J. Wang *et al.*, *Phys. Chem. Chem. Phys.* **2017**, *19*, 21165.

45. T. Uyar, L. Toppare, J. Hacaloglu, *J. Macromol. Sci. - Pure Appl. Chem.* **2001**, *38 A*, 1141.

46. B. Zinger, P. Shaier, A. Zemel, *Synth. Met.* **1991**, *40*, 283.

47. N. N. Ha, N. T. Cuong, H. Van Hung, H. M. Hung, V. Q. Trung, *J. Mol. Model.* **2017**, *23*.

48. R. C. D. Peres, V. F. Juliano, M. A. De Paoli, S. Panero, B. Scrosati,

*Electrochim. Acta* **1993**, *38*, 869.

49. M. A. De Paoli, R. C. D. Peres, S. Panero, B. Scrosati, *Electrochim. Acta* **1992**, *37*, 1173.
50. H. K. Lim, S. O. Lee, K. J. Song, S. G. Kim, K. H. Kim, *J. Appl. Polym. Sci.* **2005**, *97*, 1170.
51. U. Carragher, C. B. Breslin, *Electrochim. Acta* **2018**, *291*, 362.
52. C. Arribas, D. Rueda, *Synth. Met.* **1996**, *79*, 23.
53. T. M. Wu, H. L. Chang, Y. W. Lin, *Polym. Int.* **2009**, *58*, 1065.
54. C. Jin, F. Yang, W. Yang, *J. Appl. Polym. Sci.* **2006**, *101*, 2518.
55. A. Kaynak, *Fibers Polym.* **2009**, *10*, 590.
56. L. A. Samuelson, M. A. Druy, *Macromolecules* **1986**, *19*, 824.
57. H. Hou, Q. Liao, J. Duan, S. Liu, Y. Yao, *Surf. Innov.* **2018**, *6*, 56.
58. I. Sultana *et al.*, *Electrochim. Acta* **2012**, *60*, 201.
59. C. Jérôme, L. Martinot, D. Strivay, G. Weber, R. Jérôme, *Synth. Met.* **2001**, *118*, 45.
60. H. Zhao, W. E. Price, C. O. Too, G. G. Wallace, D. Zhou, *J. Memb. Sci.* **1996**, *119*, 199.
61. R. Ansari Khalkhali, W. E. Price, G. G. Wallace, *React. Funct. Polym.* **2003**, *56*, 141.
62. M. Pyo, J. R. Reynolds, L. F. Warren, H. O. Marcy, *Synth. Met.* **1994**, *68*, 71.
63. P. Murray, G. M. Spinks, G. G. Wallace, R. P. Burford, *Synth. Met.* **1997**, *84*, 847.
64. J. Chengyou, Y. Fenglin, *Sensors Actuators, B Chem.* **2006**, *114*, 737.
65. S. Li, Y. Qiu, X. Guo, *J. Appl. Polym. Sci.* **2009**, *114*, 2307.
66. T. Raudsepp, M. Marandi, T. Tamm, V. Sammelselg, J. Tamm, *Electrochim.*

*Acta* **2014**, *122*, 79.

67. V. Syritski, A. Öpik, O. Forsén, *Electrochim. Acta* **2003**, *48*, 1409.
68. Y. Fang *et al.*, *J. Power Sources* **2010**, *195*, 674.
69. T. Qian *et al.*, *Biosens. Bioelectron.* **2014**, *58*, 237.
70. J. Zhang, X. S. Zhao, *J. Phys. Chem. C* **2012**, *116*, 5420.
71. W. Li *et al.*, *Nano Lett.* **2013**, *13*, 5534.
72. C. Zhu, J. Zhai, D. Wen, S. Dong, *J. Mater. Chem.* **2012**, *22*, 6300.
73. A. Esfandiari, *World Appl. Sci. J.* **2008**, *3*, 470.
74. C. Ding, X. Qian, G. Yu, X. An, *Cellulose* **2010**, *17*, 1067.
75. L. Yuan *et al.*, *Energy Environ. Sci.* **2013**, *6*, 470.
76. Y. Lu, P. Tao, N. Zhang, S. Nie, *Carbohydr. Polym.* **2020**, *245*, 116463.
77. Y. Zhang, N. Hao, X. Lin, S. Nie, *Carbohydr. Polym.* **2020**, *234*, 115888.
78. Y. Wang, G. A. Sotzing, R. A. Weiss, *Chem. Mater.* **2008**, *20*, 2574.
79. D. E. Henton, P. Gruber, J. Lunt, J. Randall, *Nat. Fibers, Biopolym. Biocomposites* **2005**, *48674*, 527.
80. J. Lunt, *Polym. Degrad. Stab.* **1998**, *3910*, 145.
81. P. Mróz, S. Białas, M. Mucha, H. Kaczmarek, *Thermochim. Acta* **2013**, *573*, 186.
82. M. C. Araque-Monrós *et al.*, *Polym. Degrad. Stab.* **2013**, *98*, 1563.
83. Y. Ramot, M. Haim-Zada, A. J. Domb, A. Nyska, *Adv. Drug Deliv. Rev.* **2016**, *107*, 153.
84. D. da Silva *et al.*, *Chem. Eng. J.* **2018**, *340*, 9.
85. J. Schindelin *et al.*, *Nat. Methods* **2012**, *9*, 676.
86. D. Garlotta, *J. Polym. Environ.* **2001**, *9*, 63.
87. J. P. Mofokeng, A. S. Luyt, T. Tábi, J. Kovács, *J. Thermoplast. Compos. Mater.* **2012**, *25*, 927.

88. B. W. Chieng, N. A. Ibrahim, W. M. Z. W. Yunus, M. Z. Hussein, *Polymers (Basel).* **2014**, *6*, 93.

89. H. K. Chitte, G. N. Shinde, N. V. Bhat, V. E. Walunj, *J. Sens. Technol.* **2011**, *01*, 47.

90. T. Uyar, L. Toppare, J. Hacaloğlu, *J. Anal. Appl. Pyrolysis* **2002**, *64*, 1.

91. H. J. Schütt, E. Gerdes, *J. Non. Cryst. Solids* **1992**, *144*, 1.

92. H. J. Schütt, E. Gerdes, *J. Non. Cryst. Solids* **1992**, *144*, 14.

93. T. S. Sørensen, V. Compañ, R. Diaz-Calleja, *J. Chem. Soc. - Faraday Trans.* **1996**, *92*, 1947.

94. J. R. Sangoro *et al.*, *Phys. Rev. E - Stat. Nonlinear, Soft Matter Phys.* **2008**, *77*.

95. A. Serghei, M. Tress, J. R. Sangoro, F. Kremer, *Phys. Rev. B - Condens. Matter Mater. Phys.* **2009**, *80*, 184301.

96. D. Fragiadakis, S. Dou, R. H. Colby, J. Runt, *J. Chem. Phys.* **2009**, *130*, 064907.

97. I. S. Chronakis, S. Grapenson, A. Jakob, *Polymer (Guildf).* **2006**, *47*, 1597.

98. Y. Zou *et al.*, *ACS Appl. Mater. Interfaces* **2016**, *8*, 12576.

99. T. Bashir *et al.*, *Polym. Sci. - Ser. A* **2017**, *59*, 902.

100. A. A. Khan, R. Hussain, S. Shaheen, *New J. Chem.* **2016**, *40*, 2200.

# 5.10. Supporting information

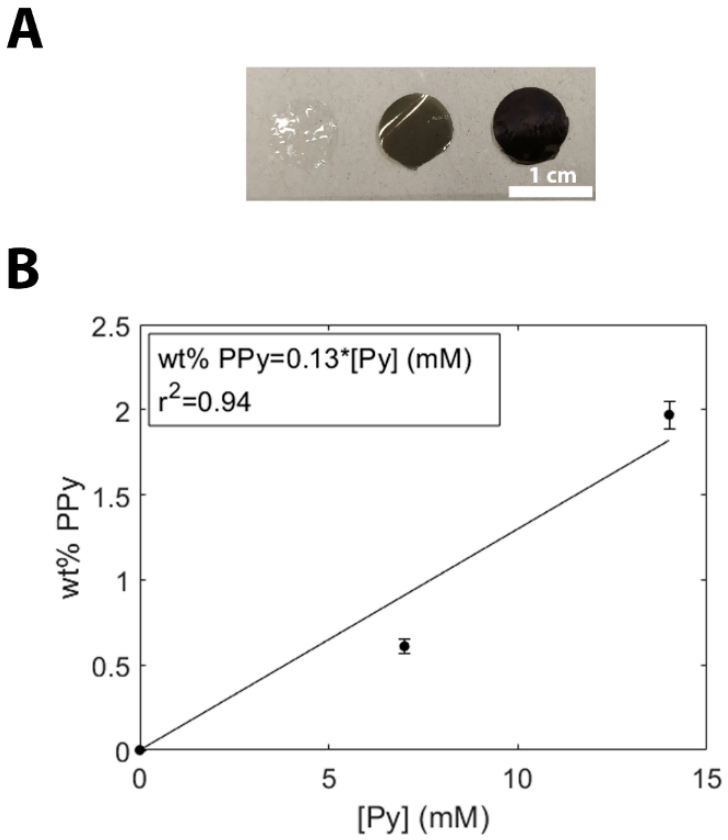


**Figure S1. A**: From left to right, macroscopic images of PLA (CPLA) and PLA-PPy (C1 and C2) casting films. **B**: PPy mass fraction of casting films for the different Py concentrations used in the coating process. A linear relationship between both parameters can be observed.

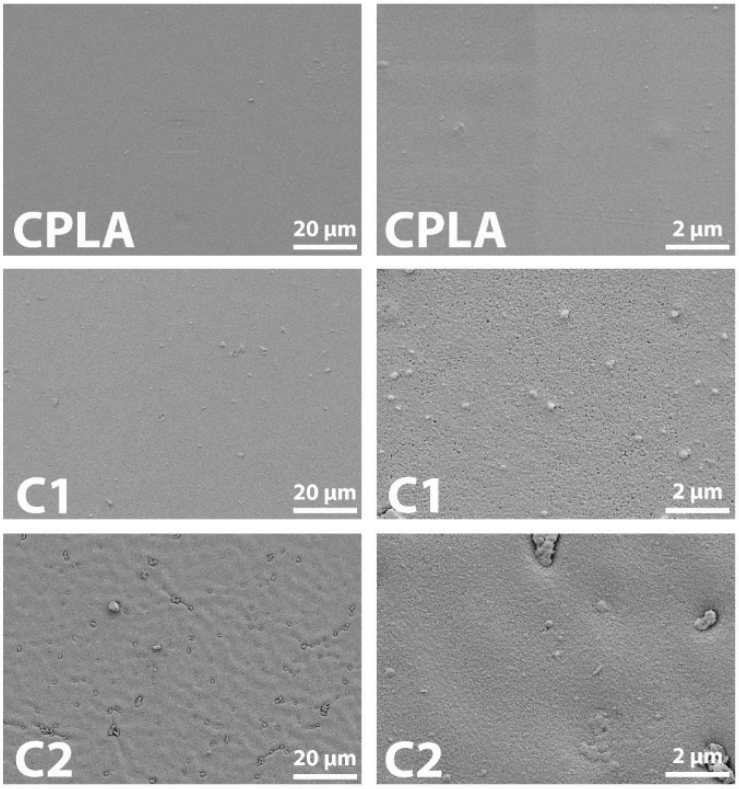


**Figure S2.** FESEM images of PLA (CPLA) and PLA-PPy (C1 and C2) casting films. A flat and smooth surface without porosity can be observed for CPLA, while a rougher surface is observed when the PPy is present (C1 and C2).

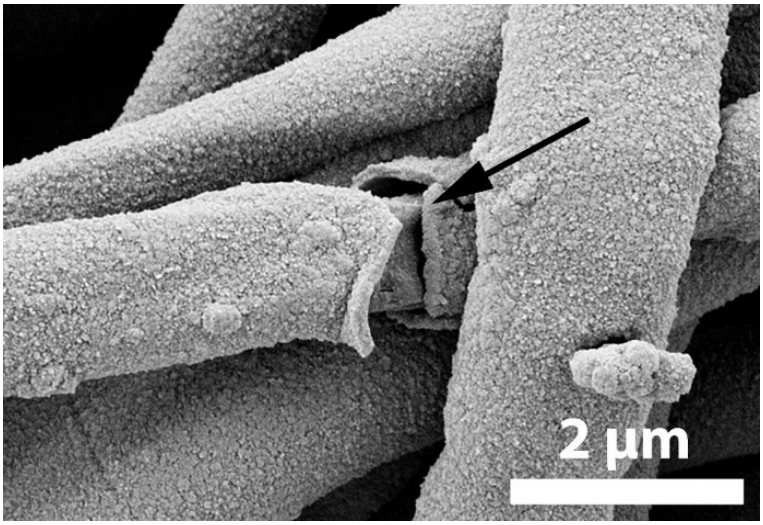


**Figure S3.** Detail of E23 showing a cross-section of the PPy coating, with a thickness of the coating of around 100 nm.

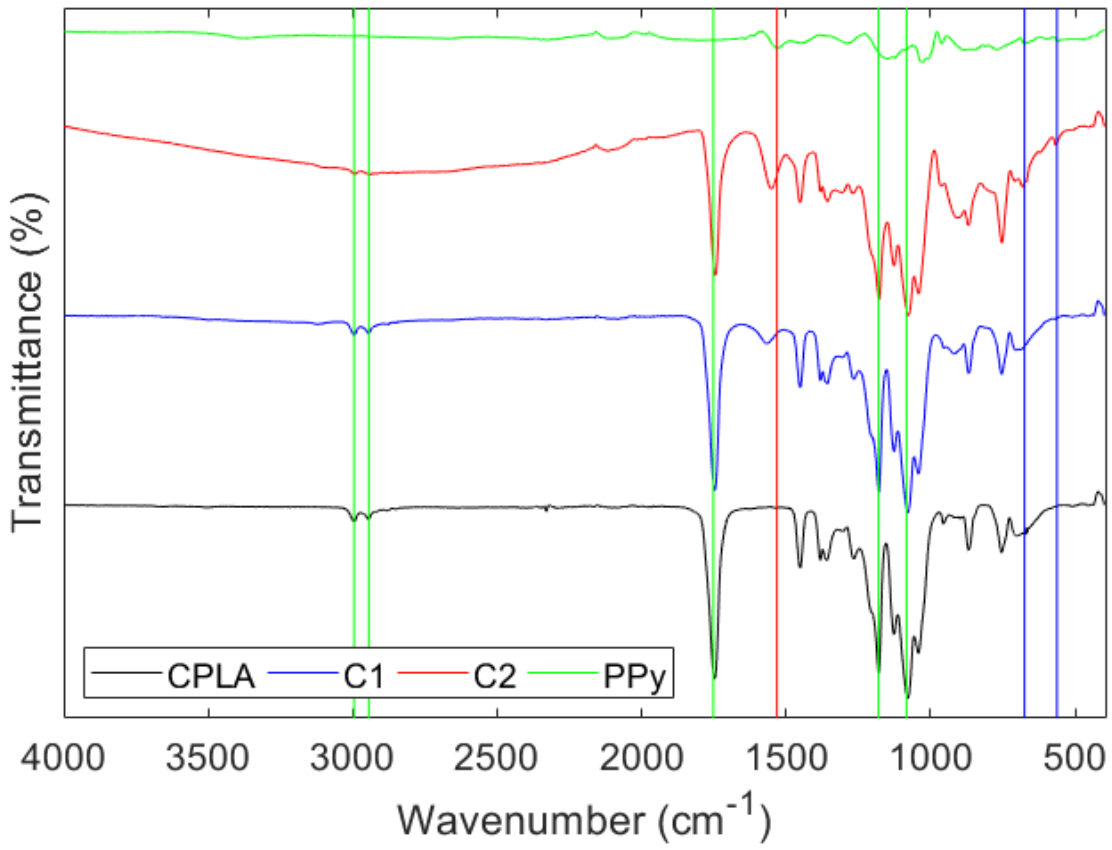


**Figure S4.** FTIR spectra of PLA (CPLA) and PLA-PPy (C1 and C2) casting films, as well as pure PPy. Green, red and blue vertical lines indicate the characteristic peaks of PLA, PPy and pTS, respectively.

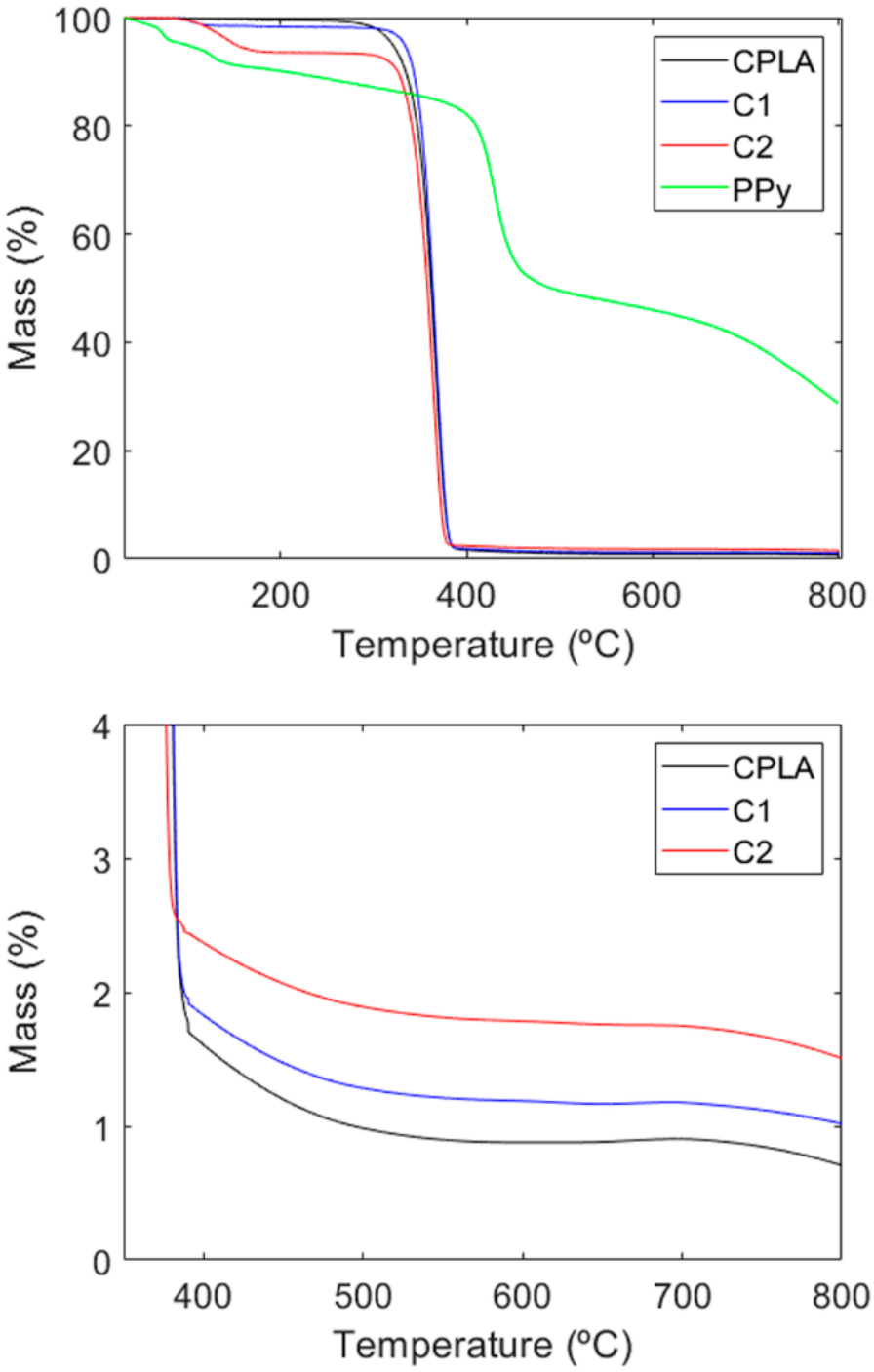


**Figure S5.** TGA of PLA (CPLA) and PLA-PPy (C1 and C2) casting films, as well as pure PPy. Up: Complete graph. Down: Detail of the graph.

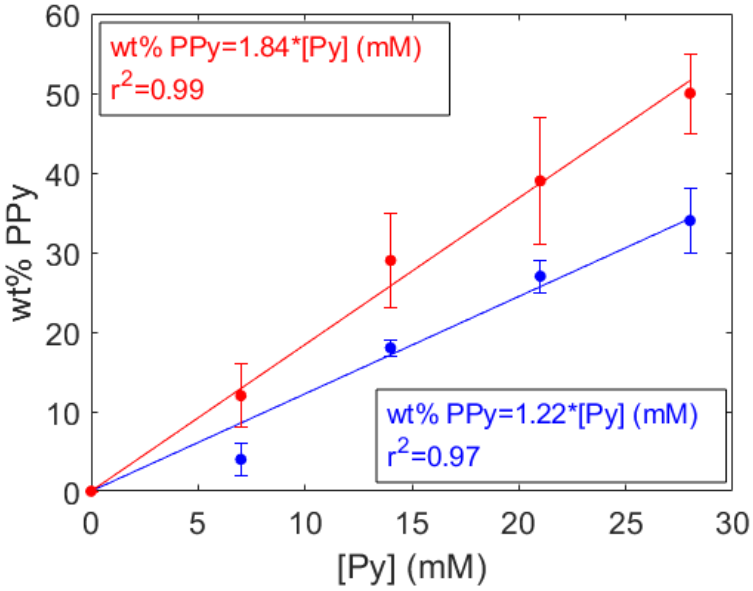


**Figure S6.** Mass fraction of PPy in function of the Py concentration used for the coating obtained by two different methods: weighing the electrospinning membranes before and after the PPy coating (in blue) and using the TGA residues (in red). There is an oversizing of 50% of the mass fraction of PPy when using TGA residues that could be produced by a greater retention of PLA volatiles by the PPy coating.

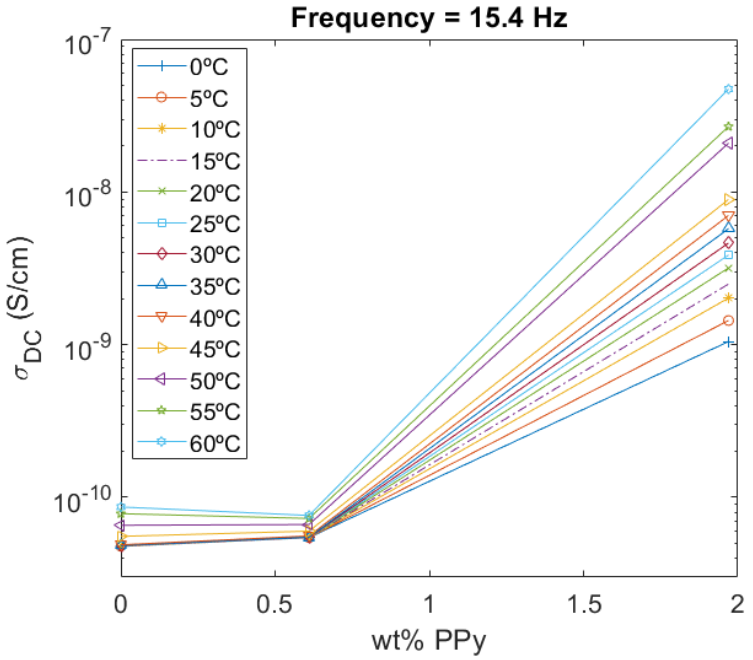


**Figure S7.** Electrical conductivity vs. mass fraction of PPy for PLA (CPLA) and PLA-PPy (C1 and C2) casting films.

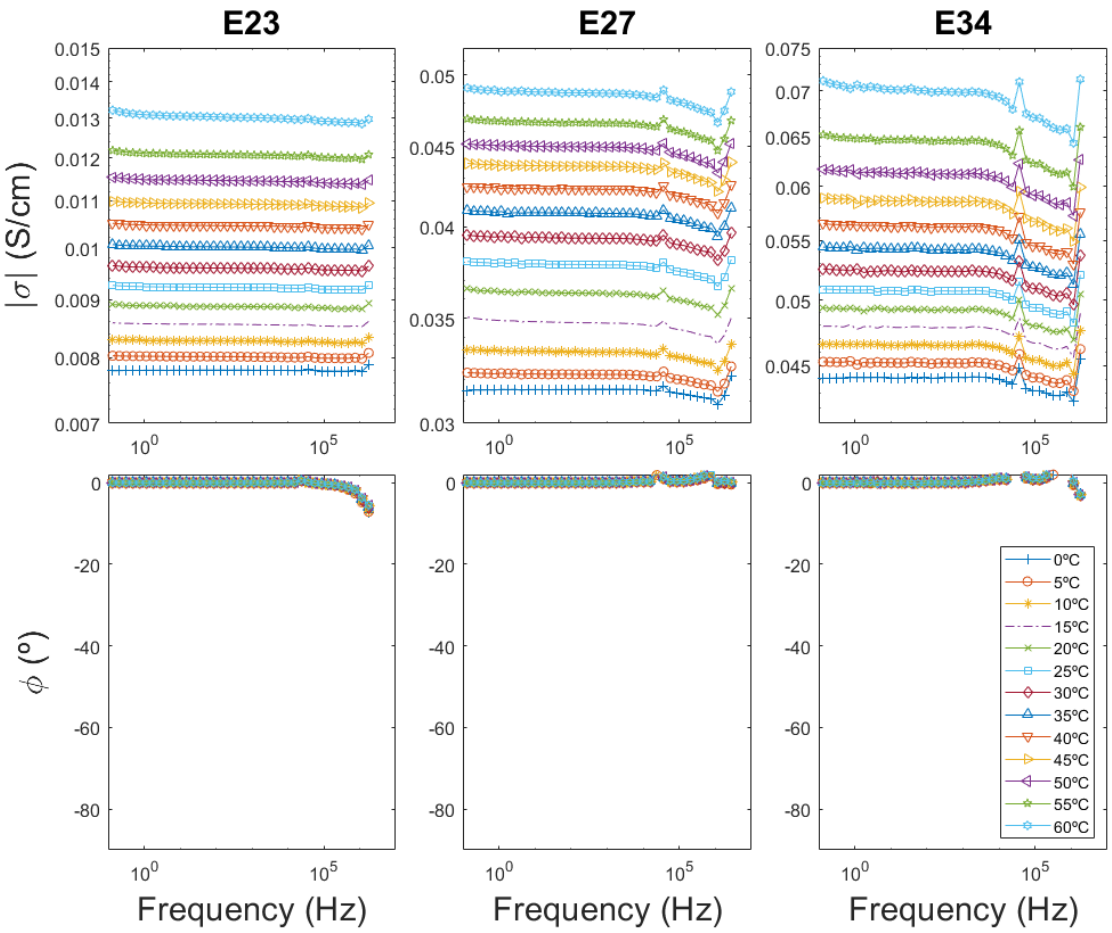


**Figure S8.** Bode diagram for PLA-PPy (E23, E27 and E34) electrospinning membranes.

# 5.11. Addendum

In this section, **Figure 12** and **Figure 13** are included with a logarithmic representation of the conductivity in **Figures 12C**, **12D**, **13B**, **13C** for a better visualization of the percolation phenomenon thanks to which the previous estimation of the percolation threshold data can be improved.

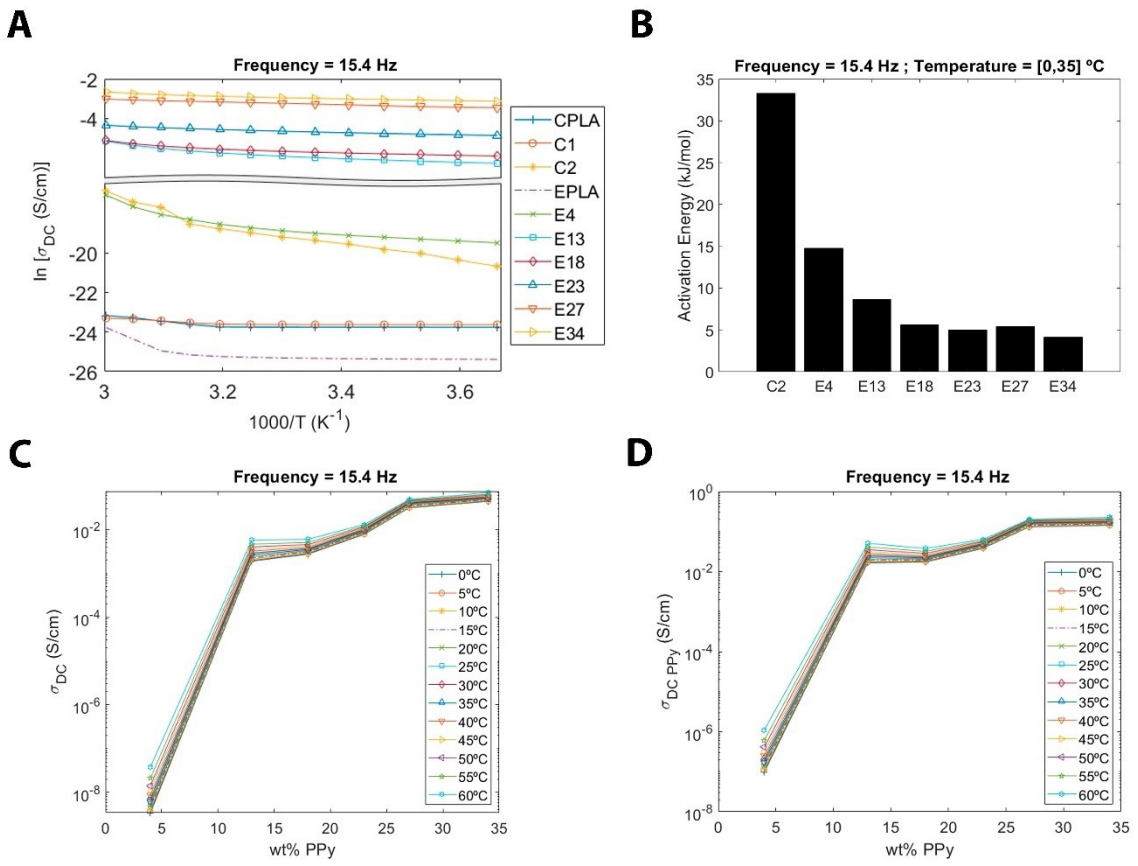


**Figure 12.** Through-plane electrical characterization of PLA-PPy composites. **A**: Arrhenius plot for the DC conductivity obtained from the Bode diagrams for CPLA, C1, C2, EPLA, E4, E13, E18, E23, E27 and E34 (frequency = 15.4 Hz). **B**: Activation energy for C2, E4, E13, E18, E23, E27 and E34 (frequency = 15.4 Hz, temperature = [0, 35] °C). **C**: Electrical conductivity vs. mass fraction of PPy for PLA-PPy electrospun membranes. **D**: PPy electrical conductivity vs. mass fraction of PPy for electrospun membranes.

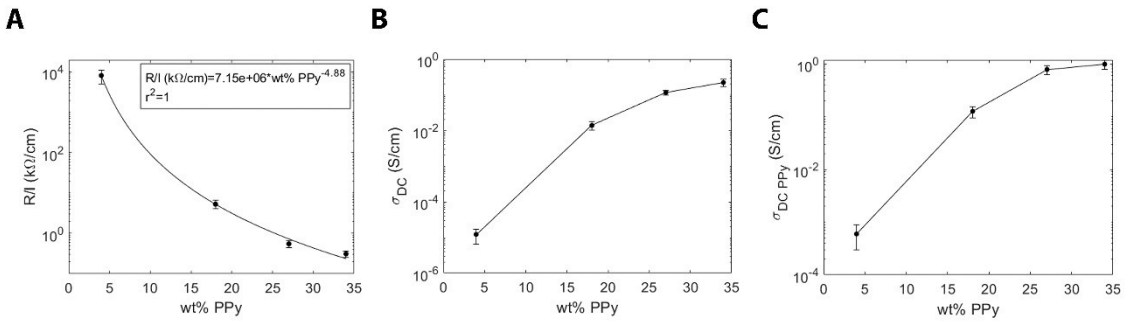


**Figure 13.** In-plane electrical characterization of PLA-PPy electrospun membranes (E4, E18, E27 and E34) at room temperature. **A**: Surface resistance normalized by the distance between contacts. **B**: Electrical conductivity vs. mass fraction of PPy. **C**: PPy conductivity vs. mass fraction of PPy.

# 6. Paper 4: Axonal extension from dorsal root ganglia on fibrillar and highly aligned poly (lactic acid)-polypyrrole substrates obtained by two different techniques: electrospun nanofibres and extruded microfibres

# Axonal extension from dorsal root ganglia on fibrillar and highly aligned poly (lactic acid) - polypyrrole substrates obtained by two different techniques: electrospun nanofibres and extruded microfibres

Fernando Gisbert Roca [a], Jorge Más Estellés [a], [b], Manuel Monleón Pradas [a], [b] and Cristina Martínez-Ramos [a], [c], *

[a] Center for Biomaterials and Tissue Engineering. Universitat Politècnica de València. Camino de Vera s/n, 46022, Valencia, Spain.

[b] CIBER-BBN, Biomedical Research Networking Center in Bioengineering Biomaterials and Nanomedicine, Spain

[c] Universitat Jaume I, Unitat predepartamental de Medicina, Avda/Sos Baynat, s/n, 12071 Castellón de la Plana, Spain

*Corresponding author: Cristina Martínez Ramos. Centro de Biomateriales e Ingeniería Tisular, Universidad Politécnica de Valencia, Camino de Vera s/n E-46022 Valencia, España. Tel.: +34963877000. E-mail: crimarr2@upvnet.upv.es

**Keywords:** polylactic acid, polypyrrole**,** aligned substrates, biological behaviour, Schwann cells, dorsal root ganglia

Published online: 15 November 2020

Reprinted with permission from International Journal of Biological Macromolecules 163 (2020) 1959-1969 

# 6.1. Abstract

The biological behaviour of Schwann cells (SCs) and dorsal root ganglia (DRG) on fibrillar, highly aligned and electroconductive substrates obtained by two different techniques is studied. Mats formed by nanometer-sized fibres of poly(lactic acid) (PLA) are obtained by the electrospinning technique, while bundles formed by micrometer-sized extruded PLA fibres are obtained by grouping microfibres together. Both types of substrates are coated with the electrically conductive polymer polypyrrole (PPy) and their morphological, physical and electrical characterization is carried out. SCs on micrometer-sized substrates show a higher motility and cell-cell interaction, while a higher cell-material interaction with a lower cell motility is observed for nanometer-sized substrates. This higher motility and cell-cell interaction of SCs on the micrometer-sized substrates entails a higher axonal growth from DRG, since the migration of SCs from the DRG body is accelerated and, therefore, the SCs tapestry needed for the axonal growth is formed earlier on the substrate. A higher length and area of the axons is observed for these micrometer-sized substrates, as well as a higher level of axonal sprouting when compared with the nanometer-sized ones. These substrates offer the possibility of being electrically stimulated in different tissue engineering applications of the nervous system.

# 6.2. Introduction

The treatment of injuries both at the central nervous system (CNS) and at the peripheral nervous system (PNS) presents great difficulties since the loss of cells, the creation of neurotoxic environments with axonal growth inhibiting factors and the effect of other partially unknown factors make it very difficult to achieve a functional axonal regeneration, especially at the CNS and at long PNS injuries [1,2]. Therefore, the current

approach for the treatment of nerve injuries is based on multi-combinatorial techniques based on the transplantation of cells seeded on biomaterials capable of both guiding axonal growth and protecting transplanted cells [3,4]. In addition, the application of various types of stimuli (mechanical, electrical and biochemical) has also been widely studied with the aim of improving axonal growth [5–8]. Within this approach, electrically conductive substrates have been used to improve the axonal extension of neurons and induce a greater release of neurotrophins by glial cells when subjected to an exogenous electric field [9,10].

The interaction between cells and biomaterials is mainly based on topographic interactions through adhesion and mechanotransduction signals [11,12]. Therefore, it is of great importance to study the topography of the substrates in order to direct axonal growth towards a target through the mechanical constriction of cells [13,14]. Many studies have concluded that a substrate based on aligned fibres is capable of guiding axonal growth, whereas in a flat substrate such as a glass cover or a substrate with randomly oriented fibres, axons grow unoriented [13–18]. Besides the relevance of having an aligned substrate, the size of the fibres that form the substrate is also critical. Different studies have concluded that the diameter of the fibres that form the substrate is able to influence the biological behaviour in terms of neurite outgrowth, Schwann cell migration and differentiation and proliferation of neural stem cells [19–21]. However, these studies have focused solely on electrospun nanometer-sized fibres, with a maximum diameter of the nanofibres of around 1,000 nm.

Two basic techniques can be used to manufacture poly(lactic acid) aligned fibre substrates, either producing the fibres from a solution by electrospinning, or to employ fibres obtained by mechanical extrusion. The electrospinning technique is based on the electrostatic production of nanofibres by applying electrical forces to a polymer solution

and yields nanofibres with diameters between ten and one thousand nanometers [22,23]. On another hand, fibres obtained by the extrusion technique are larger, typically with diameters in the range between the tens and the hundreds of micrometers [24].

A key role in axonal regeneration is played by glial nerve cells since they supply growth factors and biochemical signals that are necessary for axonal growth [25–30]. Among them the Schwann cells (SCs) stand out because they are essential for neuronal survival and axonal regeneration in the peripheral nervous system [31–33]. SCs are responsible of maintaining the myelin sheath around the axons and secrete different neurotrophic factors like the nerve growth factor (NGF), the brain-derived neurotrophic factor (BDNF) and the neurotrophin-3 (NT-3), among others [31–33]. These neurotrophic factors are essential to create a biochemical environment that favours axonal growth. Furthermore, in the case of injury SCs promote axonal regeneration by forming cell columns (called Büngner bands) that guide the regenerating axons [34,35]. SCs also release cytokines as LIF and IL-6 that promote the survival of neurons [31].

Axon regeneration can also be enhanced through mechanical and electrical stimuli, which has directed attention to electroconductive biomaterials such as electroconductive polymers. Among them, polypyrrole (PPy), polyaniline (PANI) and poly(3,4-ethylenedioxythiophene) (PEDOT) have been well studied. PPy has been widely used in biomedical applications, especially in nerve tissue engineering scaffolds, due to its high electrical conductivity, long-term ambient stability, good biocompatibility, low cost and facile synthesis by chemical or electrochemical polymerization [15,36–43]. It must be considered that PPy is an intractable solid with poor mechanical processability, which limits its direct application to obtain substrates with a specific topography [36]. For that reason, the strategy of coating the surface of other insulating polymers with PPy is interesting in order to exploit both the intrinsic electrical conductivity of PPy and the

better mechanical properties of the insulating host polymer [15,36,44]. We chose poly-L-lactic acid (PLA) as host polymer of the substrates because it is a low cost, renewable, environmentally friendly and biodegradable biomaterial [45,46]. The biocompatibility of both PLA and PPy makes it possible to use PLA-PPy substrates in tissue engineering and biomedical applications [47,48]. In addition, despite PPy is a nonbiodegradable polymer, it has been observed that the PPy coating of PLA substrates do not prevent the biodegradation of PLA and it only could retard slightly its degradation, while the PPy content is low [49–51].

In this study, we compare axonal growth on flat, fibrillar and unidirectional substrates obtained by two different techniques: electrospinning and mechanical extrusion. Thus, fibre sizes of two different orders of magnitude are obtained: nanofibres and microfibres. On the one hand, aligned nanofibre mats were prepared using the electrospinning technique in order to obtain nanometer-sized fibres (approx. 500 nm diameter). On the other hand, 10 μm diameter microfibres were grouped in parallel with polycaprolactone (PCL) fasteners placed in their ends to obtain flat rail shaped microfibre bundles. PCL was used as fastening material for the microfibres bundles due to its low melting point (around 60°C), which facilitated the manufacture of the microfibre bundles. PCL is a biodegradable and biocompatible polymer widely used in biomedical applications as an implantable biomaterial [52,53]. Both kinds of substrates were then coated with the electroconductive polymer PPy.

To study the axonal extension on our substrates, we chose dorsal root ganglia (DRG) as neuron source since the DRG body can be taken as a starting point for the axon's growth from the neuron somas that remain inside the DRG during axon extension. Furthermore, the cells that migrate from the DRG body (mostly SCs) generate a cellular environment that favours axonal extension [19,21]. Thus, flat and highly aligned PPy-

coated PLA substrates were manufactured based on fibrils with diameters of two different orders of magnitude (nanofibres and microfibres), with the goal of studying the influence of this parameter on axonal extension. This study may be of interest to optimize fibre diameter in electroconductive substrates that could find use as part of an electrical stimulation bioreactor and in applications in neural tissue engineering.

# 6.3. Experimental section

## Preparation of nanofibre mats and microfibre bundles

Aligned PLA nanofibre (NF) mats (approximately 500 nm diameter) were obtained by the electrospinning technique. First, PLA (INGEO 40420 RESINEX) (10% wt%) was dissolved in dichloromethane (DCM)/dimethylformamide (DMF) (70/30 v/v) and stirred for 12 hours at room temperature. Then, the solution was introduced into a 12 mL syringe with an internal diameter of 15.77 mm attached to a precision stainless steel needle with 0.15 mm of internal diameter (30G). Aligned nanofibres were obtained by applying a voltage of 20 kV between the needle tip and the collector, maintaining the flow rate at 3 mL/h and collecting the nanofibres during 1.5 hours on a round plate wrapped with an aluminium foil with a diameter of 15.5 cm which centre was located 20 cm from the needle tip and that was rotating at 32 rps. These parameters were chosen from preliminary experiments carried out to establish the optimal conditions (homogeneous fibres, absence of precipitates, etc).

After electrospinning, PLA membranes were air-dried for 2 days and introduced in a desiccator with a fixed vacuum at room temperature for another 2 days. Finally, PLA membranes were introduced between two glass plates subjected to compression and they underwent a tempering process consisting of stove heating at 90°C with 100% of ventilation for 15 min and subsequent cooling at -20°C for 2 hours. With this tempering

process, a stiffening of the PLA membranes was achieved, which prevented them from wrinkling when they were introduced into water.

Aligned PLA microfibre (MF) bundles were obtained by grouping 1,200 PLA microfibres with a diameter of 10 μm (Aitex, Spain). In order to maintain the alignment of the lane-shaped microfibre bundles, they were fastened using PCL bands, which were placed in a solid state on both extremes of the lane and melted by temperature so that, once cooled, the microfibres were attached by the PCL bands.

NF and MF substrates with dimensions of 20 mm x 4 mm (length x width) were used. It should be noted that the auxiliary PCL bands that hold the MFs together are not considered when defining the dimensions of the MF substrates.

## Polypyrrole coating

Both substrates were coated with the electrically conductive polymer PPy via *in situ* polymerization. As a previous step, the substrates were immersed in deionized water under compression and a fixed vacuum was applied until they stopped floating and, therefore, the introduction of water inside the spaces between fibres was achieved, in order to obtain a homogeneous coating of all nano and micro fibres, not only the most superficial ones. Next, each substrate was put into a polypropylene tube with an aqueous solution of pyrrole monomer (Py, Sigma-Aldrich 131709) and sodium para-toluene sulfonate (pTS, Sigma-Aldrich, 152536), followed by ultrasonication for 1 min in order to allow the membrane to be saturated with Py/pTS solution. The substrates were incubated with shaking at 4°C for 1 h. The ratio between the substrate area (length x width) and the final volume of the Py/pTS aqueous solution was 0.6 $cm^2$/mL and the different concentrations of Py and pTS that were used are described in **Table 1**. Then, an aqueous solution of ferric chloride ($FeCl_3$, Sigma-Aldrich 157740) was added and incubated with shaking at 4°C for 24 h for the polymerization and deposition of PPy on

the PLA substrates. The ratio between the substrate area (length x width) and the final volume of the $FeCl_3$ aqueous solution was 0.6 $cm^2$/mL and the different concentrations of $FeCl_3$ that were used are described in **Table 1**. PPy-coated membranes were washed with deionized water with agitation for 10 min for three times and ultrasonicated for 30 min in deionized water for three times. Finally, the membranes were dried in a desiccator with a fixed vacuum at 40°C for 2 days.

| Coating protocol | [Py] (mM) | [pTS] (mM) | [$FeCl_3$] (mM) | Reaction time (h) |
|---|---|---|---|---|
| C1 | 7 | 7 | 19 | 24 |
| C2 | 14 | 14 | 38 | 24 |

**Table 1.** Reaction parameters used for the PPy coating of NF and MF substrates.

## Mass fraction and effective coating thickness of PPy

The mass fraction of PPy ($\omega_{PPy}$) deposited on PLA substrates was measured by weighing them before ($m_0$) and after ($m_f$) the PPy coating using a precision balance (AX205, Mettler-Toledo Inc., sensibility of 0.01 mg) and applying **Equation (1)** (n=3).

$$\omega_{PPy} = \frac{m_{PPy}}{m} = \frac{m_f - m_0}{m_f} \quad (1)$$

The effective coating thickness of PPy (e) was obtained by applying **Equation (2)**, approximating the section of the PPy coating on each fibre to a rectangle due to its low thickness. $V_{PPy}$, $m_{PPy}$ and $\rho_{PPy}$ are the volume, mass and density of PPy, respectively, and r, L and n are the radius, length and number of fibres, respectively.

$$V_{PPy} = \frac{m_{PPy}}{\rho_{PPy}} = 2 \cdot \pi \cdot r \cdot e \cdot L \cdot n \quad (2)$$

The number of NFs ($n_{NF}$), the ratio of the number of fibres ($n_{NF}/n_{MF}$) and the surface area ratio between NF and MF substrates ($S_{NF}/S_{MF}$) were obtained by applying **Equation (3)**, **Equation (4)** and **Equation (5)**, respectively, where $V_{NF}$ is the volume of a NF substrate, $V_{1\,NF}$ is the volume of one NF, $m_{NF}$ is the mass of a NF substrate, $m_{MF}$ is the mass of a MF substrate and $\rho_{PLA}$ is the density of PLA.

$$n_{NF} = \frac{V_{NF}}{V_{1\,NF}} = \frac{\frac{m_{NF}}{\rho_{PLA}}}{\pi \cdot {r_{NF}}^2 \cdot L} \tag{3}$$

$$\frac{n_{NF}}{n_{MF}} = \frac{\frac{n_{NF}}{m_{NF}}}{\frac{n_{MF}}{m_{MF}}} \tag{4}$$

$$\frac{S_{NF}}{S_{MF}} = \frac{2 \cdot \pi \cdot r_{NF} \cdot L \cdot \frac{n_{NF}}{m_{NF}}}{2 \cdot \pi \cdot r_{MF} \cdot L \cdot \frac{n_{MF}}{m_{MF}}} \tag{5}$$

## Morphological characterization by field emission scanning electron microscopy (FESEM)

For the characterization of the surface morphology of membranes, a field emission scanning electron microscope (FESEM; ULTRA 55, ZEISS Oxford Instruments) was used. The preparation of the samples consisted primarily in desiccation under vacuum conditions during the 24 h prior to the test to avoid interferences due to evaporated water. Subsequently, samples were placed on a carbon tape and a carbon bridge was created between the sample and the carbon tape. Finally, samples were coated with a thin layer of platinum. The voltage used was 2 kV.

## Electrical characterization

The electrical behaviour was studied by measuring superficially the circulating electric current (DC) when applying a known voltage, that allowed us to calculate the apparent surface electrical resistance of the materials (R) by Ohm's law. After measuring the distance between contacts (d) and the cross section of the substrates (S), the in-plane apparent DC-conductivity ($\sigma_{DC}$) of the materials was obtained by **Equation (6)** (n=6). By applying **Equation (7)** the conductivity of the PPy coating ($\sigma_{DC\ PPy}$) was also obtained (n=6).

$$\sigma_{DC} = \frac{d}{R \cdot S} \tag{6}$$

$$\sigma_{DC\ PPy} = \frac{d}{R \cdot S_{PPy}} = \frac{d}{R \cdot 2 \cdot \pi \cdot r \cdot e \cdot n} \tag{7}$$

## Substrates sanitization and preconditioning

Before cell seeding, substrates were sanitized by 30 min exposure to UV irradiation (UV lamp, wavelength 254 nm) on each side and immersion in 70% ethanol (ET00021000, Scharlab) for 3 washes of 10 min. Thereafter the ethanol residues were removed by performing 4 washes of 10 min with ultrapure water (Mili-Q®). The preconditioning of the materials was done by immersion in Dulbecco's Modified Eagle Medium with a high glucose level (4.5 g/L) (21331020, Life Technologies) supplemented with 10% of Fetal Bovine Serum (10270- 106/A3381E, Life Technologies) and 1% Penicillin/Streptomycin (15140122, Life Technologies) and incubation at 37°C for 24 h in a humidified atmosphere containing 5% $CO_2$.

## Schwann cells culture

Culture of rat Schwann cells (SCs; P10301, Innoprot) for 5 days (n=3 per group) was performed on NF (PLA-18.2% PPy) and MF (PLA-3.5% PPy) substrates in order to study the cell adhesion and proliferation of glial cells.

After the expansion of the SCs in a cell culture flask, they were washed with PBS and a trypsin/EDTA solution (T/E; 25200-072, Life Technologies) was then added to break the cell-matrix and cell-cell interactions in order to remove the cells from the bottom of the culture bottle. After centrifugation at 1080 rpm for 5 min, the pellet was resuspended in Schwann cell culture medium (P60123, Innoprot). At this moment, the seeding with SCs in passage 7 was performed with a seeding density of 100.000 cells per substrate. Finally, the culture was introduced in an incubator at 37 °C with a humid atmosphere containing 5% $CO_2$ for 5 days, renewing the Schwann cell culture medium every 48 h.

## Dorsal root ganglia culture

DRG from E10 chick embryos (n=5 per group) were cultivated during 3 days on NF (PLA-18.2% PPy) and MF (PLA-3.5% PPy) substrates in order to study the axonal extension on both types of substrates.

DRG were grown for 3 days in Ham F12 culture medium (11765054, Thermo Fisher Scientific) with 1% HEPES 1M (15630049, Thermo Fisher Scientific), 1% L-Glutamine 200 mM (25030024, Thermo Fisher Scientific), 1% N2 supplement (17502048, Thermo Fisher Scientific), 1% Penicillin/Streptomycin (15140122, Life Technologies) and 10 ng/mL of nerve growth factor (NGF) (13257019, Thermo Fisher Scientific).

## Immunostaining of SCs and DRG

For the immunostaining, after removing the cell medium and washing the materials with PBS, cells were fixed with 4% paraformaldehyde (PFA; 47608, Sigma-Aldrich) for 20 min at room temperature. After cell fixation, 3 washes of 10 min with DPBS were performed to remove PFA residues. At this point, the non-specific bindings were blocked and the cell membrane was permeabilized by the use of a blocking buffer composed of DPBS with 3% bovine serum albumin (BSA; A7906, Sigma-Aldrich) and 0.1% Tween20 (P1379, Sigma-Aldrich) for 1 h at room temperature.

On the one hand, SCs were stained with FITC-phalloidin (B607, Life Technologies) at a 1/200 dilution to mark the cytoskeleton actin filaments (green colour) and with DAPI (D9564, Sigma-Aldrich) at a 1/1000 dilution for 10 min to mark the cells' nuclei (blue colour). The imaging was performed using a confocal microscope (LEICA TCS SP5, Leica microsystems).

On the other hand, DRG were stained with TUJ-1 (neuron-specific class III beta-tubulin, Neuromics, MO15013) at a 1/500 dilution in green colour. The imaging was performed using a MacroFluo Fluorescence Magnifier (MZZ16F, Leica microsystems) with Digital Camera (DFC300 FX, Leica microsystems).

## Quantification of axonal extension and axonal sprouting

In order to quantify the axonal extension, two different parameters were obtained (**Figure 1**). On the one hand, the maximum length of axons was measured as the distance between the edge of the DRG body and the end of the longest axon (maximum of both sides and sum of both sides). On the other hand, the area of axons was obtained by subtracting the area of the DRG body from the total area of the DRG. Both parameters were measured using the ImageJ/FIJI image processing software [54].

The DRG images were also processed and analysed using an in-house software developed under MATLAB R2018a (The MathWorks, Inc.) to quantify the axonal sprouting (**Figure 2**). All images of DRG stained with TUJ-1 were cropped to the region of interest and grey scaled. The grey intensity value (0–256) of all pixels in each transversal section (Y-axis, image height) was measured and, thus, the mean value was calculated for each section. The mean data from images were normalized (up to 1) considering 0 and 1 the lowest and highest grey intensity values of the entire image, respectively. The centre of the DRG was obtained as the maximum point of the relative intensity. By representing the relative intensity gradient, the left and right edges of the DRG body were obtained as the maximum and minimum values of the gradient respectively within a window of values.

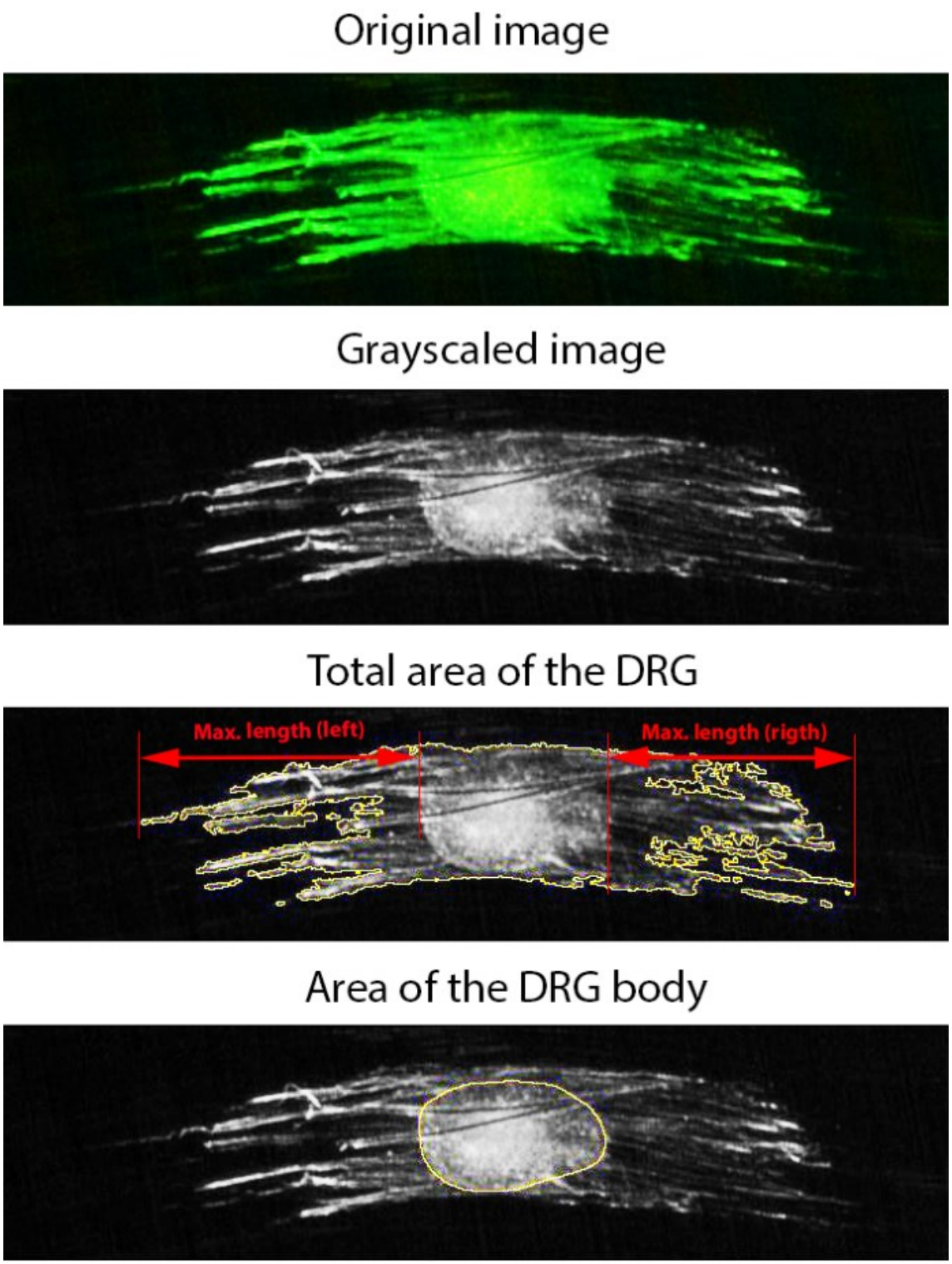


**Figure 1.** Different steps for the quantification of axonal extension of DRG. The maximum length of axons was calculated as the maximum value of both sides and the sum of both sides. The area of axons was obtained by subtracting the area of the DRG body from the total area of the DRG.

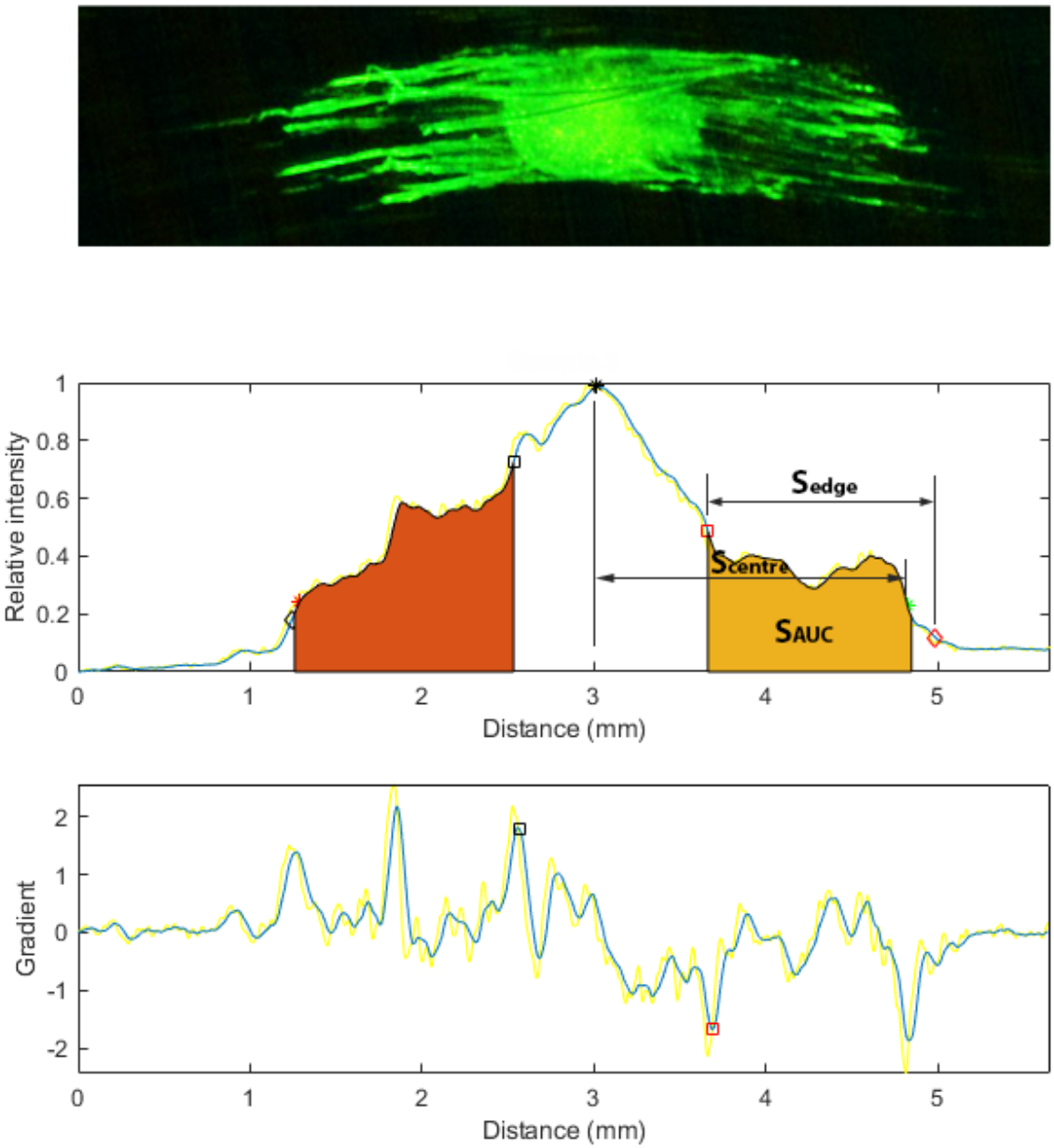


**Figure 2.** Quantification of axonal sprouting from DRG bodies using the relative intensity of the images. The edges of DRG bodies were obtained using the relative intensity gradient. Three parameters were obtained: $S_{centre}$ (Equation (8)), $S_{edge}$ (Equation (9)) and $S_{AUC}$ (Equation (10)). The sum of both sides was considered for each parameter.

Once the centre and edges of the DRG body were marked, three different parameters were obtained to measure axonal sprouting: $S_{centre}$ as the distance between the point that corresponds to the relative intensity of the centre of the DRG body ($I_{centre}$) and the point

where $I_{centre}$ is reduced by 75% $\left(\frac{I_{centre}}{4}\right)$ (**Equation (8)**), $S_{edge}$ as the distance between the point that corresponds to the relative intensity of the edge of the DRG body ($I_{edge}$) and the point where $I_{edge}$ is reduced by 75% $\left(\frac{I_{edge}}{4}\right)$ (**Equation (9)**) and $S_{AUC}$ as the area under the curve (AUC) between the point that corresponds to the relative intensity of the edge of the DRG body ($I_{edge}$) and the point where $I_{centre}$ is reduced by 80% $\left(\frac{I_{centre}}{5}\right)$ (**Equation (10)**). The three parameters were obtained for both the left and right sides and the sum of both values was considered.

$$S_{centre} = Distance\left(I_{centre}, \frac{I_{centre}}{4}\right) \quad (8)$$

$$S_{edge} = Distance\left(I_{edge}, \frac{I_{edge}}{4}\right) \quad (9)$$

$$S_{AUC} = Area\left(I_{edge}, \frac{I_{centre}}{5}\right) \quad (10)$$

## Statistical analysis

Results were expressed as mean ± standard deviation (SD) or as mean ± standard error of the mean (SEM). The statistical analysis of the results was performed with GraphPad Prism® software using the one-way ANOVA test together with a multiple sample mean comparison (Tuckey's multiple comparisons test with a significance degree of 95%) in order to reveal significant differences between conditions. Statistically significant differences are indicated by *, **, *** or ****, indicating a p-value below 0.05, 0.01, 0.001 or 0.0001 respectively.

# 6.4. Results and discussion

## Characterization of NF and MF substrates

On the one hand, macroscopic images of NF and MF substrates are shown in **Figure 3**, before and after the PPy coating using the coating protocol C2. On the other hand, microscopic images of NF and MF substrates are shown in **Figure S1** and **Figure 4**, before and after the PPy coating using the coating protocols C1 and C2, respectively.

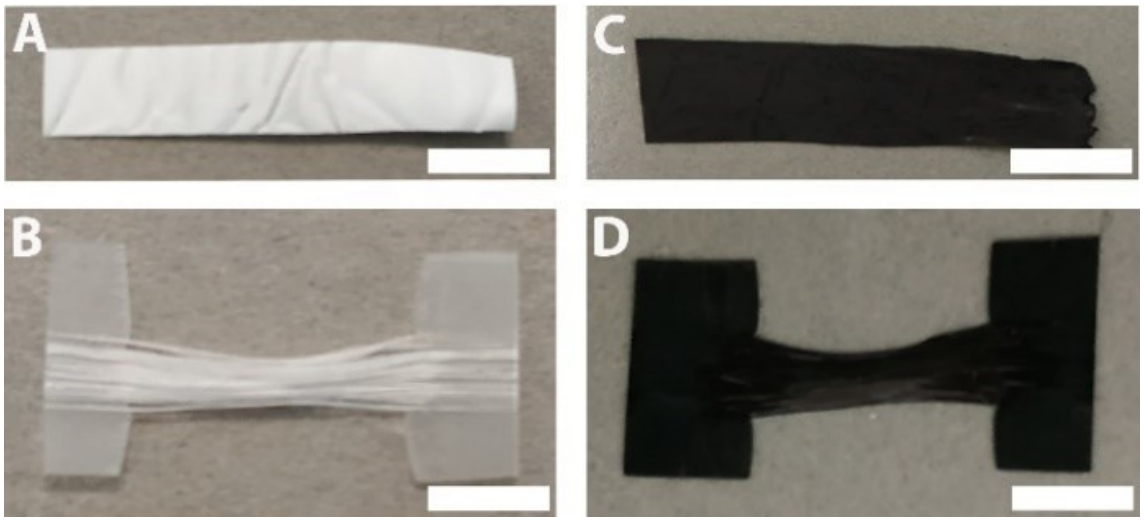


**Figure 3.** Macroscopic images of PLA and PLA-PPy substrates before and after the PPy coating using the coating protocol C2. **A**: PLA NF mat. **B**: PLA MF bundle. **C**: PLA-PPy NF mat. **D**: PLA-PPy MF bundle. At the extremes of the MF bundles (B and D) the auxiliary PCL bands that act as fasteners and hold MFs together can be observed. Scale bar = 5 mm.

When the coating protocol C1 was employed (**Figure S1**), the PPy coating presented several areas where the PPy coating failed to completely cover the fibres, so some parts of the PLA fibres were visible. In addition, the PPy coating had a granular appearance, which indicates that the different PPy grains have not come together to form a continuous layer. All this is indicative of a less homogeneous coating, without forming a continuous layer of PPy in all fibres for the coating protocol C1. However, when the

coating protocol C2 is employed (**Figure 4**), FESEM images of NF (**Figure 4 C, D**) and MF (**Figure 4 G, H**) substrates showed a smooth surface, without non-covered areas and without the grainy appearance that was observed for the coating protocol C1. Therefore, with the coating protocol C2 a continuous (without interruptions or bald spots) and homogeneous (with a uniform coating thickness and without PPy aggregates) PPy coating is obtained.

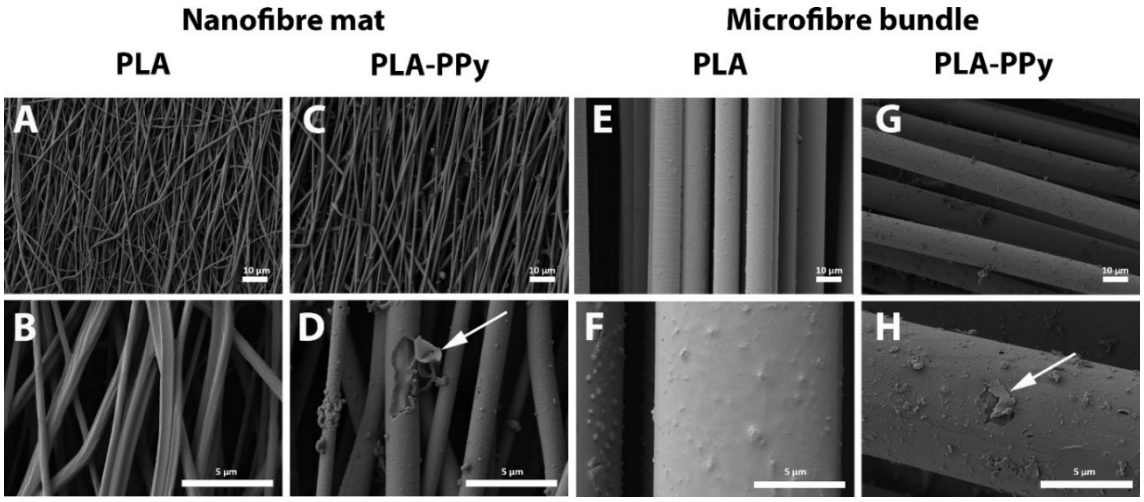


**Figure 4.** FESEM images of PLA and PLA-PPy NF and MF substrates before and after the PPy coating using the coating protocol C2. The arrows in D and H indicate a peeling of the PPy coating allowing its visual appreciation. Scale bar = 10 µm (A, C, E, G) and 5 µm (B, D, F, H).

The mass fraction of PPy for NF and MF substrates coated following the coating protocol C2 was of 18.2% and 3.5%, respectively. Therefore, for the same coating protocol, more PPy was deposited in NF substrates due to their higher surface area and number of fibres $\left(\frac{S_{NF}}{S_{MF}} = 4.8 \pm 0.2; \frac{n_{NF}}{n_{MF}} = 97 \pm 4\right)$, with a higher mass fraction of PPy for NF substrates (**Table 2**). The effective coating thickness of PPy ($e$) was higher for MF substrates, with a ratio between NF and MF substrates $\left(\frac{e_{NF}}{e_{MF}}\right)$ of 0.21, that was obtained by applying **Equation (11)** in the case of substrates with the same mass and length ($m_{NF} = m_{MF},\ L_{NF} = L_{MF}$).

$$\frac{m_{NF}}{m_{MF}} = \frac{V_{NF} \cdot \rho_{PPy}}{V_{MF} \cdot \rho_{PPy}} = \frac{2 \cdot \pi \cdot r_{NF} \cdot e_{NF} \cdot L_{NF} \cdot n_{NF} \cdot \rho_{PPy}}{2 \cdot \pi \cdot r_{MF} \cdot e_{MF} \cdot L_{MF} \cdot n_{MF} \cdot \rho_{PPy}} \quad (11)$$

The electric characterization (**Table 2**) showed that, for the same type of substrate, the greater the mass fraction of PPy the greater the conductivity of the material. For the same coating protocol, similar conductivities were obtained for NF and MF substrates. However, for the same mass fraction of PPy, MF substrates reached higher conductivities due to the lower tortuosity of the path that electric charges must travel, with fewer interfaces. The smaller values obtained for $\sigma_{DC\ PPy}$ when using NF substrates are indicative of this tortuosity of the path.

The ratio between the $\omega_{PPy}/S$ values for NFs and MFs showed values close to 1 for both coating protocols, which is indicative that a homogeneous coating is obtained with few aggregates. However, the high standard deviation obtained for the coating protocol C1 is indicative of a less homogeneous PPy coating which is corrected when the coating protocol C2 is used. This, along with the higher electrical conductivities obtained for the coating protocol C2 led us to choose the substrates coated with this protocol for the following biological characterization of the substrates.

## Schwann cells culture

The culture of SCs (**Figure 5**) showed that the cells were capable of adhering and proliferating in both NF and MF substrates without needing a previous coating of cell adhesive proteins or peptides. The cells were able to completely cover the substrates, without observing a notable difference when PPy was present.

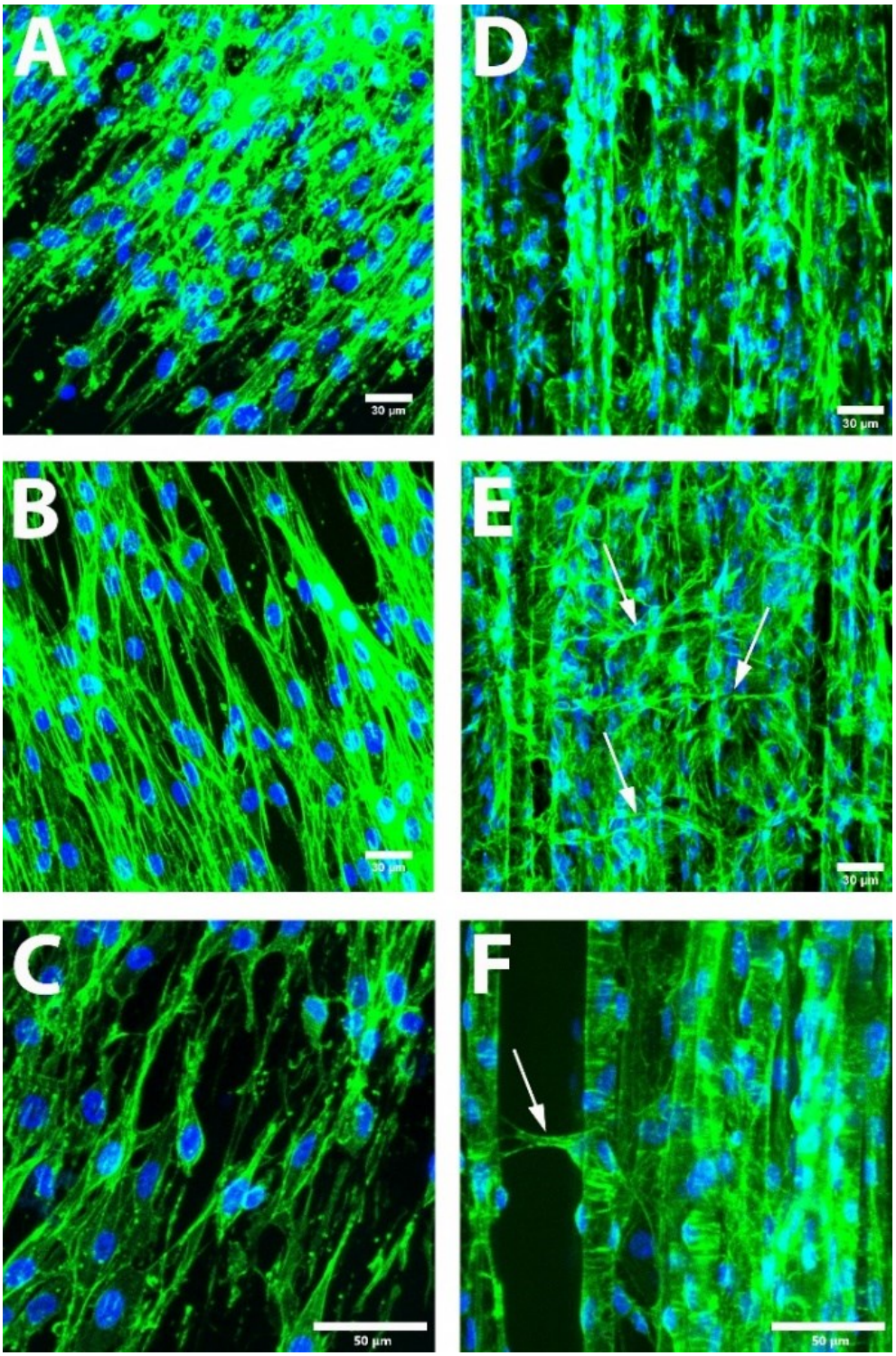


**Figure 5.** Images of SCs after being cultured for 5 days on PLA NF mat (**A**), PLA-PPy NF mat (**B**), PLA MF bundle (**D**) and PLA-PPy MF bundle (**E**). **C** and **F** show detail images of PLA-PPy NF mat and MF bundle, respectively. Cells seeded on NF substrates presented an aligned cytoskeleton in the direction of NFs, while cells seeded on MF substrates did not present a clear orientation, connecting with contiguous MFs (see arrows in E and F). Scale bar = 30 µm (A, B, D, E) and 50 µm (C, F).

On the one hand, SCs seeded on NF substrates (**Figure 5 A, B and C**) presented a very aligned cytoskeleton, clearly oriented in the direction of NFs. Thus, the further expansion of their cytoskeleton takes place preferentially along the direction of the fibril axis, resulting in a highly elongated shape of each cell. The cytoskeleton of the cells presented a high aspect ratio, indicative of a strong cell-material interaction. The cell's cytoplasm wrapped and followed some particular NF, without other cells above it and without connecting other contiguous NFs. Therefore, the use of NFs entailed a higher cell-fibre interaction with a high actin cytoskeleton polarization of the cells, presenting a stretched morphology in the direction of the fibres. This intimate relationship between the cells and the substrate entails a weaker cell-cell interaction and a smaller motility of SCs, as previously observed for electrospun substrates with a small diameter of NFs [19,21].

| Coating protocol | Microfibre bundle | | | | Nanofibre mat | | | | $\frac{\omega_{PPy\,NF}/S_{NF}}{\omega_{PPy\,MF}/S_{MF}}$ |
|---|---|---|---|---|---|---|---|---|---|
| | $\omega_{PPy}$ (%) | e (nm) | $\sigma_{DC}$ (S/m) | $\sigma_{DC\,PPy}$ (S/m) | $\omega_{PPy}$ (%) | e (nm) | $\sigma_{DC}$ (S/m) | $\sigma_{DC\,PPy}$ (S/m) | |
| C1 | 0.9 ± 0.2 | 28 ± 5 | 0.012 ± 0.003 | 23 ± 5 | 4 ± 2 | 5 ± 2 | 0.0012 ± 0.0005 | 0.08 ± 0.05 | 0.9 ± 0.7 |
| C2 | 3.5 ± 0.7 | 122 ± 8 | 1.36 ± 0.08 | 590 ± 35 | 18.2 ± 0.7 | 25 ± 2 | 1.4 ± 0.4 | 21 ± 4 | 1.1 ± 0.3 |

**Table 2.** Physical and electric characterization of PLA-PPy NF and MF substrates. The mass fraction of PPy ($\omega_{PPy}$), the effective coating thickness of PPy ($e$), the DC-conductivity of substrates ($\sigma_{DC}$) and the DC-conductivity of PPy ($\sigma_{DC\,PPy}$) were obtained for MF and NF substrates. Values are expressed as mean ± SD.

On the other hand, the cytoskeleton of SCs seeded on MF substrates (**Figure 5 D, E and F**) did not present any clear orientation and are much less polarised. This results in a way of adhesion more spread of each cell, with much less polarized shape than in the case of nanofibres. As can be observed, the cells presented a more spread cytoskeleton because they were wrapping much bigger fibres and, therefore, they had a much bigger smooth surface for growing radially. In addition, as can be observed in **Figure 5 E** and

F, the nuclei of cells seeded on MFs are much closer to each other, often overlapping. This, together with the greater thickness of the cell mat in the case of MF substrates (26 µm and 38 µm for images 5E and F versus 8 µm and 10 µm for images 5B and C), indicates that cells are arranged in stacks, forming multilayers of cells. Therefore, there is an increase of cell-cell interactions, providing a greater freedom of movement for the cells and, therefore, a greater motility and ability to reorganize than in the case of NFs. For this reason, many cells presented a cytoskeleton that was connecting with other contiguous MFs, growing perpendicular to the direction of the MFs (see arrows in **Figure 5 E** and **F**).

It has been previously observed that cells respond to different physical signals derived of the local geometry of the substrates where they are seeded [55–57]. One of these signals is the substrate curvature, which has a direct effect on the cell's mechanoreceptors [55]. It has been observed that the substrate curvature plays a key role on the cells spreading area, the actin cytoskeleton organization, the focal adhesion points, the filopodia formation and the cell motility and migration [19,21]. As previously reported in the case of electrospun NFs, increasing the diameter of the fibres that form the substrate entails a decrease of actin cytoskeleton organization and fewer focal adhesion points [19,21]. This can be related to the lower organization and alignment of the SCs cytoplasms when MFs were used. In addition, it has also been observed that increasing the fibre diameter in the case of electrospun NFs enhances filopodia formation and increases cell motility and migration [19,21], which can explain the increased cell-cell interactions when MF substrates were used. This is of great importance for axonal extension from DRG because, as previously reported [58,59], SCs first migrate, and then the axons grow and extend on top of the SCs. Therefore, it is critical to use a substrate that enhances the motility and accelerates the migration of SCs

in order to speed up the axonal extension from DRG. This is in accordance with previous studies carried out on electrospun NFs, were a higher SCs migration from DRG was observed when the larger diameters were used, with a direct correlation with axonal extension [19,21].

It was thus shown that aligned NF substrates could guide SCs migration directedly and with a strong cell-biomaterial association, at the price of reducing the freedom of movement and the migration speed of cells. When using MFs with a higher radius of curvature, the cell's freedom of movement and the cell-cell associations were increased, and the SCs had a less polarized cytoskeleton. This increased freedom of movement and motility observed on SCs seeded on MF substrates is critical in order to accelerate the SCs migration from the DRG body and, therefore, to speed up the axonal extension from DRG.

## Quantification of axonal extension and axonal sprouting

To further verify the potential of aligned NF and MF substrates on neuronal cells, DRG were isolated and cultured on four different substrates: PLA and PLA-PPy NF mats; PLA and PLA-PPy MF bundles. TUJ-1 immunofluorescence images of DRG after 3 days of culture on the different substrates are shown in **Figure 6**. As can be observed, the neurites were extended from DRG bodies following the uniaxial alignment of the fibres.

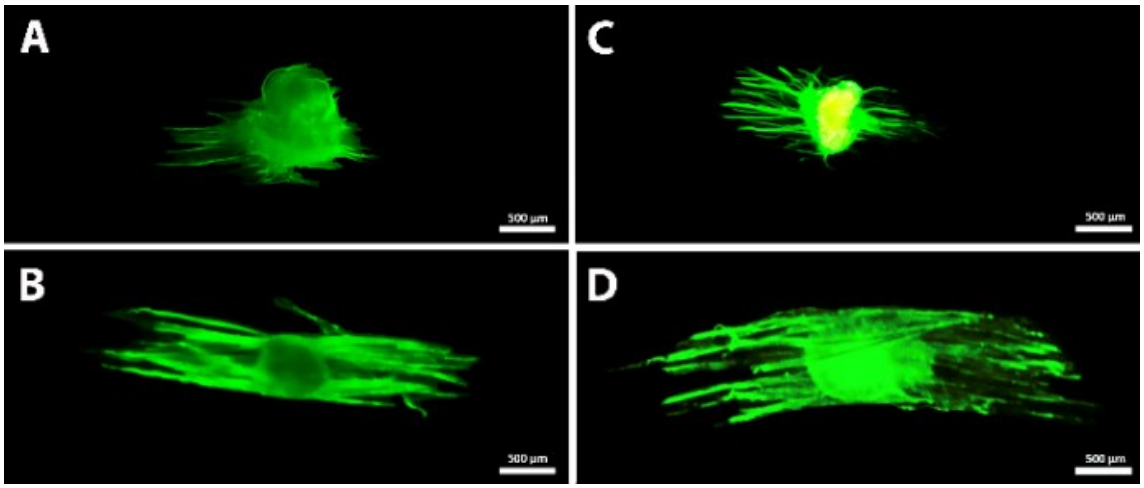


**Figure 6.** Images of DRG after being cultured for 3 days on PLA NF mat (**A**), PLA MF bundle (**B**), PLA-PPy NF mat (**C**) and PLA-PPy MF bundle (**D**). A clear alignment of the axons can be observed in the direction of the fibres, with a higher axonal extension and sprouting when MF substrates were used. Scale bar = 500 µm.

After the quantification of the maximum length and area of axons (**Figure 7**) we observed an increased axonal extension for MF substrates. On the one hand, for PLA MF substrates the maximum length of axons (sum of both sides) increased by a factor of 2.1 and the area of axons increased by a factor of 2.74 versus PLA NF substrates. On the other hand, for PLA-PPy MF substrates the maximum length of axons (sum of both sides) increased by a factor of 2.77 and the area of axons increased by a factor of 3.26 versus PLA-PPy NF substrates.

Regarding axonal sprouting, three different parameters ($S_{centre}$, $S_{edge}$ and $S_{AUC}$) were measured to quantify the growth and density of axons. When MF substrates were used, a clear increase in all the parameters was observed (**Figure 7**), which increased by a factor of 2.71, 4.27 and 5.67 for $S_{centre}$, $S_{edge}$ and $S_{AUC}$, respectively, when PLA-PPy MF substrates were used instead of PLA-PPy NF substrates. Therefore, the axon density of neurons from the DRG was higher on PLA and PLA-PPy MF substrates than on PLA and PLA-PPy NF substrates, with a higher spreading area (**Figure 7**).

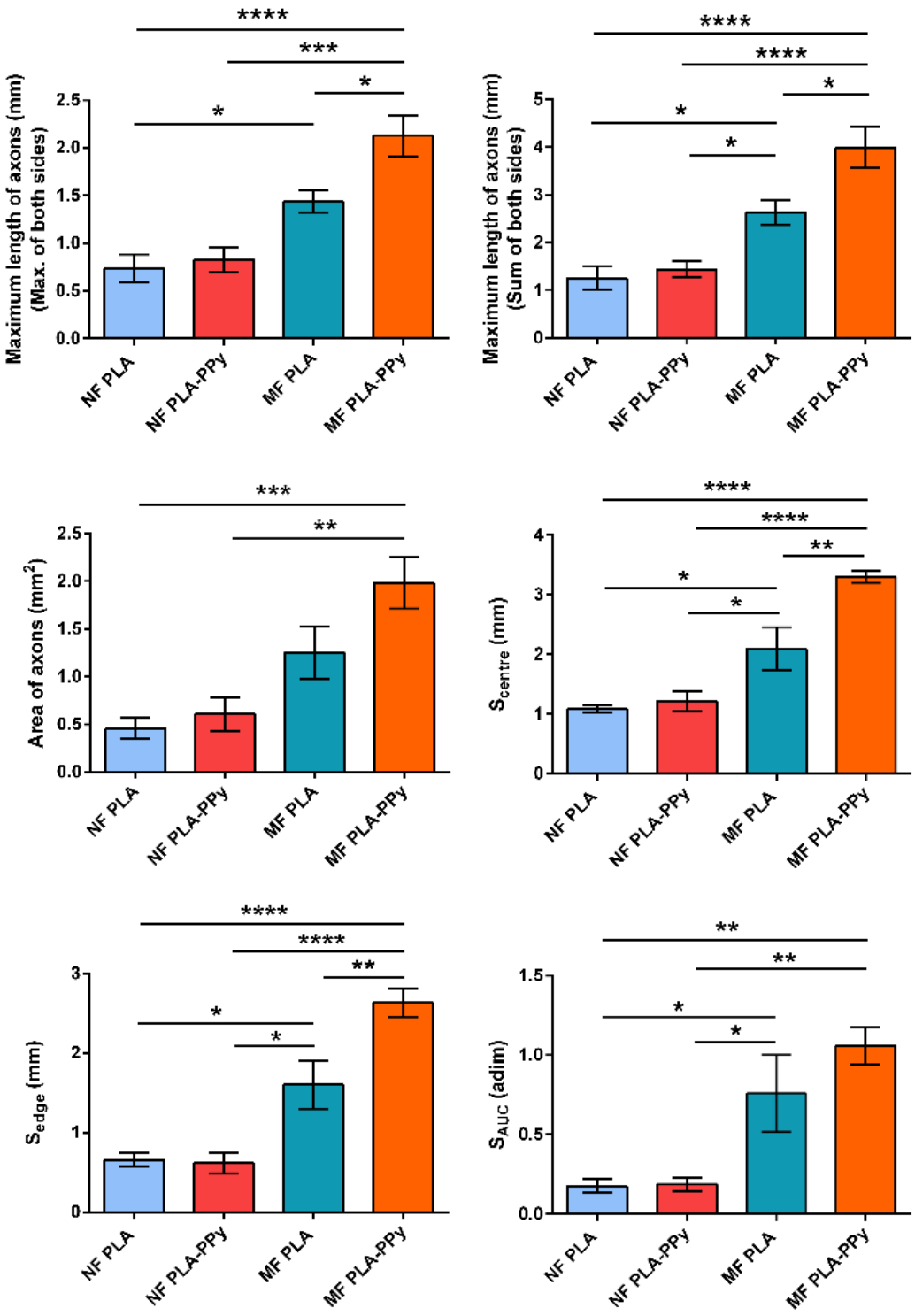


**Figure 7**. Quantification of axonal extension (maximum length of axons and area of axons) and axonal sprouting ($S_{centre}$, $S_{edge}$ and $S_{AUC}$) on different substrates after 3 days of DRG culture. The use of MF substrates enhances both axonal extension and axonal sprouting. In addition, the PPy coating additionally enhances axonal extension and axonal sprouting when MFs are used. Values are expressed as mean ± SEM.

The presence of the PPy coating did not make a statistically significant difference when using NF substrates. However, when MF substrates were used, an increase in all the measured parameters could be observed when PPy was present, becoming statistically significant for the maximum length of axons, $S_{centre}$ and $S_{edge}$. This may be due to the greater surface roughness of the PPy-coated MF substrates, which could favour the DRG adhesion.

The greater axonal growth when MF substrates are used may be directly related to a greater and accelerated migration of SCs from the DRG body. It has been previously reported for electrospun NF substrates that an increase in the diameter of NFs entails a higher motility and migration capacity of SCs [19,21]. This accelerated migration of SCs on microfibre-based substrates is of great importance to speed up axonal extension because, as it has been reported [58,59], the formation of a cellular tapestry on the substrate made by migrating SCs is a necessary prerequisite for axonal extension from the DRG body. Sprouting and extension from the DRG body takes place always accompanied by Scs. It has been previously reported that, in the case of electrospun NFs, the migration distance of SCs from the DRG increases when increasing the diameter of the fibres [19,21]. In addition, it was observed that this migration distance of SCs is directly related to the neurite length, observing an enhanced axon outgrowth when increasing the fibre diameter.

In accordance with the results, the use of MF substrates plays a key role in order to increase the cell's freedom of movement and the cell-cell interactions, which enhances the axonal growth from DRG. The SCs seeded on the NF substrates present a high cell-biomaterial interaction without forming cell stacks, which entails a lower cell motility and migration capacity as well as a fewer number of cells able to interact with the axons. The SCs seeded on MF substrates, by contrast, have a more dynamic behaviour,

forming cell layers with cell-cell interactions dominating over cell-material interactions. This entails a greater ability to reorganize and a higher availability of cells, which can associate with the growing axons, thus increasing the interactions between SCs and axons, which is critical in order to accelerate axonal growth. Therefore, the higher freedom for rearrangement that the migrated SCs have on the MF substrate entails more interactions between SCs and axons, which is critical to enhance axonal growth and survival. With that, we have found an indirect effect of the fibre radii on axonal extension, through the different constraining effect they have on the SCs adhesion configuration on the fibres.

# 6.5. Conclusions

Our experimental data demonstrate the ability to obtain poly(lactic acid)-polypyrrole electrically conductive, biodegradable and biocompatible substrates that can be used in neural tissue engineering for implantable devices applications.

The different biological behaviour of SCs seeded on highly aligned PLA-PPy substrates which differed in diameter have been studied. On nanosized fibres (500 nm diameter) we find that single SCs can completely embrace and surround the circumference of each fibril. By contrast, on microsized fibres (10 μm diameter) the SCs cannot embrace the fibre circumference: the effective curvature radius of the substrate on which they adhere is much larger than in the case of the nanofibrils. Moreover, on microsized fibres the cells can stack on top of each other, probably because their mobility is much less hindered than when they are completely embracing the circumference of nanofibres. Therefore, whereas on NFs the SCs interact essentially with the fibre surface, on MFs we find the cell-fibre but also many cell-cell interactions.

This circumstance seems to be proactive for the extension of axons from the neurons when the DRG explants are seeded on the substrates. We find that axons extend more

rapidly and for larger distances on the microfibered substrate than on the nanofibered ones. We think this is related to the higher migration speed of SCs from the DRG body, since the higher motility that SCs have on the MF substrate accelerates this migration, which is directly related to the axonal extension since it is well known that this extension is accompanied by SCs.

The PPy coating of the PLA substrates resulted in an additional promoting effect on axonal growth, possibly produced by the greater surface roughness that favours the adhesion of the DRG. In addition, the electroconductive coating of the substrates allows its future electrical stimulation to enhance the axonal growth.

## 6.6. Authorship contribution statement

F.G.R.: Methodology, Software, Formal analysis, Investigation, Writing – Original Draft, Visualization. J.M.E.: Writing – Review & Editing, Supervision, Funding acquisition. M.M.P.: Conceptualization, Writing – Review & Editing, Supervision, Funding acquisition. C.M.-R.: Conceptualization, Methodology, Writing - Review & Editing, Supervision, Funding acquisition.

## 6.7. Conflicts of interest

There are no conflicts to declare.

## 6.8. Acknowledgements

The authors acknowledge financing from the Spanish Government's State Research Agency (AEI) through projects DPI2015-72863-EXP and RTI2018-095872-B-C22/ERDF. FGR acknowledges scholarship FPU16/01833 of the Spanish Ministry of Universities. We thank the Electron Microscopy Service at the UPV, where the FESEM images were obtained.

# 6.9. References


1. E. a Huebner, S. M. Strittmatter, *Results Probl. Cell Differ.* **2009**, *48*, 339.
2. K. S. Houschyar *et al.*, *Plast. Surg. Int.* **2016**, *2016*, 1.
3. W. Daly, L. Yao, D. Zeugolis, A. Windebank, A. Pandit, *J. R. Soc. Interface* **2012**, *9*, 202.
4. G. C. W. de Ruiter, M. J. A. Malessy, M. J. Yaszemski, A. J. Windebank, R. J. Spinner, *Neurosurg. Focus* **2009**, *26*, E5.
5. M. D. Tang-Schomer, *Brain Res.* **2018**, *1678*, 288.
6. M. D. Sarker, S. Naghieh, A. D. McInnes, D. J. Schreyer, X. Chen, *Prog. Neurobiol.* **2018**, *171*, 125.
7. I. A. Kim *et al.*, *J. Biosci. Bioeng.* **2006**, *101*, 120.
8. A. W. English, G. Schwartz, W. Meador, M. J. Sabatier, A. Mulligan, *Dev. Neurobiol.* **2007**, *67*, 158.
9. C. E. Schmidt, V. R. Shastri, J. P. Vacanti, R. Langer, *Proc. Natl. Acad. Sci. U. S. A.* **1997**, *94*, 8948.
10. J. Huang, Z. Ye, X. Hu, L. Lu, Z. Luo, *Glia* **2010**, *58*, 622.
11. P. M. Tsimbouri, L. E. McNamara, E. V. Alakpa, M. J. Dalby, L. A. Turner, *Tissue Eng. Second Ed.* **2014**, doi:10.1016/B978-0-12-420145-3.00007-9.
12. H. Amani *et al.*, *Adv. Mater. Interfaces* **2019**, *6*, 1.
13. W. Zhu, F. Masood, J. O'Brien, L. G. Zhang, *Nanomedicine Nanotechnology, Biol. Med.* **2015**, *11*, 693.
14. Y. S. Lee, G. Collins, T. Livingston Arinzeh, *Acta Biomater.* **2011**, *7*, 3877.
15. J. Y. Lee, C. A. Bashur, A. S. Goldstein, C. E. Schmidt, *Biomaterials* **2009**, *30*, 4325.
16. Y. Wang *et al.*, *Chin. Med. J. (Engl).* **2011**, *124*, 2361.

17. Y. Zou *et al.*, *ACS Appl. Mater. Interfaces* **2016**, *8*, 12576.

18. Y. Xu, Z. Huang, X. Pu, G. Yin, J. Zhang, *Cell Prolif.* **2019**, *52*, 1.

19. H. B. Wang, M. E. Mullins, J. M. Cregg, C. W. McCarthy, R. J. Gilbert, *Acta Biomater.* **2010**, *6*, 2970.

20. G. T. Christopherson, H. Song, H. Q. Mao, *Biomaterials* **2009**, *30*, 556.

21. S. Gnavi *et al.*, *Mater. Sci. Eng. C* **2015**, *48*, 620.

22. N. Bhardwaj, S. C. Kundu, *Biotechnol. Adv.* **2010**, *28*, 325.

23. S. Agarwal, J. H. Wendorff, A. Greiner, *Polymer (Guildf).* **2008**, *49*, 5603.

24. T. Karthik, *Synth. Fibres* **2004**, *33*, 5.

25. A. Markus, T. D. Patel, W. D. Snider, *Curr. Opin. Neurobiol.* **2002**, *12*, 523.

26. P. Lu, M. H. Tuszynski, *Exp. Neurol.* **2008**, *209*, 313.

27. M. Lykissas, A. Batistatou, K. Charalabopoulos, A. Beris, *Curr. Neurovasc. Res.* **2007**, *4*, 143.

28. B. S. Bregman, M. McAtee, H. N. Dai, P. L. Kuhn, *Exp. Neurol.* **1997**, *148*, 475.

29. M. R. Freeman, *Curr. Opin. Neurobiol.* **2006**, *16*, 119.

30. E. Pompili *et al.*, *Eur. J. Histochem.* **2020**, *64*.

31. N. El Seblani, A. S. Welleford, J. E. Quintero, C. G. van Horne, G. A. Gerhardt, *J. Neurosci. Methods* **2020**, *335*, 108623.

32. K. R. Jessen, P. Arthur-Farraj, *Glia* **2019**, *67*, 421.

33. G. Nocera, C. Jacob, *Cell. Mol. Life Sci.* **2020**, 1, doi:10.1007/s00018-020-03516-9.

34. K. R. Jessen, R. Mirsky, A. C. Lloyd, *Cold Spring Harb. Perspect. Biol.* **2015**, *7*, 1.

35. J. A. Gomez-Sanchez *et al.*, *J. Neurosci.* **2017**, *37*, 9086.

36. L. X. Wang, X. G. Li, Y. L. Yang, *React. Funct. Polym.* **2001**, *47*, 125.

37. T. H. Le, Y. Kim, H. Yoon, *Polymers (Basel).* **2017**, *9*.

38. M. Mattioli-Belmonte *et al.*, *Mater. Sci. Eng. C* **2005**, *25*, 43.

39. G. Sabouraud, S. Sadki, N. Brodie, *Chem. Soc. Rev.* **2000**, *29*, 283.

40. C. Li, H. Bai, G. Shi, *Chem. Soc. Rev.* **2009**, *38*, 2397.

41. S. Aznar-Cervantes *et al.*, *Bioelectrochemistry* **2012**, *85*, 36.

42. J. F. Zhou *et al.*, *Neural Regen. Res.* **2016**, *11*, 1644.

43. P. M. George *et al.*, *Biomaterials* **2005**, *26*, 3511.

44. A. Esfandiari, *World Appl. Sci. J.* **2008**, *3*, 470.

45. D. E. Henton, P. Gruber, J. Lunt, J. Randall, *Nat. Fibers, Biopolym. Biocomposites* **2005**, *48674*, 527.

46. J. Lunt, *Polym. Degrad. Stab.* **1998**, *3910*, 145.

47. Y. Ramot, M. Haim-Zada, A. J. Domb, A. Nyska, *Adv. Drug Deliv. Rev.* **2016**, *107*, 153.

48. D. da Silva *et al.*, *Chem. Eng. J.* **2018**, *340*, 9.

49. Y. Wan, D. Wen, *J. Memb. Sci.* **2005**, *246*, 193.

50. G. Shi, M. Rouabhia, Z. Wang, L. H. Dao, Z. Zhang, *Biomaterials* **2004**, *25*, 2477.

51. Z. Wang *et al.*, *J. Biomed. Mater. Res. - Part A* **2004**, *70*, 28.

52. M. A. Woodruff, D. W. Hutmacher, *Prog. Polym. Sci.* **2010**, *35*, 1217.

53. C. X. F. Lam, D. W. Hutmacher, J. T. Schantz, M. A. Woodruff, S. H. Teoh, *J. Biomed. Mater. Res. A* **2009**, *90*, 906.

54. J. Schindelin *et al.*, *Nat. Methods* **2012**, *9*, 676.

55. S. J. P. Callens, R. J. C. Uyttendaele, L. E. Fratila-Apachitei, A. A. Zadpoor, *Biomaterials* **2020**, *232*, 119739.

56. C. G. Rolli *et al.*, *Biomaterials* **2012**, *33*, 2409.

57. K. Doxzen *et al.*, *Integr. Biol.* **2013**, *5*, 1026.

58. Y. tae Kim, V. K. Haftel, S. Kumar, R. V. Bellamkonda, *Biomaterials* **2008**, *29*, 3117.

59. E. Schnell *et al.*, *Biomaterials* **2007**, *28*, 3012.

# 6.10. Supporting information

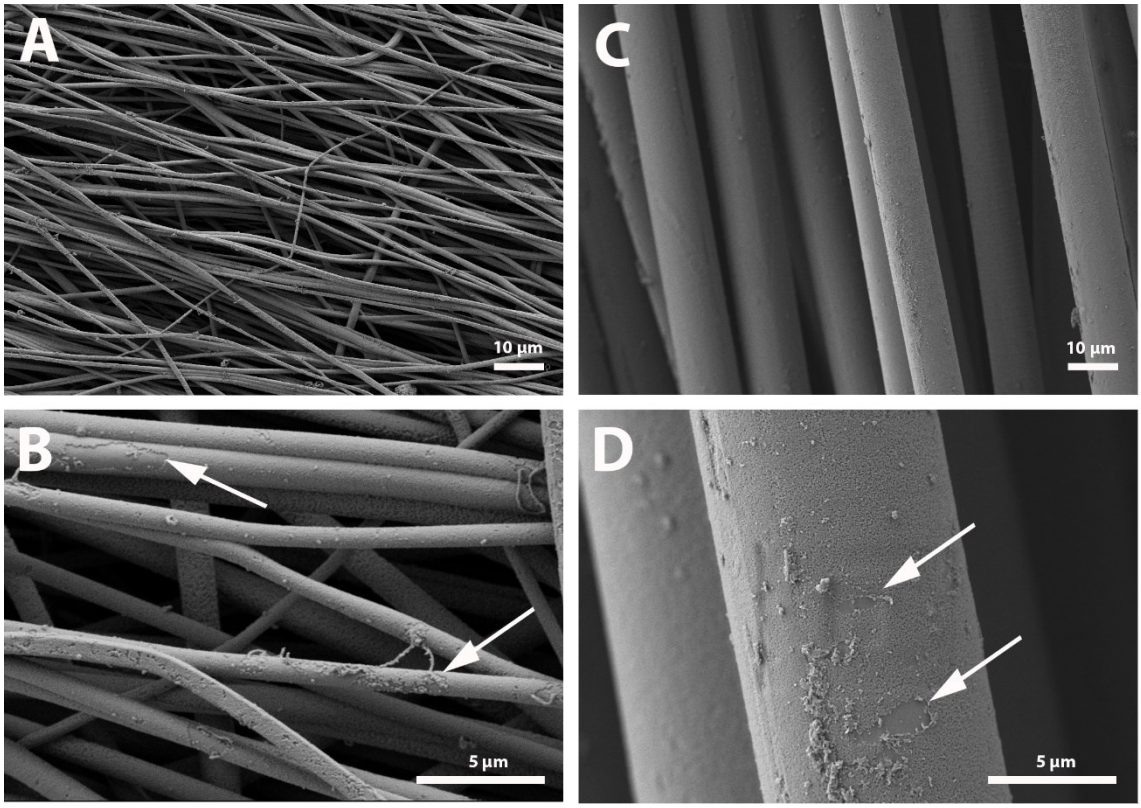


**Figure S1.** FESEM images of PLA-PPy NF (**A** and **B**) and MF (**C** and **D**) substrates after the PPy coating using the coating protocol C1. The arrows in B and D indicate areas where the PPy coating fails to completely coat the fibres, leading to an inhomogeneous coating. Scale bar = 10 µm (A and C) and 5 µm (B and D).

# 7. Paper 5: Electrical stimulation increases axonal growth from dorsal root ganglia co-cultured with Schwann cells in highly aligned PLA-PPy-Au microfiber substrates

# Electrical stimulation increases axonal growth from dorsal root ganglia co-cultured with Schwann cells in highly aligned PLA-PPy-Au microfiber substrates

Fernando Gisbert Roca [a], *, Sara Serrano Requena [a], Manuel Monleón Pradas [a], [b] Cristina Martínez-Ramos [a], [c]

[a] Center for Biomaterials and Tissue Engineering. Universitat Politècnica de València. Camino de Vera s/n, 46022, Valencia, Spain.

[b] CIBER-BBN, Biomedical Research Networking Center in Bioengineering Biomaterials and Nanomedicine, Spain

[c] Universitat Jaume I, Unitat predepartamental de Medicina, Avda/Sos Baynat, s/n, 12071 Castellón de la Plana, Spain

*Corresponding author: Fernando Gisbert Roca. Center for Biomaterials and Tissue Engineering, Universitat Politècnica de València, Camino de Vera s/n E-46022 Valencia, España. Tel.: +34963877000. E-mail: ferrogi1@upv.es

**Keywords:** electrical stimulation; alternating current; axonal growth; aligned substrates; polylactic acid; polypyrrole; Schwann cells

Published online: 7 June 2022

Reprinted with permission from International Journal of Molecular Sciences 2022, 23, 6362 

# 7.1. Abstract

Nerve regeneration is a slow process that needs to be guided for distances greater than 5 mm. For this reason, different strategies are being studied to guide axonal growth and accelerate the axonal growth rate. In this study, we employ an electroconductive fibrillar substrate that is able to topographically guide axonal growth while accelerating the axonal growth rate when subjected to an exogenous electric field. Dorsal root ganglia were seeded in co-culture with Schwann cells on a substrate of polylactic acid microfibers coated with the electroconductive polymer polypyrrole, adding gold microfibers to increase its electrical conductivity. The substrate is capable of guiding axonal growth in a highly aligned manner and, when subjected to an electrical stimulation, an improvement in axonal growth is observed. As a result, an increase in the maximum length of the axons of 19.2% and an increase in the area occupied by the axons of 40% were obtained. In addition, an upregulation of the genes related to axon guidance, axogenesis, Schwann cells, proliferation and neurotrophins was observed for the electrically stimulated group. Therefore, our device is a good candidate for nerve regeneration therapies.

# 7.2. Introduction

Nervous system regeneration involves great challenges due to its scarce intrinsic repair and needs to be guided when the injury is longer than 5 mm to achieve a successful regeneration [1]. For this reason, substrates with different topographic cues have been studied, with the aim of guiding axonal growth and thus preventing axons from growing randomly [2,3]. One of these strategies consists of the use of highly aligned fibrillar substrates, which guide axonal growth in the direction of the fibers [2–7]. In this study we have employed a substrate based on highly aligned polylactic acid (PLA)

microfibers for this purpose. PLA is a synthetic polymer that has been proven to be biocompatible, biodegradable and bioabsorbable in the human body [8–11]. It has been widely employed in tissue engineering as it safely degrades along the same metabolic pathway as lactic acid [12], being approved by the U.S. Food and Drug Administration (FDA) [13–15]. PLA substrates based on aligned microfibers have been shown to highly support neural stem cell culture and improve neurite growth, guiding axonal growth in an aligned direction [16]. In addition, an increase in axonal growth and extension has been previously observed when microfiber-based substrates are employed instead of nanofiber-based ones [17]. Due to these properties of PLA and the positively developed studies in the field of nerve regeneration, this material has been chosen for the present work.

One of the major problems with nerve regeneration is that it is a very slow process, with an average rate of axonal growth of 1 mm/day that cannot sustain itself for more than 12 months [18–20]. For this reason, different strategies have been studied to accelerate axonal growth. One of these strategies is electrical stimulation employing electrically conductive substrates, which have shown to increase the axonal extension of neurons and to induce a higher release of neurotrophins by glial cells when subjected to an exogenous electric field [21,22], supporting the idea that electrical stimulation plays a very important role in promoting nerve regeneration. For this reason, here the PLA microfibers are coated with the electroconductive polymer polypyrrole (PPy). PPy presents a good biocompatibility both *in vitro* and *in vivo*, good chemical stability, long-term ambient stability and high electrical conductivity under physiological conditions [23]. In addition, it can be easily synthesized by chemical or electrochemical polymerization with different porosities and surfaces [24–27], which makes it an ideal material for biomedical applications [23,28]. PPy has been widely employed in biomedical

applications, particularly in nerve tissue engineering, exploiting its good biocompatibility and high electrical conductivity [4,24,27,29–32]. PPy has shown to improve the axonal extension of neurons, favour cell adhesion and induce a greater secretion of growth factors by glial cells when subjected to an exogenous electric field [6,33–35]. Another electrically conductive material that is employed in this work is gold (Au). It is chemically inert with low chemisorption capacity [36,37]. The use of gold as a biomaterial for nerve regeneration has recently increased, usually conjugated with other materials [38,39]. Au has been employed for the stimulation and modulation of neural activity with different applications, such as improving cell growth [38]. Furthermore, Au presents a good biocompatibility when in contact with body fluids and tissues, as well as adequate characteristics to avoid immunogenic reactions [36,37].

In this study, PLA-PPy-Au microfiber substrates were employed for the cell culture of Schwann cells (SCs) and dorsal root ganglia (DRG) to demonstrate the regenerative effects of electrical stimulation. A key role in axonal regeneration is played by glial nerve cells, since they supply growth factors and biochemical signals that are necessary for axonal growth [40–45]. Among them, SCs stand out because they are essential for neuronal survival and axonal regeneration in the peripheral nervous system [46–48]. SCs are responsible of maintaining the myelin sheath around the axons and secrete different neurotrophic factors such as nerve growth factor (NGF), brain-derived neurotrophic factor (BDNF) and neurotrophin-3 (NT-3), among others [46–48]. These neurotrophic factors are essential to create a biochemical environment that favours axonal growth. Furthermore, in the case of injury, SCs promote axonal regeneration by forming cell columns, called Büngner bands, that guide the regenerating axons [49,50]. SCs also release cytokines, such as LIF and IL-6, that promote the survival of neurons [46].

The aim of this work is to obtain highly aligned electroconductive PLA-PPy-Au microfiber substrates and characterize their physicochemical and electric properties, as well as their biological validity, to increase axonal growth and sprouting when subjected to an exogenous electric field. For this, a bioreactor was designed and manufactured to arrange the PLA-PPy-Au microfiber substrate at the bottom of the culture wells with a highly aligned and flat arrangement. To take advantage of the electroconductivity of PLA-PPy-Au substrates, the bioreactor was designed in such a way that it was possible to establish an electrical contact between the electrodes and the substrate outside the culture well, thus avoiding the direct contact of the electrodes with the culture medium. With this starting point, the goal of this work is to study if, by means of the electrical stimulation of the developed electroconductive substrates, a beneficial effect can be obtained on the axonal growth and sprouting of the neurons present in the DRG body, exploring its suitability as an electroconductive bioactive substrate for nerve regeneration applications.

# 7.3. Results and discussion

## Stability and degradation study of PLA-PPy microfibers

In this work, substrates made of highly aligned PLA microfibers were coated with the electrically conductive polymer polypyrrole (PPy) via in situ polymerization with a mass fraction of PPy of 3.5% (**Figure S1**). In previous studies [17,51], it was observed by scanning electron microscopy that these PLA-PPy substrates showed a continuous and homogeneous PPy coating with a fine grain texture. Only small PPy aggregates were observed and most of them disappeared with repeated washing, so this coating protocol with PPy was applied.

To verify the stability of the electrical conductivity of the PLA-PPy microfibers, the conductivity of the samples stored under atmospheric conditions and under vacuum conditions was monitored for 35 days. As can be seen in **Figure 1**, a loss of conductivity of the PLA-PPy microfibers was observed in both conditions. However, a significant difference was observed between both storage conditions. The samples stored under atmospheric conditions suffered a greater loss of conductivity, losing 30 ± 4% of conductivity after 35 days, while samples stored under vacuum conditions only suffered a 11 ± 2% loss of conductivity after 35 days, which is a small loss in a relatively long time. These results indicate that storing the PLA-PPy microfibers in vacuum conditions protects them against environmental agents that produce oxidation effects that affect the conductive properties of the PPy coating. Therefore, the PLA-PPy microfibers employed in the following experiments were stored under vacuum conditions to increase the stability of the PPy coating. However, it was decided to reduce the storage time of the samples as much as possible, never exceeding 5 days. Furthermore, the short duration of the experiments (4 days) meant that the conductivity loss was only around 5%.

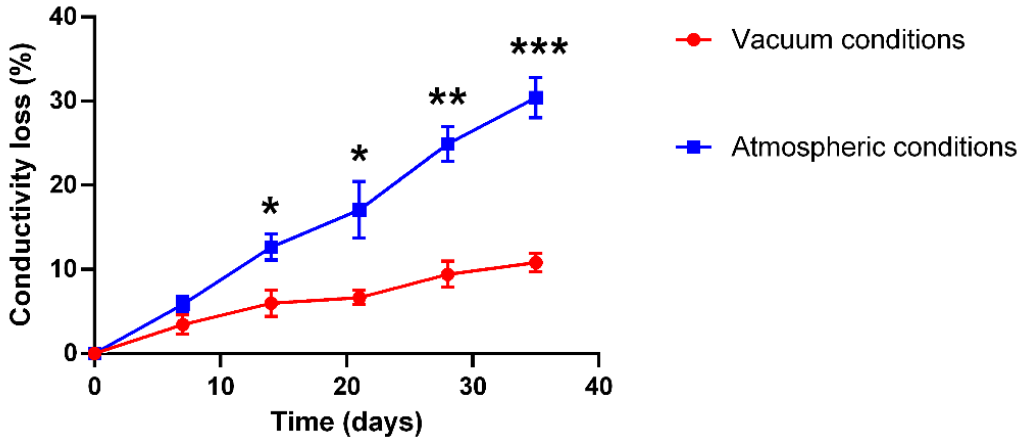


**Figure 1.** Conductivity loss of PLA-PPy microfibers stored under vacuum conditions and under atmospheric conditions for 35 days. The samples stored under atmospheric

conditions suffered a higher conductivity loss than the samples stored under vacuum conditions. Statistically significant differences are indicated by *, ** or ***, indicating a p-value below 0.05, 0.01 or 0.001, respectively.

By means of a Fourier transform infrared spectroscopy (FTIR) analysis, the characteristic peaks of pure PPy, PLA microfibers and PLA-PPy microfibers were characterized and analysed (**Figure 2**). In addition, samples of PLA-PPy microfibers degraded in atmospheric conditions for 180 days and degraded in PB 0.1M and 37 °C for 90 days were also studied. At 985 $cm^{-1}$, a characteristic peak of the PPy dopant element (pTS) is observed for all the PLA-PPy samples, which corresponds to the stretching vibration of the S=O bonds of the $-SO_3^-$ group [52,53]. The peak is attenuated when there is a degradation process, being more attenuated for the group degraded in PB 0.1M and 37 °C than for the group degraded in atmospheric conditions. Around 1546 $cm^{-1}$, a characteristic PPy peak corresponding to the fundamental vibration of the PPy ring is observed for PPy and all PLA-PPy samples [54]. For the PLA-PPy samples degraded in atmospheric conditions, this peak appears slightly attenuated, which could be related to a degradation process in atmospheric conditions that has affected the stability of PPy. For the PLA-PPy samples degraded in PB 0.1M and 37 °C, this peak is practically inexistent, indicating that the PPy has been completely affected by the treatment carried out. Finally, for the degraded groups, two peaks that are not present in the other groups are observed. These peaks correspond to a wavelength around 2849 $cm^{-1}$ and 2917 $cm^{-1}$ and show the bending and tension of the aliphatic C-H group [55]. These groups originate after a rupture of the pyrrole rings [55], which leads us to think that this rupture is due to the degradation of the PPy produced in the degraded samples under the different conditions.

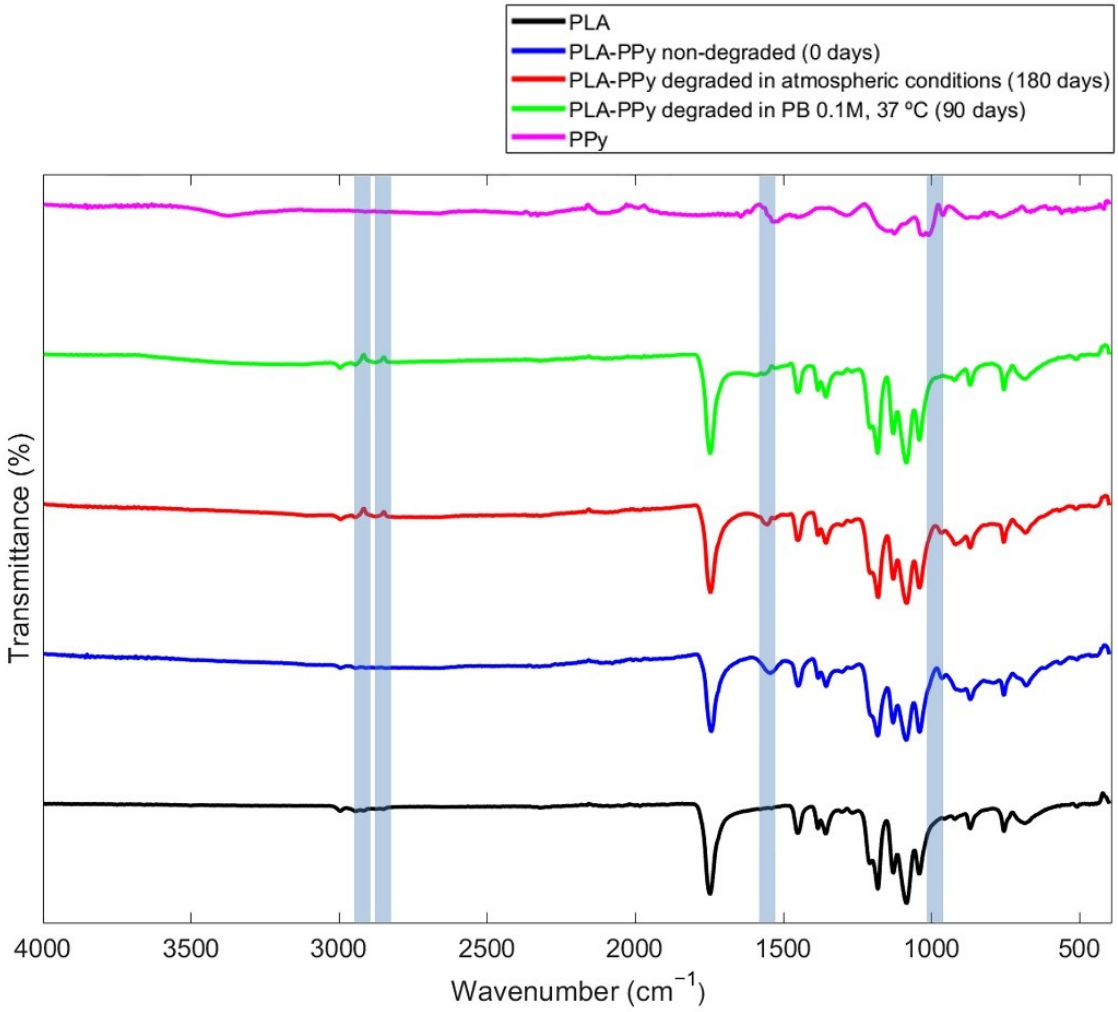


**Figure 2.** FTIR spectra of PLA microfibers (PLA), non-degraded PLA-PPy microfibers, PLA-PPy microfibers degraded in atmospheric conditions for 180 days, PLA-PPy microfibers degraded in PB 0.1 M at 37 °C for 90 days and pure PPy (PPy). The vertical shaded areas are highlighting the differential characteristic peaks that are studied.

Through a thermogravimetric analysis (TGA), the stability of PLA-PPy samples after the different degradation processes (180 days in atmospheric conditions and 90 days in PB 0.1 M and 37 °C) was studied. As can be observed in **Figure 3**, in the curve that corresponds to the PPy group, there is a loss of mass between 50 °C and 100 °C, which is mainly due to the evolution of the pTS dopant adsorbed on the sample and to the evaporation of $H_20$ [56]. However, this weight loss is not observed for the samples composed of both materials (PLA-PPy) since the mass fraction of PPy in the samples is

only around 3.5%. Regarding the mass loss of the PLA-PPy samples between 300 °C and 400 °C, it is due to the degradation of the polymer chain. This thermal degradation of the polymer chain occurs at a lower temperature when the material is degraded, which is why the samples degraded in atmospheric conditions and in PB 0.1 M and 37 °C have a thermal degradation of the polymer chain that occurs at a lower temperature than for the PLA-PPy non-degraded samples. This effect is more pronounced for the case of samples degraded in PB 0.1 M and 37 °C, since it is a more aggressive degradation, being produced at a lower temperature than for the PLA group. This is produced because the PPy coating that acted as a protective layer for the non-degraded PLA-PPy samples has been lost, since PPy degrades later than PLA, but also because the PB 0.1M has caused a hydrolytic degradation of the PLA polymer chain. Therefore, after the treatment of PLA-PPy microfibers with PB 0.1 M and 37 °C, both materials (PLA and PPy) are affected by the degradation process. In the case of PLA-PPy fibers degraded in atmospheric conditions, there was only a partial degradation of the PPy coating and, therefore, its thermal degradation curve occurs later than the one corresponding to the PLA group. This allows us to conclude that the degradation in atmospheric conditions mainly affects the PPy coating, while the degradation in PB 0.1M and 37 °C affects both the PLA microfibers and the PPy coating.

It is important to highlight that this is an *in vitro* study with ideal conditions. Regarding the *in vivo* situation after its implantation, the regeneration of nerves takes several months and we expect a loss of conductivity of PPy in this situation, but the PPy performance should be effective at least during the first weeks that are the more critical ones. Despite this should be further studied in future experiments, many groups have already reported the biodegradation properties of PLA-PPy blends [4,57–59]. PLA-PPy composites showed a good electroconductivity for long time in a simulated

physiological solution (15% of the conductivity remained after 1000 h) and the *in vivo* biodegradation of the composites showed the non-toxicity of degradation products [57–60]. Therefore, we expect that the *in vivo* degradation of the PLA-PPy substrates will not lead to a problematic immune response. In addition, we have proved that the PPy coverage does not prevent the degradation of PLA microfibers, which is an advantage for the *in vivo* application since the PLA-PPy microfibers will be satisfactorily resorbed.

Regarding gold microfibers, gold is considered chemically inert with a high stability and its surface shows low chemisorption capacity [37]. This causes gold to exhibit low chemical reactivity, little catalytic activity, high stability against corrosion and oxidation [36,61,62]. Therefore, clinically, gold presents biocompatibility when in contact with body fluids and tissues, adequate characteristics to avoid immunogenic reactions [36,37]. Furthermore, as it is a metal, it has excellent conductivity and has been used in electrodes for electrical neurostimulation [63,64]. Gold is highly stable *in vivo*, and its conductivity should not vary during the time needed for nerve regeneration. In addition, on our study gold is not a coating of the PLA-PPy microfibers, but is incorporated in the form of independent microfibers, so there should be no chemical interaction between PPy and gold microfibers. For these reasons, the stability and degradation of gold microfibers has not been studied.

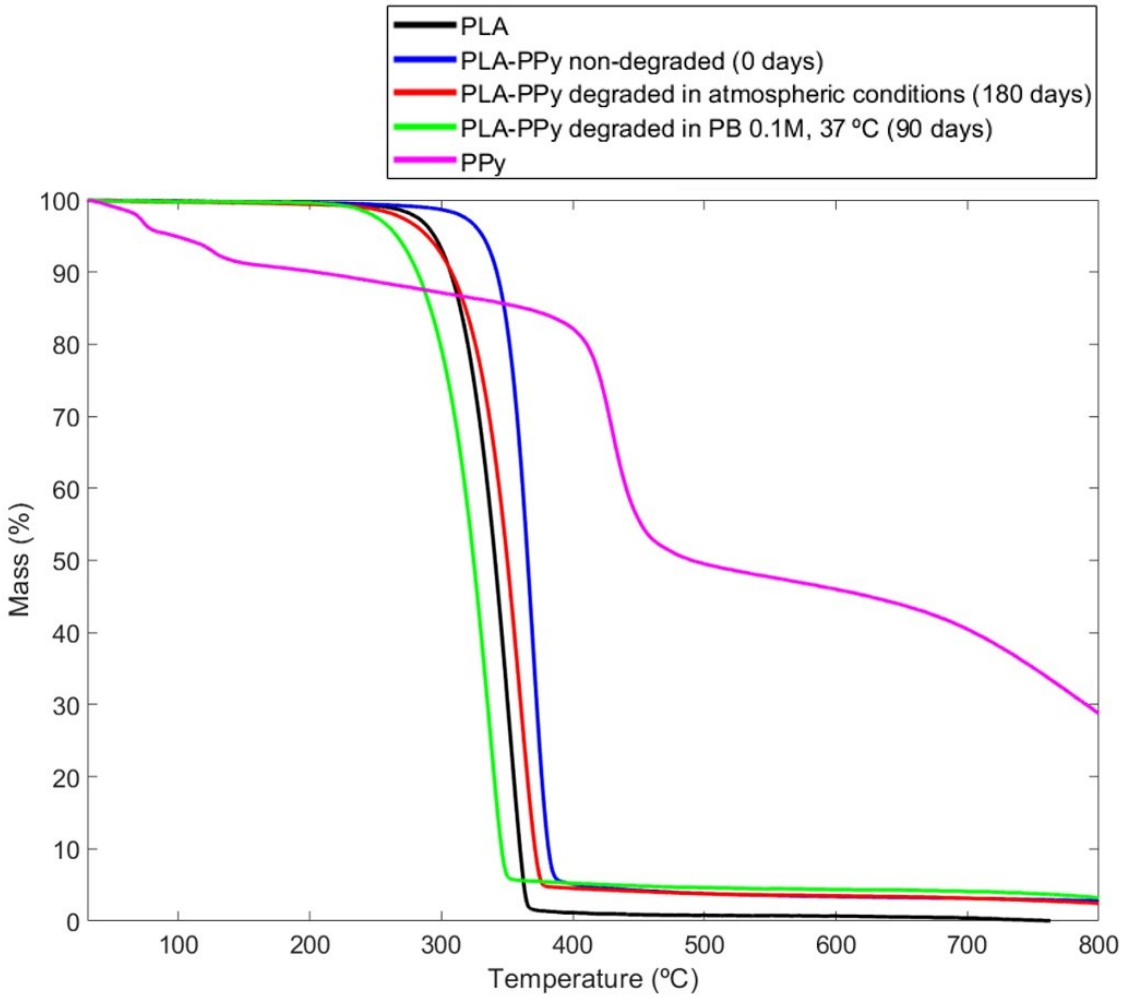


**Figure 3** Thermogravimetric analysis (TGA) of PLA microfibers (PLA), non-degraded PLA-PPy microfibers, PLA-PPy microfibers degraded in atmospheric conditions for 180 days, PLA-PPy microfibers degraded in PB 0.1M at 37 °C for 90 days and pure PPy (PPy).

## Bioreactor for the electrical stimulation

Our work presents various novelties within the field of nervous tissue engineering. On the one hand, the diameter of the electroconductive fibers is 10 microns, which is not the usual size used in this type of studies. Since the fiber substrates obtained by means of the electrospinning technique are normally used, nanofibers with a diameter below 1 micron are commonly employed [4,6]. We previously observed that the use of microfiber substrates led to an increased axonal extension and axonal sprouting than the

use of nanofiber substrates, since on microfibers the cell mobility was much less hindered than on nanofibers, and the cell–cell interactions were favoured, resulting in a higher motility of SCs that accelerated their migration speed from the DRG body, which is directly related to the axonal extension [17]. In addition, the PPy coating of the PLA microfibers resulted in an additional beneficial effect on axonal growth, possibly produced by the greater surface roughness that favoured the adhesion of DRG [17].On the other hand, most studies of electrical stimulation of DRG or isolated neurons apply stimulation by introducing electrodes into the culture medium, commonly using non-electroconductive substrates, since the current circulates through the culture medium and not through the culture substrate [65–67]. Furthermore, the few studies that apply the electrical stimulation through an electroconductive substrate do not employ microfibers [35,68,69]. Therefore, the fact that we use a substrate based on electroconductive microfibers that is connected outside the culture well (without medium-electrode contact)—so that the current circulates mainly through the culture substrate and not through the culture medium—represents a novelty in this field of study. In addition, the combination of PPy-coated microfibers with gold microfibers is also a novelty and, with this disposition, an electric field around the gold microfibers is created, generating an additional type of stimulation.

For the electrical stimulation of the SCs and DRG, an 8-well bioreactor was designed and manufactured, were the PLA-PPy-Au substrates were placed at the bottom of the wells and on which the SCs and the DRG were seeded. As can be observed in **Figure 4**, an 8-well Millicell® EZ slide was employed, thanks to the fact that it can be disassembled and assembled in its different components, allowing the incorporation of PLA-PPy-Au microfiber substrates between the slide and the wells. The substrates were produced with a length greater than that of the slide in order to allow the contact of the

electrodes with the electroconductive substrate outside the slide chamber, thus avoiding introducing the electrodes into the culture medium. This was done with the aim of maximizing the circulating current through the substrate and minimizing the circulating current through the culture medium.

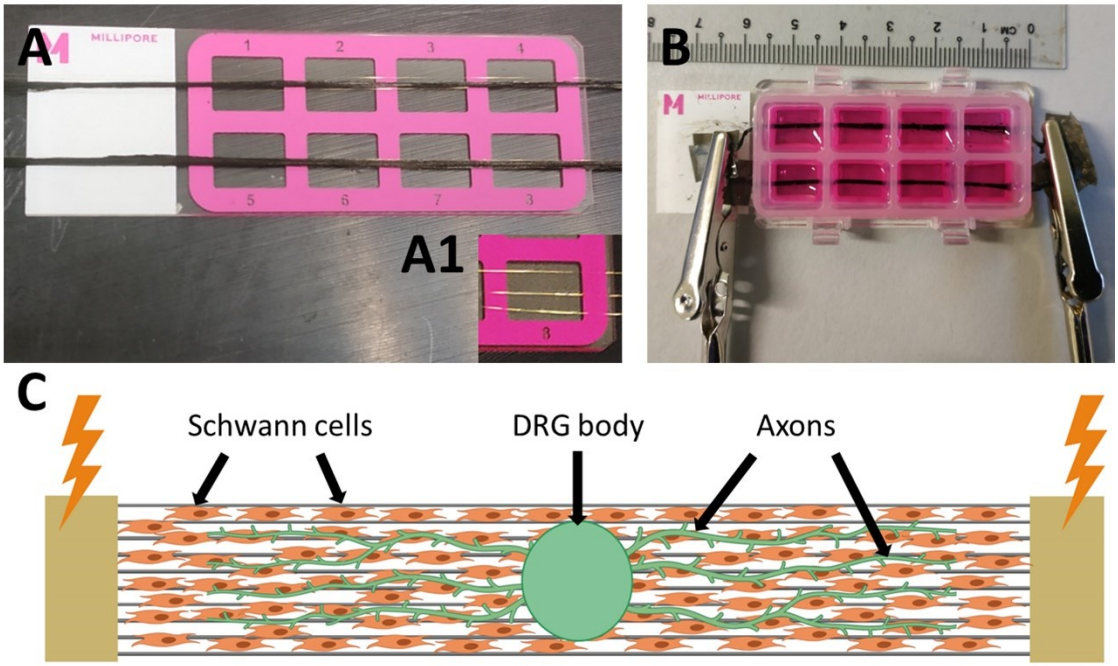


**Figure 4.** Images of the bioreactor for electrical stimulation. (**A**) Image of the PLA-PPy-Au microfiber lane placed on the top of the slide. The gold microfibers are placed below the PLA-PPy microfibers, as can be appreciated in insert A1. (**B**) Image of the fully assembled device, showing the electrodes placed at the extremes of the microfibers. Two PLA-PPy-Au substrates are placed between the slide and the wells, one per row, and connected in parallel to the electrodes avoiding contact with the culture medium. (**C**) Scheme showing the microfiber lane corresponding to one of the wells with the coverage of pre-seeded Schwann cells, the DRG body containing the somas of the neurons and the axons sprouting from the DRG body in an aligned way following the direction of the microfibers.

For the electrical stimulation, it was decided to establish the applied current as the main parameter to control. Despite the setup, it was observed that if stimulation with direct current (DC) was applied for a period of several hours, an accumulation of the

ionic charges of the culture medium led to a variation of its pH, turning into a yellow colour (**Figure S2A**). This implied that an important part of the current was circulating through the culture medium. This was because the conductivity of the culture medium and that of the PLA-PPy substrate were similar: 1.70 ± 0.02 S/m and 1.4 ± 0.2 S/m, respectively. Despite being two different types of conduction (ionic for the culture medium versus electronic for the PLA-PPy substrate), this did not prevent the diversion of part of the current through the culture medium. For this reason, it was necessary to increase the conductivity of the substrates. One option could have been to increase the mass fraction of PPy present in the microfibers, but this implied the appearance of large PPy aggregates that would make it difficult for the axons to extend on the surface of the microfibers [56]. Furthermore, the increase in conductivity was not large enough to prevent current flow through the culture medium. For this reason, it was decided to introduce three gold microfibers of 25 μm in diameter below the PLA-PPy substrate. Thus, it was possible to increase the conductivity of the substrate by several orders of magnitude, up to $2.4 \times 10^5 \pm 0.1$ S/m. When gold microfibers were employed, no colour change was observed in the culture medium despite using DC (**Figure S2B**), so the circulating current through the culture medium had been greatly reduced.

However, this does not imply the lack of usefulness of PLA-PPy substrates since DRG do not adhere properly to a bare gold substrate, as can be observed in **Figure S3**, where DRG seeded on top of gold substrates show a poor adherence to the substrate so there is no axonal extension after 4 days of cell culture. We attribute this to the fact that the electrochemical nature of bare gold is very neutral, which is why it does not favour the adsorption of proteins on gold during the pre-conditioning process of the substrate and, therefore, greatly hinders the adhesion of DRG to gold. Anchorage-dependent cells make integrin-mediated cell adhesion, which has no affinity for bare gold, so the gold

surface must be modified—for example, with thiol-functionalized RGD peptide—in order to achieve cell adhesion to gold [70]. In addition, the high autofluorescence of gold prevents the realization of fluorescence images. For these reasons, it was decided to place the gold microfibers below the PLA-PPy substrate, so the SCs and DRG only had direct contact with the PLA-PPy microfibers. In addition, the use of PLA-PPy microfibers presents more advantages in front of using non-conductive PLA microfibers. On the one hand, part of the current will circulate through the PLA-PPy microfibers, although it will be small compared to the current that circulates through the gold microfibers. On the other hand, the electric field that is created around the gold microfibers would be much more shielded if non-conductive PLA microfibers were used instead of PLA-PPy microfibers.

In addition, to minimize the effect of the accumulation of charges that could occur with part of the current circulating through the culture medium, even if it is low, it was decided to switch from DC to alternating current (AC). Another possible solution could have been to continue using DC but including salt bridges to maintain the charges balance. However, the developed bioreactor was an 8-well system, and this implementation was very complex to perform. In addition, several studies had previously successfully applied stimulation with alternating current to stimulate axonal growth [35,66,69,71,72], so it was decided to apply this type of current for the electrical stimulation. Regarding the future *in vivo* application of the electroconductive substrate, it would be necessary to study the need to include gold microfibers according to the conductivities of the surrounding tissue but, if necessary, gold is a biocompatible material that is already used in various biomedical applications in the nervous system [62,73–75]. Furthermore, since gold microfibers represent a very small percentage of the total number of microfibers (0.5%), and their diameter is similar to the diameter of

PLA-PPy microfibers (25 μm vs. 10 μm), there is not a significant stiffening of the system.

To increase the number of stimulated samples in the same experiment, three devices were connected in parallel, as shown in **Figure 5**. In this way, the current will be distributed uniformly throughout the six stimulated lanes, since it is the parameter that we wanted to set. As can be observed in the diagram, an ammeter was connected in series to set the circulating current, being six times the current that was desired to circulate through each PLA-PPy-Au lane. A potentiometer connected in series was also introduced to increase the electrical resistance of the system, since the incorporation of gold microfibers made the resistance of the system too low for the voltage generator that was used. This AC voltage generator was set to the desired frequency with a sinusoidal signal. In turn, the voltage generator was connected to a 24-h timer to set the hours that the system should be connected.

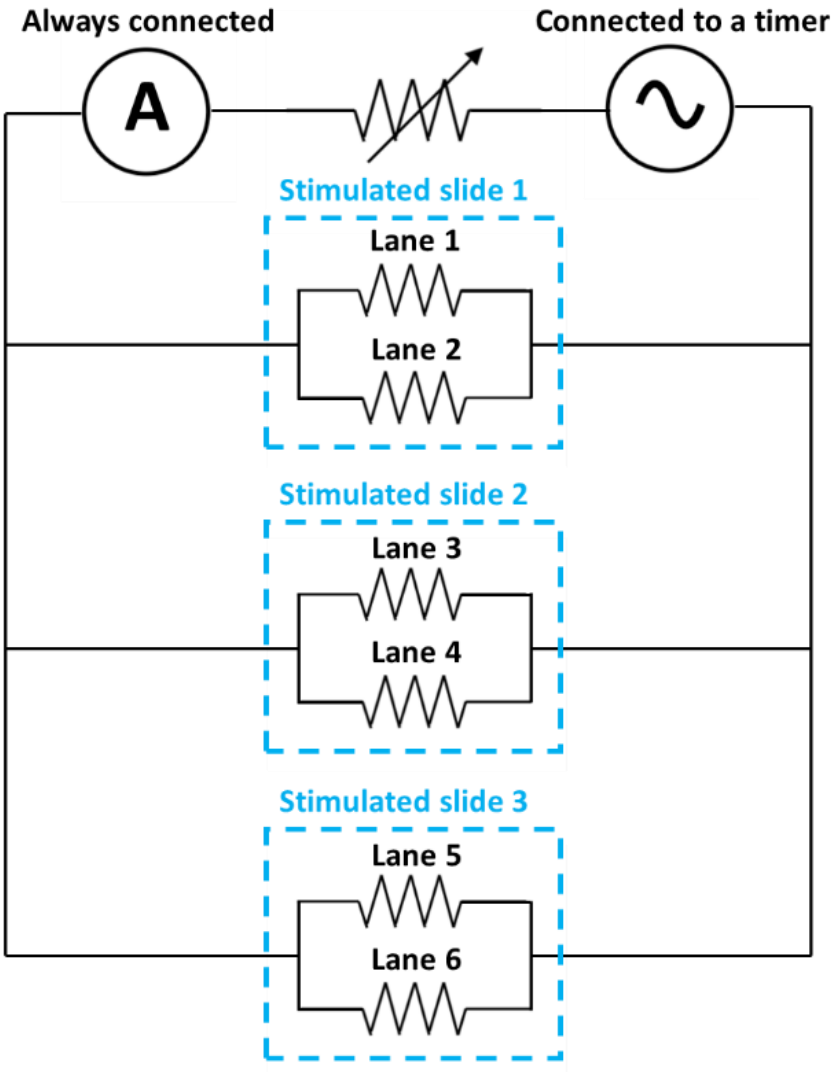


**Figure 5.** Electrical diagram of the different elements used. Six PLA-PPy-Au lanes were connected in parallel using three different slide chambers so that the same current circulated through each lane. An AC generator at a given frequency and with a sinusoidal signal fed the circuit and the circulating current was measured in real time with an ammeter connected in series. A potentiometer was also connected in series to raise the total electrical resistance of the circuit in order to use a voltage that was not excessively low for the voltage generator.

## Electrical stimulation of DRG and SCs

The aim of this study is the electrical stimulation of entire DRG (not just isolated neurons) in a co-culture with pre-seeded SCs, so it is a co-stimulation of DRG and pre-seeded SCs. The type of current typically used in the stimulation of neurons or DRG is

direct current (DC), introducing salt bridges to minimize the exposure of cells to changes in pH due to the accumulation of ionic charges in the culture medium [65,67]. In this study, we applied alternating current (AC) in order to avoid the accumulation of ionic charges of the culture medium and thus avoided having to use salt bridges. AC also has been applied in several studies for the electrical stimulation of axonal growth with good results [35,71].

As can be observed in **Table 1**, different stimulation conditions were studied, varying the applied electrical current and the frequency of the sinusoidal signal, keeping constant the stimulation time, the culture time, the number of pre-seeded SCs and the origin and age of the DRG. As a result, when a frequency of 250 Hz and a current of 3 mA was applied (experiment #1), an adverse effect of the stimulation was obtained, after which it was decided to lower the applied current to 1 mA without changing the frequency (experiment #2), which also gave rise to an adverse effect. In view of these results, it was decided to reduce both parameters, lowering the current to 0.5 mA and the frequency to 50 Hz (experiment #3), after which no effect of stimulation was observed on the growth of DRG axons, neither positive nor negative. Finally, the current was maintained in 0.5 mA and the frequency was lowered to 3 Hz (experiment #4), which gave rise to a positive effect on axonal growth, showing an increased axonal extension and axonal sprouting for the electrically stimulated DRG, compared with the non-stimulated ones. Several studies of neurostimulation of DRG have observed that low frequencies (<20 Hz) have a beneficial effect on pain relief, inducing the dorsal horn of the spinal cord inhibition via the activation of low threshold mechanoreceptors and the release of endorphins and dynorphins [76–79]. Therefore, we could say that the applied stimulation frequency of 3 Hz is within the physiological range of DRG activation. Regarding the applied current, a current of 1 mA has been applied also for

neural activation during DRG stimulation [76], so the applied frequency of 0.5 mA is also in the physiological range of DRG activation. The results of experiment #4 are explained below.

| Experiment Number | Current per Lane (mA) | Voltage per Lane (mV) | Frequency (Hz) | Effect on Axonal Growth |
|---|---|---|---|---|
| #1 | 3 | 30.6 | 250 | Adverse effect |
| #2 | 1 | 10.2 | 250 | Adverse effect |
| #3 | 0.5 | 5.1 | 50 | No effect |
| #4 | 0.5 | 5.1 | 3 | Favourable effect |

**Table 1.** Stimulation parameters: different electric currents and frequencies were applied to the cultures, evaluating their effect on axonal growth. The total stimulation time (3 days), the continuous stimulation time per day (8 h), the culture duration (4 days), the pre-seeding of SCs (40,000 cells/well), the origin of DRG (chicken embryos) and the age of DRG (E8) were kept constant.

In previous studies [17,51], confocal images of the SCs cultured on PLA-PPy microfiber substrates showed an effective adherence and proliferation of the cells together with a high cell alignment. Immunofluorescence images of the DRG cultured on PLA-PPy microfiber substrates also showed a highly aligned axonal extension, without a detrimental effect when the PPy coating was present [17]. In this work, as can be observed in **Figure 6**, control and electrically stimulated samples were stained with Neuron-specific β-III Tubulin antibody in green colour (**Figure 6A** and **6D**, respectively), with S100β antibody in red colour (**Figure 6B, E**, respectively) and DAPI in blue colour (**Figure 6C, F**, respectively). As can be observed in **Figure 6A** and **6D**, the staining with Neuron-specific β III Tubulin antibody was employed to test the

differences in axonal extension and sprouting. In the centre of the images, the DRG body can be observed, which contains the neuronal somas and from which the axons arise in a highly aligned way thanks to the highly aligned PLA-PPy microfiber substrate. The staining with S100β antibody was employed to observe the SCs, both the pre-seeded ones and those that migrated from the DRG body. It has been previously observed [51,80,81] that, when there are not pre-seeded SCs, the SCs that migrated from the DRG body are only present near to the axons, with no SCs in areas where axons are not present. Therefore, observing SCs at the ends of the microfiber lane, far away from the axons, indicates the presence of the pre-seeded SCs. This can be also observed with the DAPI staining, since the nuclei of the pre-seeded SCs can be observed far away from the axons.

As can be observed, both the maximum length of the axons and the area occupied by them is greater for the stimulated DRG (**Figure 6D**) than for the non-stimulated DRG (**Figure 6A**). These two parameters were quantified as explained in the experimental section (quantification of axonal extension and axonal sprouting) with a total amount of 16 samples per group ($n$ = 16) and the results are presented in **Figure 6G, H**. As can be observed in **Figure 6G**, the quantification of the maximum length of axons shows a statistically significant increase for the stimulated samples. Since the axons grow at both sides of the DRG body, this parameter was measured as the maximum, the sum and the average of both sides in order to study the symmetry of axonal growth. As a result, an increase in the stimulated samples of 17.9% (2.8 ± 0.1 mm vs. 3.3 ± 0.1 mm), 19.2% (5.2 ± 0.2 mm vs. 6.2 ± 0.2 mm) and 19.2% (2.6 ± 0.1 mm vs 3.1 ± 0.1 mm) was observed, respectively. This proved that the measures were constant and symmetrical since similar results were obtained for the three cases. Likewise, the total area covered by the axons was also quantified, which is indicative of

the degree of axonal sprouting. As seen in **Figure 6H**, an increase in the area of axons of 40% (0.48 ± 0.04 $mm^2$ vs. 0.67 ± 0.04 $mm^2$) was obtained for the electrically stimulated DRG compared to the non-stimulated ones.

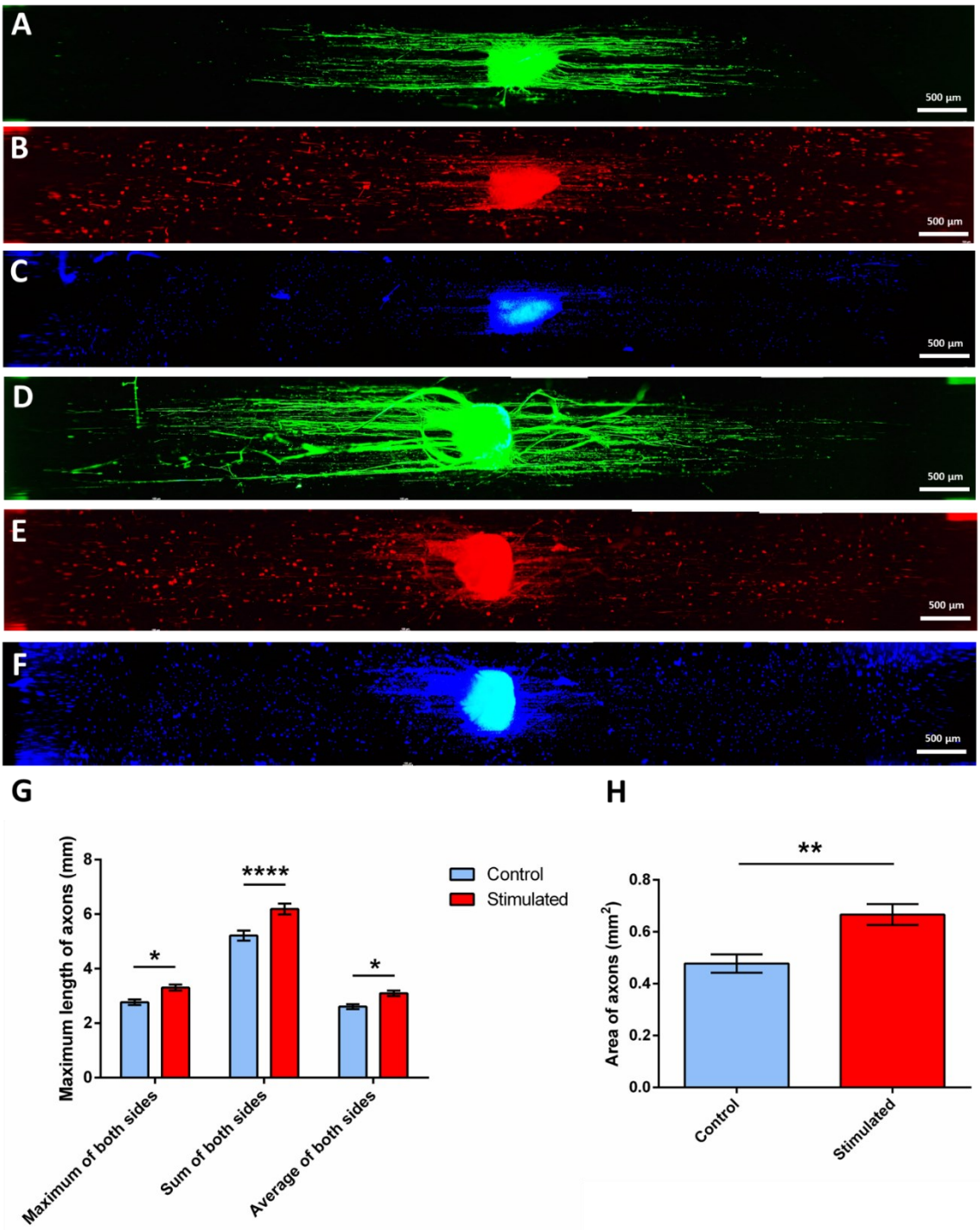


**Figure 6.** Example of control (**A**–**C**) and electrically stimulated (**D**–**F**) samples. Axons marked with β III Tubulin are shown in green colour (**A**,**D**), Schwann cells marked with

S100β are shown in red colour (**B**,**E**) and the cell nuclei marked with DAPI are shown in blue colour (**C**,**F**). It can be observed the increase in the length and in the total area occupied by axons for the electrically stimulated sample. The presence of pre-seeded Schwann cells also can be confirmed since they are present far away from the axons. (**G**) Quantification of axonal extension through the measurement of the maximum length of axons as the maximum, sum and average at both sides of the DRG body. (**H**) Quantification of axonal sprouting through the measurement of the area occupied by axons. The data in G and H are presented as the mean ± SEM ($n$ = 16). Statistically significant differences are indicated by *, ** or ****, indicating a p-value below 0.05, 0.01 or 0.0001, respectively.

As can be observed in a detailed confocal image of an area far from the DRG body (**Figure 7**), the axons (in green colour) grow on the top of PLA-PPy microfibers in a highly directed manner (marked with *), both in the control group (**Figure 7A**) and in the stimulated group (**Figure 7B**). Likewise, the SCs are also observed (in red colour), which are also arranged on the top of PLA-PPy microfibers accompanying the axons. In addition, it is observed that the SCs have a highly elongated cytoskeleton in the direction of the microfibers (marked with arrows).

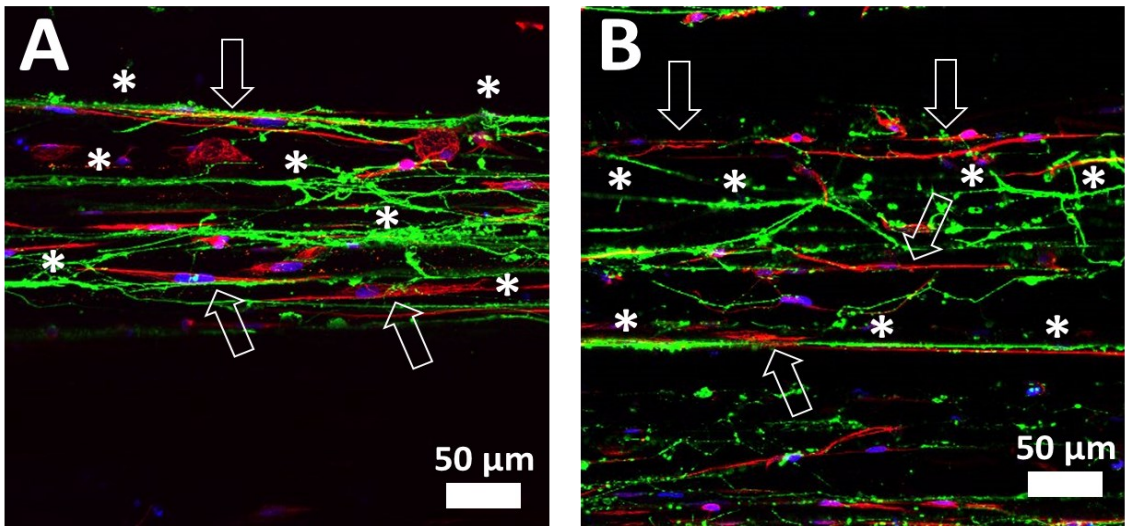


**Figure 7.** Confocal images of control (**A**) and electrically stimulated (**B**) samples. This confocal images in a region far from the DRG body allows to observe the axons (Neuron-specific β III Tubulin antibody in green colour) and the Schwann cells (S100β

antibody in red colour), as well as the cell nuclei (DAPI in blue colour). It can be observed how the axons grow in a highly aligned manner in the direction of the PLA-PPy microfibers (marked with *). Likewise, it is also observed that the cytoskeletons of Schwann cells are elongated in the direction of PLA-PPy microfibers (marked with arrows), accompanying the axons.

## qRT-PCR analysis after the electrical stimulation

As can be observed in **Figure 8**, the relative expression of the genes related with axon guidance and axonogenesis, Schwann cells, cell proliferation and neurotrophins was determined by real-time qPCR.

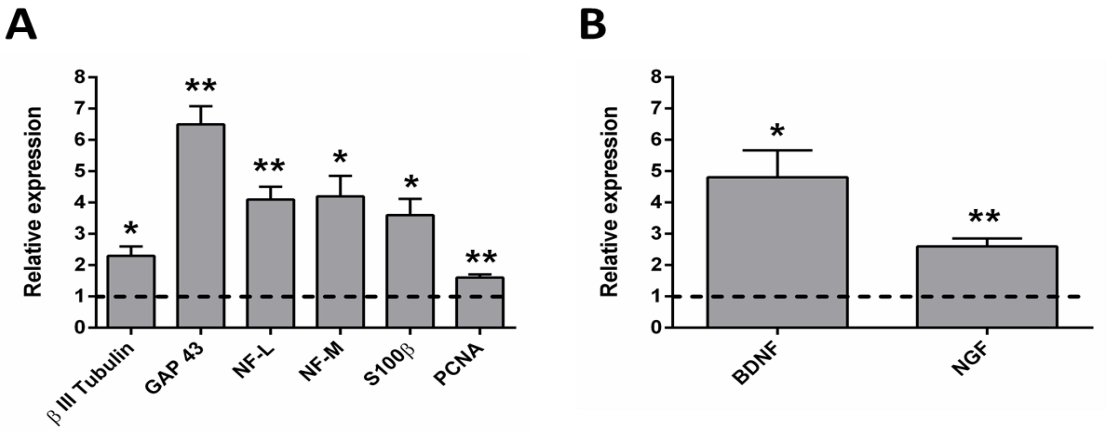


**Figure 8** Relative expression levels of the genes studied by RT-qPCR. (**A**) Chicken genes related with axonal growth (β III Tubulin, GAP 43, neurofilament low chain (NF-L) and neurofilament medium chain (NF-M)), with Schwann cells (S100β) and with cell proliferation (PCNA), normalized to chicken GAPDH. (**B**) Rat genes related with brain-derived neurotrophic factor (BDNF) and nerve growth factor (NGF), normalized to rat GAPDH. Statistically significant differences are indicated by * or **, indicating a p-value below 0.05 or 0.01, respectively.

The axon guidance- and axonogenesis-related genes, the β III Tubulin, the growth associated protein 43 (GAP 43), the neurofilament middle chain (NF-M) and the neurofilament light chain (NF-L) were studied. Since all the proteins encoded by these genes are located in neurons, the chicken sequences of these genes were studied (see

**Table 2**). The β III Tubulin protein is a microtubule element that plays an important role in normal neural development, regulating ligand interactions and microtubule formation. It has implications in neurogenesis and axon guidance and maintenance [82,83]. The GAP 43 is a protein related with the neuronal growth and plasticity. It is expressed in neuronal growth cones during axonal regeneration. It is a key component of the axon and the presynaptic terminal, and it is a widely used marker of axonal sprouting. It mediates axonal growth, branching, and pathfinding during development but also in axonal remodelling [84–86]. Neurofilaments are the most abundant cytoskeletal molecules in myelinated neurons. These proteins expressed in neurons play an important role in the intracellular transport of molecules throughout the axons and dendrites, contributing to the integrity of neuronal cytoarchitecture. They increase the diameter of neuronal axons, facilitating electrical conduction and neuronal signalling [87]. As can be observed in **Figure 8A**, an upregulation of all these genes was observed for the electrically stimulated group, being specially elevated for the GAP 43. This implies that the stimulated group presents an increased rate of neuronal growth.

The SCs-related protein S100β, is considered as a glial marker protein, since it is very abundant in Schwann cells, astrocytes and oligodendrocytes, among others [88,89]. It is involved in cell proliferation, survival and differentiation as an intracellular regulator and as an extracellular signal [88]. It regulates cell shape, cell-to-cell communication, intracellular signal transduction, energy metabolism and cell growth, among other functions [89]. As can be observed in **Figure 8A**, a clear upregulation of S100β can be observed. Since most of the cells that migrate from the DRG body are SCs [80,81], this upregulation can be related to a higher proliferation, survival and cell-to-cell communication of SCs for the electrically stimulated group. This is of great importance for axonal growth since the support of SCs directly influences the guidance and growth

of axons, by the release of neurotrophic factors and other signals that favour axonal growth. It is important to note that this result is related with the chicken SCs that migrate from the DRG body, not with the pre-seeded rat SCs.

The cell proliferation-related protein (PCNA) is a nuclear protein synthesized in the early G1 phase and in the S phase of the cell cycle. It is located in the nuclei of cells that undergo cell division and promotes DNA synthesis, as it is a cofactor for DNA polymerase delta. PCNA has a key function in the cell cycle regulation and DNA replication and also plays a role in other processes involving the cell genome [90–92]. As can be observed in **Figure 8A**, it is also upregulated for the electrically stimulated group. Since it is expected that most of the chicken cells present in the culture are SCs that migrated from the DRG body [80,81], this upregulation of PCNA can be related to a higher proliferation of SCs in the electrically stimulated group.

In addition, rat genes related to the neurotrophins BDNF (brain-derived neurotrophic factor) and NGF (nerve growth factor) were also studied to assess if the electrical stimulation had a beneficial effect on the release of neurotrophins from pre-seeded SCs. On the one hand, BDNF helps to support the survival of neurons, activating the growth and differentiation of new neurons [93,94]. It is one of the most active neurotrophins, helping to stimulate and control neurogenesis and playing a key role in normal neural development [95–98]. On the other hand, NGF is involved in the growth and maintenance of neurons, stimulating its proliferation and survival [99,100]. As can be observed in **Figure 8B**, both neurotrophins were upregulated for the electrically stimulated group, indicating an increased secretion of this neurotrophic factors by the pre-seeded rat SCs. Thus, this is another factor that may be of great importance in accelerating axonal growth.

Therefore, we have studied the main biomarkers that are related with axonal growth and regeneration: β III Tubulin related with neural development, GAP 43 related with growth cones during axonal regeneration and neurofilament related with the integrity of neuronal cytoarchitecture, which were more expressed for the electrically stimulated group. Furthermore, two of the main neurotrophic factors (BDNF and NGF) were studied, which were also more expressed for the electrically stimulated group. Since the electrically stimulated group has a higher expression of neuronal, SCs, proliferation and neurotrophins biomarkers, we can conclude that this group has a stronger nerve regeneration potential. It is also important to highlight that all the chicken and rat genes that were studied were species-specific (including the GAPDH), so there is no expression at all when only DNA from the other species is present.

# 7.4. Experimental section

## Preparation of PLA microfiber bundles

Highly aligned PLA microfiber bundles were obtained by grouping 600 PLA microfibers with a diameter of 10 μm each (AITEX Textile Research Institute, Alcoy, Spain). In order to maintain the alignment of the lane-shaped microfiber bundles, they were fastened using polycaprolactone (PCL) bands, which were placed in a solid state on both extremes of the lane and melted by temperature so that, once cooled, the microfibers were attached by the PCL bands.

## Coating of PLA microfibers with PPy

The PLA substrates were coated with the electrically conductive polymer polypyrrole (PPy) via in situ polymerization with a mass fraction of PPy of 3.5%. As a previous step, the substrates were immersed in deionized water under compression and

a fixed vacuum was applied until they stopped floating and, therefore, the introduction of water inside the spaces between fibers was achieved, in order to obtain a homogeneous coating of all microfibers, not only the most superficial ones. Next, each substrate was put into a polypropylene tube with an aqueous solution of pyrrole monomer (Py, Sigma-Aldrich, 131709, Madrid, Spain) and sodium para-toluene sulfonate (pTS, Sigma-Aldrich, 152536, Madrid, Spain), followed by ultrasonication for 1 min in order to allow the microfibers to be saturated with the Py/pTS solution. The substrates were incubated with shaking at 4 °C for 1 h. The ratio between the substrate area (length × width) and the final volume of the Py/pTS aqueous solution was 0.6 $cm^2$/mL. A concentration of 14 mM was used for both Py and pTS. Then, an aqueous solution of ferric chloride ($FeCl_3$, Sigma-Aldrich, 157740, Madrid, Spain) was added and incubated with shaking at 4 °C for 24 h for the polymerization and deposition of PPy on the PLA substrates. The ratio between the substrate area (length × width) and the final volume of the $FeCl_3$ aqueous solution was 0.6 $cm^2$/mL. The concentration of $FeCl_3$ was 38 mM. PPy-coated membranes were washed with deionized water with agitation for 10 min for three times and ultrasonicated for 30 min in deionized water three times. Finally, the membranes were dried in a desiccator with a fixed vacuum at 40 °C for 2 days.

## Bioreactor for electrical stimulation

The Millicell® EZ slide chamber (Merck Millipore, PEZGS0816, Madrid, Spain) was employed to develop a bioreactor that allowed the direct contact between the electrodes and the electroconductive substrate while avoiding the direct contact between the electrodes and the culture medium (**Figure 4**). This commercial device was chosen as it was completely removable and allowed the substrate to be placed at the bottom of the wells. To do this, the substrate was first placed between the slide and the wells and,

once the slide was assembled, the ends of the microfibers remained outside the slide, available to connect to the electrodes. In order to increase the conductivity of the PLA-PPy substrate, gold microfibers with a diameter of 25 μm each (GoodFellow, AU00-WR-000121, Madrid, Spain) were used. These gold microfibers were placed below the PLA-PPy microfiber substrate and a total of three gold microfibers were arranged in parallel and equally spaced from each other (**Figure 4A**). The gold microfibers were placed below the PLA-PPy lane because their larger diameter and their poorly adherent surface hindered the adhesion of SCs and, especially, of the DRG, which did not adhere to the substrate if they were in direct contact with the gold microfibers. Once the microfiber substrate was introduced in the slide chamber, the contact between the slide and the wells was no longer perfectly sealed. Thus, to avoid leaks of the culture medium, a cellulose-based sealant was added, which, once the chamber was closed and the solvents were evaporated, exerted a sealing and adhesive role that prevented the leakage of culture medium. As can be observed in **Figure 4B**, in the final arrangement of the device one microfiber substrate or lane is placed in the centre of each of the two rows of the slide. These lanes protrude from the slide in order to proceed to the connection with the electrodes outside the wells, in order to avoid direct contact with the culture medium. Therefore, the device consists of two lanes connected in parallel and, therefore, the circulating current will be distributed approximately 50% for each lane.

## Stability and degradation of PLA-PPy microfibers

To study the stability of the PPy coating of PLA microfibers, electrical conductivity measurements were made every 7 days for a total of 35 days. The samples were stored both under atmospheric conditions ($n$ = 6) and vacuum conditions ($n$ = 6) and the electrical characterization was performed calculating the conductivity loss relative to the

initial conductivity value (in %). To study the degradation of PPy-coated PLA microfibers, they were subjected to two different conditions. On the one hand, they were kept for 180 days under atmospheric conditions ($n$ = 6), and on the other hand, they were kept submerged in phosphate buffer (PB) 0.1M at 37 °C for 90 days ($n$ = 6). After this time, the samples were studied by FTIR and TGA.

## Electrical characterization

The electrical resistance of the different samples was measured at room temperature placing one electrode at each extreme of the sample, with a space between them (d) of 10 cm, and applying a constant voltage of 5 V. The circulating current was measured with a multimeter, and the apparent surface electrical resistance (R) was calculated applying the Ohm's law. The average value was reported from five different samples ($n$ = 5). Once the electrical resistance was obtained, it was divided by the distance at which the electrodes were placed when taking the measurement. After measuring the cross section of the substrates (S), the in-plane apparent DC conductivity ($\sigma_{DC}$) of the samples was obtained by **Equation (1)**.

$$\sigma_{DC} = \frac{d}{R \times S} \quad (1)$$

## Field Emission Scanning Electron Microscopy (FESEM)

The morphological characterization of the surface of PLA-PPy microfibers was performed using a field-emission scanning electron microscope (FESEM; ULTRA 55, ZEISS, Oxford Instruments, Wiesbaden, Germany). The preparation of samples consisted in desiccation under vacuum conditions during the 24 h prior to the test, in order to avoid interferences due to evaporated water. Then, samples were placed on top

of a carbon tape and a carbon bridge was created between the sample and the carbon tape. Finally, samples were coated with a thin layer of platinum. To obtain the images a voltage of 2 kV was employed.

## Fourier transform infrared spectroscopy (FTIR)

To study the degradation of PLA-PPy microfibers, the Fourier transform infrared spectroscopy (FTIR) analysis of samples belonging to three groups was carried out: PLA-PPy microfibers as control group; PLA-PPy microfibers degraded for 90 days in PB 0.1M and stored at 37 °C; and PLA-PPy microfibers degraded at room temperature and atmospheric conditions for 180 days. FTIR analysis allows obtaining specific spectra for each sample, since each molecule or chemical bond generates transmittance and absorbance values at specific wavelengths. Subsequently, these spectra can be analysed to determine the bonds present in each sample after the degradation process. FTIR spectra of the samples were obtained using a Cary 630 FTIR (Agilent Technologies, Santa Clara, CA, USA) in the attenuated total reflection mode (ATR). The spectra resulted from averages of 24 scans at 4 $cm^{-1}$ resolution, between 400 and 4000 $cm^{-1}$. Four different samples ($n = 4$) of each group were studied, plotting the most representative curve for each one.

## Thermogravimetric analysis (TGA)

The thermogravimetric analysis (TGA) allows to study the thermal degradation of materials as well as their composition. In this case, to carry out the degradation study, the following experimental groups were studied: PLA-PPy microfibers as a control group; PLA-PPy microfibers after 90 days of degradation in PB 0.1M at 37 °C; PLA-PPy microfibers after a degradation process of 180 days at room temperature and atmospheric conditions. A thermogravimetric analyser (TGA/SDTA 851 Mettler-

Toledo operated using the METTLER: STARe Default DB V13.00 software, Barcelona, Spain) was employed. Samples with a mass of approximately 2 mg were processed, monitoring the mass loss while heating up to 800 °C at a rate of 10 °C/min under a positive nitrogen ($N_2$) flow of 20 mL/min. Thermograms representing the mass loss of the sample as a function of temperature were obtained. Four different samples ($n = 4$) of each group were studied, plotting the most representative curve for each one.

## Substrates sanitization and preconditioning

Before the seeding of cells, substrates were sanitized by 30 min of exposure to UV irradiation (UV lamp, wavelength 254 nm) on each side and by immersion in 70% ethanol (ET00021000, Scharlab, Madrid, Spain) for 3 washes of 10 min. Then the ethanol residues were removed by 4 washes of 10 min with ultrapure water (Milli-Q®, Sigma-Aldrich, Madrid, Spain). The substrates were then preconditioned by immersion in Dulbecco's Modified Eagle Medium with a high glucose level (4.5 g/L) (21331020, Life Technologies, Madrid, Spain) supplemented with 10% foetal bovine serum (10270-106/A3381E, Life Technologies, Madrid, Spain) and 1% penicillin/streptomycin (15140122, Life Technologies, Madrid, Spain) and incubation at 37 °C for 24 h in a humidified atmosphere containing 5% $CO_2$.

## Seeding of SCs and DRG

Rat Schwan cells (SCs, P10301, Innoprot, Bizkaia, Spain), 8th cell passage, were grown at 37 °C, 5% $CO_2$, in a SCs medium (P60123, Innoprot, Bizkaia, Spain) until confluence. SCs were seeded with a density of 20,000 cells suspended in a 3 µL drop of the SCs medium. For each well, 40,000 SCs were seeded (one drop of 3 µL at each end of the well). After 3 days of SCs culture, dorsal root ganglia (DRG) from E8 chicken embryo were seeded (one at the centre of each well, $n$ = 16 per group). To obtain the

DRG, firstly chicken embryos were immersed in a Petri dish containing phosphate-buffered saline (PBS) 0.1M to remove traces of the yolk and remaining fragments of the extra-embryonic tissue. Then, employing a dissecting microscope, the embryos were dissected using forceps to remove the tail, the peritoneal organs and the fat deposits in order to expose the spinal cord and the peripheral DRG in the sacro-lumbar region. The dorsal entry tracts of the sacro-lumbar DRG were exposed and DRG were carefully excised with ultrafine forceps by gently pulling away from the spine. Next, individual DRG explants were placed in the middle of every Millicell® EZ slide well (**Figure 4C**). DRG were grown for 4 days in Ham F12 culture medium (11765054, ThermoFisher Scientific, Madrid, Spain) with 1% HEPES 1M (15630049, ThermoFisher Scientific, Madrid, Spain), 1% L-Glutamine 200 mM (25030024, Thermo Fisher Scientific, Madrid, Spain), 1% N2 supplement (17502048, Thermo Fisher Scientific, Madrid, Spain) and 1% penicillin/streptomycin (15140122, Life Technologies, Madrid, Spain) and 10 ng/mL of nerve growth factor (NGF, 13257019, Thermo Fisher Scientific, Madrid, Spain).

## Electrical stimulation parameters

After 1 day of DRG culture, the electrical stimulation was applied with the following parameters: alternating current of 0.5 mA, frequency of 3 Hz, 8 h of continuous stimulation per day, and 3 days of total stimulation time. An AC voltage generator (PHYWE Function Generator, Germany) was used with the desired frequency and a sinusoidal signal. An ammeter (FLUKE 45 Dual Display Multimeter, Madrid, Spain) was connected in series to set the circulating current.

## Immunostaining of SCs and DRG

After cell culture, the cell medium was removed and samples were washed in PB 0.1M and fixed with 4% paraformaldehyde (PFA, 47608, Sigma-Aldrich, Madrid, Spain) for 20 min at room temperature. After cell fixation, 3 washes of 10 min with PB 0.1M were performed to remove PFA residues. Then, the non-specific bindings were blocked, and the cell membrane was permeabilized by immersion in a blocking buffer composed of PB 0.1M with 3% bovine serum albumin (BSA, A7906, Sigma-Aldrich, Madrid, Spain) and 0.1% Tween20 (P1379, Sigma-Aldrich, Madrid, Spain) for 1 h at room temperature. SCs were stained with rabbit monoclonal anti-S100β antibody (ab52642, Abcam, Cambridge, United Kingdom, 1/200 dilution) and DRG were stained with Neuron-specific β III Tubulin Antibody (MAB1195, R&D Systems, Madrid, Spain, 1/100 dilution). Samples were incubated with primary antibodies at 4 °C overnight. Next, secondary antibodies, goat anti-rabbit IgG Alexa Fluor® 555 (A-21429, Thermo Fisher Scientific, Madrid, Spain, 1/200 dilution) and goat anti-mouse IgG Alexa Fluor® 488 (A28175, ThermoFisher Scientific, Madrid, Spain, 1/200 dilution) were incubated for another 2 h at room temperature in the darkness. Afterward, samples were incubated with 4′,6-diamidino-2-phenylindole (DAPI, D9564, Sigma-Aldrich, Madrid, Spain, 1/1000 dilution) for 10 min to mark the cell nuclei. The imaging was performed using a confocal microscope (LEICA TCS SP5, Leica microsystems, Germany) and a fluorescence microscope (Leica DM5000, Leica microsystems, Germany, 5× magnification). For the axonal quantification images, the following parameters were used in the Leica DM5000 fluorescence microscope: exposure of 1.2 s, gain of 8.1×, saturation of 1.15 and gamma of 0.97.

## Quantification of axonal extension and axonal sprouting

To quantify the axonal extension, two different parameters were obtained. On the one hand, the maximum length of axons was measured as the distance between the edge of the DRG body and the end of the longest axon, as the maximum, sum and average of left and right sides of the DRG body. On the other hand, the area of axons was obtained by subtracting the area of the DRG body from the total area of the DRG. Both parameters were measured with the ImageJ/FIJI image processing software [101].

## RNA extraction and cDNA synthesis

To evaluate the effect of the electrical stimulation on the gene expression of the co-culture of SCs and DRG, the total RNA was extracted employing QIAzol lysis reagent (79306, Qiagen, Madrid, Spain). First, 350 µL of QIAzol were added to each sample, and then they were incubated at room temperature for 5 min. The supernatant was transferred, 70 µL of chloroform were added, and the samples were incubated at room temperature for 5 min. Then, the samples were centrifuged (15 min, 14,000 rpm, 4 °C). The aqueous layer was mixed with 175 µL of isopropanol and kept at room temperature for 5 min. Samples were centrifuged (10 min, 14,000 rpm, 4 °C). The pellet was resuspended in 350 µL of 75% ethanol and the samples were centrifuged (5 min, 14,000 rpm, 4 °C). The ethanol was evaporated at room temperature. The resulting pellet was dissolved in 30 µL of RNAse free water. RNA concentration, integrity and quality were measured with a Q3000 UV Spectrophotometer (Quawell, San Jose, CA, USA).

For cDNA synthesis, approximately 500 ng of total RNA was converted into cDNA using the Maxima First Strand cDNA Synthesis Kit for RT-qPCR with dsDNase (K1671, ThermoFisher Scientific, Madrid, Spain) in a reaction volume of 20 µL. The reaction was conducted with the following conditions: 25 °C for 10 min, 55 °C for 20

min, 85 °C for 5 min and a final hold at 4 °C. The resulting cDNA quality and concentration were measured using a Q3000 UV Spectrophotometer (Quawell, San Jose, USA) and it was stored at −80 °C until further analysis. The experiment was carried out in quadruplicate ($n = 4$).

## Quantitative real-time PCR

Quantitative real-time polymerase chain reactions (qRT-PCR) were carried out on 96-well plates (Applied Biosystems®, ThermoFisher Scientific, Madrid, Spain) with each sample represented by the gene of interest and one housekeeping gene (Glyceraldehyde Phosphate Dehydrogenase, GAPDH). The primers for each gene were designed with the PRIMER3plus software (www.bioinformatics.nl accessed on 7 February 2022) based on specific DNA sequences from NCBI (https://www.ncbi.nlm.nih.gov/nucleotide/ accessed on 7 February 2022), which were purchased from ThermoFischer Scientific (Madrid, Spain). The primer sequences of the target genes are shown in **Table 2**. All the primer sequences of target genes were species specific, so no amplification of chicken genes was obtained for samples containing only rat RNA and no amplification of rat genes was obtained for samples containing only chicken RNA. This allowed us to study genes of a specific species in a co-culture of two different species (chicken and rat), allowing us to study separately the biomarkers of DRG-related cells and of pre-seeded SCs. Individual reactions contained 2 µL of cDNA with a concentration of 1 ng/µL, 1 µL of specific primers (forward and reverse at a concentration of 10 µM), 5 µL of SYBR™ PowerUp™ SYBR™ Green Master Mix (15350929, Fisher Scientific, Madrid, Spain) and 1 µL of RNAse-free water in a final total volume of 10 µL. Amplification efficiency was analysed before qRT-PCR to optimize measurements. Reactions were carried out in a StepOne Plus™ Real-Time PCR System (Applied Biosystems®, ThermoFisher Scientific, Madrid, Spain)

with a holding stage of 50 °C for 2 min and 95 °C for 2 min, followed by a cycling stage of 40 cycles of 95 °C for 15 s and 60 °C for 1 min. The data were obtained using the StepOne Plus™ Software 2.3 (Applied Biosystems®, ThermoFisher Scientific, Madrid, Spain). Fold changes were calculated using the 2−ΔΔCt method. Four biological replicates and four technical replicates were measured for each sample. The data were represented as the relative expression for the electrically stimulated group with respect to the control group for each one of the genes.

| Species | Gen | Primer Forward | Primer Reverse |
|---|---|---|---|
| Chicken (Gallus Gallus) | β III Tubulin | TCCTCTCACAAGTACGTGCC | CCCCGCTCTGACCGAAAAT |
| | NF-L | AAGACGCTGGAGATCGAAGC | CACCTTCCAGCAGTTTCCTGT |
| | NF-M | CACCACCTATCAGGACACGAT | GGGTCCAGTGATGCTTCCAG |
| | GAP 43 | CATAAGGCAGCCACCAAAAT | CGGAAGCCTCACTCTCTTTG |
| | S100β | TGCTTGCCATGAGTTCTTTG | GCACTGTCCAAGAGGCTTTC |
| | PCNA | GAGACCTCAGCCACATTGGT | AGTCAGCTGGACTGGCTCAT |
| | GAPDH | AGTCAACGGATTTGGCCGTA | ACAGTGCCCTTGAAGTGTCC |
| Rat (Rattus norvegicus) | BDNF | GCGGCAGATAAAAAGACTGC | GTAGTTCGGCATTGCGAGTT |
| | NGF | TGATCGGCGTACAGGCAGA | GAGGGCTGTGTCAAGGGAAT |
| | GAPDH | AGACAGCCGCATCTTCTTGT | GACCAGCTTCCCATTCTCAG |

**Table 2.** Primer sequences for the chicken and rat target genes that were studied.

## Statistical analysis

Results are expressed as the mean ± standard error of the mean (SEM). The statistical analysis of the results was performed with GraphPad Prism® v.6 software (GraphPad Software, San Diego, CA, USA) in order to reveal significant differences between conditions. The two-sided, unpaired t-test was applied (confidence level of 95%). Statistically significant differences are indicated by *, **, *** or ****, indicating a *p*-value below 0.05, 0.01, 0.001 or 0.0001, respectively.

## 7.5. Conclusions

The experimental data proves the ability to obtain electrically conductive, highly aligned and biocompatible PLA-PPy-Au substrates based on microfibers, which greatly expands the potential of this composite material to be used for neural tissue engineering and implantable-device applications. A high axonal extension and axonal sprouting is observed for DRG cultured on the PLA-PPy-Au microfiber substrates, reaching an increment of 19.2% in the maximum length of the axons and 40% in the area of the axons when electrically stimulated. In addition, the electrically stimulated group presented a higher expression of neuronal-, Schwann cell-, proliferation- and neurotrophin-related biomarkers, also confirming that this group has stronger nerve regeneration potential. In conclusion, the usefulness of the substrate to increase and accelerate axonal growth when subjected to an exogenous electrical stimulus is proved.

## 7.6. Author contribution statement

Conceptualization, F.G.R., M.M.P. and C.M.-R.; formal analysis, F.G.R. and S.S.R.; funding acquisition, M.M.P. and C.M.-R.; investigation, F.G.R. and S.S.R.; methodology, F.G.R., M.M.P. and C.M.-R.; project administration, M.M.P.; supervision, M.M.P. and C.M.-R.; validation, F.G.R., M.M.P. and C.M.-R.; visualization, F.G.R.; writing—original draft, F.G.R.; writing—review and editing, M.M.P. and C.M.-R. All authors have read and agreed to the published version of the manuscript.

## 7.7. Conflicts of interest

The authors declare no conflict of interest.

## 7.8. Acknowledgements

F.G.R. acknowledges the scholarship FPU16/01833 from the Spanish Ministry of Universities.

## 7.9. References

1. X. Jiang, S. H. Lim, H. Q. M. Hai-Quan, S. Y. Chew, *Exp. Neurol.* **2010**, *223*.
2. W. Zhu, F. Masood, J. O'Brien, L. G. Zhang, *Nanomedicine Nanotechnology, Biol. Med.* **2015**, *11*, 693.
3. Y. S. Lee, G. Collins, T. Livingston Arinzeh, *Acta Biomater.* **2011**, *7*, 3877.
4. J. Y. Lee, C. A. Bashur, A. S. Goldstein, C. E. Schmidt, *Biomaterials* **2009**, *30*, 4325.
5. Y. Wang *et al.*, *Chin. Med. J. (Engl).* **2011**, *124*, 2361.
6. Y. Zou *et al.*, *ACS Appl. Mater. Interfaces* **2016**, *8*, 12576.
7. Y. Xu, Z. Huang, X. Pu, G. Yin, J. Zhang, *Cell Prolif.* **2019**, *52*, 1.
8. D. E. Henton, P. Gruber, J. Lunt, J. Randall, *Nat. Fibers, Biopolym. Biocomposites* **2005**, *48674*, 527.
9. J. Lunt, *Polym. Degrad. Stab.* **1998**, *3910*, 145.
10. Y. Ramot, M. Haim-Zada, A. J. Domb, A. Nyska, *Adv. Drug Deliv. Rev.* **2016**, *107*, 153.
11. D. da Silva *et al.*, *Chem. Eng. J.* **2018**, *340*, 9.
12. R. Fitzgerald, L. M. Bass, D. J. Goldberg, M. H. Graivier, Z. P. Lorenc, *Aesthetic Surg. J.* **2018**, *38*, S13.
13. L. S. Nair, C. T. Laurencin, *Prog. Polym. Sci.* **2007**, *32*, 762.
14. H. H. Lu *et al.*, *Biomaterials* **2005**, *26*, 4805.
15. M. Zilberman, K. D. Nelson, R. C. Eberhart, *J. Biomed. Mater. Res. Part B Appl. Biomater.* **2005**, *74B*, 792.

16. F. Yang, R. Murugan, S. Wang, S. Ramakrishna, *Biomaterials* **2005**, *26*, 2603.

17. F. Gisbert Roca, J. Más Estellés, M. Monleón Pradas, C. Martínez-Ramos, *Int. J. Biol. Macromol.* **2020**, *163*, 1959.

18. O. A. R. Sulaiman, T. Gordon, *Glia* **2000**, *32*.

19. B. J. Pfister *et al.*, *Crit. Rev. Biomed. Eng.* **2011**, *39*.

20. K. S. Katiyar *et al.*, *Front. Bioeng. Biotechnol.* **2020**, *8*, 1.

21. C. E. Schmidt, V. R. Shastri, J. P. Vacanti, R. Langer, *Proc. Natl. Acad. Sci. U. S. A.* **1997**, *94*, 8948.

22. J. Huang, Z. Ye, X. Hu, L. Lu, Z. Luo, *Glia* **2010**, *58*, 622.

23. R. Balint, N. J. Cassidy, S. H. Cartmell, *Acta Biomater.* **2014**, *10*, 2341.

24. T. H. Le, Y. Kim, H. Yoon, *Polymers (Basel).* **2017**, *9*.

25. C. Li, H. Bai, G. Shi, *Chem. Soc. Rev.* **2009**, *38*, 2397.

26. G. Sabouraud, S. Sadki, N. Brodie, *Chem. Soc. Rev.* **2000**, *29*, 283.

27. L. X. Wang, X. G. Li, Y. L. Yang, *React. Funct. Polym.* **2001**, *47*, 125.

28. J. Mao, Z. Zhang, *Adv. Exp. Med. Biol.* **2018**, *1078*, 347.

29. M. Mattioli-Belmonte *et al.*, *Mater. Sci. Eng. C* **2005**, *25*, 43.

30. S. Aznar-Cervantes *et al.*, *Bioelectrochemistry* **2012**, *85*, 36.

31. J. F. Zhou *et al.*, *Neural Regen. Res.* **2016**, *11*, 1644.

32. P. M. George *et al.*, *Biomaterials* **2005**, *26*, 3511.

33. Y. Li *et al.*, *Colloids Surfaces B Biointerfaces* **2020**, *191*, 1.

34. Y. Zhao *et al.*, *Biomaterials* **2020**, *255*, 120164.

35. A. F. Quigley *et al.*, *Adv. Mater.* **2009**, *21*, 4393.

36. M. Das, K. H. Shim, S. S. A. An, D. K. Yi, *Toxicol. Environ. Health Sci.* **2011**, *3*, 193.

37. S. Alex, A. Tiwari, *J. Nanosci. Nanotechnol.* **2015**, *15*, 1869.

38. C. Paviolo, P. R. Stoddart, *Nanomater. 2017, Vol. 7, Page 92* **2017**, *7*, 92.

39. Z.-R. Lu, S. Sakuma, **2016**, doi:10.1007/978-1-4939-3121-7.

40. A. Markus, T. D. Patel, W. D. Snider, *Curr. Opin. Neurobiol.* **2002**, *12*, 523.

41. P. Lu, M. H. Tuszynski, *Exp. Neurol.* **2008**, *209*, 313.

42. M. Lykissas, A. Batistatou, K. Charalabopoulos, A. Beris, *Curr. Neurovasc. Res.* **2007**, *4*, 143.

43. B. S. Bregman, M. McAtee, H. N. Dai, P. L. Kuhn, *Exp. Neurol.* **1997**, *148*, 475.

44. M. R. Freeman, *Curr. Opin. Neurobiol.* **2006**, *16*, 119.

45. E. Pompili *et al.*, *Eur. J. Histochem.* **2020**, *64*.

46. N. El Seblani, A. S. Welleford, J. E. Quintero, C. G. van Horne, G. A. Gerhardt, *J. Neurosci. Methods* **2020**, *335*, 108623.

47. K. R. Jessen, P. Arthur-Farraj, *Glia* **2019**, *67*, 421.

48. G. Nocera, C. Jacob, *Cell. Mol. Life Sci.* **2020**, 1, doi:10.1007/s00018-020-03516-9.

49. K. R. Jessen, R. Mirsky, A. C. Lloyd, *Cold Spring Harb. Perspect. Biol.* **2015**, *7*, 1.

50. J. A. Gomez-Sanchez *et al.*, *J. Neurosci.* **2017**, *37*, 9086.

51. F. Gisbert Roca *et al.*, *Macromol. Biosci.* **2021**, *21*, 2000391.

52. E. Håkansson, T. Lin, H. Wang, A. Kaynak, *Synth. Met.* **2006**, *156*, 1194.

53. T. Raudsepp, M. Marandi, T. Tamm, V. Sammelselg, J. Tamm, *Electrochim. Acta* **2014**, *122*, 79.

54. H. K. Chitte, G. N. Shinde, N. V. Bhat, V. E. Walunj, *J. Sens. Technol.* **2011**, *01*, 47.

55. O. Fabela-Sánchez *et al.*, *J Mater Sci Mater Med* **2018**, *29*, 13.

56. F. Gisbert Roca, A. García-Bernabé, V. Compañ Moreno, C. Martínez-Ramos,

M. Monleón Pradas, *Macromol. Mater. Eng.* **2020**, 2000584, doi:10.1002/mame.202000584.

57. Z. Wang *et al.*, *J. Biomed. Mater. Res. - Part A* **2004**, *70*, 28.
58. Z. Wang *et al.*, *J. Biomed. Mater. Res. - Part A* **2003**, *66*, 738.
59. Z. B. Huang, G. F. Yin, X. M. Liao, J. W. Gu, *Front. Mater. Sci.* **2014**, *8*, 39.
60. X. Wang *et al.*, *J. Biomed. Mater. Res. - Part A* **2004**, *68*, 411.
61. F. Vigneron, V. Caps, *Comptes Rendus Chim.* **2016**, *19*, 192.
62. P. M. Tiwari, K. Vig, V. A. Dennis, S. R. Singh, *Nanomater. 2011, Vol. 1, Pages 31-63* **2011**, *1*, 31.
63. A. Domínguez-Bajo *et al.*, *Biomaterials* **2021**, *279*.
64. S. Lienemann, J. Zötterman, S. Farnebo, K. Tybrandt, *J. Neural Eng.* **2021**, *18*.
65. A. N. Koppes *et al.*, *J. Neural Eng.* **2014**, *11*, 046002.
66. P. J. Kumar, R. D. Adams, A. B. Harkins, E. D. Engeberg, R. K. Willits, *IEEE Trans. Biomed. Eng.* **2016**, *63*, 1257.
67. C. Bertucci, R. Koppes, C. Dumont, A. Koppes, *Brain Res. Bull.* **2019**, *152*, 265.
68. M. Imaninezhad *et al.*, *J. Neural Eng.* **2018**, *15*.
69. Z. Zhou *et al.*, *Biomater. Sci.* **2018**, *6*, 2375.
70. S. H. Yoon, M. R. K. Mofrad, *Biomaterials* **2011**, *32*, 7286.
71. Y. J. Chang, C. M. Hsu, C. H. Lin, M. S. C. Lu, L. Chen, *Biochim. Biophys. Acta - Gen. Subj.* **2013**, *1830*, 4130.
72. L. Ghasemi-Mobarakeh *et al.*, *J. Tissue Eng. Regen. Med.* **2011**, *5*, e17.
73. M. Yadid, R. Feiner, T. Dvir, *Nano Lett.* **2019**, *19*, 2198.
74. N. Elahi, M. Kamali, M. H. Baghersad, *Talanta* **2018**, *184*, 537.
75. M. Adel *et al.*, *Microelectron. Eng.* **2017**, *173*, 1.
76. R. D. Graham, T. M. Bruns, B. Duan, S. F. Lempka, *Neuromodulation* **2021**, *24*,

655.

77. I. Vuka *et al.*, *Neuromodulation* **2018**, *21*, 213.

78. M. J. Bauman, T. M. Bruns, J. B. Wagenaar, R. A. Gaunt, D. J. Weber, *Conf. Proc. IEEE Eng. Med. Biol. Soc.* **2011**, *2011*, 7246.

79. G. Franken, P. Douven, J. Debets, E. A. J. Joosten, *Neuromodulation* **2021**, *24*, 639.

80. H. B. Wang, M. E. Mullins, J. M. Cregg, C. W. McCarthy, R. J. Gilbert, *Acta Biomater.* **2010**, *6*, 2970.

81. S. Gnavi *et al.*, *Mater. Sci. Eng. C* **2015**, *48*, 620.

82. A. Latremoliere *et al.*, *Cell Rep.* **2018**, *24*, 1865.

83. M. Mariani *et al.*, *Gene* **2015**, *563*, 109.

84. G. Grasselli, P. Strata, *Front. Neural Circuits* **2013**, *7*, 1.

85. C. J. Donnelly *et al.*, *J. Neurosci.* **2013**, *33*, 3311.

86. J. Denny, *Curr. Neuropharmacol.* **2006**, *4*, 293.

87. A. Bocquet *et al.*, *J. Neurosci.* **2009**, *29*, 11043.

88. G. Sorci, *World J. Biol. Chem.* **2013**, *4*, 1.

89. L. Wu *et al.*, *Oncol. Rep.* **2017**, *38*, 2309.

90. G. Maga, U. Hübscher, *J. Cell Sci.* **2003**, *116*, 3051.

91. S. N. Naryzhny, *Cell. Mol. Life Sci.* **2008**, *65*, 3789.

92. T. Paunesku *et al.*, *Int. J. Radiat. Biol.* **2001**, *77*, 1007.

93. A. Acheson *et al.*, *Nat. 1995 3746521* **1995**, *374*, 450.

94. E. J. Huang, L. F. Reichardt, *http://dx.doi.org/10.1146/annurev.neuro.24.1.677* **2003**, *24*, 677.

95. T. Zigova, V. Pencea, S. J. Wiegand, M. B. Luskin, *Mol. Cell. Neurosci.* **1998**, *11*, 234.

96. A. Benraiss, E. Chmielnicki, K. Lerner, D. Roh, S. A. Goldman, *J. Neurosci.* **2001**, *21*, 6718.

97. V. Pencea, K. D. Bingaman, S. J. Wiegand, M. B. Luskin, *J. Neurosci.* **2001**, *21*, 6706.

98. P. Ernfors, J. Kucera, K. F. Lee, J. Loring, R. Jaenisch, *Int. J. Dev. Biol.* **2003**, *39*, 799.

99. R. S. Freeman *et al.*, *Prog. Brain Res.* **2004**, *146*, 111.

100. C. Wiesmann, A. M. De Vos, *Cell. Mol. Life Sci. C. 2001 585* **2001**, *58*, 748.

101. J. Schindelin *et al.*, *Nat. Methods* **2012**, *9*, 676.

# 7.10. Supporting information

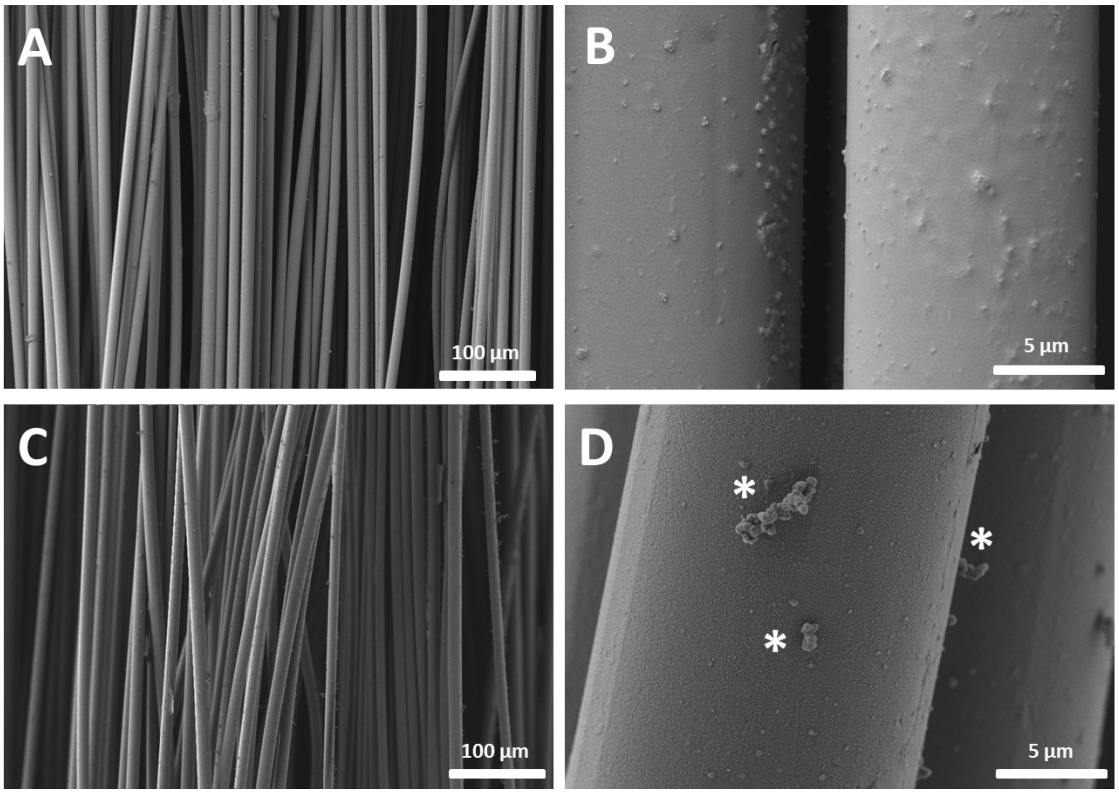


**Figure S1. A**: PLA microfiber lane previously to the PPy coating. Microfibers with a diameter of 10 µm were employed. **B**: Detail of the PLA microfibers previously to the PPy coating. **C**: PLA-PPy microfiber lane. **D**: Detail of the PLA-PPy microfibers. A homogeneous PPy coating can be observed, with a fine grain texture. Only some aggregates (marked with *) were present and most of them disappeared with repeated washing.

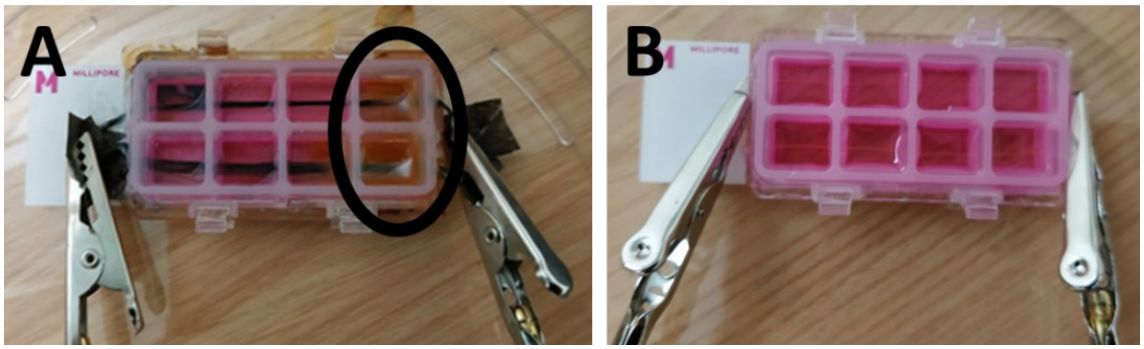


**Figure S2.** PLA-PPy microfibers (**A**) and gold microfibers (**B**) stimulated for 8 hours with direct current (DC). As can be observed, when PLA-PPy microfibers were employed, there was a change in the culture medium colour, that changed from pink to yellow. However, when gold microfibers were used, this effect did not appear.

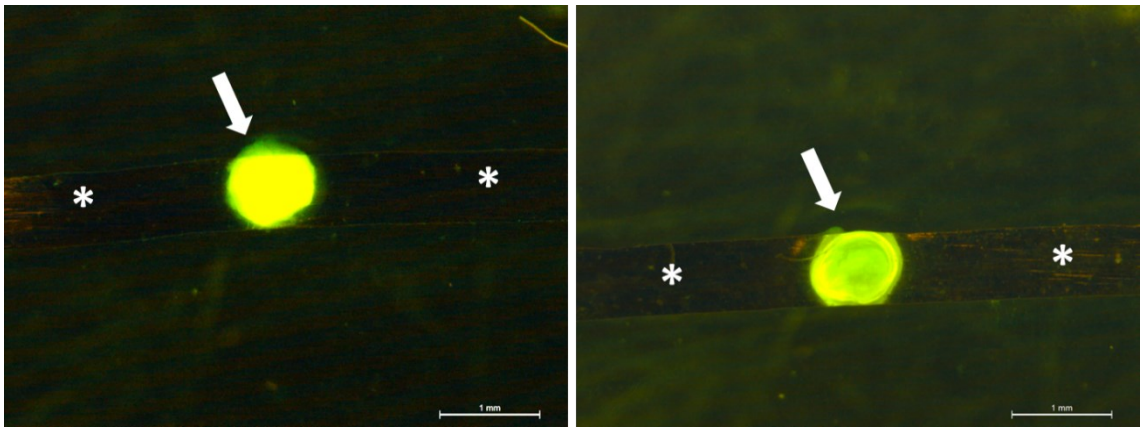

**Figure S3.** Chicken DRG (marked with arrows) seeded on top of a gold substrate (marked with *) after 4 days of cell culture. Immunostaining with β III Tubulin is observed in green colour. As can be observed, there is no axonal extension from the DRG bodies, indicating a poor adhesion of DRG bodies to the gold substrate.

# 8. Paper 6: BDNF-gene transfected Schwann cell-assisted axonal extension and sprouting on new PLA–PPy microfiber substrates

# BDNF-gene transfected Schwann cells-assisted axonal extension and sprouting on new PLA-PPy microfiber substrates

Fernando Gisbert Roca [a], Franck M. André [d], Jorge Más Estellés [a], Manuel Monleón Pradas [a], [c], Lluis M. Mir [d] and Cristina Martínez-Ramos [a], [b], *

[a] Center for Biomaterials and Tissue Engineering. Universitat Politècnica de València. Camino de Vera s/n, 46022, Valencia, Spain.

[b] Universitat Jaume I, Unitat predepartamental de Medicina, Avda/Sos Baynat, s/n, 12071 Castellón de la Plana, Spain

[c] CIBER-BBN, Biomedical Research Networking Center in Bioengineering Biomaterials and Nanomedicine, Spain

[d] Metabolic and systemic aspects of oncogenesis (METSY), Université Paris-Saclay, CNRS, Institut Gustave Roussy, 94805, Villejuif, France

*Corresponding author: Cristina Martínez Ramos. Centro de Biomateriales e Ingeniería Tisular, Universidad Politécnica de Valencia, Camino de Vera s/n E-46022 Valencia, España. Tel.: +34963877000. E-mail: crimarr2@upvnet.upv.es

**Keywords:** bioengineering, biological applications of polymers, biomaterials, fibers, polypyrroles, conducting polymers, tissue engineering

Published online: 13 May 2021

Reprinted with permission from Macromolecular Bioscience 2021, 21, 2000391 

# 8.1. Abstract

The work here reported analyses the effect of increased efficiency of brain-derived neurotrophic factor (BDNF) production by electroporated Schwann cells (SCs) on the axonal extension in a co-culture system on a biomaterial platform that can be of interest for the treatment of injuries of the nervous system, both central and peripheral. Rat SCs are electrotransfected with a plasmid coding for the BDNF protein in order to achieve an increased expression and release of this protein into the culture medium of the cells, performing the best balance between the level of transfection and the number of living cells. Gene-transfected SCs show an about 100-fold increase in the release of BDNF into the culture medium, compared to non-electroporated SCs. Co-cultivation of electroporated SCs with rat dorsal root ganglia (DRG) is performed on highly aligned substrates of polylactic acid (PLA) microfibers coated with the electroconductive polymer polypyrrol (PPy). The co-culture of DRG with electrotransfected SCs increase both the axonal extension and the axonal sprouting from DRG neurons compared to the co-culture of DRG with non-electroporated SCs. Therefore, the use of PLA-PPy highly aligned microfiber substrates pre-seeded with electrotransfected SCs with an increased BDNF secretion is capable of both guiding and accelerating axonal growth.

# 8.2. Introduction

Injuries produced at the central nervous system (CNS) or at the peripheral nervous system (PNS) are very difficult to treat because they involve cell loss, development of neurotoxic environments and a multiplicity of factors only partially known, which makes spontaneous regenerative processes extremely unlikely[1,2]. For this reason, hope for progress towards a greater effectiveness in the regeneration of the nervous system lies in multi-combinatorial solutions that use cell transplantation and

biomaterials to guide axonal growth and protect transplanted cells[3,4], as well as the use of different types of stimuli (mechanical, electrical, biochemical) that trigger and accelerate the necessary processes[5–8].

Axonal extension is accompanied and influenced by interactions with auxiliary cells that behave as factories for the biological factors and that play a decisive role in axonal growth[9,10]. Schwann cells (SCs) are essential in both the development and the regeneration in the PNS, while oligodendrocytes are essential in the CNS[11–14]. SCs are naturally present in the PNS, forming the myelin sheath around the axons and playing a key role in neuronal survival and axonal regeneration[10,15–17]. In case of injury, SCs are necessary to achieve the axonal regeneration since they form regeneration columns (called Büngner's bands) that guide the regenerating axons[11,12]. SCs also release cytokines such as LIF and IL-6 that promote the survival of neurons[15]. In addition, SCs secrete different neurotrophic factors like the nerve growth factor (NGF), brain-derived neurotrophic factor (BDNF) and neurotrophin-3 (NT-3), among others, necessary for axonal regeneration[15–17].

The BDNF protein is present throughout the CNS and is important for the regulation of neuronal survival and differentiation, connectivity, and synaptic plasticity[18,19]. BDNF is necessary for the continued survival and phenotypic maintenance of neurons[19], promotes survival of dorsal root ganglion neurons[20], enhances neurogenesis[20] and promotes nerve healing and axonal growth, improving axonal regeneration[21–25]. The delivery of BDNF *in vivo* to achieve a therapeutic efficacy presents some problems, such as its low stability and short *in vivo* half-life [19]. In addition, the use of mini pumps for the delivery of BDNF creates a steep concentration gradient, leading to different problems like the alteration of the infused tissue and different adverse effects such as edemas[26]. For these reasons, different

techniques can be used to protect the BDNF from the environment and to achieve a controlled and sustained delivery of it without the use of pumps, like the encapsulation of BDNF in biodegradable and biocompatible nano or micro carriers[27,28] or the genetic modification of glial cells able to secrete high quantities of this growth factor[29,30], on which this study focuses. In this study, BDNF has been used as a model of neurotrophic factor whose secretion can be increased by genetically modified SCs.

Biological, chemical and physical techniques can be employed to achieve the genetic modification of cells[31]. Biological, virus-mediated, transfection is the most used technique in clinical research, since it is highly efficient and it easily achieves a stable transfection[31,32]. With this technique, the foreign DNA is integrated into the genome of the cell and it replicates as the host genome does, enabling a sustainable transgene expression[33,34]. However, it has been reported that viral vectors integrate into the host genome randomly, which may disrupt tumour suppressor genes, activate oncogenes, or interrupt essential genes, leading to a malignant transformation[31,35,36]. For these reasons, non-viral transfection techniques such as electroporation have been widely applied[31,37].

The transfection of SCs to achieve a greater expression and release of BDNF has been previously studied using retroviral vectors, observing an increase in the secretion of BDNF by infected cells which is between 4.6 and 26 times higher than the BDNF release of non-transfected SCs [29,30]. SCs transfection using electroporation techniques to achieve an increased BDNF secretion *in vitro* or *in vivo* has not been previously studied. Electroporation is a physical technique that offers a safe and fast alternative to achieve the introduction of the plasmid of interest into the target cells and to transiently express the protein that it encodes[31,37,38]. If appropriate parameters are determined and used, the electric pulses have exclusively reversible effects (the transient rupture of the

membrane impermeability) with no addition of foreign substances. This makes a very important difference with respect to the non-viral transfection techniques based on the chemical vectorization of the nucleic acids, particularly in the case of delicate cells. Indeed, these methods provoke the penetration in the cells or in the cell's membrane of the foreign molecules that transport the nucleic acid, such as liposomal cationic lipids, block-copolymers, etc. or of large supra-molecular complexes such as many types of nanoparticles, organic or inorganic. These residues of the transfection technology may have longer effects than the consequences of the physical approaches such as electroporation, particularly if electric pulses are well tuned to the target cells. Moreover, when electroporation is used, there is no plasmid integration[31,37], which fits with the purposes of the work reported in this manuscript. In our case, a transient transfection of SCs to obtain an increased secretion of BDNF by these cells should be sufficient since the transient expression will last for enough time to carry out the *in vitro* studies. It will also allow future *in vivo* applications with short term, controlled and sustained release of BDNF by SCs. The same approach with little modifications (such as the adjustment of the electric pulses parameters depending on the size of the plasmid) can be foreseen in future studies to achieve increased secretion by the SCs of other neurotrophic factors such as NGF or NT-3.

In order to study the axonal growth, dorsal root ganglia (DRG) are interesting as neuron source because they provide projecting neurons with somata that remain in place while the axon extends. Furthermore, they also contain other auxiliary cells that migrate from the DRG body (mostly SCs) and generate a cellular environment that favours axonal growth and survival[39,40]. Finally, the DRG body edge can be taken as the starting point for the axon's growth, facilitating a reference for the measurement of axonal extension.

Biomaterials interact with cells essentially topographically, through adhesion and mechanotransduction signals[41,42], and they can direct axonal growth towards a target through the mechanical constriction of cells[43,44]. However, biomaterials cannot supply the multitude of growth factors and biochemical signals that are necessary for axonal growth and regeneration[45–48]. It is essential to understand the behaviour of cells that adhere to the biomaterial, and to check if their trophic factors secretory capacity remains unchanged. The planned strategy was to develop a methodology to enhance this secretory role of SCs, and to check its effect on the extension of axons from DRG neurons over growth-guiding biomaterials.

In previous studies we have developed highly aligned substrates based on the use of polylactic acid (PLA) nano and micro fibers covered with different amounts of the conductive polymer polypyrrole (PPy) [49,50]. After performing a scanning of different reaction parameters, the physicochemical and dielectric properties of the substrates were characterized. As a result, the substrates with the least amount of PPy that allowed to obtain a homogeneous coating of the PLA fibers was chosen to carry out the *in vitro* studies with cells. PLA was used as host polymer of the substrates since it is a low cost, renewable, environmentally friendly and biodegradable biomaterial[51,52]. Furthermore, its biocompatibility is critical in order to use PLA-PPy substrates for tissue engineering applications[53,54]. In addition, the coating of the PLA microfibers with PPy via *in situ* polymerization seemed a good approach, since PPy is an intractable and brittle solid with poor mechanical processability[55]. With this strategy we can exploit both the intrinsic electrical conductivity of PPy and the better mechanical properties of the insulating host polymer[55–57].

It is important to note that PPy is an interesting electroconductive material due to its high electrical conductivity, long-term ambient stability, good biocompatibility, low

cost and facile synthesis by chemical polymerization[55,58–61]. Furthermore, PPy has been commonly used in biomedical applications, especially in nerve tissue engineering scaffolds, due to its good biocompatibility and high electrical conductivity[56,62–64].

Electrically conductive substrates based on intrinsically conductive polymers have been extensively studied in order to improve the axonal extension of neurons and induce a greater release of neurotrophins by glial cells when subjected to an exogenous electric field[65–67]. Among all electroconductive polymers, there are well-studied ones like PPy, polyaniline (PANI) and poly(3,4-ethylenedioxythiophene) (PEDOT). Herein, we sought to use PLA - PPy electroconductive highly aligned substrates based on microfibers since we have previously observed that they offer an enhanced axonal guidance and growth versus flat, non-aligned, or smaller fiber sized substrates[49]. In addition, the use of electroconductive substrates offers the possibility of its electrically stimulation in future experiments.

Regarding the topography of the substrates, we focus on the use of aligned substrates because they induce a high axonal orientation, whereas in a flat substrate such as a glass cover or a substrate with randomly oriented fibers, axons grow unoriented[43,44,56,68–70]. In addition, the diameter of the fibers that form the substrate is an important parameter since it influences the neurite outgrowth and the SCs migration from DRG[39,40,71]. We have previously studied different fiber diameters, concluding that micrometer sized fibers (10 μm diameter) provide the best axonal growth[49]. Here, we have grouped in parallel 10 μm diameter microfibers with polycaprolactone (PCL) bands that act as fasteners in the extremes to obtain rail shaped microfiber bundles. PCL was used as fastening material for the microfibers bundles due to its low melting point (around 60°C), making possible the fabrication of the microfiber bundles. PCL is a

biodegradable and biocompatible polymer that has been commonly used for biomedical applications as an implantable biomaterial[72,73].

In this study, we develop a bioactive device based on the combination of a biocompatible substrate formed by highly aligned electroconductive microfibers (PLA/PPy) and genetically modified SCs with the aim of accelerating the repair of lesions both in the CNS and in the PNS. The highly aligned topography can guide axonal growth to maximize the linear distance that regenerating axons cover, and the use of genetically modified support cells can increase their secretion of growth factors, allowing to increase and accelerate the axonal growth of the neurons seeded on the device. In the frame of optimized biological conditions using rat DRG co-cultured or not with genetically modified rat SCs, we evaluated the new highly aligned microfiber-based substrates, hoping to reach a large axonal sprouting and a sustained and directional axonal growth along these substrates. In addition, the device has electroconductive characteristics, so it is susceptible to electrical excitation and to transmit this type of stimuli.

# 8.3. Experimental section

## Electroporation of rat Schwann cells

The plasmid pCMV-GFP (3,487 bp) containing the GFP reporter gene under the cytomegalovirus (CMV) promoter was produced by PlasmidFactory (Bielefeld, Germany) and stored at -20°C at a concentration of 1 µg plasmid/µl of Milli-Q® ultrapure water. The gene transfection of rat Schwann cells (SCs; P10301, Innoprot) in passage 5 using the pCMV-GFP plasmid was carried out with the BIORAD gene pulser (Gene Pulser Xcell Electroporation System, BIORAD) applying 8 square pulses with a duration of 100 µs/pulse and a frequency of 1 Hz in a 100 µl total volume cuvette with 1

mm between electrodes. The time between the electroporation and the dilution of the cells in culture medium and their introduction into the incubator was 15 min. Apart from these parameters which were kept constant, we varied the other parameters: number of cells; amplitude of the applied voltage (thus of the electric field); volume of Spinner Minimum Essential Medium (SMEM, Thermo Fisher Scientific); volume of Milli-Q® ultrapure water and mass (thus amount) of plasmid. As indicated in **Table 1**, two controls with a different number of cells (C1 - C2) and seven different electroporation protocols (P1 – P7) were studied in order to determine the best conditions for the electrotransfection of the Schwann cells, based on our previous experience on other cell types[74,75]. The goal of these experiments was to produce the maximum amount of transfected living cells which is a trade between the level of electroporation/transfection and the number of cells remaining alive.

Once the best electroporation parameters were obtained using the pCMV-GFP plasmid (protocol P7), it was applied again to rat SCs in passage 5 using the BDNF-SEP plasmid [76] which was a gift from Ryohei Yasuda (Addgene plasmid # 83955 ; http://n2t.net/addgene:83955 ; RRID:Addgene_83955). We purified this plasmid from Escherichia coli-transformed cells using the NucleoBond PC2000 EF kit (Macherey-Nagel, Hoerdt, France) and then we diluted it in Milli-Q® ultrapure water. Light absorption at 260 nm was used to determine DNA concentration and the quality of the plasmid was assessed by calculating the ratios of light absorption at 260/280 nm and 260/230 nm. It was stored at a concentration of 4.3 µg plasmid/µl Milli-Q® ultrapure water.

After the electroporation of SCs, control and gene-transfected SCs were diluted in normal Schwann cell culture medium and introduced in an incubator at 37°C with a

humid atmosphere containing 5% $CO_2$. All the cells from a single electroporation cuvette were introduced in a single T25 culture flask.

## Quantification of pCMV-GFP plasmid transfection results

SCs transfected with the pCMV-GFP plasmid were analyzed at different times: after 1, 4, 6 and 11 days of cell culture. Firstly, cells were observed using an inverse microscope (Axio Observer Z1, Carl Zeiss Microscopy) to appreciate the green fluorescence of transfected cells. Then, after removing the culture medium and thus the dead cells, culture flasks were washed with PBS and a trypsin/EDTA solution (T/E; 25200-072, Life Technologies) was then added to break the cell-matrix and cell-cell interactions in order to remove the cells from the bottom of the culture flask. After centrifugation at 1,080 rpm for 5 min, the pellet was resuspended in Schwann cell culture medium (P60123, Innoprot) and the total number of cells was counted. Half of the cells in suspension were re-seeded in a T25 flask and the rest were analysed by flow cytometry (10,000 events were recorded) using the green fluorescence channel (excitation 488 nm, emission 530 nm) in a C6 Accuri flow cytometer (BD, San José, California, USA). As a result, the number of living cells (total number of cells), the level of transfection (percentage of cells showing green fluorescence) and the number of transfected living cells (multiplication of the two previous parameters) were collected.

## Preparation of PLA-PPy microfiber bundles

Highly aligned PLA microfiber (MF) bundles were manufactured by grouping 1,200 PLA MFs with a diameter of 10 μm (Aitex, Spain). PCL bands that acted as fasteners were used at the extremes of the MFs to maintain the alignment and the lane-shaped disposition. PCL bands were placed in a solid state on both extremes of the bundle and melted so, once cooled, the MFs were attached by the PCL bands. MF

substrates with dimensions of 17 mm x 3 mm (length x width) were used. The auxiliary PCL bands that maintain the MF together are not considered when defining the dimensions of the MF substrates.

MF substrates were coated with the electrically conductive polymer PPy via *in situ* polymerization. Firstly, the substrates were immersed in deionized water and a fixed vacuum was applied until the substrates stopped floating. With this procedure the introduction of water inside the spaces between fibers was achieved to obtain a homogeneous coating of all MFs, not only the superficial ones. Next, each substrate was introduced into a polypropylene tube with an aqueous solution of pyrrole monomer (Py, Sigma-Aldrich 131709) and sodium para-toluene sulfonate (pTS, Sigma-Aldrich, 152536) that acted as dopant. It was followed by ultrasonication for 1 min to allow the membrane to be saturated with Py/pTS aqueous solution. The substrates were incubated with shaking at 4°C for 1 h. The ratio between the substrates area (length x width) and the final volume of the Py/pTS aqueous solution was 0.6 $cm^2$/ml and a concentration of 14 mM was used for both Py and pTS. Then, an aqueous solution of ferric chloride ($FeCl_3$, Sigma-Aldrich 157740) that acted as oxidant was added and incubated with shaking at 4°C for 24 h for the polymerization and deposition of PPy on the PLA substrates. The ratio between the substrates area (length x width) and the final volume of the $FeCl_3$ aqueous solution was 0.6 $cm^2$/ml and a concentration of 38 mM of $FeCl_3$ was used. PPy-coated membranes were washed with deionized water with agitation for 10 min for three times and ultrasonicated for 30 min in deionized water for three times. Finally, the membranes were dried in a desiccator with a fixed vacuum at 40°C for 2 days.

## Morphological characterization by field emission scanning electron microscopy (FESEM)

In order to characterize the surface morphology of PLA-PPy substrates a field emission scanning electron microscope (FESEM; ULTRA 55, ZEISS Oxford Instruments) was employed. During the 24 h prior to the test the samples were desiccated under vacuum conditions to avoid interferences caused by evaporated water. After that, samples were placed on the top of a carbon tape creating a carbon bridge between the samples and the carbon tape and they were coated with a thin layer of platinum. Finally, the images were taken applying a voltage of 2 kV.

## Substrates sanitization and preconditioning

To sanitize the PLA-PPy MF substrates prior to the cell culture, they were immersed in 70% ethanol (ET00021000, Scharlab) for 3 washes of 10 min. Following, 4 washes of 10 min with sterile Milli-Q® ultrapure water were applied to remove the ethanol residues.

Finally, the substrates were preconditioned by immersion in Dulbecco's Modified Eagle Medium with a high glucose level (4.5 g/L) (21331020, Life Technologies) supplemented with 10% Fetal Bovine Serum (10270- 106/A3381E, Life Technologies), Penicillin (100 U/mL) and Streptomycin (0.1 mg/mL) (Penicillin/Streptomycin, 15140122, Life Technologies) and incubation at 37°C for 24 h in a humidified atmosphere containing 5% $CO_2$.

## Schwann cells culture on PLA-PPy substrates

The culture of rat Schwann cells (SCs) in passage 5 and BDNF-SEP transfected SCs (eSCs) 24 h after electroporation was performed on PLA-PPy MF substrates (n=12

per group) during 24 h in order to allow the cells to attach to the substrates before the DRG seeding.

Firstly, the culture medium was removed in order to discard dead cells. Next, the cell culture flasks containing the cells were washed with PBS and then a trypsin/EDTA solution (T/E; 25200-072, Life Technologies) was incorporated to break the cell-matrix and cell-cell interactions with the objective of detach cells from the bottom of the flasks. Finally, a centrifugation at 1080 rpm for 5 min was applied and the pellet was resuspended in Schwann cell culture medium (P60123, Innoprot). After counting the number of cells present, SCs and eSCs were seeded with a seeding density of 100,000 cells per substrate through the deposit of 2 drops of 5 µl (50,000 SCs per drop) at equidistant points from the substrate extremities to spread the cells along the substrate, specially at its extremes (**Figure 1**). Each substrate was placed in a different well of a P12 well plate (Nunc A/s, Roskilde, Denmark) containing 1 ml of Schwann cell culture medium. Finally, the samples were introduced in an incubator at 37°C with a humid atmosphere containing 5% $CO_2$ for 24 h, until the next day in which the DRG were seeded.

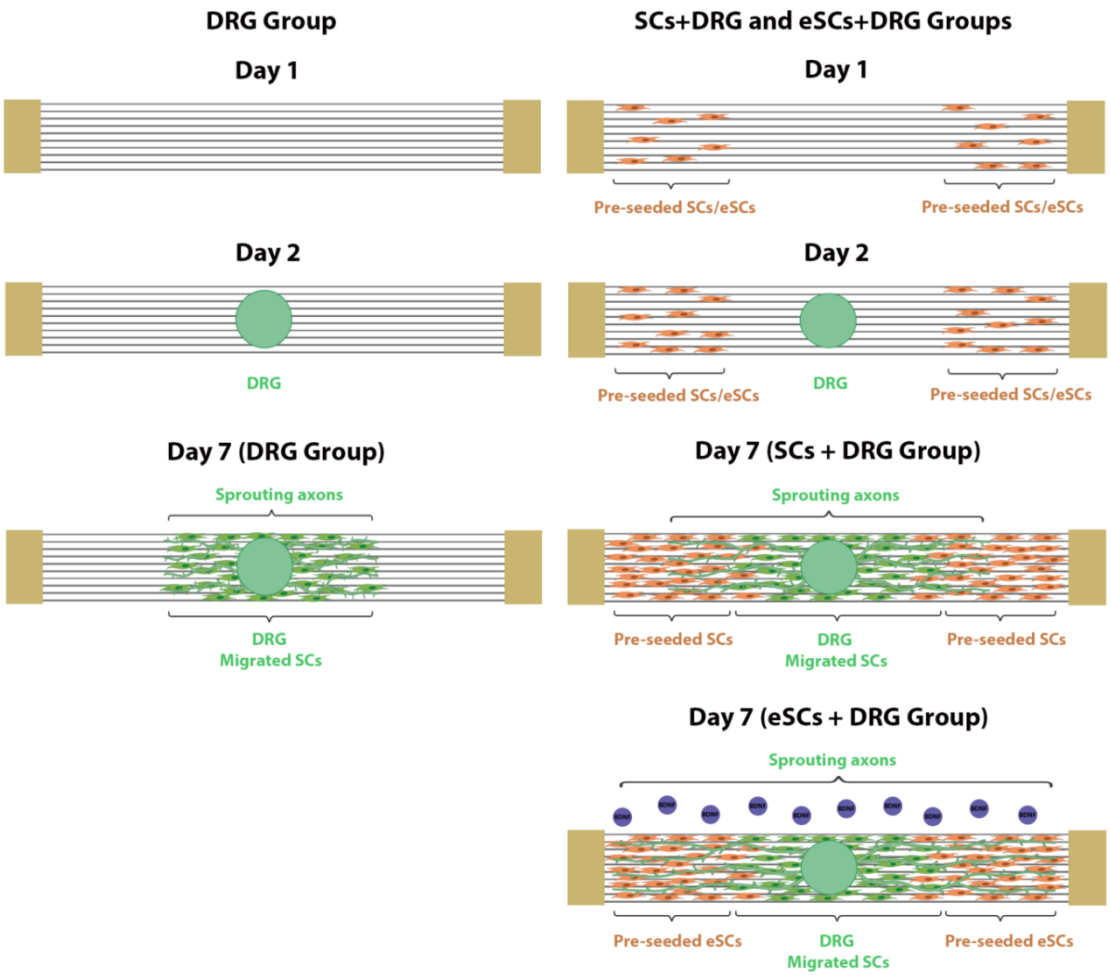


**Figure 1.** Scheme of the different stages of cell culture. First (day 1) the Schwann cells (SCs) and BDNF-SEP transfected Schwann cells (eSCs) are seeded on the substrate extremes for the SCs + DRG and eSCs + DRG groups, respectively. After 24 hours (day 2) one DRG is seeded in the centre of the substrate for all groups. Evaluation is performed after another 5 days of culture (day 7). The neurons present in the DRG body extend their axons over the surface than the SCs covered on the substrate. In the case of the DRG group, the SCs coverage is formed only by SCs that migrated from the DRG body, while in the case of the SCs + DRG and eSCs + DRG groups the SCs coverage is made up of both cells that migrated from the DRG body and the pre-seeded Schwann cells (SCs and eSCs, respectively). The presence of pre-seeded SCs is capable of increasing the speed of axonal growth, since the sprouting axons can be accompanied in their growth by the pre-seeded SCs and are not limited by the speed of migration of the SCs originating from the DRG body. Furthermore, in the case of the eSCs + DRG group, the eSCs possess an increased secretion of BDNF that increases even more the axonal growth rate. Created with *BioRender.com*.

## Dorsal root ganglions culture on PLA-PPy substrates

Dorsal root ganglia (DRG) from 5 days old Wistar rats were extracted and seeded on the centre of PLA-PPy substrates (**Figure 1**). Three different groups were studied (n=12 per group): DRG seeded on substrates without pre-seeded SCs (DRG), DRG seeded on substrates pre-seeded with SCs (SCs + DRG) and DRG seeded on substrates pre-seeded with BDNF-SEP transfected SCs (eSCs + DRG). Each substrate was placed in a different well of a P12 well plate containing 3 ml of neurobasal culture medium (21103-049, Thermo Fisher Scientific) with 2% D-(+)-Glucose 0.56 M (G8644, Sigma-Aldrich), 0.25% L-Glutamine 200 mM (25030024, Thermo Fisher Scientific), Penicillin (100 U/mL) and Streptomycin (0.1 mg/mL) and 1% Fetal Bovine Serum (10270- 106/A3381E, Life Technologies). Finally, the samples were introduced in an incubator at 37°C with a humid atmosphere containing 5% $CO_2$ for 5 days to study the axonal growth and axonal extension.

## Quantification of BDNF secretion

The quantity of BDNF present in the cell culture supernatant of the three studied groups (DRG, SCs + DRG and eSCs + DRG) was quantified after 1, 2 and 5 days of cell culture. For it, 100 µl of culture medium were removed from every well at each time and the total BDNF Quantikine ELISA Kit (DBNT00, R&D Systems) was employed (n=3) for the quantification. A standard curve was performed to convert the obtained absorbance into BDNF concentration.

## Immunostaining of SCs and DRG

After culture, cells were fixed with 4% paraformaldehyde (PFA; 47608, Sigma-Aldrich) for 20 min at room temperature. Then, 3 washes of 10 min with PB 0.1M were carried out and the cell membrane was permeabilized by the use of a blocking buffer

composed of PB 0.1M with 3% bovine serum albumin (BSA; A7906, Sigma-Aldrich) and 0.1% Tween-20 (P1379, Sigma-Aldrich) for 1 h at room temperature.

SCs were stained with rabbit monoclonal anti-S100 beta antibody (ab52642, abcam, 1/200 dilution) and neurons were stained with mouse monoclonal anti-beta III tubulin antibody (ab7751, abcam, 1/500 dilution), and then incubated at 4°C overnight. Secondary antibodies, goat anti-rabbit IgG Alexa Fluor® 555 (A-21429, Thermo Fisher Scientific, 1/200 dilution) and goat anti-mouse IgG Alexa Fluor® 488 (A-11029, Thermo Fisher Scientific, 1/200 dilution), were used for another 2 hours at room temperature in the darkness. Afterwards, samples were incubated with DAPI (D9564, Sigma-Aldrich, 1/1000 dilution) for 10 min to mark the cells' nuclei. The imaging was performed employing an inverse microscope (Axio Observer Z1, Carl Zeiss Microscopy).

## Quantification of axonal extension, axonal sprouting and SCs coverage

The methodology followed for the quantification of axonal extension and axonal sprouting is explained in detail in[49]. Below we proceed to explain it briefly.

Using the ImageJ/FIJI image processing software [77] both the maximum length and the area of axons were measured. On the one hand, the maximum length of axons was considered as the distance between the edge of the DRG body and the end of the longest axon (studying both the maximum of both sides and the sum of both sides). On the other hand, the area of the axons was calculated by subtracting the area of the DRG body from the total area of the DRG.

In addition, the axonal sprouting was quantified by analysing the DRG images using an in-house software developed under MATLAB R2018a (The MathWorks, Inc.). The

centre and the left and right edges of the DRG body were obtained as the maximum point of the relative intensity and as the maximum and minimum values of the relative intensity gradient, respectively. Then, three different parameters were obtained: the distance covered by the Sprouts between the point that corresponds to the centre of the DRG body ($I_{centre}$) and the point where $I_{centre}$ is reduced by 75% ($S_{centre}$, **Equation (1)**), the distance covered by the Sprouts between the point that corresponds to the edge of the DRG ($I_{edge}$) and the point where $I_{edge}$ is reduced by 75% ($S_{edge}$, **Equation (2)**) and the area under the curve (AUC) between the point that corresponds to the edge of the DRG body ($I_{edge}$) and the point where $I_{centre}$ is reduced by 80% ($S_{AUC}$, **Equation (3)**). All the parameters were obtained for both sides of the DRG body and the sum of both values was considered.

$$S_{centre} = Distance\left(I_{centre}, \frac{I_{centre}}{4}\right) \quad (1)$$

$$S_{edge} = Distance\left(I_{edge}, \frac{I_{edge}}{4}\right) \quad (2)$$

$$S_{AUC} = Area\,(I_{edge}, \frac{I_{centre}}{5}) \quad (3)$$

In addition, the length and the area of the SCs coverage formed on the substrate were quantified. These parameters were obtained for both sides of the DRG body and the mean of both values was considered.

## Quantification of axonal alignment

In order to characterize the alignment of axon bundles in the direction of PLA-PPy microfibers, we compared the angle of the microfibers with the angle of the axon bundles that were present over each specific microfiber (using the ImageJ/FIJI image

processing software). After measuring the angle of a microfiber and the angle of the axon bundle that was present over that specific microfiber, the difference between both values was obtained in absolute value (**Figure S1**). The process was repeated for several different microfibers in each sample (n=6) and the mean of those values was obtained. Finally, the mean value for all the samples in each studied group (DRG, SCs+DRG and eSCs+DRG) was obtained. In this procedure only axon bundles that follow the direction of the microfibers are considered, discarding the axon bundles that occasionally cross or jump from one fiber to another.

### Statistical analysis

Results are expressed as mean ± standard error of the mean (SEM). The statistical analysis of the results was performed with GraphPad Prism® software using the one-way ANOVA test together with a multiple sample mean comparison (Tuckey's multiple comparisons test with a significance degree of 95%) in order to reveal significant differences between conditions. Statistically significant differences are indicated by *, **, *** or ****, indicating a p-value below 0.05, 0.01, 0.001 or 0.0001, respectively.

## 8.4. Results and discussion

### Optimization of electroporation parameters of Schwann cells using the pCMV-GFP plasmid

In order to obtain the electroporation parameters that provide the maximum number of transfected living cells, a scan of the electroporation conditions that were considered more critical (applied electric field, amount of plasmid, amount of water and number of cells) was carried out based on our previous experience[74,75]. The rest of

parameters (number, shape, duration and frequency of pulses and time between the electric pulses delivery and the dilution and introduction of the cells in the incubator) remained unmodified. Cuvettes with a volume of 100 µl and a gap between electrodes of 1 mm were used to apply the highest electric field amplitudes with small currents.

| | **C1** | **C2** | **P1** | **P2** | **P3** | **P4** | **P5** | **P6** | **P7** |
|---|---|---|---|---|---|---|---|---|---|
| Number of cells | $5 \cdot 10^5$ | $1 \cdot 10^6$ | $5 \cdot 10^5$ | $5 \cdot 10^5$ | $5 \cdot 10^5$ | $5 \cdot 10^5$ | $5 \cdot 10^5$ | $5 \cdot 10^5$ | $1 \cdot 10^6$ |
| SMEM (% v/v) / Water (% v/v) | 100/0 | 100/0 | 96/4 | 44/56 | 44/56 | 44/56 | 44/56 | 25/75 | 44/56 |
| Plasmid mass (µg) | 0 | 0 | 4.5 | 4.5 | 4.5 | 50 | 50 | 50 | 50 |
| Electric field amplitude (V/cm) | 0 | 0 | 1,000 | 1,000 | 1,500 | 1,500 | 2,000 | 2,000 | 2,000 |

**Table 1.** Detail of the variable parameters of the 2 control conditions and the 7 protocols explored.

P1, P2 and P3 protocols were performed to know the effect of the amount of water and the applied electric field in the case of low quantities of cells and plasmid. On the one hand, it was observed (**Figure 2**) that increasing from 4% to 56% the volume percentage of water (P1 vs P2) considerably improved both the level of transfection and the number of transfected living cells, thanks to increasing the difference in concentrations between the inside and the outside of cells. On the other hand, according to **Figure 2**, increasing the applied electric field from 1,000 V to 1,500 V (P2 vs P3), keeping the volume percentage of water at 56%, further improved the level of transfection and the number of transfected living cells.

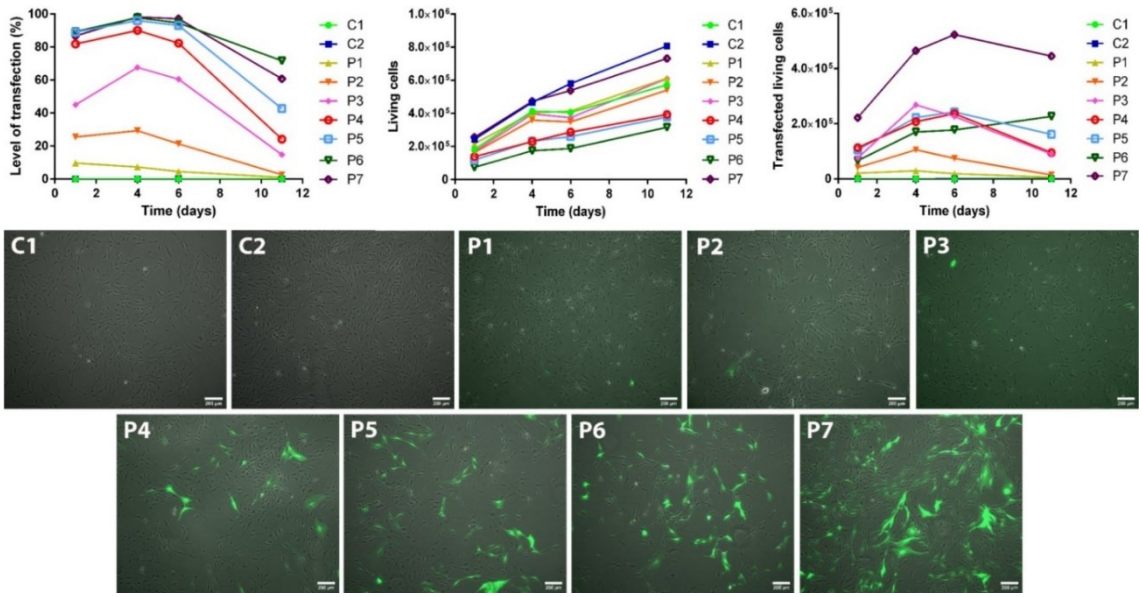


**Figure 2.** Level of transfection, living cells and transfected living cells obtained with the electroporation protocols explained in Table 1. Increasing the quantity of water, the quantity of plasmid and the applied electric field increased the level of transfection but with the cost of a higher cell death. The quantity of transfected living cells was the parameter used to obtain the best balance. To obtain the highest quantity of living cells, a protocol with a high level of transfection (P5) was used but doubling the number of cells (P7). Images of fluorescence microscope after 4 days of cell culture are also included, where can be visually appreciated that the electroporation protocol P7 provides the highest quantity of transfected living cells.

With the P4 protocol the effect of increasing the amount of plasmid was studied, increasing the plasmid mass from 4.5 µg to 50 µg (P3 vs P4). As can be seen in **Figure 2**, it increased the level of transfection, but the higher cell death led to obtain a quantity of transfected living cells similar to that obtained with the P3 protocol.

To study the effect of increasing the applied electric field from 1,500 V to 2,000 V (P4 vs P5) protocol P5 was carried out. As it can be observed in **Figure 2**, an increase of the level of transfection was obtained with a low increase of cell death, resulting in the increase of the transfected living cells. Therefore, SCs are able to tolerate this applied electric field quite well. With the P6 protocol, the volume percentage of water

was increased from 56% to 75% (P5 vs P6). According to **Figure 2**, the higher water content slightly improved the level of transfection, but the higher level of cell death caused a considerable decrease in the number of transfected living cells. Consequently, SCs cannot tolerate this high quantity of water in the cell culture medium.

Since the objective was to achieve the largest number of transfected living cells, the P5 protocol was modified and the number of cells present in the electroporation cuvette was doubled from 500,000 to 1 million cells (protocol P7). The P7 protocol derives from the P5 protocol because the latter provided already a high level of transfection and the highest number of transfected living cells when 500,000 cells were used. As a result, a level of transfection slightly higher to the one obtained with P5 protocol was obtained, with a quite low cell death, using the same amount of DNA. This, together with the higher number of cells that were used, led to a very high number of transfected living cells, doubling the results obtained with P5 protocol. Therefore, the P7 protocol was chosen to carry out the electroporation of SCs with the BDNF-SEP plasmid, since it provided the largest number of transfected living cells per cuvette and per µg of DNA. As it can be observed in **Figure 2**, the survival of the SCs transfected using the P7 protocol is very high, similar to the survival in the C2 control group, at least for 11 days. In addition, the images of fluorescence microscopy reveal not only the level of transfection, but also that the transfected SCs survive well and display a healthy morphology.

## Quantification of secreted BDNF by Schwann cells transfected with the BDNF-SEP plasmid

Using the P7 electroporation protocol (**Table 1**), SCs in passage 5 were transfected with the BDNF-SEP plasmid. Next, SCs and eSCs (24 hours after

electroporation) were seeded on PLA-PPy MF substrates (**Figure 3**) by 2 equidistant drops of 5 µl (50,000 SCs per drop) to spread the cells along the substrate, specially at its extremes. As can be observed in **Figure 3**, PLA-PPy microfibers have a high alignment thanks to the PCL bands that act as fasteners at its extremes. In addition, there is a homogeneous coating with PPy in the form of fine grain texture that can be seen in the whole surface, with just some loose aggregates that mostly disappear with repeated washing. The physico-chemical and electrical properties of the PLA-PPy substrates employed in this study have been extensively characterized in previous papers.[49,50] The presence of the PPy coating was confirmed by Fourier-Transform Infrared Spectroscopy (FTIR), observing the characteristic peaks of PLA, PPy, and pTS.[50] The mass fraction of PPy (3.5 ± 0.7 %) and the thickness of the PPy coating (122 ± 8 nm) were also quantified.[49] Regarding the electrical characterization, a conductivity of 1.36 ± 0.08 S/cm was obtained for the PLA-PPy substrates used in this study.[49] The distribution and the morphology of pre-cultured SCs and DRG on PLA-PPy substrates were also studied.[49] Regarding the SCs, no significant effect of the PPy coating was observed on the distribution, motility, or morphology of these cells.[49] For the DRG, the PPy coating resulted in an additional promoting effect on axonal growth, possibly produced by the greater surface roughness of the PPy-coated substrates that favors the adhesion of the DRG.[49]

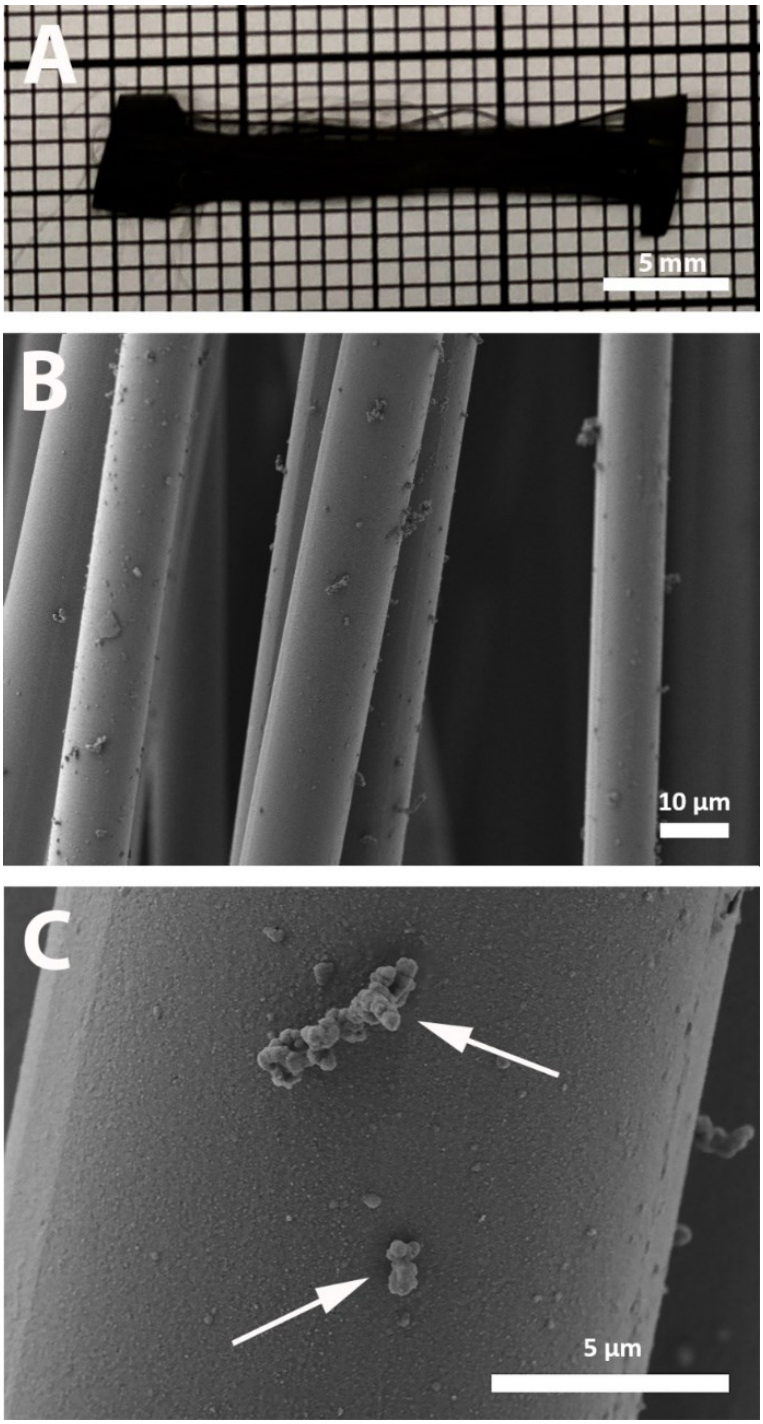


**Figure 3.** Macroscopic (**A**) and microscopic (**B** and **C**) images of PLA-PPy MF substrates used for the co-culture of SCs, eSCs and DRG. PLA MFs (10 µm diameter) were arranged together with a rail shaped form using PCL bands at the extremes that acted as fasteners and coated with PPy via *in situ* polymerization. A homogeneous PPy coating can be observed, forming a fine grain texture. Just some loose aggregates (arrows in C) are present and most of them disappear with repeated washing. Scale bars = 5 mm (A), 10 µm (B) and 5 µm (C).

To allow cell adhesion, SCs and eSCs were cultured on PLA-PPy substrates for 24 hours. Then, DRG were seeded in the middle of three different substrates (one DRG per substrate): substrates without precultured cells (DRG), substrates with a previous culture of SCs during 24 h (SCs + DRG) and substrates with a previous culture of eSCs during 24 h (eSCs + DRG). One, two and five days after the DRG seeding, the quantity of BDNF present in the cell culture supernatant was measured by ELISA. As it can be observed in **Figure 4A**, when DRG are seed alone without precultured SCs (DRG) there is a weak liberation of BDNF from SCs that migrate from the DRG body. However, when DRG are seeded in substrates with precultured SCs (SCs + DRG) there is an increase of the secreted BDNF due to the higher amount of SCs that are present (precultured SCs and SCs that come from the DRG). This corroborates that SCs secrete naturally the BDNF protein, but at low quantities.

Regarding the group with a previous culture of eSCs (eSCs + DRG) the secretion of BDNF to the culture medium greatly increases (**Figure 4B**). As it can be observed, when genetically unmodified SCs are used, the quantity of BDNF present in the medium after 5 days of cell culture is around 8 pg/ml, while when eSCs are used the quantity of BDNF increases to around 800 pg/ml (100 times more). With this result we can confirm that the BDNF-SEP plasmid has been correctly taken up by almost of the cells and that the transcription machinery of SCs is able to express the BDNF protein. In addition, the SCs are able to naturally secrete this excess of BDNF protein into the culture medium, secreting much more BDNF than non-electroporated SCs.

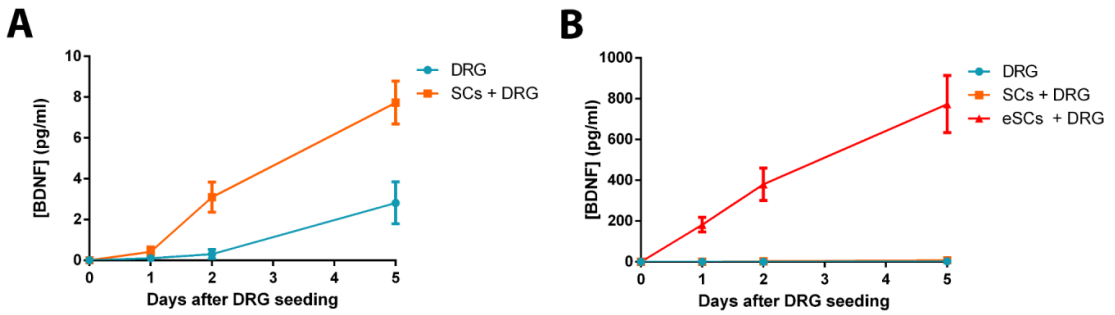


**Figure 4. A**: Magnified detail of B. **B**: Quantity of BDNF present in the culture medium after 1, 2 and 5 days of cell culture. As can be observed, the BDNF gene transfection of SCs increases a lot the quantity of BDNF protein that is secreted to the culture medium. Values are expressed as mean ± SEM.

In order to check the presence of precultured SCs and eSCs, fluorescent images (β III Tubulin, DAPI and S 100 β) of samples after 5 days of DRG culture were studied (**Figure 5**). Firstly, a global image of each sample is presented for each group (A-C for the DRG group, D-F for the SCs + DRG group and G-I for the eSCs + DRG group). Secondly, two different zones are presented for each sample: one at the end of the axons (A1-C1 for the DRG group, D1-F1 for the SCs + DRG group and G1-I1 for the eSCs + DRG group) and another far away from the axons (A2-C2 for the DRG group, D2-F2 for the SCs + DRG group and G2-I2 for the eSCs + DRG group).

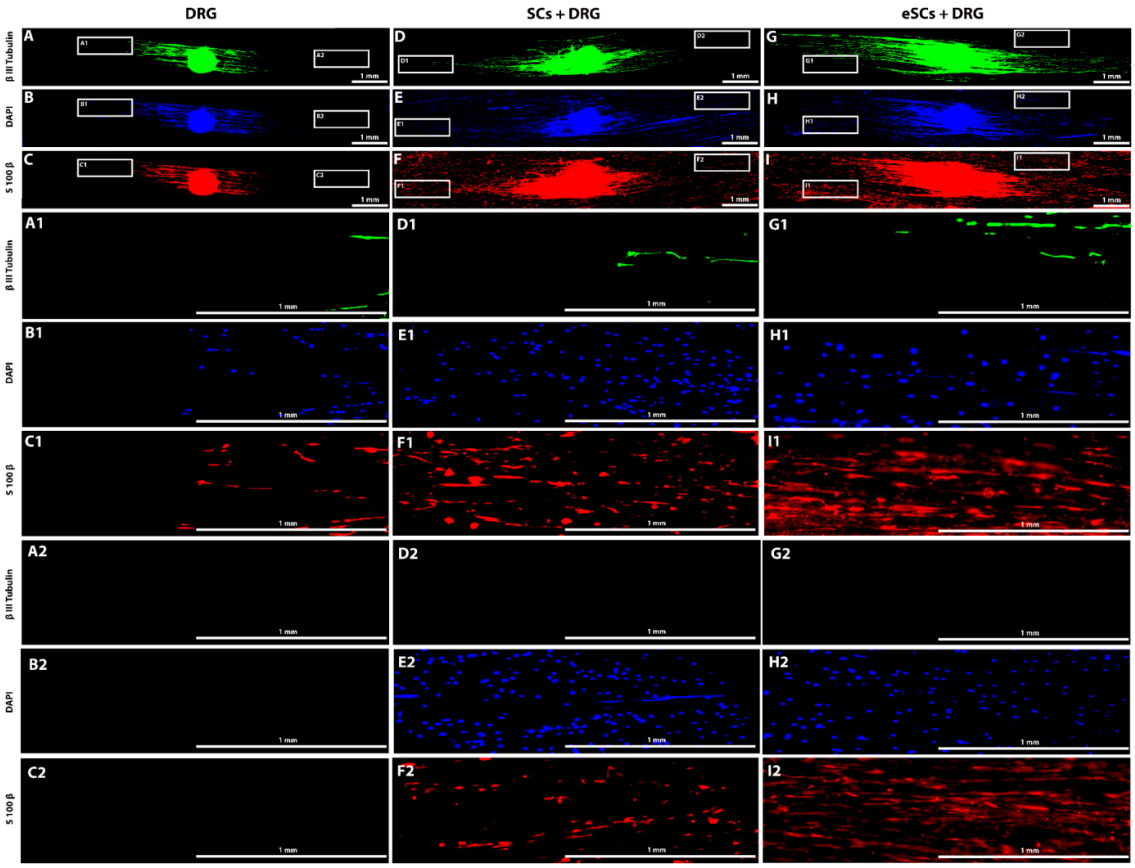


**Figure 5.** Fluorescent microscope images of samples after 5 days of DRG culture. Samples are marked with β III Tubulin to observe the neurons (green colour), DAPI to observe the cell nuclei (blue colour) and S 100 β to observe the Schwann cells (red colour). Firstly, a global image of one representative sample is presented for each studied group: DRG (A-C), SCs + DRG (D-F) and eSCs + DRG (G-I). As can be observed, there is a great increment of axonal extension and axonal sprouting when eSCs are used (G) when compared with the sample without SCs (A). For the sample with non-electroporated SCs (D) there is an intermediate behaviour. Therefore, the co-culture of the DRG with non-electroporated SCs increases axonal growth, but the use of eSCs increases this growth even more. The presence of pre-cultured SCs and eSCs is corroborated with image details at two different places of the sample: one at the end of the axons (A1-C1 for the DRG group, D1-F1 for the SCs + DRG group and G1-I1 for the eSCs + DRG group) and another far away from the axons (A2-C2 for the DRG group, D2-F2 for the SCs + DRG group and G2-I2 for the eSCs + DRG group). As can be observed, at the DRG group SCs are only present very near to the axons, indicating that the SCs are migrating from the DRG body along with the axons. However, for SCs + DRG and eSCs + DRG samples, the SCs are present far away from the axons, indicating that those cells are the pre-seeded ones, and not SCs that come from the DRG body. Scale bars = 1 mm.

For the DRG group the SCs are only present very near to the axons, with no SCs in areas where axons are not present (**Figure 5A-C**). This indicates that axons grow together with SCs that migrate from the DRG body, and therefore, the presence of SCs is a necessary requirement for axonal growth. However, for the SCs + DRG (**Figure 5D-F)** and eSCs + DRG (**Figure 5G-I**) groups, SCs are present far away from the axons, indicating that these cells are the pre-seeded ones, and not SCs that come from the DRG body. In order to confirm this presence of the pre-seeded SCs (both unmodified and genetically transfected) we measured the length and the area of the SCs coverage present on the substrate after 5 days of DRG culture (**Figure 6**). Both the length and the area of the SCs coverage are clearly larger for the groups with pre-seeded SCs (SCs + DRG and eSCs + DRG), confirming the presence of the pre-seeded SCs. Furthermore, there is no statistically significant difference in the length or in the area covered by the SCs between the SCs + DRG and eSCs + DRG groups, which is indicative of the good survival of the eSCs.

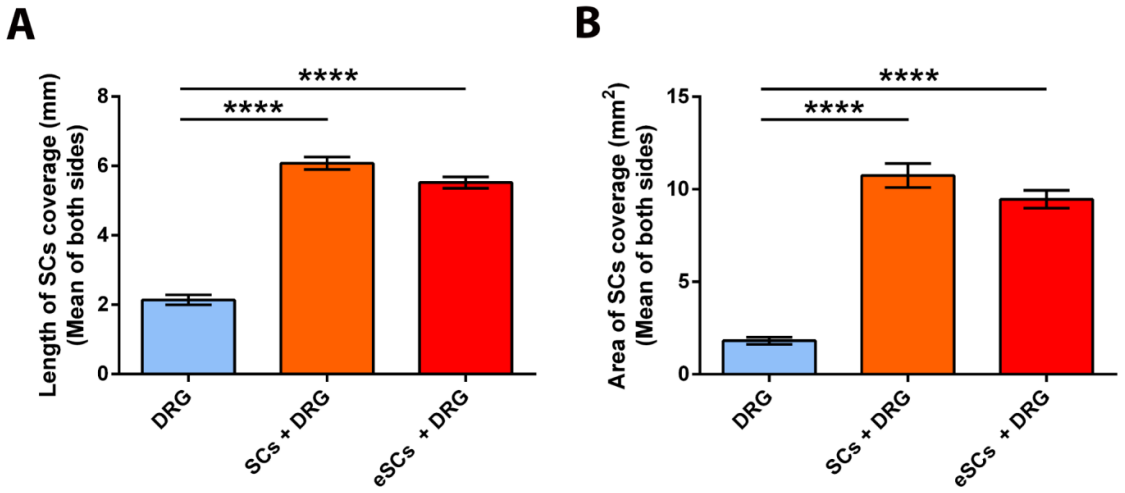


**Figure 6.** Length (A) and area (B) of the SCs coverage present on the substrate after 5 days of DRG culture. As can be observed, the presence of the pre-seeded SCs and eSCs is confirmed by the greater length and area covered by SCs on the substrate for the SCs + DRG and eSCs + DRG groups, respectively. Values are expressed as mean ± SEM.

In addition, there is a great increment of axonal growth when precultured eSCs are used (eSCs + DRG group) when compared with the DRG cultured without precultured SCs (DRG group) (**Figure 5**). For the DRG + SCs group there is an intermediate behaviour. This indicates that the precultured SCs are able to support the axons, increasing the axonal growth rate. In addition, the increased secretion of BDNF by eSCs to the culture medium increases even more the axonal growth rate.

## Quantification of axonal extension and axonal sprouting on PLA-PPy substrates

In order to quantify the axonal growth on the three different groups (DRG, SCs + DRG and eSCs + DRG), both the axonal extension and the axonal sprouting were quantified. It is important to study these two characteristics because the axonal extension refers to the maximum length that axons can reach, and the axonal sprouting refers to the quantity of axons that are emerging from the DRG body. To do so, six different parameters were measured from fluorescent microscope images (β III Tubulin) of samples after 5 days of DRG culture. On the one hand, the maximum length of axons (maximum and sum of both sides) and the area of axons were obtained to quantify the axonal extension. On the other hand, the parameters $S_{centre}$, $S_{edge}$ and $S_{AUC}$ were obtained to study the axonal sprouting. As it can be observed in **Figure 5**, the high alignment of PLA-PPy substrates results in a high directionality of axons in the direction of the fibers, maximizing the lineal distance that axons travel. This high directionality was quantified by measuring the angular difference between the direction of axon bundles and the direction of microfibers, obtaining a very low difference between both directions: 1.4 ± 0.2 °, 1.5 ± 0.2 °, and 1.2 ± 0.1 ° for the DRG, SCs + DRG and eSCs + DRG groups, respectively.

As it can be observed in **Figure 7**, the presence of precultured SCs is critical in order to increase the axonal extension, since the maximum length of axons (sum of both sides) displays a 91.8% increase and the area of axons a 126.2% increase when the SCs are present. According to **Figure 5**, when DRG are seeded alone without precultured SCs, the axons arrive as far as the SCs that migrate from the DRG body. This proves that axons do not grow without the direct support of SCs and so their growth rate depends directly on the migration rate of SCs from the DRG body. However, when precultured SCs are present in areas far away from the DRG body, axons are able to increase their growth rate thanks to the support of the precultured SCs cells, since axons do not have to wait for SCs from the DRG. The effect of precultured SCs is also noticeable for axonal sprouting, since an increase in $S_{centre}$, $S_{edge}$ and $S_{AUC}$ of 57.1%, 25.8% and 68.3%, respectively, is observed when precultured SCs are present. This indicates an effect of precultured SCs that are near the DRG body, so the axons do not need to wait for the SCs migration from the DRG body and can start to grow earlier.

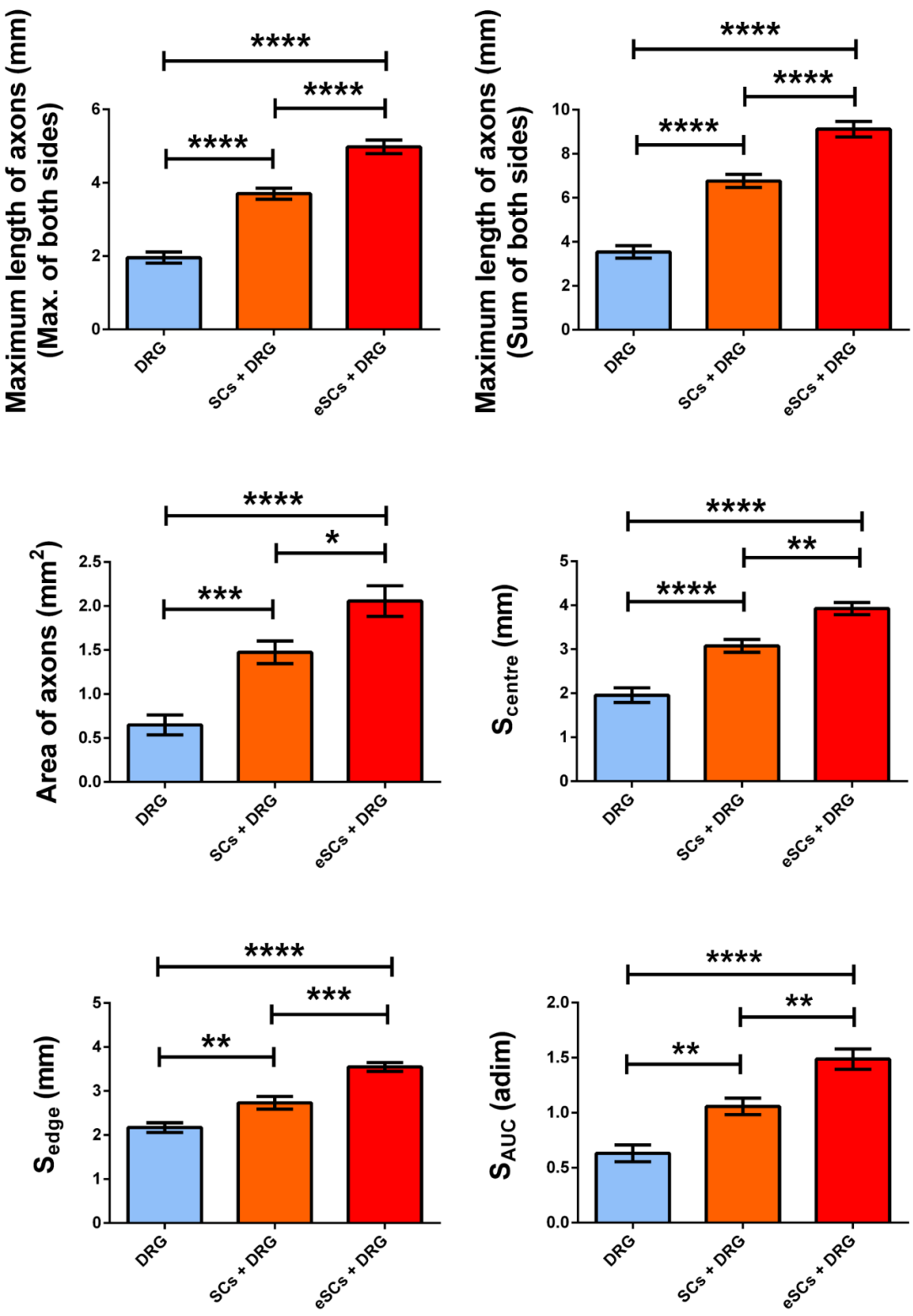


**Figure 7.** Quantification of axonal extension (maximum length of axons and area of axons) and axonal sprouting ($S_{centre}$, $S_{edge}$ and $S_{AUC}$) after 5 days of DRG culture. The higher values of BDNF protein secreted by eSCs to the culture medium enhanced both axonal extension and axonal sprouting. Values are expressed as mean ± SEM.

Regarding the effects of eSCs, we observe that, in addition to the effect observed when non-electroporated SCs are used, the higher concentration of BDNF that is present in the cell culture medium when eSCs are used is able to further increase the axonal growth, observing an increase of both axonal extension and axonal sprouting. For the eSCs + DRG group, an increase of 34.7% and 40.1% was observed in the maximum length of axons (sum of both sides) and in the area of axons, respectively, comparing with the SCs + DRG group. Therefore, the BDNF-rich culture medium produces an additional increase in the growth rate of axons, so they can growth faster. In addition, an increase of 27.6%, 30.0% and 40.6% was observed for $S_{centre}$, $S_{edge}$ and $S_{AUC}$, respectively, for the eSCs + DRG group when compared with the SCs + DRG group. This shows an increase of axonal sprouting, so more axons migrate from the DRG body.

Thus, with the eSCs + DRG group we are observing the combined effect of the high alignment of the substrate, the preculture of SCs and the continuous release of BDNF by these cells that increases neuronal regeneration and protection. Therefore, this group would be the one considered to be used as a device for the regeneration of lesions in the nervous system. Furthermore, it should be noted that thanks to the SCs electrotransfection we are achieving an effective and regular release of large amounts of BDNF during the first 10-15 days after its implantation *in vivo*. This is of great importance since the first days after the injury occurs are the most critical ones in the process of remodelling and regenerating an injury of the nervous system. In addition, thanks to the continuous release of BDNF by SCs, it is possible to have a stable BDNF-rich cell environment, solving the problem of the short half-life and the rapid diffusion of BDNF when it is supplied directly in the lesion and avoiding the use of a continuous infusion pump which could lead to greater wound complications and an increased risk of infection[78,79].

# 8.5. Conclusions

We have obtained a SCs electroporation protocol that provides a high level of transfection with low cell death, obtaining a large number of live transfected cells. Thanks to this protocol, SCs have been successfully transfected with a plasmid encoding the BDNF protein, which is necessary for the continued survival and maintained phenotype of neurons, promotes survival of dorsal root ganglion neurons, enhances neurogenesis and promotes nerve healing and axonal growth, improving axonal regeneration. Electroporated SCs have been able to both express higher quantities of BDNF protein and secrete them naturally into the culture medium. This has not been previously reported using electroporation techniques with this type of cells *in vitro*. In addition, the quantity of BDNF secreted by electroporated SCs was very high, multiplying by 100 the level of BDNF secretion of non-electroporated SCs.

The co-culture of DRG with non-electroporated and electroporated SCs revealed that the use of PLA-PPy MF substrates precultured with non-electroporated SCs increases both axonal extension and axonal sprouting, but when electroporated SCs are used, there is an additional increment of them. The preculture of SCs is critical so that the axons that grow from the DRG neurons do not have to wait for the SCs that migrate from the DRG body and can be accompanied by the precultured SCs that are present on the substrate, being able to considerably increase its growth rate. Furthermore, when the precultured SCs that are present on the substrate have been previously electroporated with the plasmid encoding the BDNF protein, they release large additional quantities of BDNF to the culture medium, which helps to obtain an additional increase of axonal growth.

Therefore, our system based on a PLA-PPy highly aligned microfiber substrate pre-seeded with electroporated SCs with an increased BDNF secretion is capable of

both guiding and accelerating axonal growth and regeneration. For this, the device can be of application for the treatment of injuries of the nervous system, both central and peripheral. The device can be used either alone or in combination with other devices such as conduits for an inside nerve guidance. In addition, the electrical conductivity of PLA-PPy microfibers allows the electrical stimulation of the device in future studies.

## 8.6. Author contribution statement

F.G.R.: Methodology, Software, Formal analysis, Investigation, Writing – Original Draft, Visualization. F.M.A.: Methodology, Writing – Review & Editing, Supervision. J.M.E.: Writing – Review & Editing, Supervision, Funding acquisition. M.M.P.: Conceptualization, Writing – Review & Editing, Supervision, Funding acquisition. L.M.M.: Methodology, Writing – Review & Editing, Supervision, Funding acquisition. C.M.-R.: Conceptualization, Methodology, Writing – Review & Editing, Supervision, Funding acquisition.

## 8.7. Conflicts of interest

The authors declare no competing interests.

## 8.8. Acknowledgements

The authors acknowledge financing from the Spanish Government's State Research Agency (AEI) through projects DPI2015-72863-EXP and RTI2018-095872-B-C22/ERDF. FGR acknowledges the scholarship FPU16/01833 and the short stay mobility aid EST18/00524 of the Spanish Ministry of Universities. FGR also acknowledges the hosting at the Vectorology and Anti-cancer Therapies Centre (UMR 8203 CNRS). We thank the Electron Microscopy Service at the UPV, where the FESEM images were obtained.

# 8.9. References


1. E. a Huebner, S. M. Strittmatter, *Results Probl. Cell Differ.* **2009**, *48*, 339.
2. K. S. Houschyar *et al.*, *Plast. Surg. Int.* **2016**, *2016*, 1.
3. W. Daly, L. Yao, D. Zeugolis, A. Windebank, A. Pandit, *J. R. Soc. Interface* **2012**, *9*, 202.
4. G. C. W. de Ruiter, M. J. A. Malessy, M. J. Yaszemski, A. J. Windebank, R. J. Spinner, *Neurosurg. Focus* **2009**, *26*, E5.
5. M. D. Tang-Schomer, *Brain Res.* **2018**, *1678*, 288.
6. M. D. Sarker, S. Naghieh, A. D. McInnes, D. J. Schreyer, X. Chen, *Prog. Neurobiol.* **2018**, *171*, 125.
7. I. A. Kim *et al.*, *J. Biosci. Bioeng.* **2006**, *101*, 120.
8. A. W. English, G. Schwartz, W. Meador, M. J. Sabatier, A. Mulligan, *Dev. Neurobiol.* **2007**, *67*, 158.
9. M. R. Freeman, *Curr. Opin. Neurobiol.* **2006**, *16*, 119.
10. E. Pompili *et al.*, *Eur. J. Histochem.* **2020**, *64*.
11. K. R. Jessen, R. Mirsky, A. C. Lloyd, *Cold Spring Harb. Perspect. Biol.* **2015**, *7*, 1.
12. J. A. Gomez-Sanchez *et al.*, *J. Neurosci.* **2017**, *37*, 9086.
13. M. Bradl, H. Lassmann, *Acta Neuropathol.* **2010**, *119*, 37.
14. D. M. McTigue, R. B. Tripathi, *J. Neurochem.* **2008**, *107*, 1.
15. N. El Seblani, A. S. Welleford, J. E. Quintero, C. G. van Horne, G. A. Gerhardt, *J. Neurosci. Methods* **2020**, *335*, 108623.
16. K. R. Jessen, P. Arthur-Farraj, *Glia* **2019**, *67*, 421.
17. G. Nocera, C. Jacob, *Cell. Mol. Life Sci.* **2020**, 1, doi:10.1007/s00018-020-03516-9.

18. A. H. Nagahara, M. H. Tuszynski, *Nat. Rev. Drug Discov.* **2011**, *10*, 209.

19. C. Zuccato, E. Cattaneo, *Nat. Rev. Neurol.* **2009**, *5*, 311.

20. D. K. Binder, H. E. Scharfman, *Growth Factors* **2004**, *22*, 123.

21. K. Hanamura, A. Harada, R. Katoh-Semba, F. Murakami, N. Yamamoto, *Eur. J. Neurosci.* **2004**, *19*, 1485.

22. T. Lopatina *et al.*, *PLoS One* **2011**, *6*.

23. P. Lu, L. L. Jones, M. H. Tuszynski, *Exp. Neurol.* **2005**, *191*, 344.

24. R. M. Lindsay, *J. Neurosci.* **1988**, *8*, 2394.

25. S. Liu *et al.*, *Acta Biomater.* **2017**, *60*, 167.

26. S. S. Gill *et al.*, *Nat. Med.* **2003**, *9*, 589.

27. G. J. R. Delcroix, P. C. Schiller, J. P. Benoit, C. N. Montero-Menei, *Biomaterials* **2010**, *31*, 2105.

28. E. M. André, C. Passirani, B. Seijo, A. Sanchez, C. N. Montero-Menei, *Biomaterials* **2016**, *83*, 347.

29. P. Menei, C. Montero-Menei, S. R. Whittemore, R. P. Bunge, M. B. Bunge, *Eur. J. Neurosci.* **1998**, *10*, 607.

30. S. T. Sayers, N. Khan, Y. Ahmed, R. Shahid, T. Khan, *J. Mol. Neurosci.* **1998**, *10*, 143.

31. T. K. Kim, J. H. Eberwine, *Anal. Bioanal. Chem.* **2010**, *397*, 3173.

32. A. Pfeifer, I. M. Verma, *Annu. Rev. Genomics Hum. Genet.* **2001**, *2*, 177.

33. S. Hacein-Bey-Abina *et al.*, *N. Engl. J. Med.* **2002**, *346*, 1185.

34. J. Roesler *et al.*, *Blood* **2002**, *100*, 4381.

35. N. B. Woods *et al.*, *Blood* **2003**, *101*, 1284.

36. S. Hacein-Bey-Abina *et al.*, *N. Engl. J. Med.* **2003**, *348*, 255.

37. C. Rosazza, S. H. Meglic, A. Zumbusch, M.-P. Rols, D. Miklavcic, *Curr. Gene*

*Ther.* **2016**, *16*, 98.

38. M. Aspalter *et al.*, *J. Neurosci. Methods* **2009**, *176*, 96.

39. H. B. Wang, M. E. Mullins, J. M. Cregg, C. W. McCarthy, R. J. Gilbert, *Acta Biomater.* **2010**, *6*, 2970.

40. S. Gnavi *et al.*, *Mater. Sci. Eng. C* **2015**, *48*, 620.

41. P. M. Tsimbouri, L. E. McNamara, E. V. Alakpa, M. J. Dalby, L. A. Turner, *Tissue Eng. Second Ed.* **2014**, doi:10.1016/B978-0-12-420145-3.00007-9.

42. H. Amani *et al.*, *Adv. Mater. Interfaces* **2019**, *6*, 1.

43. W. Zhu, F. Masood, J. O'Brien, L. G. Zhang, *Nanomedicine Nanotechnology, Biol. Med.* **2015**, *11*, 693.

44. Y. S. Lee, G. Collins, T. Livingston Arinzeh, *Acta Biomater.* **2011**, *7*, 3877.

45. A. Markus, T. D. Patel, W. D. Snider, *Curr. Opin. Neurobiol.* **2002**, *12*, 523.

46. P. Lu, M. H. Tuszynski, *Exp. Neurol.* **2008**, *209*, 313.

47. M. Lykissas, A. Batistatou, K. Charalabopoulos, A. Beris, *Curr. Neurovasc. Res.* **2007**, *4*, 143.

48. B. S. Bregman, M. McAtee, H. N. Dai, P. L. Kuhn, *Exp. Neurol.* **1997**, *148*, 475.

49. F. Gisbert Roca, J. Más Estellés, M. Monleón Pradas, C. Martínez-Ramos, *Int. J. Biol. Macromol.* **2020**, *163*, 1959.

50. F. Gisbert Roca, A. García-Bernabé, V. Compañ Moreno, C. Martínez-Ramos, M. Monleón Pradas, *Macromol. Mater. Eng.* **2020**, 2000584, doi:10.1002/mame.202000584.

51. D. E. Henton, P. Gruber, J. Lunt, J. Randall, *Nat. Fibers, Biopolym. Biocomposites* **2005**, *48674*, 527.

52. J. Lunt, *Polym. Degrad. Stab.* **1998**, *3910*, 145.

53. Y. Ramot, M. Haim-Zada, A. J. Domb, A. Nyska, *Adv. Drug Deliv. Rev.* **2016**,

*107*, 153.

54. D. da Silva *et al.*, *Chem. Eng. J.* **2018**, *340*, 9.

55. L. X. Wang, X. G. Li, Y. L. Yang, *React. Funct. Polym.* **2001**, *47*, 125.

56. J. Y. Lee, C. A. Bashur, A. S. Goldstein, C. E. Schmidt, *Biomaterials* **2009**, *30*, 4325.

57. A. Esfandiari, *World Appl. Sci. J.* **2008**, *3*, 470.

58. T. H. Le, Y. Kim, H. Yoon, *Polymers (Basel).* **2017**, *9*.

59. M. Mattioli-Belmonte *et al.*, *Mater. Sci. Eng. C* **2005**, *25*, 43.

60. G. Sabouraud, S. Sadki, N. Brodie, *Chem. Soc. Rev.* **2000**, *29*, 283.

61. C. Li, H. Bai, G. Shi, *Chem. Soc. Rev.* **2009**, *38*, 2397.

62. S. Aznar-Cervantes *et al.*, *Bioelectrochemistry* **2012**, *85*, 36.

63. J. F. Zhou *et al.*, *Neural Regen. Res.* **2016**, *11*, 1644.

64. P. M. George *et al.*, *Biomaterials* **2005**, *26*, 3511.

65. C. E. Schmidt, V. R. Shastri, J. P. Vacanti, R. Langer, *Proc. Natl. Acad. Sci. U. S. A.* **1997**, *94*, 8948.

66. J. Huang, Z. Ye, X. Hu, L. Lu, Z. Luo, *Glia* **2010**, *58*, 622.

67. H. T. Nguyen *et al.*, *J. Biomed. Mater. Res. - Part A* **2014**, *102*, 2554.

68. Y. Wang *et al.*, *Chin. Med. J. (Engl).* **2011**, *124*, 2361.

69. Y. Zou *et al.*, *ACS Appl. Mater. Interfaces* **2016**, *8*, 12576.

70. Y. Xu, Z. Huang, X. Pu, G. Yin, J. Zhang, *Cell Prolif.* **2019**, *52*, 1.

71. G. T. Christopherson, H. Song, H. Q. Mao, *Biomaterials* **2009**, *30*, 556.

72. M. A. Woodruff, D. W. Hutmacher, *Prog. Polym. Sci.* **2010**, *35*, 1217.

73. C. X. F. Lam, D. W. Hutmacher, J. T. Schantz, M. A. Woodruff, S. H. Teoh, *J. Biomed. Mater. Res. A* **2009**, *90*, 906.

74. A. Liew *et al.*, *Hum. Gene Ther. Methods* **2013**, *24*, 289.

75. L. L. Lesueur, L. M. Mir, F. M. André, *Mol. Ther. - Nucleic Acids* **2016**, *5*, e291.

76. S. C. Harward *et al.*, *Nature* **2016**, *538*, 99.

77. J. Schindelin *et al.*, *Nat. Methods* **2012**, *9*, 676.

78. J. Guan *et al.*, *Biomaterials* **2012**, *33*, 1386.

79. E. Palasz *et al.*, *Int. J. Mol. Sci.* **2020**, *21*.

## 8.10. Supporting information

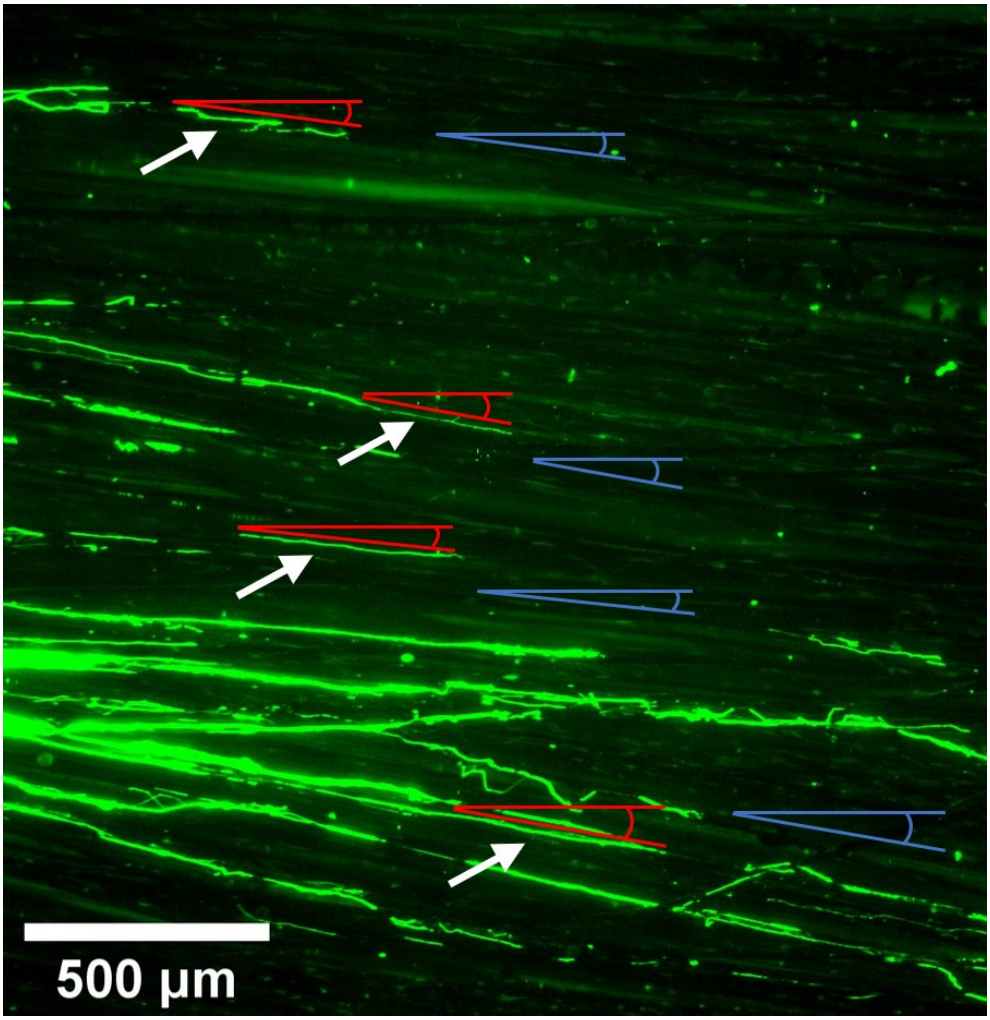


**Figure S1.** Image showing in detail the process followed to measure the angular difference between the direction of axon bundles and the direction of PLA-PPy microfibers. The angle of selected axon bundles (white arrows) is displayed in red colour, while the angle of near PLA-PPy microfibers is displayed in blue colour.

# 9. General discussion

# 9.1. Dimensional adaptation of the nerve guidance conduits

Hyaluronic acid (HA) conduits with an internal diameter of 400 μm were previously developed by the research group for *in vitro* studies, but it was necessary to scale the dimensions to adapt them to the dimensions of the rabbit sciatic nerve. For this, it was necessary to increase the internal diameter from 400 μm to 4 mm, which implied several problems to maintain a suitable wall thickness, porosity, and continuity of the conduit. This implied a change in the conduit manufacturing, since the type of mold used for small conduits did not allow obtaining valid conduits of the desired dimensions because they fractured and did not have a homogeneous wall thickness.

Therefore, it was necessary to manufacture a new type of mold, going from using a 1-piece polytetrafluoroethylene (PTFE) mold with open channels and a disposable policaprolactone (PCL) fiber inside of each channel to using a 2-piece PTFE mold, one piece with cylindrical channels and another piece with solid rods allocated in the center of the channels (**Figure 1**). In this way, it was possible to obtain continuous conduits with the desired dimensions and with a thin and homogeneous wall, while maintaining the desired porosity of the conduit walls and with a smooth internal wall of the conduit that avoided the loss of the cells seeded inside.

It is important to highlight that the method for the manufacturing of HA conduits is highly customizable and it is possible to obtain different wall thicknesses depending on the mold used. Likewise, the procedure for the crosslinking of HA with divinyl sulfone (DVS) is also adjustable, obtaining a more or less rigid scaffold. The mold used, as well as the concentrations and reaction times employed in the crosslinking procedure,

were adjusted to obtain a hydrogel with a high swelling ratio in water, but which in turn was sufficiently resistant to allow handling and had a suitable wall thickness.

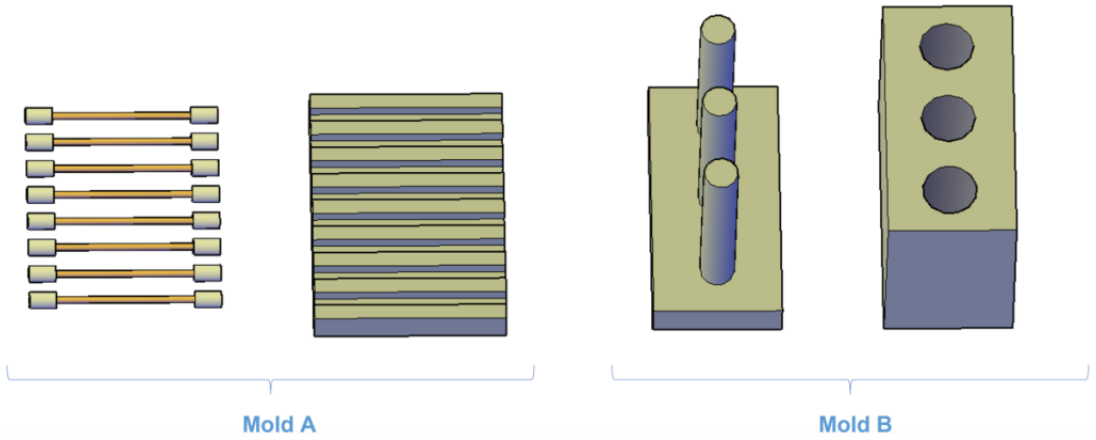


**Figure 1.** Mold A: Mold used for manufacturing HA conduits with an internal diameter of 400 µm. Mold B: Mold developed for manufacturing HA conduits with an internal diameter of 4 mm.

Increasing the internal diameter of the HA conduits also required an adaptation of the Schwan cells (SCs) seeding and culture protocol, since the previous protocol was not adequate to obtain a continuous SCs sheath inside the larger HA conduits. Increasing the curvature radius hinders the SCs coverage of the lumen of the conduits and it was unknown if it was possible to obtain a continuous internal sheath of pre-seeded SCs inside bigger HA conduits. This was achieved with 400 µm internal diameter HA conduits, but with larger conduits it was necessary to adapt the number of SCs seeded inside the conduit and the total culture time to obtain a complete and homogeneous sheath. Thus, it was necessary to go from seeding 17,000 cells for every mm of conduit length to 83,000 cells for every mm of conduit length, for a culture time of 10 days.

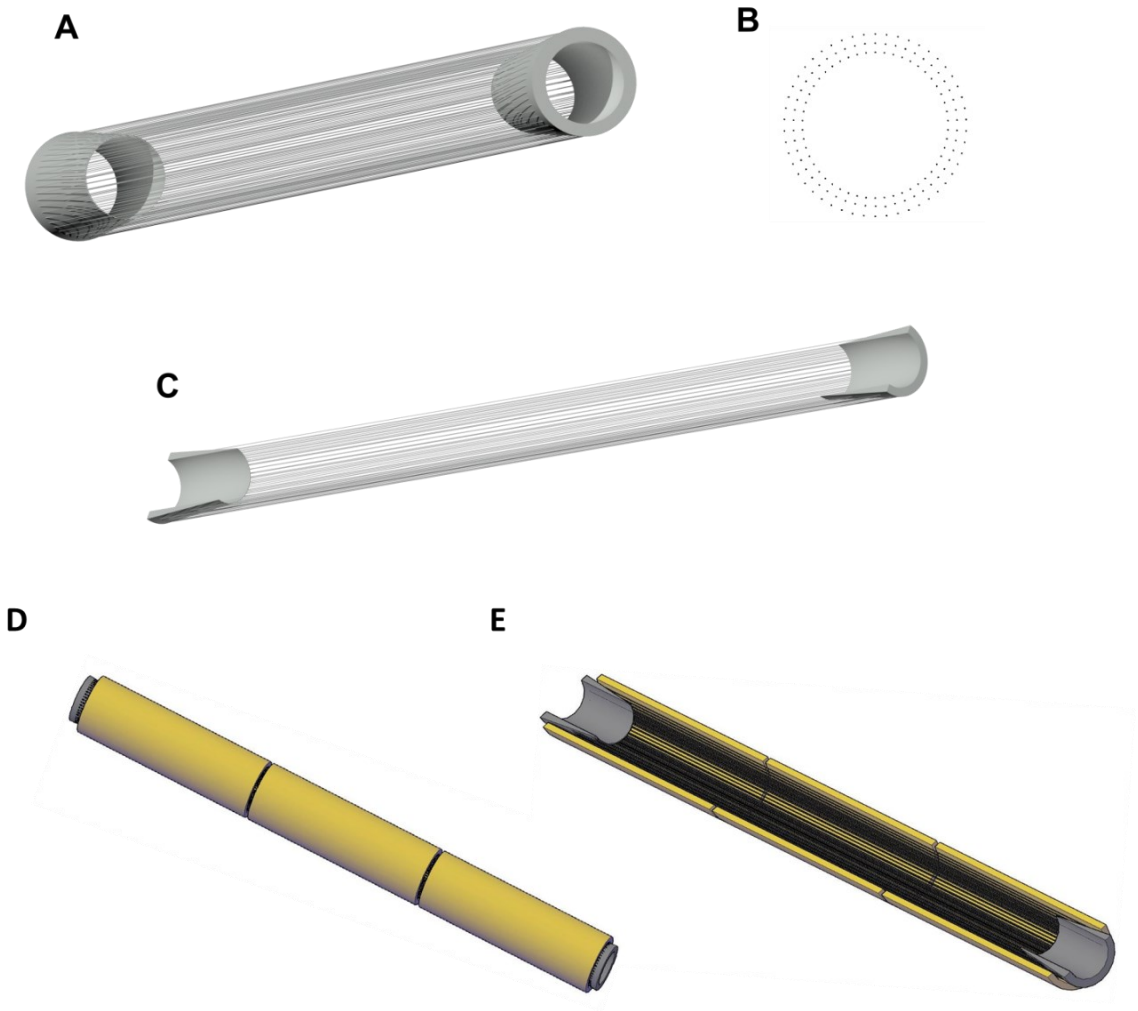


**Figure 2**. **A**: Tridimensional representation of the fibrillar tubular structure of PLA microfibers. The conical fastening structures can be observed at the extremes of the microfibers. **B**: Cross-section of the fibrillar tubular structure representing the several layers of PLA microfibers. **C**: Longitudinal section of the fibrillar tubular structure. **D**: Representation of the whole multimodular device with the fibrillar structure inside the lumen of three HA modules. The extremes of the fastening structures are outside the HA conduits to allow their suture to the nerve stumps. **E**: Longitudinal section of the multimodular device, showing the distribution of the PLA microfibers inside the HA conduits.

Regarding the polylactic acid (PLA) fibers used in the case of HA conduits with an internal diameter of 400 µm, it was not necessary any special procedure to maintain the PLA fibers in the center of the lumen of the conduit. However, with bigger HA

conduits, it was necessary to develop an auxiliary structure to obtain a uniform distribution and separation of the PLA fibers in the lumen of the HA conduit, avoiding their agglomeration in a reduced location of the lumen. For this, a system that achieved a tube-shaped distribution of the PLA fibers was developed, so that they were arranged parallel to the longitudinal axis of the lumen thanks to two conical fastening structures at the extremes (**Figure 2**). In this way the fibers were arranged surrounding the lumen, forming several layers of fibers. In addition, the two fastening structures allowed, on the one hand, to maintain the structure of the multimodular device when using more than one HA module and, on the other hand, to offer a more resistant surface that allowed the device to be sutured to both stumps of the damaged nerve, since the suture on the HA conduits is not viable due to their high fragility (**Figure 2**).

## 9.2. Application in rabbit sciatic nerve injury model

A group of rabbits underwent surgery to ensure that the sciatic nerve was large enough to insert at least two HA modules. The 15 mm-long unimodular conduit was compared with the multimodular conduit with two 7.5 mm-long HA modules and these, in turn, with the multimodular conduit with pre-seeded SCs.

As a result, it was observed that the multimodular conduit presented a greater nerve regeneration than the unimodular conduit. This could be related to the greater vascularization observed for the multimodular model, which allows a better supply of oxygen via blood circulation that is essential during nerve regeneration [1,2]. When a nerve guidance conduit is implanted, the vascularization between the nerve stumps only occurs longitudinally, not perpendicularly from the surrounding tissues. For this reason, the necrosis in the center of the conduit before the host's blood vessels can invade the entire graft is a common limitation for long nerve guidance conduits [1–3]. Thus, the multimodular approach is critical to achieve a good vascularization in the central part of

long nerve guidance conduits, since it offers a slight separation between modules (around 100 μm) that allows blood vessels growing around the conduit to enter the interior of the device in the central areas, leading to a greater blood supply inside the device that favors axonal growth.

Likewise, as previously observed *in vitro*, adding pre-seeded SCs considerably improved nerve regeneration compared to the multimodular model without pre-seeded SCs. SCs are cells of the nerve glia that form the Büngner bands, forming temporary channels that support and guide the regeneration of axons. In addition, SCs naturally release neurotrophic factors that enhance axonal growth, such as NGF, BDNF or NT-3, creating a microenvironment that favors nerve regeneration [4–8].

## 9.3. Upgrading developments

With the aim of improving the results of the *in vivo* study, different upgrades were studied to try to increase the mechanical and biological properties of the modular conduits, as well as to increase the number of axons and its growth velocity. To increase the mechanical and biological properties of HA conduits, the incorporation of proteins was studied, specifically the incorporation of silk fibroin. Regarding the strategies to increase axonal growth, literature shows different cues that can be incorporated to the multimodular device to improve and accelerate nerve regeneration. They can be grouped in biochemical, chemical, electrical, and mechanical stimulations and they have shown to increase axonal growth and nerve regeneration *in vitro* and *in vivo* [9–20]. This work has focused on the development of an electrical stimulation system and on the improvement of the biochemical stimulation that SCs provide through the secretion of neurotrophic factors. These upgrades were studied and tested *in vitro* and will be included in future *in vivo* trials of the multimodular device.

## 9.4. Incorporation of silk fibroin

The use of conduit-shaped hydrogels based solely on HA has a certain disadvantage related to its relative fragility. Therefore, as indicated in section 9.1, an internal fibrillar structure has been developed that ends in more rigid conical structures on which perform the suture. However, the fragility of the HA conduits, specifically against shear forces, could imply a certain disadvantage of the device in terms of its manipulability when inserted surgically, since it requires great delicacy and the risk of breakage when manipulated by the surgeon is important. For this reason, it was decided to investigate the improvement of its mechanical properties through the introduction of silk fibroin, which is a biocompatible and biodegradable material that is commonly used for biomedical applications in combination with HA [21–28]. SF was combined with HA before its crosslinking and once crosslinked with DVS, the mechanical properties against shear stress of the hydrogel improved thanks to the interaction of both polymeric chains. In addition, the incorporation of silk fibroin provided a better adhesion and proliferation of SCs, since SF presents binding motifs with a great number of basic amino acids, especially arginine, which can be recognized by transmembrane cell adhesion proteins such as integrins [29–31]. This led to a faster formation of the SCs sheath inside the HA-SF conduit, which can be of interest in the future medical application of the conduits.

## 9.5. Electroconductive substrates

Apart from improving the structural properties of the device, the incorporation of strategies to increase axonal growth were also studied. One of these strategies is the electrical stimulation using an electroconductive substrate, for which the incorporation of electroconductive properties to the fibrillar substrate was studied for the electrical

stimulation of nearby cells. For this, the coating of PLA fibers with an electroconductive polymer that homogeneously covered its surface was carried out. Different electroconductive polymers were considered, finally opting for an *in situ* chemical coating with polypyrrole (PPy) using different coating protocols and studying their physicochemical and electrical characteristics, since the geometry of the fibers and substrates could affect the PPy coating. Chemical polymerization is superior to electrochemical polymerization in being able to combine with templates to prepare PPy with designed nanostructures, which demonstrates great conductivity, high specific surface area, light weight, rapid ion exchange, and superior mechanical properties [32].

PPy is a heterocyclic polymer that is both electrically conductive and ionically active [33]. Specifically, PPy doped with p-toluenesulfonate (pTS) presents a good ion exchange behavior, presenting both cation and anion transporting properties [34–38]. This ion exchange ability is crucial for many practical applications were PPy/pTS films are used as solid polymer electrolytes. Therefore, our material can be applied as a solid polymer electrolyte since, in this application, there will be ion transport without electron transport and PPy will act as a porous electrode, with no electron transfer between the electrolyte and the polymer [39]. Consider the redox reaction in a conducting polymer. Since the electrolyte is inert, no electrons are transferred between electrolyte and polymer, however, as the polymer charges, ions must move in or out to maintain electroneutrality [39].

In section 5 (Paper 3), the electrical characterization of PLA-PPy materials is performed by electrochemical impedance spectroscopy (EIS) in order to study the complex conductivity and permittivity of the compounds. However, this study was not performed to study the ion exchange properties of the materials, since the measurements are performed in dry conditions, not in wet conditions. The ion exchange properties of

PPy/pTS substrates are well known [34–38], presenting cation-transporting properties, anion-transporting properties and a combination of them. However, it was not the aim of the paper to go deeper into this topic and we were more interested in characterizing the molecular processes of the material. We just indicate the possible commercial application of these substrates as solid polymer electrolytes based on their electrical properties and on the previous literature on PPy doped with pTS.

In section 7 (Paper 5), due to the configuration of the device, the material will not work as a solid polymer electrolyte, since there will be electronic transport, which is a configuration similar to the ones performed in Paper 3 for the in-plane measurements. In this configuration, the material works by closing an electrical circuit with direct contact of the electrodes, where the anode and cathode at each side of the substrate are metals. The objective of performing "in-plane" measurements was to have a conductivity measurement more similar to the one that, in the following papers, the substrate would have, in which the electrodes are located at the ends of the substrate, not at both sides with a sandwich type connection.

To study the effect on the PPy coating of different factors such as the curvature radius of the fibers, the specific surface area and the amount of material, PLA substrates made of electrospun nanofibers and extruded microfibers were compared. The results showed that for small concentrations of the pyrrole (Py) monomer (≤10.5 mM) the coating was not homogeneous, presenting discontinuities, while high concentrations of Py (≥28 mM) led to the appearance of many PPy aggregates. Therefore, an intermediate concentration of Py (14 mM) was chosen for the coating of PLA fibers used *in vitro*, trying that the amount of PPy was the minimum necessary. Comparing nanofibers and microfibers, for the same coating protocol more PPy was deposited in nanofiber substrates due to their higher surface area, but with a lower thickness of the PPy

coating, so similar conductivities were obtained. However, for the same mass fraction of PPy, higher conductivities were obtained for microfiber substrates due to the lower tortuosity of the path that travel the electrical charges and the lower number of interfaces.

The electrical conductivity measurements showed that the PLA fibers coated with PPy became electrically conductive, with a conductivity that increased with the mass fraction of PPy that was present. When the mass fraction of PPy was high enough (around 27%), a percolation effect was observed with a stabilization of the conductivity, indicating a perfect continuity between PPy grains. In addition, the stability of the PPy coverage was studied, showing a high stability of the conductivity when storaged at vacuum conditions.

The *in vitro* biological behavior of SCs and dorsal root ganglia (DRG) seeded on PLA fibers coated with PPy was studied. Both microfiber and nanofiber substrates were manufactured with a high fiber alignment, since it was previously observed that a unidirectional topographic cue is key to guide the growth of axons in a specific direction, avoiding a radially and randomly growth of axons [40–44]. In this way, the effect of fibers with two different diameters (microfibers and nanofibers) on SCs behavior and on axonal extension and sprouting was studied, as well as the biological effect of the PPy coating. It was observed that a greater radius of curvature of the fibers (microfibers) favored the motility and cell-cell interaction of SCs, improving the axonal growth. On the fibers coated with PPy the SCs adhered and proliferated satisfactorily, and, in addition, a greater axonal extension was observed when PPy was present, possibly due to the greater surface nanoroughness of the substrate that could improve DRG adhesion.

## 9.6. Electrical stimulation of SCs and DRG

Since the best biological results were obtained for the PPy coated microfibers, a sequential culture of SCs and DRG was electrically stimulated using these electroconductive substrates. It is important to highlight at this point the confusing panorama presented by the literature regarding the electrical stimulation of cells from the nervous system, both glial cells and neurons. On the one hand, the majority of related papers do not employ an electroconductive substrate and therefore the current circulates through the culture medium, giving the stimulation parameters in terms of electric field. On the other hand, papers that employ electroconductive substrates present a very high dispersion of parameters. Regarding the substrates, very different types of substrates are employed and only the applied electric field is provided, without providing the electrical resistance of the substrates, making it impossible to infer the electric current that is circulating through the substrate. In addition, the high conductivity of the culture medium that presents a high number of ions, makes it even more difficult to know the current that circulates through the substrate. Regarding the electrical parameters, there are not a clear set of parameters that provide beneficial effects for nervous system cells. Alternating and direct current, short and long duration stimulation, continuous and discontinuous stimulation, as well as different waveforms and frequencies are applied with good results according to literature. It makes it very difficult to pre-establish the electrical stimulation parameters from literature, and it is not possible to have a preliminary clear orientation, forcing to test different stimulation alternatives.

As the objective was to have a beneficial current circulating through the electroconductive substrate, a new bioreactor for electrical stimulation was developed that allowed to have an electrode-substrate connection avoiding contact of the

electrodes with the culture medium, while preventing the leakage of cell culture medium. It was considered to use direct current (DC) for the stimulation, but it was observed that after a few hours of stimulation, the medium turned from pinkish to yellowish in color. This happened because there was an accumulation of the ionic charges of the culture medium and, therefore, it led to a variation in the pH. This indicated that there was a certain amount of current circulating through the culture medium, even though the electrode-substrate connection was made outside the culture wells. This was due to the similarity between the conductivity of the culture medium (1.95 S/m) and that of the PLA-PPy substrate (1.4 S/m).

As the objective was to minimize the current that circulated through the culture medium and maximize the current that circulated through the electroconductive substrate, it was necessary to increase the conductivity of the substrate. It was thought to increase the amount of PPy present in the microfibers to increase their conductivity, but for the difference to be significant, a very high amount of PPy was required, which gave rise to large PPy aggregates that put the directionality of the axons at risk. Thus, it was decided to include 3 gold microfibers as part of the PLA-PPy microfiber substrate but avoiding a direct contact between the gold microfibers and the cells because DRG didn't attach properly when the gold microfibers were placed on top of the substrate. With the incorporation of the gold microfibers, it was possible to increase the conductivity of the substrate up to $2.4 \cdot 10^5$ S/m, several orders of magnitude above the conductivity of the culture medium, while maintaining a vast majority of PLA-PPy microfibers, so the amount of current circulating through the culture medium was minimized.

In addition, to minimize the effect of the accumulation of charges that could occur with part of the current circulating through the culture medium, it was decided to

switch from DC to alternating current (AC). Another possible solution could have been to continue using DC but including salt bridges to maintain the charges balance. However, the developed bioreactor was an 8-well system, and this implementation was very complex to perform. In addition, several studies had used AC for neuronal stimulation with success [17,45–48], so it was decided to investigate this pathway. Regarding the future *in vivo* application of the electroconductive substrate, it would be necessary to study the need to include gold microfibers according to the conductivities of the surrounding tissue but, if necessary, gold is a biocompatible material that is already used in various biomedical applications in the nervous system [49–52]. Furthermore, since it is a very small percentage of the total microfibers (0.5%), there is not a significant stiffening of the system.

Regarding the stimulation parameters employed, it was difficult to rely on bibliographic data since there were a multitude of aspects that made impossible to transfer the results to our conditions. For example, most previous studies used two electrodes placed in contact with the culture medium, without an electroconductive substrate through which the current could flow. Likewise, both in these types of studies and in those that do use an electroconductive substrate, DC was usually used instead of AC. In the cases in which an electroconductive substrate with DC was employed, the use of salt bridges was necessary to avoid the accumulation of charges and the change in pH of the culture medium. As previously mentioned, the use of salt bridges in each of the wells of the developed device meant introducing a technical complexity and a risk of contamination and leaks that was not affordable. Likewise, this did not prevent the current from circulating through the culture medium, so it was decided to employ AC instead of DC, since the AC maintains the balance of the ionic charges of the medium.

In addition, the use of low frequencies allows obtaining situations very similar to those of DC.

Another aspect that should be noted is that it was decided to set the circulating current as a fixed parameter, not the electric field, because of the use of an electroconductive substrate through which the current circulates. The circulating electric current is a key parameter to avoid possible thermal effects on the culture medium and to avoid cell death, since a high electric current may affect to the orientation of the membrane lipids and may also cause an irreversible permeabilization of the cell membrane or directly oxidize cellular constituents [53–56]. This introduced a new complexity, since the papers of electrical stimulation of cells usually only give the applied electric field, without giving data of resistances or conductivities, reason why the circulating current cannot be inferred. This was another reason that made it difficult to apply the parameters of previous studies, since knowing the circulating current is a key parameter.

Based on the studies with an electroconductive substrate that could be taken as a reference [17–19,43,48,57,58], it was decided to set the stimulation time at 8 hours/day, since it was a parameter found recurringly. The total culture time was limited by the length of the wells, seeking to prevent the axons from touching the edges of the well, so that it could not exceed 4 days. One day was left between the end of the stimulation and the fixation of the culture, since it was a parameter found on a recurring basis, limiting the total stimulation time to 3 days. Once these parameters were set, a scanning of currents (between 0.5 mA and 3 mA) and frequencies (between 3 Hz and 250 Hz) was performed, looking for a favorable effect on axonal growth. It was observed that currents above 0.5 mA and frequencies above 50 Hz had a negative effect, obtaining a favorable effect on axonal growth for a current of 0.5 mA and a frequency of 3 Hz.

These results imply, in first place, that there is an important effect of the circulating electric current on axonal growth, being harmful above 0.5 mA. According to literature, an excess of electric current may have a harmful effect on cellular membrane, and may lead to an irreversible permeabilization of it [53–56]. In second place, there is also an important effect of the frequency, being low frequencies more beneficial than high frequencies. This agree with the papers that find a beneficial effect on axonal growth when using DC, because the mechanism of AC with a frequency of 3 Hz is similar to the one of DC.

## 9.7. Neurotrophic factors

Another widely studied strategy to improve axonal regeneration is the stimulation by neurotrophic factors. Unmodified SCs are capable of naturally generating and secreting neurotrophic factors such as the nerve growth factor (NGF), the brain-derived neurotrophic factor (BDNF) and the neurotrophin-3 (NT-3), which can improve axonal growth, but at relatively low concentrations [59–61]. Given that the developed system already had pre-seeded SCs integrated, it was decided to improve the biological stimulation through the gene transfection of these cells. Therefore, the aim of the gene transfection of SCs was to increase the levels of secretion of neurotrophic factors, especially BDNF. BDNF was chosen for its proven positive effect on neurons survival and on axonal regeneration [62–64], but the method can be extended to other neurotrophic factors such as NGF or NT-3.

Electroporation was chosen as the method to perform the gene transfection, since it is a method with high levels of transfection and a low cell death rate. For this, a scan of different parameters (number of cells, content of water in the culture medium, plasmid mass and electric field amplitude) was carried out until the optimal method was achieved. With this, it was possible to obtain SCs with a BDNF secretion 100 times

higher than not transfected SCs. Furthermore, thanks to said increased secretion of BDNF, an increase in the maximum length of axons of 35% and an increase in the area of axons of 40% was observed *in vitro*, compared to using non-transfected SCs. This provides us a robust and repetitive system to generate large amounts of transfected SCs with an increased secretion of BDNF that can be used in future *in vivo* assays in animal models.

It should be noted that the increased secretion of BDNF has a limited duration (approximately 15 days), since the plasmid encoding BDNF enters into the nucleus but does not integrate into the chromosomal DNA of the cell. Therefore, although the transcription and translation mechanisms of the cell do use these plasmids, their quantity decreases with each cycle of cell mitosis, so after approximately 15 days the quantity of plasmids in each cell decreases greatly. Therefore, using this transfection method would have a more acute than chronic effect on nerve regeneration *in vivo*. There are other gene transfection techniques by which said secretion could be prolonged, such as viral transfection or by selecting and amplifying the electrotransfected SCs that have incorporated the plasmid into their genetic code by chance (a very low %). However, they have some drawbacks such as possible mutations since the plasmid sequence is randomly integrated into the genetic code of the cell [65–67].

## 9.8. Incorporation of the improvement development into the multimodular device

The upgrades developed have been tested *in vitro*, but with the intention of being incorporated into the multimodular system in future *in vivo* tests in animal models for long peripheral nerves. Regarding the stimulation of the electroconductive microfibers,

it could be applied in 2 different ways *in vivo*. One possible option is the stimulation directly applying an electric current, placing a ring-type electrode at each end of the internal microfiber conduit in contact with PLA-PPy and gold microfibers (**Figure 3**). This would require the electrode leads to connect to a generator that can be placed subcutaneously and replaced or recharged periodically, without the need of having leads coming out of the body and thus avoiding the possible risk of infection/breakage. This is already done with pacemakers, defibrillators and devices for deep-brain stimulation for Parkinson's disease and for the spinal cord stimulation for chronic pain [68–74].

Another option that would also eliminate the need of having electrodes coming out from the body would be to use the closed circuits (loops) that could be formed with the electroconductive microfibers if they were connected at the extremes. That would allow the generation of an induced current circulating through the electroconductive loops when an alternating magnetic field was applied. This could be achieved by employing an approach similar to that applied for the transcranial magnetic stimulation, by which an alternating magnetic field is employed to induce an electric current at a specific area of the brain by the phenomenon of electromagnetic induction [75,76].

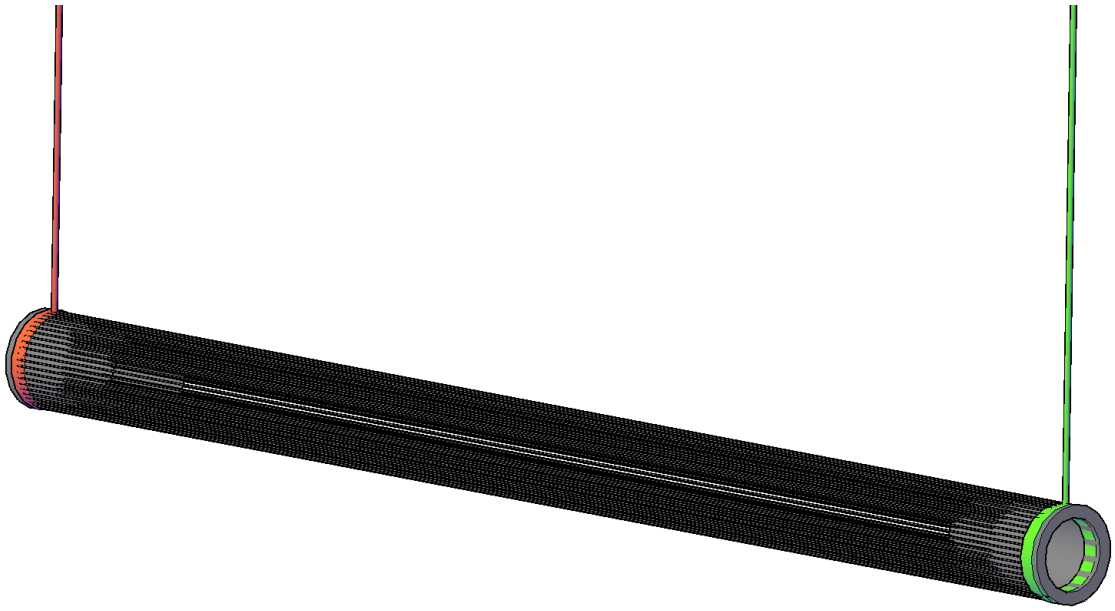

**Figure 3**. Representation of the inner electroconductive microfibers with annular electrodes at the extremes for the electrical stimulation of the device *in vivo* with a direct application of current.

Regarding the incorporation of the electrotransfected SCs in the human clinic, an intermediate step related to extracting SCs from the patient and transfecting them would be necessary. Other option could be to use previously extracted SCs from other patients to save time, but it could require the immunosuppression of the patient. Apart from this aspect, SCs physiology do not differ too much between mammals[77] and the electrotransfection protocol validated with rat SCs should be applicable for human SCs with little changes. Then the procedure would be quite the same, following a similar seeding method.

# 9.9. References

1. A. Thibodeau, T. Galbraith, C. M. Fauvel, H. T. Khuong, F. Berthod, *Biomaterials* **2022**, *280*, 121269.
2. T. M. Saffari, M. Bedar, C. A. Hundepool, A. T. Bishop, A. Y. Shin, *Neural Regen. Res.* **2020**, *15*, 1573.

3. C. Chalfoun *et al.*, *Microsurgery* **2003**, *23*, 60.

4. Q. Min, D. B. Parkinson, X. P. Dun, *Glia* **2021**, *69*, 235.

5. F. J. Rodríguez, E. Verdú, D. Ceballos, X. Navarro, *Exp. Neurol.* **2000**, *161*, 571.

6. K. R. Jessen, R. Mirsky, A. C. Lloyd, *Cold Spring Harb. Perspect. Biol.* **2015**, *7*, a020487.

7. K. R. Jessen, R. Mirsky, *J. Physiol.* **2016**, *594*, 3521.

8. Y. Niu, M. Galluzzi, *J. Mater. Chem. B* **2020**, *8*, 11063.

9. S. V. More *et al.*, *Molecules* **2012**, *17*, 6728.

10. K. Moore, M. Macsween, M. Shoichet, *Tissue Eng.* **2006**, *0*, 060303124145002.

11. S. Higgins, J. S. Lee, L. Ha, J. Y. Lim, *Biores. Open Access* **2013**, *2*, 212.

12. Z. Q. Feng *et al.*, *J. Biomed. Mater. Res. - Part A* **2016**, *104*, 966.

13. C. Deister, C. E. Schmidt, *J. Neural Eng.* **2006**, *3*, 172.

14. X. Cao, M. S. Shoichet, *Neuroscience* **2001**, *103*, 831.

15. C. Labelle, N. Leclerc, *Dev. Brain Res.* **2000**, *123*, 1.

16. Y. Zou *et al.*, *ACS Appl. Mater. Interfaces* **2016**, *8*, 12576.

17. A. F. Quigley *et al.*, *Adv. Mater.* **2009**, *21*, 4393.

18. Y. Zhao *et al.*, *Biomaterials* **2020**, *255*, 120164.

19. M. Imaninezhad *et al.*, *J. Neural Eng.* **2018**, *15*.

20. Y. Ishibashi, K. Uesugi, K. Morishima, *SII 2016 - 2016 IEEE/SICE Int. Symp. Syst. Integr.* **2017**, 797, doi:10.1109/SII.2016.7844097.

21. N. H. Chi, M. C. Yang, T. W. Chung, N. K. Chou, S. S. Wang, *Carbohydr Polym* **2013**, *92*, 591.

22. N. H. Chi *et al.*, *Biomaterials* **2012**, *33*, 5541.

23. J. Zhou *et al.*, *Carbohydr Polym* **2016**, *143*, 301.

24. S. Yan, M. Li, Q. Zhang, J. Wang, *Fibers Polym.* **2013**, *14*, 188.

25. C. Foss, E. Merzari, C. Migliaresi, A. Motta, *Biomacromolecules* **2013**, *14*, 38.

26. T. W. Chung, Y. L. Chang, *J Mater Sci Mater Med* **2010**, *21*, 1343.

27. N. R. Raia *et al.*, *Biomaterials* **2017**, *131*, 58.

28. S. Yan *et al.*, *Acta Biomater* **2013**, *9*, 6771.

29. N. Minoura *et al.*, *Biochem. Biophys. Res. Commun.* **1995**, *208*, 511.

30. G. A. Monteiro, A. V Fernandes, H. G. Sundararaghavan, D. I. Shreiber, *Tissue Eng. Part A* **2011**, *17*, 1663.

31. C. Calcagno, M. E. Lobatto, P. M. Robson, A. Millon, *Hum Mutat.* **2016**, *28*, 1304.

32. H. D. Tran, D. Li, R. B. Kaner, *Adv. Mater.* **2009**, *21*, 1487.

33. B. K. Gu, D. J. Choi, S. J. Park, Y. Kim, C. Kim, *Cutting-Edge Enabling Technol. Regen. Med. Adv. Exp. Med. Biol.* **2018**, *1078*.

34. C. Jin, F. Yang, W. Yang, *J. Appl. Polym. Sci.* **2006**, *101*, 2518.

35. J. Chengyou, Y. Fenglin, *Sensors Actuators, B Chem.* **2006**, *114*, 737.

36. S. Li, Y. Qiu, X. Guo, *J. Appl. Polym. Sci.* **2009**, *114*, 2307.

37. T. Raudsepp, M. Marandi, T. Tamm, V. Sammelselg, J. Tamm, *Electrochim. Acta* **2014**, *122*, 79.

38. V. Syritski, A. Öpik, O. Forsén, *Electrochim. Acta* **2003**, *48*, 1409.

39. M. Warren, Electron. Struct. Eff. Electrochem. Polypyrrole **2005.**

40. W. Zhu, F. Masood, J. O'Brien, L. G. Zhang, *Nanomedicine Nanotechnology, Biol. Med.* **2015**, *11*, 693.

41. Y. S. Lee, G. Collins, T. Livingston Arinzeh, *Acta Biomater.* **2011**, *7*, 3877.

42. J. Y. Lee, C. A. Bashur, A. S. Goldstein, C. E. Schmidt, *Biomaterials* **2009**, *30*, 4325.

43. Y. Zou *et al.*, *ACS Appl. Mater. Interfaces* **2016**, *8*, 12576.

44. Y. Xu, Z. Huang, X. Pu, G. Yin, J. Zhang, *Cell Prolif.* **2019**, *52*.

45. Y. J. Chang, C. M. Hsu, C. H. Lin, M. S. C. Lu, L. Chen, *Biochim. Biophys. Acta - Gen. Subj.* **2013**, *1830*, 4130.

46. P. J. Kumar, R. D. Adams, A. B. Harkins, E. D. Engeberg, R. K. Willits, *IEEE Trans. Biomed. Eng.* **2016**, *63*, 1257.

47. L. Ghasemi-Mobarakeh *et al.*, *J. Tissue Eng. Regen. Med.* **2011**, *5*, e17.

48. Z. Zhou *et al.*, *Biomater. Sci.* **2018**, *6*, 2375.

49. M. Yadid, R. Feiner, T. Dvir, *Nano Lett.* **2019**, *19*, 2198.

50. P. M. Tiwari, K. Vig, V. A. Dennis, S. R. Singh, *Nanomater. 2011, Vol. 1, Pages 31-63* **2011**, *1*, 31.

51. N. Elahi, M. Kamali, M. H. Baghersad, *Talanta* **2018**, *184*, 537.

52. M. Adel *et al.*, *Microelectron. Eng.* **2017**, *173*, 1.

53. Q. Luo, H. Wang, X. Zhang, Y. Qian, *Appl. Environ. Microbiol.* **2005**, *71*, 423.

54. K. P. Drees, M. Abbaszadegan, R. M. Maier, *Water Res.* **2003**, *37*, 2291.

55. T. Matsunaga *et al.*, *Appl. Environ. Microbiol.* **1992**, *58*, 686.

56. J. C. Weaver, Y. A. Chizmadzhev, *Bioelectrochemistry Bioenerg.* **1996**, *41*, 135.

57. S. Aznar-Cervantes *et al.*, *Mater. Sci. Eng. C* **2017**, *79*, 315.

58. Y. Li *et al.*, *Colloids Surfaces B Biointerfaces* **2020**, *191*, 1.

59. N. El Seblani, A. S. Welleford, J. E. Quintero, C. G. van Horne, G. A. Gerhardt, *J. Neurosci. Methods* **2020**, *335*, 108623.

60. K. R. Jessen, P. Arthur-Farraj, *Glia* **2019**, *67*, 421.

61. G. Nocera, C. Jacob, *Cell. Mol. Life Sci.* **2020**, *77*, 3977.

62. C. Zuccato, E. Cattaneo, *Nat. Rev. Neurol. 2009 56* **2009**, *5*, 311.

63. D. K. Binder, H. E. Scharfman, *Growth Factors* **2004**, *22*, 123.

64. S. Liu *et al.*, *Acta Biomater.* **2017**, *60*, 167.

65. T. K. Kim, J. H. Eberwine, *Anal. Bioanal. Chem.* **2010**, *397*, 3173.

66. N. B. Woods *et al.*, *Blood* **2003**, *101*, 1284.

67. S. Hacein-Bey-Abina *et al.*, *N. Engl. J. Med.* **2003**, *348*, 255.

68. E. Krames, *Best Pract. Res. Clin. Anaesthesiol.* **2002**, *16*, 619.

69. R. J. Coffey, *Artif. Organs* **2009**, *33*, 208.

70. F. V. Y. Tjong *et al.*, *Europace* **2016**, *18*, 1740.

71. M. C. Salling, D. Martinez, *Neuropsychopharmacology* **2016**, *41*, 2798.

72. J. Huang, K. K. Patton, J. M. Prutkin, *PACE - Pacing Clin. Electrophysiol.* **2016**, *39*, 1240.

73. B. J. Woodington *et al.*, *Sci. Adv.* **2021**, *7*, 1.

74. S. Santaniello, J. T. Gale, S. V. Sarma, *Wiley Interdiscip. Rev. Syst. Biol. Med.* **2018**, *10*, 1.

75. M. Hallett, *Neuron* **2007**, *55*, 187.

76. M. Kobayashi, A. Pascual-Leone, *Lancet* **2003**, *2*, 145.

77. M. D. Baker, *Prog. Biophys. Mol. Biol.* **2002**, *78*, 83.

# 10. Conclusions

Given the experimental results shown previously concerning the development, *in vivo* testing and *in vitro* upgrading of a multimodular device for the regeneration of long nerve defects, the following general conclusions can be highlighted:

1. A multimodular device adapted to the dimensions of the rabbit sciatic nerve has been obtained. It is formed by HA modular conduits joined by an internal tubular structure that allows a homogeneous distribution of PLA microfibers along the lumen of the HA conduits, serving as topographical cues for the axonal guidance. Furthermore, the multimodular device has been pre-seeded with SCs which form an internal sheath that covers both the lumen of the HA conduits and the PLA microfibers surface, turning it into a biohybrid system that favors axonal regeneration.
2. The multimodular device tested in a long gap (15 mm) rabbit sciatic nerve defect model has shown a successful nerve regeneration 6 months after its implantation. The results have shown that the multimodular device achieves a better nerve regeneration than the unimodular device, with a higher vascularization. In addition, the multimodular device with pre-seeded SCs achieves an additional increase in nerve regeneration, showing the beneficial effect of SCs.
3. SF has been successfully incorporated into the HA-based conduit manufacturing process. With the incorporation of SF, it has been possible to obtain an improvement of the mechanical properties of the hydrogel, especially against shear forces, which is of great importance due to the poor mechanical properties that HA conduits present, which complicates their handling. The *in vitro* culture of SCs has shown an improvement of the biological properties in terms of adhesion and cell proliferation on the surface of the material thanks to the addition of SF. This is because SF

provides arginine residues that interact with transmembrane cell adhesion proteins such as integrins.

4. Biocompatible and highly aligned fibrillar substrates of PLA coated with the electroconductive polymer PPy have been obtained by *in situ* chemical polymerization, studying different fiber diameters (500 nm and 10 μm) and mass fractions of PPy (4%, 13%, 18%, 23%, 27% and 34%). The substrates present a good environmental stability and electrical conductivities between $6.3 \cdot 10^{-9}$ S/cm and $5.2 \cdot 10^{-2}$ S/cm for through-plane measurements (30 °C, 15.4 Hz), while conductivities between $1.2 \cdot 10^{-5}$ S/cm and 0.22 S/cm are obtained for in-plane applications.
5. PLA-PPy substrates with a low content of PPy (<13%wt) show a combination of two processes: a temperature-dependent relaxation due to the glass transition of PLA and a temperature-independent conduction process. In this case, the conductivity varies linearly (slope $\approx 1$) in the range of high frequencies, following a capacitive behavior. For higher mass fractions of PPy, the conduction process hides the polymer relaxation process, and the real part of conductivity is constant for all range of frequencies, meaning that the impedance has only a resistive contribution, which is the typical demeanor of a conductive material. A percolation effect is observed for a mass fraction of PPy of 27%, indicating a perfect continuity between PPy grains.
6. PLA-PPy substrates with intermediate mass fractions of PPy has been tested *in vitro*, showing a good cytocompatibility with SCs and DRG. It has been observed that the PPy coating has a beneficial effect on axonal extension from DRG thanks to the greater surface roughness that favors the adhesion of the DRG. In addition, micro-sized PLA-PPy substrates present a higher axonal extension than nano-sized

ones, thanks to the higher migration speed of SCs from the DRG body, related to the higher motility that SCs present on micro-sized substrates. For this reason, micro-sized PLA-PPy substrates are chosen as the best ones.

7. Thanks to the electrical stimulation of the electroconductive substrates that have been developed, an increased axonal extension and axonal sprouting from DRG has been obtained when an alternating current of 0.5 mA with a frequency of 3 Hz is applied. In addition, the electrically stimulated group presents a higher expression of neuronal, Schwann cells, proliferation and neurotrophins related biomarkers, confirming that this group has a stronger nerve regeneration potential.
8. Gene transfected SCs with an increased secretion of the brain-derived neurotrophic factor (BDNF) have been obtained by means of the electroporation technique. In addition, these genetically modified SCs have been successfully included into the biohybrid system, acting as pumps of BDNF with a beneficial effect on axonal growth.

# 11. Future perspective

Once the proof of concept has been carried out in a rabbit sciatic nerve model with a reduced number of specimens proving the favorable effect on nerve regeneration of the multimodular nerve guidance conduit (NGC) with pre-seeded Schwann cells, more steps must be taken to approach the device to the clinic. The following step that should be taken is to carry out a study with a greater number of specimens, to confirm the results in a more robust way and to study in more detail all the possible adverse effects and problems that may appear, both during surgery and during recovery. Likewise, different time points of the regenerative process should be evaluated, not only the final time as it was done in the pilot study. In addition, an electrophysiological study should be included to verify the functional recovery of the nerve.

It will be also necessary to carry out a study in larger animals such as pigs or sheep, since this will allow the use of longer NGCs with a greater number of modules. This will serve to evaluate the nerve regeneration in gaps of more than 15 mm, using the multimodular NGC to bridge gaps even 10 times longer than the ones studied in rabbits. This study is necessary to evaluate the performance of the multimodular conduit in very long nerve lesions similar to those that can appear in humans. Nowadays, commercial conduits cannot be applied to this type of lesions since they are formed by a single piece that fractures and collapses when applied to long gaps. In addition, they cannot be adapted to the natural trajectory of the nerve and present many complications to vascularize the central part of the conduit.

Apart from these *in vivo* studies, the developed NGCs can be improved in various aspects. For example, in a similar way to the pre-seeding with Schwann cells, HUVEC cells could be pre-seeded inside the conduit modules, leading to a vascularization of the conduits prior to the surgery intervention. With this pre-vascularization it would be improved the blood supply throughout the entire length of

the NGC. This would improve both the nutrients arrival for Schwann cells and the growth of new axons. In addition, more macrophages derived from blood would be present, contributing to the cleaning process of the degenerated products of the myelin sheath and axons that are produced after the nerve injury.

In addition, as commented in the general discussion section, all the upgrades developed *in vitro* for both the electrical and biochemical stimulation of the nervous regeneration will be incorporated to the complete device and tested *in vivo*. In this case, the rabbit sciatic nerve model would be enough, since the objective will be to increase the regeneration velocity for a given gap. For the biochemical stimulation, electrotransfected Schwann cells with an increased secretion of growth factors such as BDNF, NGF or NT-3 will be pre-seeded, with a constant or gradual concentration in order to obtain a microenvironment that favors an increased speed of nerve regeneration. For the electrical stimulation, two options would be available. One option would be the stimulation by applying an electric current using two ring-type electrodes at the extremes of the microfiber conduit, that would be connected to a generator placed subcutaneously. This would avoid the use of leads coming out of the body, which would present many problems due to infections or breaks. The second option would be to apply an alternating magnetic field to induce a circulating current through the loops formed by the electroconductive microfibers. This would avoid the use of a generator and could be achieved in a way similar to the transcranial magnetic stimulation.

# 12. Contributions

As main results of this doctoral thesis, the following papers have been published in high-impact journals:

- **Fernando Gisbert Roca**, Luis Gil Santos, Manuel Mata Roig, Lara Milian Medina, Cristina Martínez-Ramos, and Manuel Monleón Pradas. Novel Tissue-Engineered Multimodular Hyaluronic Acid-Polylactic Acid Conduits for the Regeneration of Sciatic Defect. Biomedicines (2022) 10, 963. doi: 10.3390/biomedicines10050963
- **Fernando Gisbert Roca**, Paloma Lozano Picazo, José Pérez-Rigueiro, Gustavo Victor Guinea Tortuero, Manuel Monleón Pradas, and Cristina Martínez-Ramos. Conduits Based on the Combination of Hyaluronic Acid and Silk Fibroin: Characterization, *in Vitro* Studies and *in Vivo* Biocompatibility. International Journal of Biological Macromolecules (2020) 148:378–90. doi: 10.1016/j.ijbiomac.2020.01.149
- **Fernando Gisbert Roca**, Abel García-Bernabé, Vicente Compañ Moreno, Cristina Martínez-Ramos, and Manuel Monleón Pradas. Solid Polymer Electrolytes Based on Polylactic Acid Nanofiber Mats Coated with Polypyrrole. Macromolecular Materials and Engineering (2021) 306:2000584. doi: 10.1002/mame.202000584
- **Fernando Gisbert Roca**, Jorge Más Estellés, Manuel Monleón Pradas, and Cristina Martínez-Ramos. Axonal Extension from Dorsal Root Ganglia on Fibrillar and Highly Aligned Poly(Lactic Acid)-Polypyrrole Substrates Obtained by Two Different Techniques: Electrospun Nanofibres and Extruded Microfibres. International Journal of Biological Macromolecules (2020) 163:1959–69. doi: 10.1016/j.ijbiomac.2020.09.181

- **Fernando Gisbert Roca**, Franck M. André, Jorge Más Estellés, Manuel Monleón Pradas, Lluis M. Mir, and Cristina Martínez-Ramos. BDNF-Gene Transfected Schwann Cell-Assisted Axonal Extension and Sprouting on New PLA–PPy Microfiber Substrates. Macromolecular Bioscience (2021) 21:2000391. doi: 10.1002/mabi.202000391
- **Fernando Gisbert Roca**, Sara Serrano Requena, Manuel Monleón Pradas, and Cristina Martínez-Ramos. Electrical Stimulation Increases Axonal Growth from Dorsal Root Ganglia Co-cultured with Schwann Cells in Highly Aligned PLA-PPy-Au Microfiber Substrates. International Journal of Molecular Sciences (2022) 23, 6362. doi: 10.3390/ijms23126362

As other results of this doctoral thesis, the following papers have also been published in high-impact journals:

- Hoda Elkhenany, Pablo Bonilla, Esther Giraldo, Ana Alastrue Agudo, Michael J. Edel, María Jesus Vicent, **Fernando Gisbert Roca**, Cristina Martínez Ramos, Laura Rodríguez Doblado, Manuel Monleón Pradas, and Victoria Moreno Manzano. A Hyaluronic Acid Demilune Scaffold and Polypyrrole-Coated Fibers Carrying Embedded Human Neural Precursor Cells and Curcumin for Surface Capping of Spinal Cord Injuries. Biomedicines (2021) 9, 1928. doi: 10.3390/biomedicines9121928
- María Oliver-Ferrándiz, Lara Milián, María Sancho-Tello, José Javier Martín de Llano, **Fernando Gisbert Roca**, Cristina Martínez-Ramos, Carmen Carda, and Manuel Mata. Alginate-Agarose Hydrogels Improve the *In Vitro* Differentiation of Human Dental Pulp Stem Cells in Chondrocytes. A Histological Study. Biomedicines (2021) 9:834. doi: 10.3390/biomedicines9070834

Also, the following contributions to national and international conferences have been made:

- **Fernando Gisbert Roca**, Cristina Martínez Ramos, and Manuel Monleón Pradas. Nerve guidance conduits based on the combination of hyaluronic acid and silk fibroin: characterization and *in vitro* studies. II National Congress of Young Researchers in Biomedicine and IV Congress of Biomedicine PhD students in Valencia. Valencia (Spain). 23/11/2017 - 24/11/2017.
- Cristina Martínez Ramos, María José Morillo Bargues, **Fernando Gisbert Roca**, Laura Rodríguez Doblado, Tomás García Sanchez, Lluis Mir, Ester Giraldo Reboloso, Victoria Moreno Manzano, and Manuel Monleón Pradas. Electrical stimulation increases schwann cells proliferation inside hyaluronic acid conduits. 2018 EMF-Med 1st World Conference on Biomedical Applications of Electromagnetic Fields (EMF-Med 2018). Split (Croatia). 10/09/2018 - 13/09/2018.
- María José Morillo Bargues, Andrea Olivos Osorno, **Fernando Gisbert Roca**, Cristina Martínez Ramos, and Manuel Monleón Pradas. Synthesis and characterization of electrospun polylactic acid (PLLA) membranes for curcumin release. XLI Congress of the Iberian Society of Biomechanics and Biomaterials (SIBB 2018). Madrid (Spain). 18/10/2018 - 19/10/2018.
- **Fernando Gisbert Roca**, José Pérez Rigueiro, Gustavo Víctor Guinea Tortuero, Manuel Monleón Pradas, and Cristina Martínez Ramos. Improvement of the mechanical and biological properties of hyaluronic acid-based nerve guide canals thanks to the incorporation of silk fibroin. XLI Congress of the Iberian Society of Biomechanics and Biomaterials (SIBB 2018). Madrid (Spain). 18/10/2018 - 19/10/2018.

- **Fernando Gisbert Roca**, Jorge Más Estellés, Cristina Martínez Ramos, and Manuel Monleón Pradas. Characterization of electrically conductive polylactic acid (PLA) – polypyrrole (PPy) substrates for neural tissue engineering. 30th Annual Conference of the European Society for Biomaterials (ESB 2019). Dresden (Germany). 09/09/2019 - 13/09/2019.
- **Fernando Gisbert Roca**, Jorge Más Estellés, Manuel Monleón Pradas, and Cristina Martínez Ramos. Conductive polylactic acid (PLA) – polypyrrole (PPy) substrates for neural tissue engineering. 5th International Spinal Cord Repair Meeting (ISCORE 2019). Barcelona (Spain). 13/12/2019 - 14/12/2019.
- **Fernando Gisbert Roca**, Jorge Más Estellés, Cristina Martínez Ramos, and Manuel Monleón Pradas. Bioreactor based on electrically conductive polylactic acid – polypyrrole substrates for the electrical stimulation of nervous systems cells. 11th World Biomaterials Congress (WBC 2020). Online. 11/12/2020 - 15/12/2020.
- **Fernando Gisbert Roca**, Franck M. Andre, Cristina Martínez Ramos, Lluis Mir, Lluis, and Manuel Monleón Pradas. Increased brain-derived neurotrophic factor (BDNF) secretion by transfected Schwann cells enhances axonal extension from rat DRG on aligned fiber scaffolds. 11th World Biomaterials Congress (WBC 2020). Online. 11/12/2020 - 15/12/2020.